Prediction of Dowel Corrosion and Effect on Performance of Concrete Pavements

FINAL REPORT

May 2025

By (PI) Dr. Julie Vandenbossche, PE, PhD
University of Pittsburgh

IRISE CONSORTIUM

CONTRACT # PITTIRISE2018

Technical Report Documentation Page

1. Report No. IRISE-25-P23-01-01	**2. Government Accession No.**	**3. Recipient's Catalog No.**

4. Title and Subtitle Prediction of dowel corrosion and effect on performance of concrete pavements	**5. Report Date** May 2025 **6. Performing Organization Code**
7. Author(s) **Julie Vandenbossche, Charles Donnelly, Gabriela Salach, Megan Darnell, Alessandro Fascetti**	**8. Performing Organization Report No.**
9. Performing Organization Name and Address IRISE Department of Civil and Environmental Engineering University of Pittsburgh Benedum Hall 3700 O'Hara Street | Pittsburgh, PA 15261	**10. Work Unit No. (TRAIS)** **11. Contract or Grant No.** PITTIRISE2018
12. Sponsoring Agency Name and Address The Pennsylvania Department of Transportation Bureau of Planning and Research Commonwealth Keystone Building 400 North Street, 6th Floor | Harrisburg, PA 17120-0064	**13. Type of Report and Period Covered** December 2022 – December 2024 **14. Sponsoring Agency Code**

15. Supplementary Notes
PI contact info: 742 Benedum Hall, 3700 O'Hara Street, Pittsburgh, PA 15261 – jmv7@pitt.edu

16. Abstract
Corrosion of metallic dowel bars is a significant issue that can lead to a decrease in the long-term performance of jointed plain concrete pavements. The high chloride exposure from deicing agents coupled with moisture penetration at transverse joints creates a corrosive environment. Corrosion development is a complex phenomenon affected by both pavement design and climatic features. Current pavement performance prediction models are unable to account for dowel corrosion due to the limited understanding of this. This project was performed to improve the existing pavement performance models by incorporating the effect of dowel corrosion in the model framework. A review of available corrosion databases and corrosion prediction models was performed to inform the development of a novel accelerated dowel corrosion laboratory investigation. A range of dowel bars currently on the market were evaluated to quantify the development of corrosion and the effect on pavement performance. The results from the accelerated corrosion study were used to update the existing faulting prediction framework to account for the effect of corrosion on faulting development. The faulting model was calibrated with field performance data from in-service concrete pavements. The products of this project can be used to better account for the effect of corrosion on long-term dowel performance. Additionally, the revised faulting model enables the consideration of non-metallic dowels and alternative dowel coatings, which are being implemented in many long-life paving projects.

17. Key Words Concrete pavements; Dowel bars; Faulting; Corrosion; Performance prediction; Accelerated laboratory investigation; Calibration; Field data.	**18. Distribution Statement** No restrictions. This document is available from the National Technical Information Service, Springfield, VA 22161

19. Security Classif. (of this report)	**20. Security Classif. (of this page)**	**21. No. of Pages**	**22. Price**
Unclassified	Unclassified	175	

IRISE

The Impactful Resilient Infrastructure Science & Engineering consortium was established in the Department of Civil and Environmental Engineering in the Swanson School of Engineering at the University of Pittsburgh to address the challenges associated with aging transportation infrastructure. IRISE is addressing these challenges with a comprehensive approach that includes knowledge gathering, decision making, design of materials and assets and interventions. It features a collaborative effort among the public agencies that own and operate the infrastructure, the private companies that design and build it and the academic community to develop creative solutions that can be implemented to meet the needs of its members. To learn more, visit:
https://www.engineering.pitt.edu/irise/.

PITT | IRISE

Acknowledgements

The authors gratefully acknowledge the financial support of all contributing members of IRISE. In addition, we are indebted to the advice and assistance provided by technical panel members Matt Blough of the Pennsylvania Turnpike Commission, Jason Molinero of Allegheny County, Chuck Niederriter and Dave Sciullo of Golden Triangle Construction, Lydia Peddicord of the Pennsylvania Department of Transportation, and Yathi Yatheepan of the Federal Highway Administration.

The authors would also like to thank Lev Khazanovich for his assistance with coding of the Fault Executable file. The support and material/equipment donations provided by Tom Bryan and David Giehll at Bryan Materials Group, Katey Doman at TyeBar, LLC, Karl Zilske at CMC Rebar & Paving Solutions, Brad Zuan at Master Dowel, Chris Schenk at O-Dowel, and Mary Vancura at American Engineering and Testing is greatly appreciated. The following students should also be acknowledged for their assistance with lab work and data analysis: Zachary Brody, Xiangdong Yan, Edmund Jermyn, Jack Parkhurst, and Gianna Bergin.

Disclaimer

CONTENTS

1.0 INTRODUCTION

Corrosion of metallic dowel bars is a significant issue that leads to a decreased long-term performance of jointed plain concrete pavements. Dowel bars are susceptible to corrosion due to the high chloride exposure from deicing agents coupled with moisture penetration into the transverse joints. Corrosion of the dowels can decrease load transfer across the joint, resulting in faulting. Additionally, the expansive byproduct of corrosion can prevent the joint from freely opening and closing. Many states have identified that this seizing of the joint is a significant problem. It is difficult to identify or predict dowel corrosion before major distresses develop, and repairs to distressed joints are costly and disruptive to traffic. Corrosion development is a complex phenomenon affected by both pavement design and climatic features. Current pavement performance prediction models are unable to account for dowel corrosion. Many long-life pavements are being constructed with corrosion resistant dowel materials and are expected to perform for greater than 60 years. Unfortunately, the effect of the long-term corrosion resistance of the various types of dowel bars on increased performance life is not well quantified. This makes it a challenge to justify the additional expenses associated with longer-life dowels.

In this project, the development of corrosion on metallic dowels in concrete pavements is quantified as a function of critical environmental and design parameters. Current corrosion models were reviewed to identify the mechanisms of corrosion development and to identify current limitations in corrosion understanding. Critical factors identified through modeling were used to design a laboratory investigation to evaluate the loss of dowel performance as a function of corrosion development. The accelerated test consists of doweled beam specimens that are subjected to both mechanical and environmental loading conditions. Key pavement design parameters are considered, including dowel diameter, dowel material (carbon steel, stainless steel, fiber reinforced), and coating (epoxy, zinc-clad, galvanized). An accelerated testing program was designed to simulate corrosion conditions based on available field data. To determine the loss of pavement performance as a function of corrosion development, the corrosion of the doweled specimens is evaluated and correlated to the increased pavement deflection under loading. The force required to open the joint was measured to evaluate the potential damage caused by the expansive byproducts of corrosion.

Results from the laboratory investigation are used to develop predictive performance models that account for critical parameters affecting corrosion development. These algorithms establish underlying relationships between critical design and exposure parameters and loss of joint performance due to corrosion development. The performance models are validated with available performance data from in-service doweled concrete pavements. The results from the computational and experimental analyses are used to identify critical conditions for corrosion development and the corresponding loss of dowel performance. The products from this project work will improve joint performance prediction by considering corrosion, which is a common cause of joint performance degradation in doweled pavements.

2.0 LITERATURE REVIEW

2.1 Introduction

The purpose of this task report is to provide a literature review on dowel bar corrosion development in jointed plain concrete pavements (JPCPs). Corrosion of dowel bars in transverse joints is widely known to decrease the long-term performance of JPCPs, however, the mechanisms of corrosion development are not well understood. In this report, current knowledge pertaining to corrosion development was evaluated to inform the laboratory and computational modeling that will be performed in subsequent tasks of this study.

There are three components to this literature review. First, exposure conditions for doweled pavements are described. Current state practices were reviewed to estimate typical levels of joint exposure to chlorides from deicing salts. The amount of chlorides applied to concrete pavements in Pennsylvania is estimated using maintenance records provided by the Pennsylvania Department of Transportation (PennDOT). Second, current knowledge on dowel corrosion is presented. Relevant laboratory and field studies pertaining to dowel corrosion are reviewed to identify key parameters and gaps in knowledge. Lastly, current corrosion models and databases were evaluated. Key parameters identified in these models and databases are used to inform the accelerated corrosion test.

2.2 Exposure Conditions

Corrosion is an electrochemical reaction involving the movement of electrons from metal ions in dowels, such as iron (Fe), to the concrete medium. A reduction of the cross-sectional area of the dowel causes a decrease in the dowel performance. Concrete is alkaline, which normally serves to resist corrosion by forming a passive layer around the steel. This passive layer acts as a protective layer against the development of corrosion [1]. However, concrete pavements can be exposed to corrosive agents such as chlorides, typically in the form of deicing salts. There are a number of deicing materials used by state agencies, which contain chlorides, including sodium chloride (NaCl), magnesium chloride (MgCl), calcium chloride (CaCl). These are often applied as a solid, known as rock salt, or in a liquid brine [2]. Non-corrosive deicing materials, such as calcium magnesium acetate (CMA) and potassium acetate (Kac), are less commonly used due to limited availability and high costs [2] [3]. These corrosive agents break down the passive layer formed around the metallic dowel, enabling corrosion development. As a result, dowel corrosion is a function of the level of exposure to chlorides found in deicing solutions.

Dowels are exposed to corrosive solutions, when deicing salts are applied prior to or during winter weather events, which vary regionally. Deicing practices vary between states as well, with states using different deicing materials in various proportions. As a result, salt exposure varies between states and typical exposure conditions are not well established. The purpose of this section is to evaluate typical salt exposure conditions for doweled concrete pavements. First, reported road management practices are summarized. Previous studies from the literature were reviewed and summarized to present the known deicing practices in a number of states. Second, the exposure conditions for Pennsylvania were quantified using deicing records provided by PennDOT. Quantities of deicing materials were determined for individual winter weather events in the years 2020 and 2021 from these records. General trends for deicing applications were then summarized from these years. This information will be used to develop an accelerated corrosion study, which replicates typical exposure conditions for doweled JPCPs.

2.2.1 State deicing practices

This section summarizes typical deicing practices reported in the literature. The purpose of this section is to estimate the level of chloride exposure experienced by doweled JPCPs. Deicing materials and application rates vary between states. Although there are no nationally adopted practices for deicing procedures, guidelines were published by the Federal Highway Administration (FHWA) on deicing applications in the Manual of Practice for an Effective Anti-icing Program [2]. These guidelines contain recommended levels of deicing applications as a function of the severity of the weather event, type of roadway, temperature, and deicing material used. Recommendations are based on a series of field tests conducted by 15 state highway agencies with support from the Strategic Highway Research Program (SHRP) and FHWA [2, 4]. Weather events are characterized as one of the following six types: light snowstorm, light snowstorm with periods of moderate or heavy snow, moderate or heavy snowstorm, frost or black ice, freezing rainstorm, or sleet storm. A series of tables are presented, which provide ranges of deicing application rates for different deicers, in lb/lane-mile, as shown in Figure 1. Application rates vary from 25 to 300 lb/lane mile, with typical recommended rates of 100 lb/lane mile. Application rates of 200 or greater are recommended for moderate or heavy snow events under certain conditions.

Table 8. Weather event: light snow storm.

PAVEMENT TEMPERATURE RANGE, AND TREND	INITIAL OPERATION				SUBSEQUENT OPERATIONS			COMMENTS
	pavement surface at time of initial operation	maintenance action	dry chemical spread rate, kg/lane-km (lb/lane-mi)		maintenance action	dry chemical spread rate, kg/lane-km (lb/lane-mi)		
			liquid	solid or prewetted solid		liquid	solid or prewetted solid	
Above 0°C (32°F), steady or rising	Dry, wet, slush, or light snow cover	None, see comments			None, see comments			1) Monitor pavement temperature closely for drops toward 0°C (32°F) and below 2) Treat icy patches if needed with chemical at 28 kg/lane-km (100 lb/lane-mi); plow if needed
Above 0°C (32°F), 0°C (32°F) or below is imminent;	Dry	Apply liquid or prewetted solid chemical	28 (100)	28 (100)	Plow as needed; reapply liquid or solid chemical when needed	28 (100)	28 (100)	1) Applications will need to be more frequent at lower temperatures and higher snowfall rates 2) It is not advisable to apply a liquid chemical at the indicated spread rate when the pavement temperature drops below -5°C (23°F) 3) Do not apply liquid chemical onto heavy snow accumulation or packed snow
ALSO **-7 to 0°C (20 to 32°F),** remaining in range	Wet, slush, or light snow cover	Apply liquid or solid chemical	28 (100)	28 (100)				
-10 to -7°C (15 to 20°F), remaining in range	Dry, wet, slush, or light snow cover	Apply prewetted solid chemical		55 (200)	Plow as needed; reapply prewetted solid chemical when needed		55 (200)	If sufficient moisture is present, solid chemical without prewetting can be applied
Below -10°C (15°F), steady or falling	Dry or light snow cover	Plow as needed			Plow as needed			1) It is not recommended that chemicals be applied in this temperature range 2) Abrasives can be applied to enhance traction

Notes

CHEMICAL APPLICATIONS. (1) Time initial and subsequent chemical applications to *prevent* deteriorating conditions or development of packed and bonded snow. (2) Apply chemical ahead of traffic rush periods occurring during storm.

PLOWING. If needed, *plow before chemical applications* so that excess snow, slush, or ice is removed and pavement is wet, slushy, or lightly snow covered when treated.

Figure 1. Example of salt application rate data (Appendix C of Ketcham, Minsk, Blackburn, & Fleege [2]).

Additional guidelines for deicing applications rates have been published by the Salt Institute, which is a trade association that promotes use of salt for roadway safety. These guidelines contain recommended salt dosages as a function of storm severity and pavement surface temperature [5]. Deicing rates range from 50 to 350 lb/lane mile applied every two hours. The values are slightly higher than those recommended in the FHWA manual.

Prewetted salt @12' side lane (assume 2–hr route)							
Surface Temperature	(Fahrenheit)	32–30	29–27	26–24	23–21	20–18	17–15
lbs of salt to be applied per lane mile	Heavy Frost, Mist, Light Snow	50	75	95	120	140	170
	Drizzle, Medium Snow ½" per hour	75	100	120	145	165	200
	Light Rain, Heavy Snow 1" per hour	100	140	182	250	300	350
Prewetted salt @12' side lane (assume 3–hr route)							
Surface Temperature	(Fahrenheit)	32–30	29–27	26–24	23–21	20–18	17–15
lbs of salt to be applied per lane mile	Heavy Frost, Mist, Light Snow	75	115	145	180	210	255
	Drizzle, Medium Snow ½" per hour	115	150	180	220	250	300
	Light Rain, Heavy Snow 1" per hour	150	210	275	375	450	525

Figure 2. Recommended salt application rates [5].

In addition to national guidelines for deicing application, there are a number of state-specific policies currently in use across the country. State agencies were asked to report the specific policies used in a 2014 survey conducted by CTC & Assoc., LLC, as part of a research project for evaluating the impacts of salt use [6]. The survey was sent to the 26 states participating in the Clear Roads initiative, of which 19 states responded. A map of the states that responded is shown in Figure 3. The state-specific road management policies reported by the respondents are summarized in Table 1. It should be noted that some state policies have been updated since this survey.

Figure 3. Map depicting states which responded (purple) and states which did not respond (yellow) [6].

Table 1. Deicing policies reported for each of the 19 survey respondents.

State	Policy name	Deicing application rates specified
Kansas, Montana, North Dakota, Ohio, Utah, Virginia, West Virginia, Wisconsin, and Wyoming	No policy reported	
Washington State	FHWA Application Guidelines [2]	As previously described.
Colorado	Standard Operating Guide for Winter Maintenance and Operations	Application rate not specified.
Idaho	Winter Maintenance Guidelines	Application rate not specified.
Iowa	Snow and Ice Control, Instructional Memorandum No. 8.400	General guidelines provided for solid salt and brine applications. Application rates not specified.
Maine	Interstate Operating Plan, Activity 412 and 413 [7]	Application rate not specified.
Michigan	Michigan Winter Maintenance Manual [8]	Application rates of 35 to 200 lbs/lane mile specified based on storm conditions, pavement temperature, and deicer.
New Hampshire	Winter Maintenance Snow Removal and Ice Control Policy [9]	Application rates of 250 to 300 lbs/lane mile specified based on road type, storm conditions, and pavement temperature.
New York	Highway Maintenance Guidelines on Snow and Ice Control [10]	Application rates of 90 to 450 lbs/lane mile specified based on storm conditions, pavement temperature, and deicer. For snow events, application rates of 160 to 250 lbs/lane mile recommended. These guidelines specify application rates for initial action, i.e. first application, and for follow-up actions.
Pennsylvania	Maintenance Manual, Publication 23 [11]	Application rates of 120 to 350 lbs/lane mile specified based on road type, storm conditions, and temperature.
South Dakota	Winter Highway Maintenance Plan, released annually [12]	General guidelines provided for solid salt and brine applications. Application rates not specified.

The guidelines published by FHWA, the Salt Institute, and various state agencies contain a range of deicing practices. However, the application rates are typically 100 to 250 lb/lane mile for light to heavy snowstorms. These recommended application rates can be used to determine typical amounts of chlorides applied to doweled JPCP joints to establish salt exposure conditions. Assuming a 15-foot joint spacing, the range of typical application rates corresponds to 0.28 to 0.71 lbs of salt per joint per deicing application.

The number of deicing applications vary as a function of state and regional maintenance practices, number of winter events per year, and severity of winter events. No guidelines reviewed provided specific intervals for applications. As a result, the total amount of salt applied to doweled JPCP in a given year is not easily quantifiable based on maintenance policies alone.

2.2.2 Chloride exposure in Pennsylvania

Estimating dowel exposure to chlorides based on deicing guidelines alone is not a reliable approach. Therefore, a review was performed on deicing application records in Pennsylvania from the winter seasons in 2020 and 2021. During each winter event, PennDOT maintenance personnel data on the quantity and type of deicers applied to roadways using TAPER logs [11]. Each TAPER log contains records of the pavement conditions, deicer type, application rate, and deicing effectiveness on roadways serviced during a winter weather event. These records are beneficial for this analysis because TAPER logs specify both number of deicer applications and application rate, making it possible to quantify the total amount of deicers applied for each roadway. The purpose of this analysis was to determine the total chloride exposure for typical doweled joints in a given year.

An 8-mile segment of U.S. Route 22 (SR-22) located in the municipality of Murrysville in Westmoreland County was evaluated in this analysis. Maintenance personnel from PennDOT

District 12 provided TAPER logs from the 2020 and 2021 winter seasons. Each winter season contained three months of records starting in December of the specified year. For example, the records for the 2020 winter season contained the months of December of 2020, January of 2021, and February of 2021. The records were filtered to only include the westbound lane of SR-22. A total of 88 TAPER logs were reviewed, of which 58 were from the 2020 winter season and 30 were from the 2021 winter season. The total number of deicing applications per year were multiplied by the average application rate to determine the total amount of salt applied per lane-mile of roadway. Based on the 15-foot transverse joint spacing on this section of roadway, the total amount of salt per joint was then calculated. Lastly, a density of 80 lbs/cf was assumed to determine the total volume of salt per joint for each year evaluated [13]. The summary of the data obtained in the TAPER logs and analysis performed is presented in Table 2. The average application rates of 232 and 265 lbs/lane mile were within the typical ranges identified in the previous section. ***The total amount of salt per joint was 145 lbs during the 2020 winter season and 99 lbs during the 2021 winter season, or 1.8 cft and 1.2 cft, respectively***.

Table 2. Summary of deicing analysis on SR-22.

Measure	2020 Winter Season	2021 Winter Season
Avg. application rate (lb/lane mile)	232	265
Salt per joint per application (lb)	0.66	0.75
Number of applications	220	131
Total salt per mile (lbs)	51,075	34,742
Total salt per joint (lbs)	145	99
Total salt per joint (cft)	1.8	1.2

2.3 Dowel corrosion studies

Previous studies have been conducted to identify the mechanisms of dowel corrosion in JPCPs. The impetus of these studies was to explore alternative corrosion-resistant options to be used for long-life paving projects. Corrosion resistant alternatives to epoxy-coating, such as stainless steel cladding, cost significantly more than the typical epoxy coating. To justify the increased costs, several studies have been performed to evaluate the long-term load transfer and corrosion performance of various dowel materials. The methodologies and findings of these studies are presented in this section. Significant factors contributing to corrosion development are determined to inform the laboratory study to be performed under Task C of this project. Gaps in knowledge were identified to be considered in the laboratory and modeling components of this study.

2.3.1 Field investigations

A major investigation was initiated by the Highway Innovative Technology Evaluation Center (HITEC) in 1996 [14]. The purpose of this study was to identify the effect of corrosion on joint performance to inform the selection of dowel coatings and materials for long-life paving projects. A survey was sent to state departments of transportation (DOTs) as part of this study to identify key issues related to joint performance. Of the 36 responses, the second-most common issue was related to corrosion development, including "seizing" of the joint caused by expansive byproducts of corrosion development [15]. Midwestern states were more likely to report issues with dowel corrosion and expressed greater interest in dowels constructed of alternative materials to steel. A subsequent pooled-fund study was conducted in which the early performance of different dowel materials was evaluated using in-service pavements constructed in Ohio, Iowa, Illinois, and Wisconsin [14]. Cores were extracted from sections in Ohio and Wisconsin as a component of this study to evaluate corrosion development. The number of years in service ranged from 12 to 33 years for these sections, and the focus of this analysis was the performance of epoxy coated (EC) dowels. Summarized information is presented in Table 3.

Table 3. Summary information for cores extracted from doweled joints in Ohio and Wisconsin.

State	Section	Number of Years in Service	Dowel Diameter	Dowel Material	Number of Cores Extracted
Ohio	SR-50 Eastbound (EB)	14	1.5	EC and stainless steel tube	15
	SR-50 Westbound (WB)	12	1.5	EC and stainless steel clad	8
	SR-176	14	1.5	EC	8
	SR-76	15 – 17	1.5	EC	5
	SR-7	28	1.25	EC and composite	18
	SR-35	20 – 24	1.25	EC	6
Wisconsin	SR-67	33	1.5	EC	4
	I 43	30	1.5	EC	6
	I 94	25	1.5	EC	6
	SR-29	20	1.5	EC	6
	SR-18/151	20	1.5	EC	9
	SR-16	19	1.5	EC	3
	SR-29	15	1.5	EC	6

Falling weight deflectometer (FWD) testing was performed prior to extraction of cores to evaluate joint performance. Each dowel was removed from the core, and a visual inspection was performed. Of key interest was the loss of cross-section area of the dowel caused by corrosion development. The majority of dowels obtained from samples in Ohio displayed debonding of the epoxy coating and surface corrosion on the steel below. This was observed across all sections, including dowels that were in service for only 12 years. An example of a dowel with surface corrosion is shown in Figure 4. Loss of cross-sectional area was reported for 7 of the 60 dowels evaluated from Ohio. Samples taken from Wisconsin were reported to have moderate levels of dowel corrosion in sections with fewer than 20 years in service. Dowel samples from sections with greater than 25 years in service were reported to have moderate to extensive dowel deterioration.

The researchers were not able to correlate degree of corrosion development to joint performance of the pavement based on the limited sample size of the dataset.

Figure 4. Example segment of dowel obtained from a core extracted in Ohio [14].

The chloride content was measured at the joint face directly above the dowel to quantify the degree to which each dowel was exposed to corrosive agents. Chloride content was measured per ASTM C1152 [16]. Chloride content ranged from 0.017 to 0.274 percent by mass, however, there was no correlation between chloride content and observed magnitude of dowel corrosion. This may be due to the limited number of samples obtained in this study. The researchers hypothesized that early corrosion development observed in some samples was caused by poor epoxy quality or defects caused during paving. It was concluded that the performance life for EC dowels was 25 to 30 years based on these results. The researchers recommended that EC dowels would not be suitable for long-life paving projects with design lives of 50 or greater years due to the potential for corrosion progression based on laboratory and field results.

2.3.2 Laboratory investigations

The following section outlines the methodology and results from prior laboratory investigations on dowel corrosion. This report summarizes three accelerated corrosion studies, which evaluated dowel bars in different salt exposure conditions. Critical parameters for dowel corrosion identified in these studies will be used to inform the laboratory and computational modeling to be performed.

2.3.2.1 Abo-Qudias and AL-Qadi 2000

One of the earliest laboratory investigations into corrosion of dowel bars in JPCPs was performed by Abo-Qudias and Al-Qadi [17]. The purpose of this study was to evaluate the prevention of chloride and water intrusion by joint sealants. Nine slabs were constructed; one without a joint which was used as a control, two with non-sealed joints, and six with sealed joints. Two sealants were tested. The first, Sealant A, was a cold-applied low-modulus silicone sealant that did not require a primer. The second, Sealant B, was a cold-applied polyurethane which requires a primer applied to the joint one hour prior to sealant application.

Three dowels were placed at each joint, one of which was a typical EC dowel and the other was an uncoated carbon steel. The slabs were subjected to 40 weeks of cyclic ponding and drying in a 6% by weight sodium chloride (NaCl) solution. The exposure cycle consisted of three days of ponding followed by four days of drying.

Corrosion development was monitored using non-destructive test methods. Corrosion current density was calculated using linear polarization resistance (LPR) testing. In this test, an electrolytic cell is placed on the surface of the concrete above the dowel. A current is applied via embedded wires to the dowel, and the electrolytic cell potential is measured. The change in the potential of the electrolytic cell is measured with increasing magnitudes of current. For small changes in the open circuit potential, there is a linear relation between the change in applied current per area of electrode (i.e., the dowel), Δi, and the change in measured potential, ΔE. The slope of this relationship, $\Delta E/\Delta i$, is the polarization resistance, R_p. The corrosion density, i_{corr} can be calculated from R_p using the Stern-Geary relationship, seen below in Equation 1.

$$i_{corr} = B/R_p \tag{1}$$

Where i_{corr} is the corrosion density (μA/in^2), B is a constant, and R_p is the polarization resistance (Ω in^2). In order to perform LPR testing, it is assumed that the polarized area is the area of the dowel exposed to the NaCl solution, i.e., the area of the dowel in the open joint. This can be assumed for all dowels except those coated with an epoxy (either bendable or non-bendable). For any EC dowel, the portion of the surface exposed to the NaCl solution is at holidays on the dowel coating located in the joint, which are small, inconsistent between specimen, and unable to be accurately measured. As a result, LPR results for EC dowels had greater variability compared to the results for the uncoated dowels.

The results from the corrosion current density tests indicate a higher rate of corrosion for dowels in jointed slabs when compared to dowels in unjointed slabs. In the jointed slabs, Sealant A performed marginally better than Sealant B at preventing corrosion. After 40 weeks, the average corrosion density for specimens with Sealant A was 4.03 mA/ft^2 with a standard deviation of 0.38. The average corrosion density for specimens with Sealant B was 4.49 mA/ft^2 with a standard deviation of 0.34. Additionally, the use of EC dowels significantly decreases the measured rate of corrosion. On average, the corrosion density of EC dowels was less than 5% of the corrosion density of uncoated dowels. It was observed that the variability of the readings from the EC dowels were higher than the readings of the uncoated dowels due to the influence of the coating, especially at the initial readings. These results indicate that the use of EC significantly decreases the corrosion development of metallic dowels. Corrosion rate was not determined.

A chloride penetration profile was established by measuring the levels of chloride in the concrete medium throughout the depth of the slab at the joint face. The chloride content results agree with trends identified in the corrosion density tests. Unjointed slabs had an average chloride content of 0.06 lb/ft^3 at 3.7 in of depth after 40 weeks, which was significantly lower than the specimen with unsealed joints that had an average chloride content of 0.13 lb/ft^3 at the same testing location and time. Sealant A and B resulted in average chloride contents of 0.07 and 0.11 lb/ft^3, respectively, at 3.7 in of depth after 40 weeks, which supports the results from the corrosion density tests that indicated that sealant type affects chloride exposure in joints.

2.3.2.2 Caltrans 2007

A two-phase laboratory experiment was conducted as a component of the project completed in 2007 at the University of California at Davis [18]. The purpose of this study was to evaluate the corrosion performance of seven types of steel dowels through accelerated corrosion laboratory testing. The objective was to quantify the potential for corrosion development as a function of dowel material and exposure duration. The following types of dowels were evaluated: bare carbon steel (CS), stainless steel (SS) clad, grout-filled hollow stainless steel, microcomposite steel, coated with a bendable epoxy (green), and coated with a non-bendable epoxy (grey, purple). Four replicates of each dowel were evaluated. Prior to installation of dowels, a low voltage holiday detector was used to detect holidays, i.e., defects, in the EC dowels. The dowels were cast in beams measuring 5.9 in x 5.9 in x 22.4 in. A foam spacer was used to create a simulated joint, allowing the NaCl solution to come in contact with the dowel. The specimens were subjected to weekly wetting/drying cycles in a 3.5% by weight NaCl solution at room temperature for 18 months. A schematic of the specimen and accelerated corrosion experimental setup is depicted in Figure 5.

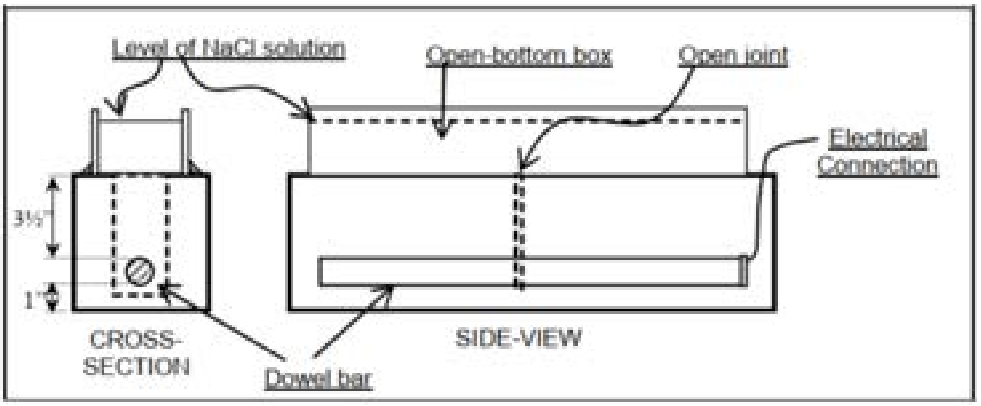

Figure 5. Schematic of accelerated corrosion experimental setup [18].

Throughout the accelerated corrosion program, both LPR and half-cell potential testing was performed. Half-cell potential tests were performed per ASTM C876 [19]. This test is commonly used to evaluate the corrosion potential for steel embedded in concrete. An electrical connection is made from one end of the dowel embedded in the concrete to a reference electrode placed above the joint on the exterior of the concrete in a similar configuration as LPR testing. A high-impedance voltmeter measures the potential of the system, which can then be correlated to the corrosion potential. An example of half-cell potential testing being performed on a specimen is shown in Figure 6. Metrics shown in Table 4 and Table 5 were used to interpret these results to estimate the likelihood of corrosion development. It should be noted that while the half-cell potential measurement enables an estimate of the probability of corrosion, this test does not quantify the rate or magnitude of corrosion development. Additionally, this test does not account for the impact of the joint as complete concrete cover of the embedded steel is assumed.

Figure 6. Half-cell potential testing being performed on a specimen during the accelerated corrosion program [18].

Table 4. Corrosion interpretation for ranges of half-cell potential results [18]

Half-Cell Potential (mV)	Corrosion Interpretation
> -200	Low Probability (10%) of Corrosion
-200 to -350	Corrosion Unknown
< -350	High Probability (90%) of Corrosion

Table 5. Correlation between corrosion current density, i_{corr}, and corrosion rate [18]

Corrosion current density, i_{corr} ($\mu A/cm^2$)	Corrosion Rate
< 0.1	Negligible
0.1 – 0.5	Low
0.5 – 1.0	Moderate
> 1.0	High

Half-cell potential and LPR readings were taken at regular intervals during testing. Average non-destructive test results at the conclusion of the 18-month corrosion program are reported in Table 6. Plain carbon steel dowels were found to be most susceptible to corrosion development, followed by EC dowels, then microcomposite steel dowels. Both stainless clad and stainless hollow dowels exhibited good corrosion resistance based on the non-destructive testing. A forensic analysis was performed upon completion of the corrosion program, with both visual inspection and scanning electron microscopy (SEM). In general, the forensics analysis results were consistent with the non-destructive testing results. The researchers did find that localized corrosion developed in EC dowels at defects or ends of the dowels. In areas with adequate epoxy coating, corrosion did not develop, indicating that the frequency and size of holidays in the coating is a significant factor contributing to the development of corrosion.

Table 6. Half-cell potential and LPR testing results [18]

Dowel Type	**Evaluation Metric**	**Half-Cell (mV)**	**Rp (Ω cm^2)**	**i_{corr} (µA/cm^2)**
Carbon Steel	Average	-641.3	3,897.5	9.01
	Std. Dev.	38.6	2,183.2	5.84
Microcomp. Steel	Average	-427.0	134,667.8	0.63
	Std. Dev.	164.1	162,343.7	0.57
Stainless Clad	Average	-256.5	284,685.0	0.09
	Std. Dev.	73.8	64,414.8	0.02
Stainless Hollow	Average	-323.0	284,360.0	0.10
	Std. Dev.	173.4	132,819.5	0.03
Purple EC (nonbendable)	Average	-583.3	-	-
	Std. Dev.	160.8	-	-
Gray EC (nonbendable)	Average	-570.0	-	-
	Std. Dev.	112.0	-	-
Green EC (bendable)	Average	-595.3	-	-
	Std. Dev.	143.2	-	-

2.3.2.3 Federal Highway Administration (2018)

The purpose of this study was to evaluate the performance of eight types of metallic dowel bars in an accelerated corrosion laboratory setting [20]. The eight dowels analyzed are as follows: uncoated (CS), EC, hot-dip zinc galvanized (HDG), zinc-clad (ZC), three types of stainless steel-clad (SCA, SCB, SCC), and Type 316L solid stainless steel (316L solid SS). In order to simulate a doweled JPCP, slabs measuring 15 in x 36 in x 5.5 in were exposed to an accelerated corrosion program in a 15% by weight NaCl solution. The accelerated corrosion program consisted of repeated cycles of 4 days of wetting followed by 3 days of drying. Each slab contained seven dowels and an artificial joint. The layout of each specimen is shown in Figure 7 and Figure 8. Prior to installation of the dowels, defects were purposefully placed on some of the dowels at two levels (0.07% and 0.59% of surface area). The purpose of these holidays was to evaluate the effect of defects on corrosion development in coated dowels.

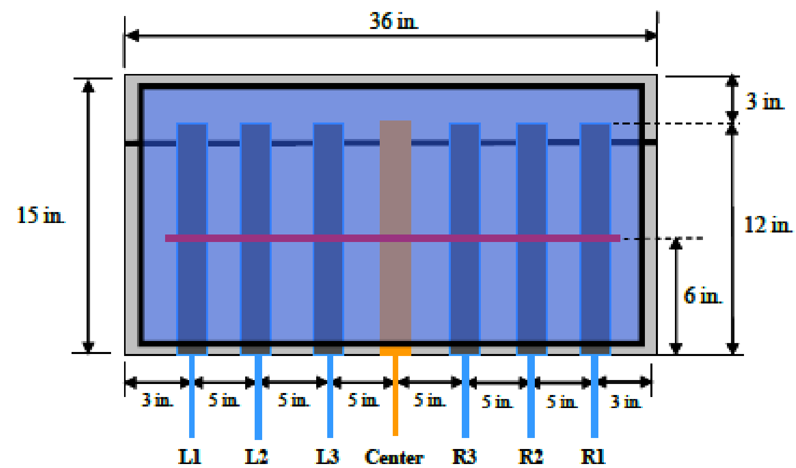

Figure 7. Plan view of accelerated corrosion specimen [20].

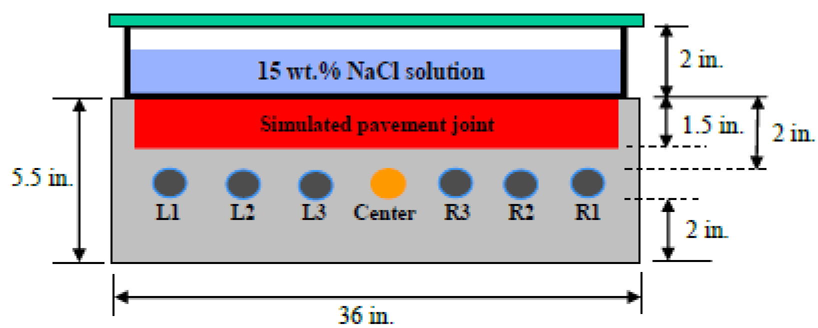

Figure 8. Elevation view of accelerated corrosion specimen [20].

Half-cell potential and LTP testing was performed throughout the corrosion program to quantify the potential for corrosion development. In this study, the mean corrosion rate of the bar in mils/year was determined by dividing the corrosion density by the area of the dowel exposed to corrosive agents. It was assumed that corrosion occurs uniformly across areas of the dowel exposed to corrosive agents, and that corrosion only developed at defects for EC dowels. It was found that plain carbon dowels exhibited the highest corrosion rate of 0.15 mil/year, followed by 0.1 and 0.05 mil/year for HDG and ZC dowels, respectively. The other dowels considered (EC, SC, and SS) exhibited negligible corrosion rates. A forensic analysis was performed on the dowels upon completion of the accelerated corrosion program. As was found in the study performed at the University of California [18], corrosion development in EC dowels was localized to defects in the coating. Corrosion initiated at the defects and caused debonding of the coating from the dowel, resulting in surface corrosion around the areas of defects. Since LPR testing did not indicate significant levels of corrosion densities for many of the EC dowels, the researchers hypothesized that debonded epoxy coating continued to provide some level of corrosion resistance.

2.3.3 Gaps in knowledge

Previous dowel corrosion studies have evaluated the potential for various types of dowels to develop corrosion when exposed to chlorides from deicing materials. These studies were primarily focused on comparing the corrosion resistance of different dowel materials and coatings. Researchers were able to collect samples of dowels with varying degrees of corrosion development and simulate corrosion development in the laboratory. However, there are gaps in knowledge that need to be addressed in order to quantify dowel corrosion as a function of key parameters. The following are gaps in the current understanding of dowel corrosion based on previous field and laboratory testing.

First, the effect of exposure conditions on the rate of corrosion development is not well established. Previous laboratory studies employed accelerated corrosion programs that varied in the duration and concentration of chloride solution used. The studies were performed for 78, 65, and 40 weeks in solutions of 3.5%, 15%, and 6% by weight NaCl solutions, respectively. The experimental conditions in the previous studies did not directly replicate the levels of chloride exposure for typical doweled JPCP.

Previous researchers were not able to quantify the loss of dowel performance resulting from dowel corrosion, likely due to the lack of available field data. It is intrinsic that the loss of material caused by corrosion would reduce joint stiffness, however, it is not known to what degree corrosion reduces dowel performance. Field studies have indicated that epoxy coating wear caused by vehicle loads commonly occurs near the joint. To date no laboratory testing has replicated the effect of vehicle loading on coating wear. As a result, the effect of vehicle load on corrosion development is unknown. Moreover, previous studies were not able to quantify the loss of joint performance caused by corrosion of the dowel.

3.0 CORROSION MODELING

This section outlines existing corrosion models and available databases to identify previously established key parameters for corrosion development. These models must be evaluated for their suitability for incorporation into models for predicting faulting.

In recent years, a large number of studies have been performed to develop generalized corrosion models that quantify loss of metal when exposed to corrosive conditions. Corrosion models are specific to forms of corrosion, such as uniform surface corrosion or pitting. Microscopic and SEM analyses performed on corroded dowels indicate pitting is the primary form of corrosion that occurs in metallic dowels [20, 14, 18]. Pitting is a localized form of corrosion which initializes in small cavities, known as pits, on the surface of the exposed metal. After formation, the pits rapidly grow in depth and diameter, causing significant loss of metal [1]. Pitting initiates at small imperfections in metals surfaces, such as holidays in the coating of dowel bars. The focus of this next section is to review pitting corrosion models.

Pitting corrosion is typically thought to occur in three main stages: initialization, meta-stable growth, and stable growth [21]. Pit initialization is difficult to predict because it occurs on the micrometer scale. Meta-stable growth occurs soon after pit initialization. During this phase, pitting can cease due to the formation of a passive layer within the pit, referred to as repassivation. It is believed that repassivation cannot occur if the local chloride concentration within the pit is sufficiently high [22]. Stable pit growth is then able to occur, which results in loss of significant mass of the exposed metal. Since both pit initialization and repassivation occur on the microscopic level in a short period of time, existing pitting corrosion models focus on replicating stable pit growth, and pit initialization and meta-stable pit growth are assumed to have occurred. In the case of EC dowel corrosion, this assumption is reasonable since pitting would most likely develop at the location of holidays in the coating.

Several pitting models have been developed to quantify the rate exposed metal is corroded. Typically, these models employ dissolution kinetics to estimate the rate metal ions are removed from the pit walls when corroded. Pit growth is limited by how quickly the corroded metal ions can be removed from the surface of the pit and the concentration of chloride ions present at the face. Therefore, pitting models must account for two processes for pit growth with each iteration of an analysis. First, the transport equations must be solved to determine the diffusion rate of metal and chloride ions within the pit. Second, the boundary of the pit face must be adjusted to account for the growth of the pit caused by loss of metal ions at the face. Two broad types of pitting models exist based on how the analysis is performed. Non-autonomous models use numerical methods to determine the dissolution kinetics and pit growth separately for each iteration of the analysis.

Autonomous models couple the dissolution kinetics and pit growth to determine pit propagation [23]. The following section describes existing pitting models while differentiating between non-autonomous and autonomous models.

Early pitting models determined pit growth as a function of diffusion-controlled kinetics using the finite element method (FEM). One of the earliest models was developed by Laycock *et. al* [24]. The researchers assumed the initial pit was hemispheric, as shown in Figure 9. Each iteration of the analysis required two steps. First, diffusion equations were solved throughout the aqueous solution within the pit. Second, the growth of the pit was determined based on the quantity of metal lost, requiring remeshing of the pit wall [24]. Remeshing the model during each increment of the analysis is computationally expensive. Subsequent research improved the model by enabling repassivation of the surface of the pit, however, these models still required frequent remeshing with each iteration [25].

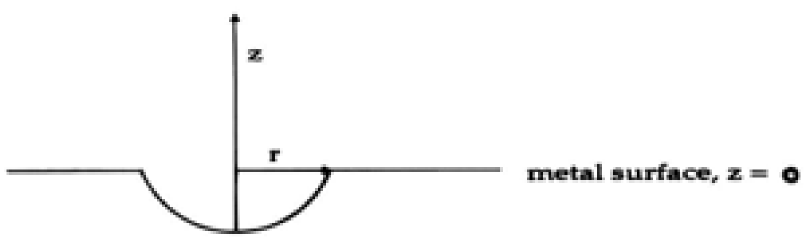

Figure 9. Schematic of initial pit [24].

These early models assumed diffusion-controlled corrosion. The rate at which the pit boundary advances is calculated as a function of the dissolution flux at the pit boundary, as calculated in Equation 2.

$$v = -\frac{M}{\rho} J_{diss}(x) \tag{2}$$

Where v is the rate at which the pit boundary moves, M is the molar mass of metal being corroded, ρ is the density of metal, and $J_{diss}(x)$ is the dissolution flux at edge of the pit. The dissolution flux is calculated as a function of the concentration of the dissolved metal ions within the aqueous solution. The concentration of ions is not constant throughout the aqueous solution, therefore models typically determine a concentration gradient throughout the solution, as shown in Equation 3.

$$\frac{\partial C}{\partial m} = \frac{L_0}{D}\frac{i}{nF}\left(\frac{1}{C_{sat}}\right) \tag{3}$$

Where $\frac{\partial C}{\partial m}$ is the concentration gradient normal to the pit edge, L_0 is the pit depth, D is the diffusion constant, i is the current density of the metal, n is the average charge of an ion, F is Faraday's constant, and C_{sat} is the saturated concentration of the aqueous solution. Improvements to non-autonomous models were made by decoupling the pit boundary face from the FEM model mesh using the level set method [26, 27]. Despite these improvements, models continued to be computationally expensive. Moreover, these models require assumptions provided by the user based on the material properties and exposure conditions. Known variables include the diffusion constant, current density, average charge of the ion, and saturated concentration. Models were validated by determining the variables to replicate laboratory results [24, 25, 26, 27, 28]. As a result, these models require independent determination of constants to replicate corrosion development.

The second group of corrosion models consists of autonomous models. Autonomous models were developed to reduce the computational time and cost. Within each increment of the analysis, the dissolution of the metal is coupled with advancement of the pit boundary. As a result, the loss of metal due to corrosion is determined in single increments without a separate calculation of the loss of metal. Early models applied the finite volume method (FVM) to calculate loss of material as the pit boundary advances [29, 30]. The solid and aqueous solution is modeled as a grid of elements, each of which are defined as either solid metal, pit surface, pit solution, or bulk solution. Corrosion is controlled by diffusion of the metal ions in the aqueous solution as was previously developed for non-autonomous models. The concentration gradient is calculated iteratively during the analysis. The pit boundary advances when the concentration of metal ions in the pit solution elements directly adjacent to pit boundary elements reaches a specified threshold. If this occurs, the pit boundary elements are redefined as pit solution elements and the concentration gradient is recalculated throughout the pit. This approach facilitates the simultaneous determination of the concentration gradient and pit boundary advancement. One limitation is that model parameters must be determined using laboratory results [29, 30].

In recent years, a novel modeling approach has been adopted based on Peridynamics, which was developed for the field of continuum mechanics. Peridynamic (PD) formulations do not contain spatial derivatives and are therefore advantageous for problems with cracks or discontinuities [31]. Nodes in a PD model are connected to other nodes with a series of predefined mechanical bonds. Researchers have identified that PD modeling can be applied to corrosion by defining the state of mechanical bonds as a function of the diffusion throughout the system, as depicted in Figure 10. When there is a sufficient concentration between elements, the mechanical bond between the elements is eliminated. When all bonds for one element are eliminated, the element is considered to be fully corroded and is considered a component of the aqueous solution.

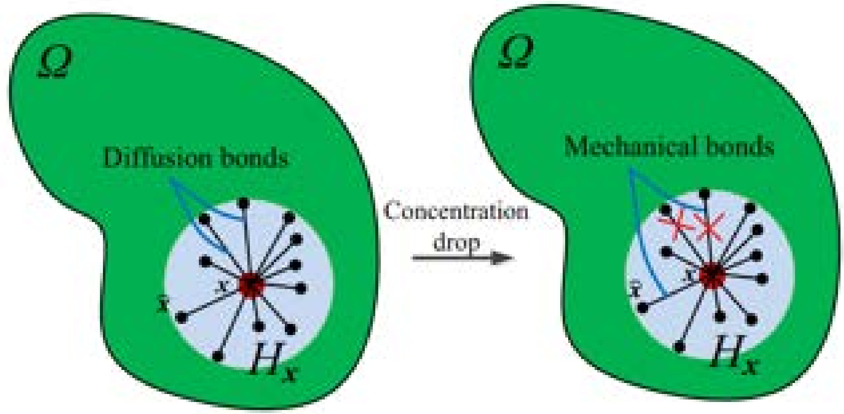

Figure 10. Depiction of a PD model of the system Ω, with node x connected to other nodes $\hat{x}$ and bonds defined by the diffusion state throughout the space H_x [32].

Several researchers have implemented PD modeling to calculate pitting development [32, 33, 34, 23]. Predicted corrosion development is a function of the diffusion and material parameters defined in the model. A significant benefit of these models is that 3-dimensional pitting can be considered to a high degree of accuracy. Researchers have demonstrated that pitting observed in laboratory experiments were able to be replicated using PD modeling. However, these analyses require significant computing power and are only able to replicate localized pitting development over a short analysis period.

The final form of autonomous corrosion modeling presented is phase field (PF) modeling. This is a recently developed branch of modeling that applies a binary phase, ϕ, to a given system. For corrosion development, elements with ϕ equal to 0 are defined as the aqueous solution and elements with ϕ equal to 1 are defined as non-corroded metal. Between the aqueous solution and non-corroded metal is a thin interphase region of elements, which has a ϕ between 0 and 1. Within this region, ϕ is calculated as a function of the diffusion throughout the solution. The pit boundary advances into the region of non-corroded metal as ϕ within the interphase region decreases due to corrosion. Decreasing boundary region thickness has been shown to increase model accuracy but dramatically increases computational time [35]. PF modeling has been performed for a number of different metals in varying corrosion scenarios with reasonable results [36, 37, 38]. Corrosion is defined as a diffusion-controlled process in these studies, therefore diffusion parameters must be determined to calculate the concentration gradient throughout the aqueous solution. Recent studies have considered the effect of micro-cracking on pit growth [37] and the effects of temperature and pH levels of the solution [38].

The results from corrosion models available in the literature were used to identify key parameters, which affect corrosion development. The models vary based on the approach used to numerically determine the increase in pit size. Diffusion was considered the controlling factor across all models. Corrosion development was shown to be a function of the rate at which metal ions diffused into the aqueous solution at the pit boundary. Diffusion rate varied as a function of the boundary metal ion average ionic charge, the concentration of metal ions in the saturated solution, and the diffusion constant within the solution. The concentration of chloride ions in the aqueous solution determines the concentration of metal ions that can be reached. Solution pH and temperature affect the diffusion rate and therefore should be considered as well [38].

3.2 Corrosion databases

The final component of this literature review is to corrosion databases that are available, which can be used to assess corrosion development for doweled JPCPs. To do so, corrosion databases which have been compiled in previous studies were considered. The first source considered was the CORR-DATA database compiled as part of a joint agreement between the National Association of Corrosion Engineers (NACE) and the National Institute of Standards and Technology (NIST) [39]. This program operated from 1982 until 1997 and over 24,000 records were compiled from over 250 separate sources. The sources are published results from laboratory experiments that tested the corrosion development of metals in corrosive environments. Of the 24,000 records, 16,648 records contain results pertaining to corrosion of steel. These records contain corrosion results for streel specimens exposed to 264 different corrosive environments.

Sources relevant to dowel corrosion were identified within the database. 547 records from 24 sources of steel specimens subjected to seawater, sodium chloride, manganese chloride, or potassium chloride were isolated. These sources were reviewed to evaluate the relevance for dowel corrosion development. Many of the sources are focused on corrosion development in hostile environments for high alloy steels, such as oil pipelines, marine environments, or manufacturing processes with high temperatures [40, 41, 42, 43]. These sources may not be relevant for dowel corrosion since the environments are subjected to significantly higher salt exposure than typical doweled joints. As a result, these databases do not appear to provide applicable corrosion rates for the purposes of dowel corrosion.

Several sources within the database provide average corrosion rates in mils/year for a range of metals exposed to various corrosive environments [44, 45]. The reported average corrosion rates do not reflect the rate at which dowel corrosion will develop but may be useful in determining key corrosion parameters. Chloride concentration is shown to significantly affect corrosion rate. Several previous studies considered the effect of exposure conditions on the rate at which corrosion develops in steel. Solution temperature and pH were considered by Malik et. al [46]. It was shown that increased corrosion development occurs with decreased pH, increased temperature, and increased chloride concentration for stainless steel. Similarly, temperature and chloride concentration were considered by Wang *et. al* [47] when evaluating AISI 304 stainless steel specimens. Experimental results indicated increased temperature and chloride concentrations caused a reduction in passive film formation and an increase in pit formation.

A significant limitation to existing corrosion databases is that corrosion is heavily dependent on the environment to which specimens are subjected. The corrosion rates provided in several databases serve as reference rates for corrosion development, however, these do not accurately reflect corrosion rates for metallic dowel bars in JPCPs.

3.3 Conclusions

This section presents currently available corrosion prediction models and corrosion databases. Based on the review of available corrosion models it was determined that models have been developed to primarily characterize corrosion propagation assuming known initiation. Moreover, these models have been developed and calibrated with specific corrosion databases that were developed for specific metals in a controlled environment. Modeling climatic conditions and salt exposure levels that a concrete pavement is exposed to is highly complex, therefore the available models developed for specific chloride exposure conditions are unable to be generalized for this application. Moreover, there are no available models which directly account for the performance of various coatings and materials used for corrosion protection in metallic dowels. Based on these findings, it was determined that available models are unable to be directly implemented into the current pavement performance prediction models to account for corrosion development. However, the general forms of the prediction models and key parameters identified in this analysis will be used to inform the development of the revised faulting prediction model.

Existing corrosion databases were evaluated to identify the potential application of these databases for calibrating a dowel corrosion model. A number of previous studies have been conducted to quantify corrosion development for a range of metals exposed to varying levels of salt exposure. A major limitation to these studies for the purpose of this project is that previous studies mainly focused on various alloys exposed to extremely corrosive environments. The corrosion rates identified in these databases are specific to the environments in which the specimens were tested. The environments considered in these studies do not accurately reflect conditions in which metallic dowel bars are exposed. Therefore, these databases are not appropriate for the purpose of developing a corrosion prediction model for dowel bars in concrete pavements.

4.0 ACCELERATED CORROSION TESTING

4.1 Introduction

The purpose of the laboratory study is to quantify the development of corrosion for typical dowels on the market and to establish the effect of corrosion on loss of performance. The performance of the dowel is a function of the ability of the protective barrier to withstand damage during construction and while in service along with its corrosion resistance properties. Therefore, both the ability to resist damage during impact or abrasion will be assessed as well as the corrosion resistance of each dowel type. Section 5.2 describes the doweled specimen, experimental design, and the novel test setup developed for investigating the potential corrosion rate for each dowel type. Section 5.3 describes the results from the accelerated corrosion study

4.2 Test Program

4.2.1 Dowel selection

The focus of this study is to quantify the development of corrosion as a function of exposure to deicing chemicals and dowel design. A total of 7 different dowel designs were evaluated to ensure the range of dowels currently on the market were included in this study. The dowels included are described in Table 7 with photos of each type provided in Figure 11. Each dowel type is assigned an ID which describes the material of the bar and the coating type and thickness. The first character in the ID denotes the core material, with C corresponding to carbon steel, G corresponds to galvanized steel, F corresponds to fiber reinforced polymer (FRP), and S corresponds to Type 316 stainless steel. The second and third characters denote the coating type and thickness. The uncoated dowels (tubular stainless steel and solid FRP) are denoted with the letter N, which corresponds to no coating. For coated dowels, the second character is the thickness of coating in tens of mils and the third character denotes the type of coating. Green epoxy (ASTM

Table 7. Description of dowels included in the accelerated corrosion study.

Dowel ID	Core material	Coating material	Approx. coating thickness (mil)	Dowel diameter (in)
G1G	Tubular carbon steel with hot-dipped zinc galvanized coating (~0.147-in wall)	A775 (green) epoxy	10	1.34
G1P	Tubular carbon steel with hot-dipped zinc galvanized coating (~0.140-in wall)	A934 (purple) epoxy	10	1.34
C2G	Solid carbon steel	A775 (green) epoxy	20	1.25
C2P	Solid carbon steel	A934 (purple) epoxy	20	1.25
FN	Solid fiber-reinforced polymer (FRP)	No coating	-	1.25
SN	Tubular Type 316L stainless steel (~0.162-in wall)	No coating	-	1.90
C4Z	Tubular carbon steel (~0.168-in wall)	Mechanically bonded zinc cladding	40	1.70

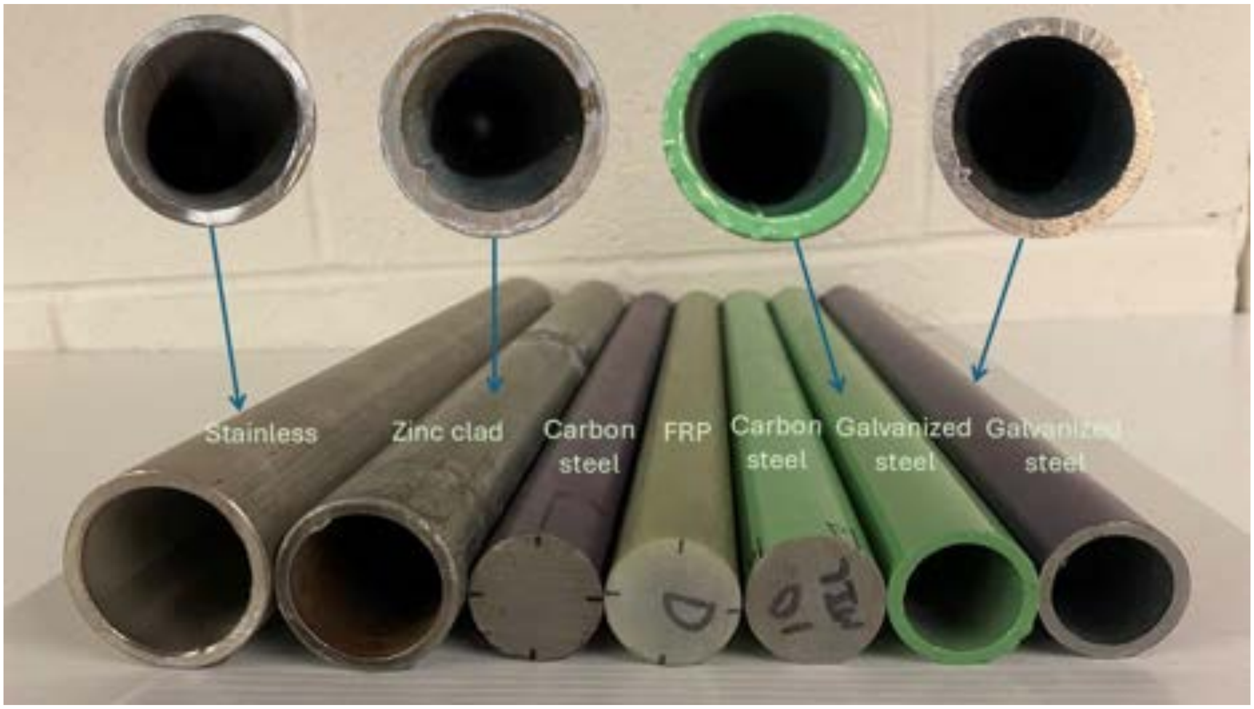

Figure 11. Dowel types included in this investigation.

A775 [48]) is denoted with G, purple epoxy (ASTM A934 [49]) is denoted with P, and mechanically bonded zinc cladding is denoted with Z. A full-factorial experimental design was developed for this study, with three replicates per test cell. The replicate number (1, 2, or 3) is added to the end of each specimen ID. For example, C2G3 corresponds to the third replicate of a solid steel dowel with 20-mil thick green epoxy. This resulted in a total of 21 specimens.

The dowel bars selected for this study were chosen to enable direct comparisons between dowel bar and coating types for the range of dowels currently available on the market. First, two types of epoxy coatings are included, which consist of a flexible, green epoxy (ASTM A775 [48]) and a stiff, purple epoxy (ASTM A934 [49]). Solid steel dowels with 20-mil thick green (C2G) and purple (C2P) epoxy coating are included to directly evaluate the resistance of each coating to impact and abrasion. The galvanized tubular dowels were evaluated with 10-mil thick green (G1G) and purple (G1P) to evaluate the resistance of the thinner coating to impact and abrasion. This study also includes the evaluation of two types of zinc-based corrosion protection systems. The first is the Grade G90 hot dipped zinc-galvanized dowels coated with either a green dipped epoxy (G1G) that coats both the inside and outside of the tubular dowel or purple (G1P) epoxy coating. The hot dipped zinc galvanization is applied using a bath metal consisting of no less than 99% zinc with a minimum coating of 0.60 oz/ft^2, per ASTM A653 specifications [50]. This corresponds to a minimum thickness of 16 mil of zinc galvanization. The galvanization process results in a protective zinc formed on the outside of the carbon steel. The second zinc-based coating evaluated in this study is the tubular steel dowels with a mechanically bonded zinc sheath sometimes referred to as cladding (C4Z) in the pavement community. These dowels have a 40-mil thick zinc coating consisting of a low copper-titanium rolled zinc alloy (UNS designation: Z41121) meeting ASTM B69 [51]. The zinc composition of this alloy is over 99%, similar to the galvanized coating. The difference in chemical composition between the zinc-galvanization and zinc-cladding is minor at the outer portion of the galvanized bar but becomes a zinc-iron alloy which increases in iron composition with increasing distance from the surface. This will be discussed further in the results section.

The last two dowels considered in this study consist of solid FRP (FN) and tubular stainless steel (SN). The FRP dowels are included to evaluate the potential for swelling of the dowel caused by moisture infiltration. Although not a product of corrosion, swelling of the FRP could cause an increase in the resistance to joint opening and a decrease in the stiffness in the dowel. Stainless steel dowels are often a more expensive alternative dowel and are therefore included in this analysis to provide measurable corrosion resistance for cost justification of long-life paving projects. It should be noted that the diameter of the stainless tube is larger than has been used in past field installations, such as Minnesota. This is still deemed to be representative as the focus is on the corrodibility of the material and not in correlating looseness to bending stiffness.

4.2.2 Accelerated corrosion experimental procedure

The following section describes the accelerated corrosion procedure and test setup developed for this study. A description of the laboratory testing regime is provided in the form of a flowchart in Figure 12. This study consists of two components 1. Defect resistance of the dowel material(s) and 2. corrosion resistance of the dowel bar. First, the coating testing and holiday placement is discussed in Section 4.2.2.1. The accelerated corrosion test setup and testing program is discussed in Section 4.2.5. Simulated joint opening/closing testing and dowel performance testing is described in Sections 4.2.6 and 4.2.7, respectively. The method used to visualize the progression of corrosion is described in Section 4.2.8. The changes in corrosion development for the 2% holiday area are discussed in Section 4.3.2.3.

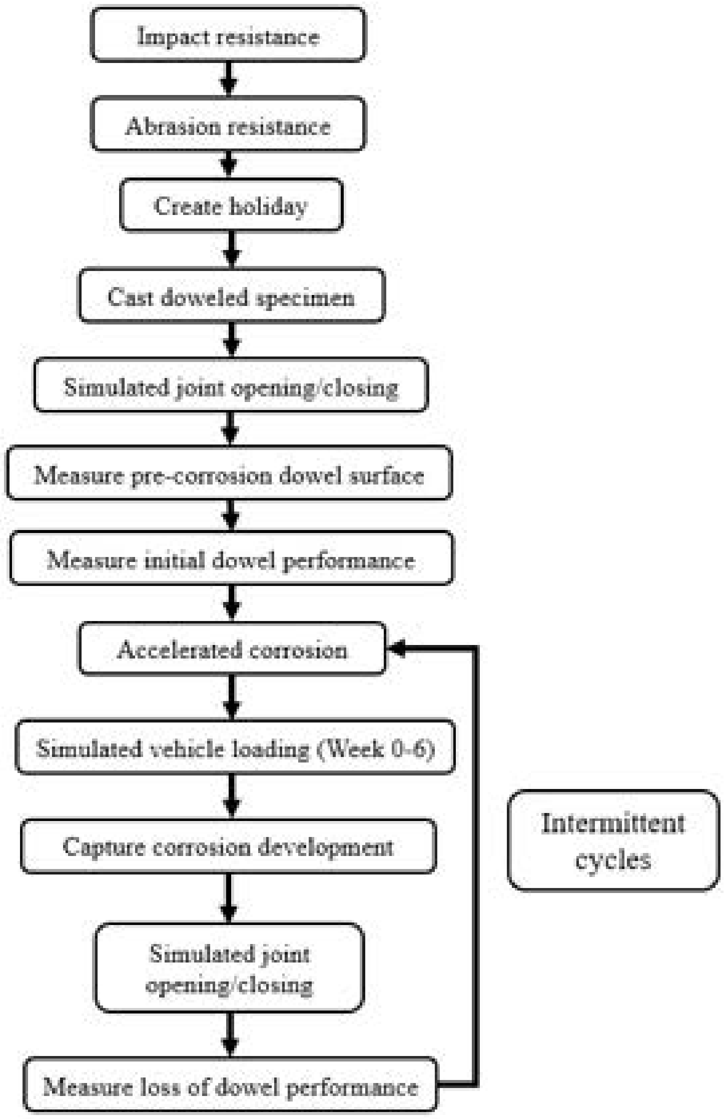

Figure 12. Description of corrosion study.

4.2.2.1 Damage resistance and holiday placement

Prior to casting, impact and abrasion resistance testing was performed on the surface of each dowel. The purpose of this testing is to evaluate the potential for corrosion barriers to be compromised due to wear or impacts thereby increasing the susceptibility to corrosion. Abrasion wear can occur with repeated joint opening and closing from temperature changes in the pavement. Impacts can occur during transit or placement of the dowels prior to paving. Abrasion and impact resistance testing was performed on each dowel included in this study. Additionally, holidays were machined on the surface of each dowel at two levels of area loss; 2 percent and 1 percent. The location of the impact and abrasion resistance testing and the holiday placement is shown in Figure 13.

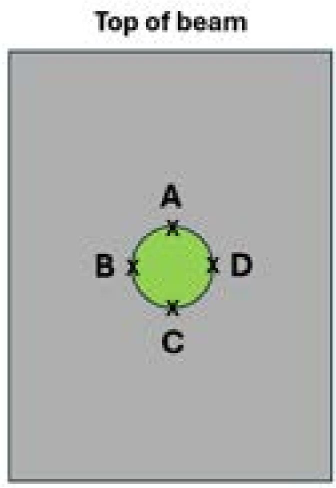

Figure 13. Cross-section of dowel depicting location of A) abrasion testing, B) impact testing, C) machined holiday equal to 2% of area, and D) machined holiday equal to 1% of area.

Abrasion resistance

Abrasion testing was performed using a custom fabricated abradometer provided by American Engineering Testing, Inc. The abradometer is shown in Figure 13. Abrasion testing was performed according to ACPA T253 specifications [52]. The abrasion blocks consist of mortar blocks measuring 4-in long, 3-in wide, and 2-in tall. Each abrasion block was cast with a mortar made from Portland cement and Ottawa sand with the proportion described in AASHTO T 106M [53]. Custom plastic forms were fabricated for each dowel diameter included in this study to ensure the abrasion block applied the load uniformly over one third of the dowel circumference. Example forms are shown in Figure 15.

A weight was fixed to the top of each abrasion block to ensure a test load of 5.5 lbs was achieved. Each dowel was tested to 10,000 double-strokes in the abradometer at a rate of 60 to 70 double-strokes per minute. Figure 16 shows a diagram of the abraded region. Loss of material due to abrasion was determined by measuring the diameter of the dowel before and after abrasion testing. Three measurements were made of the diameter at equidistant points around the circumference. The measurements made are tabulated in Appendix A, while a summary and discussion of the results are provided below.

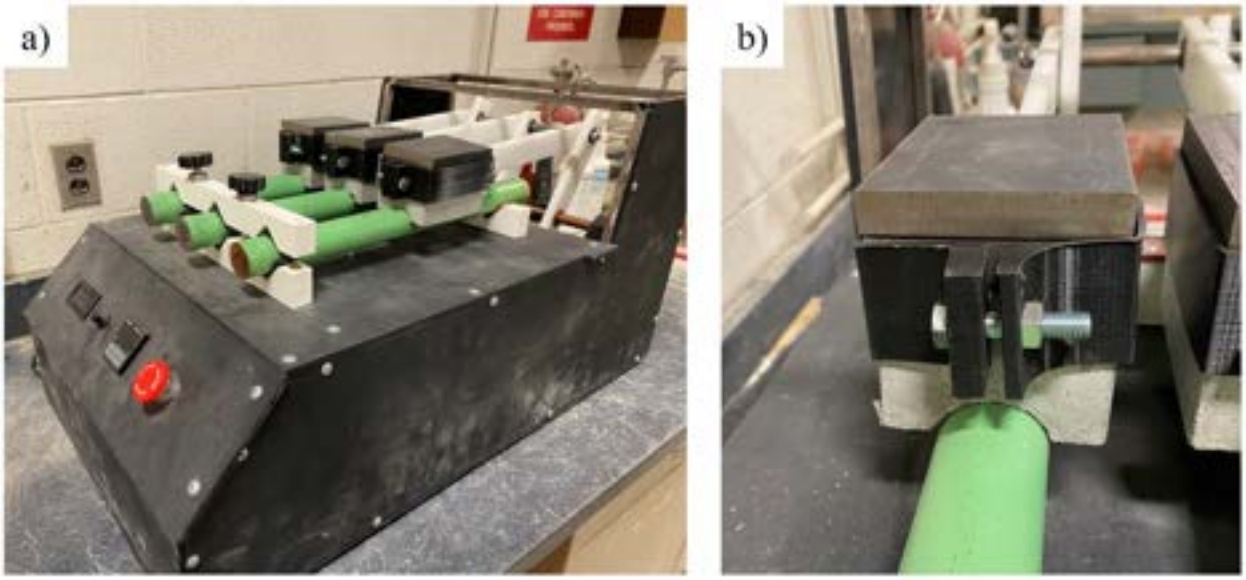

Figure 14. a) Abradometer used to perform abrasion testing for each dowel in this study, b) close up of abrasion block on dowel in abradometer.

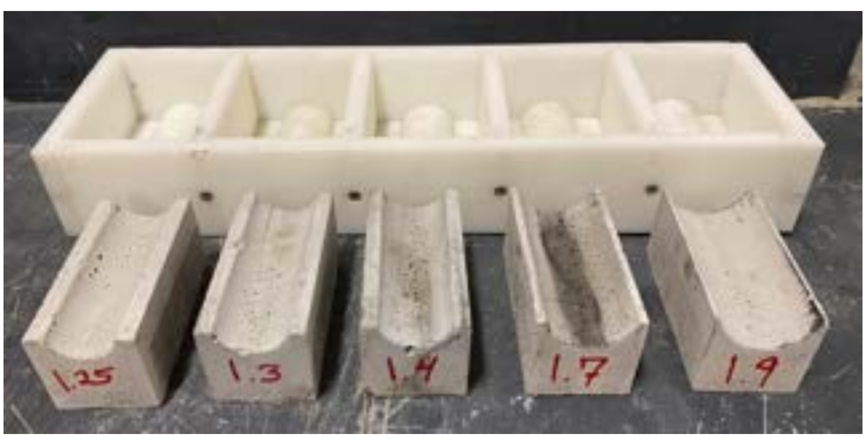

Figure 15. Plastic forms for abrasion blocks and mortar blocks for various dowel diameters included in this study.

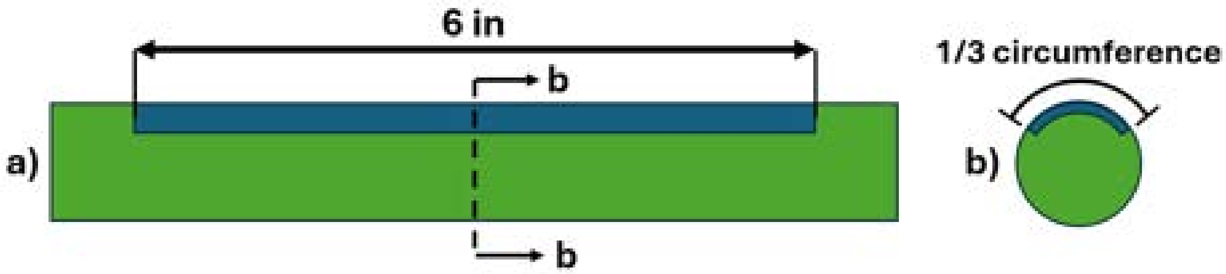

Figure 16. Diagram of dowel with abraded area depcited in blue a) profile and b) cross section.

Impact resistance

Impact testing was conducted on each dowel based on the specifications described in ACPA T253 specifications [52] to characterize the resistance to damage during the construction process. The impact tester shown in Figure 37 was fabricated for this study based on ASTM G14 specifications [54]. A 4-lb tup is dropped from a height of 20 in above the surface of the dowel to impart 80 in-lb of impact energy on the dowel. The test procedure described in ACPA T253 calls for the impact energy to be equal to 80 in-lb for ASTM 775 [48] type (green) and 40 in-lb for ASTM 934 [49] type (purple) epoxy. In this study, a constant impact energy of 80 in-lb was applied for each dowel regardless of coating type to enable direct comparison of impact resistance between dowels. Impact testing was performed at three locations along the length of the dowel with 3-in of spacing between each impact location. A diagram of the impact locations is shown in Figure 18. Depth of impact was determined by measuring the diameter of the dowel at the impact location before and after impact. Each impact was also assigned a severity rating based on visual inspection of the impact from the following options: no damage, minor indent, major indent, minor coating defect, major coating defect, full coating defect. “Defects” are defined as damage to the coating that resulted in exposure of the underlying metal or damage to the surface of the uncoated dowels. Results from the impact testing are found in Appendix A, while a summary and discussion of the results are provided below.

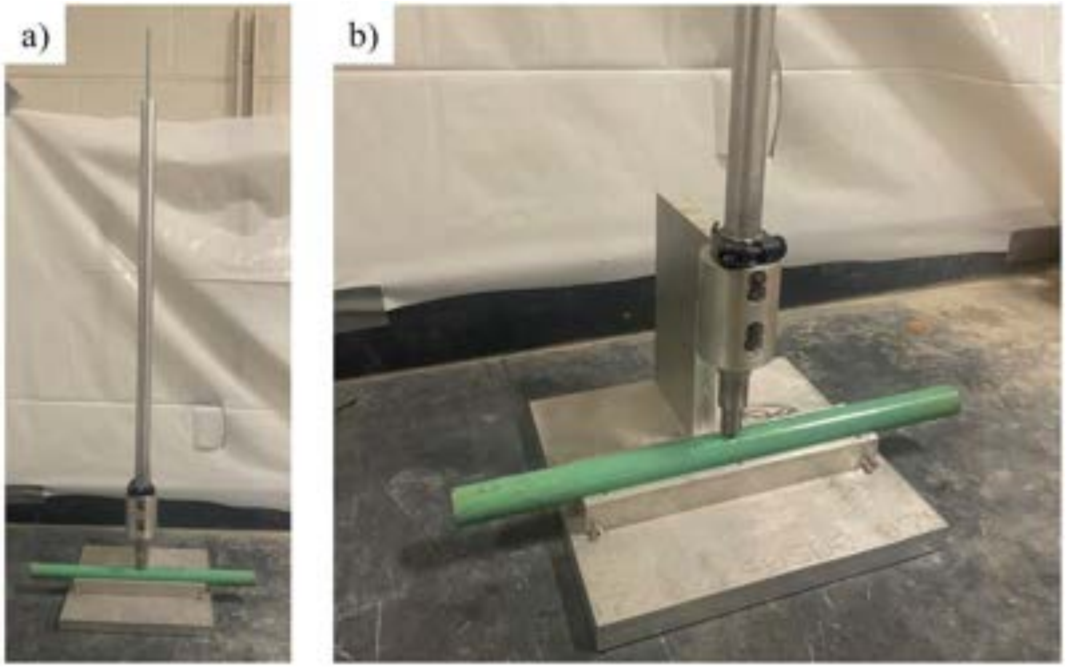

Figure 17. a) Impact tester custom fabricated for this study, and b) close up of dowel in the impact tester.

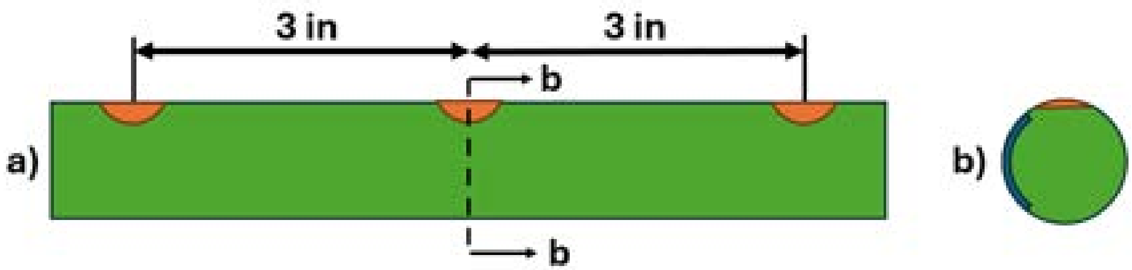

Figure 18. Diagram of dowel with impacted area depicted in orange a) profile and b) cross section views.

Holidays

In addition to abrasion and impact testing, a series of holidays were machined into the dowel. The purpose of these holidays is to enable direct comparison of corrosion development between each type of dowel included in this study. PennDOT allows a maximum of 2% surface area to be damaged through transportation and handling of the dowels prior to paving [55]. In this study, two levels of holiday sizes were milled into the dowel. Three holidays with a combined area equal to 1% of the surface area were placed using a 1/8-in diameter end mill with the holidays spaced at 3 in on-center. Three holidays, of which the sum of the area of holidays is 2% of surface area, were placed using a 1/4-in diameter end mill and again spaced at 3 in on-center. A diagram showing the location of the holidays on the dowel is shown in Figure 19. A flat-tipped mill bit was used so that the exposed metal surface was flat. The depths of the holidays were determined by drilling until the underlying metal was fully exposed along the outer circumference of each holiday. For the hot dipped zinc galvanized dowels with the epoxy coating, the mill penetrated through both the epoxy and the layer of zinc. Several trials were conducted on spare dowels to establish the depth to mill without excessively penetrating into the underlying metal. The stainless steel (SN) and FRP (FN) dowels are uncoated, however, the effect of any holidays on the surface of these dowels were still evaluated. The depth of the holidays for the stainless steel (SN) and FRP (FN) dowels are equal to the average holiday depths determined for the epoxy-coated and zinc-clad dowels. The depths of the holidays for the 1% and 2% defect size was recorded for each dowel type. The holiday depths for each dowel type and holiday size are shown in Table 8. Due to the curvature of the bar and the larger diameter of the holiday for the 2% defect, the depth of the holiday needed to be decreased to ensure the depth of the holiday extended just into the metal.

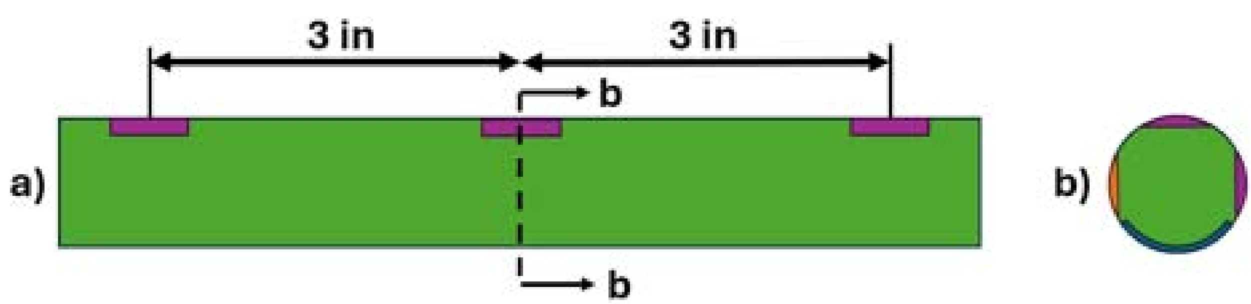

Figure 19. Diagram of dowel with holidays depicted in purple a) profile and b) cross section views.

Table 8. Depth of holidays placed on each dowel type.

Dowel ID	Depth of 1% holidays (mil)	Depth of 2% holidays (mil)
G1G	10	15
G1P	10	13
C2G	20	23
C2P	20	26
FN	21	24
SN	21	24
C4Z	43	45

4.2.3 Doweled beam specimen

After completing the assessment of the durability of the coating as well as milling the holidays, each dowel was cast into a beam. A single 18-in long dowel was embedded in a concrete beam measuring 9-in long, 6-in wide, and 8-in thick. A schematic of the specimen design is shown in Figure 20. Dowels were located at mid-depth and mid-width in the beam. The dowel extended 1.5 in out from the rear face of the beam and 7.5 in out from the front face of the beam. The portion of the dowel that extends out of the front face of the beam is exposed to the corrosive solution during the accelerated corrosion, which is described in Section 5.2.3.4.

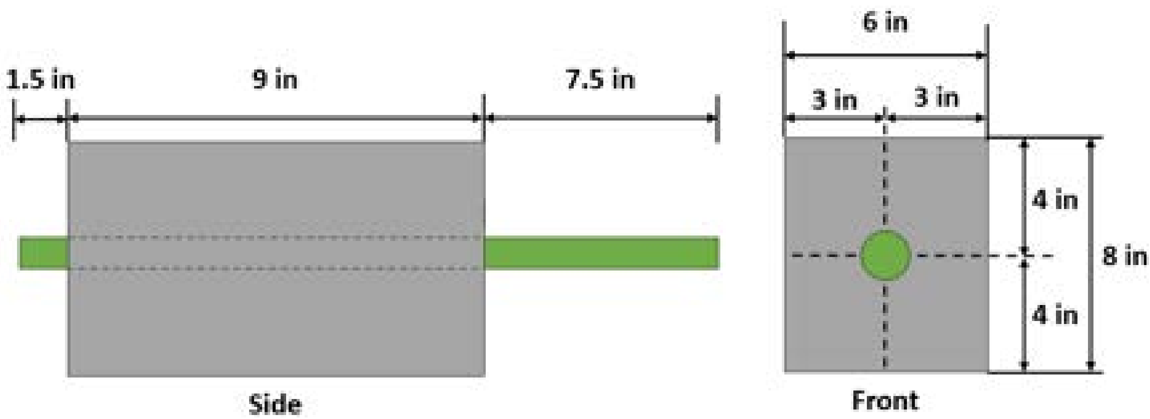

Figure 20. Schematic of beam specimen fabricated for the accelerated corrosion test.

4.2.4 Casting specimens

Each beam specimen was cast in the laboratory according to ASTM C192 [56]. Custom forms were fabricated to ensure the dowels would be maintained at the correct location during casting. An example of the assembled forms with dowels properly located prior to casting is shown in Figure 21. Prior to placement, the dowels are coated with SAE 30 motor oil, which serves as a bond breaker. The dowels are fully dipped in the motor oil and then stood on end for 30 seconds to allow for excess oil to drip off based on the procedure specified in ACPA T253 specifications [52]. Initially, the dowel was kept upright for 15 minutes, however, it was determined during initial shakedown testing that a much shorter time was required to prevent complete loss of debonding agent on the dowel. After the dowels were placed in the forms, oil was reapplied to the dowel to ensure sufficient coating since a snug fit was required between the dowel and the form and some of the release agent would be removed from the dowel during the installation process.

The mixture design used for this test is shown in Table 9 and was developed in accordance with a typical PennDOT paving mixture. The target compressive strength at the time of testing is to 5,500 psi, the target air content is 6% +/- 1%, and the target slump is 3 in +/- 0.5 in. Slump and air tests were performed according to ASTM C143 and C231, respectively, to ensure the batch meets the target values [57] [58]. All specimens were demolded after 24 hours and cured in a moist cure room according to ASTM C192 [56]. The ends of the dowels were coated with an impermeable sealant prior to placement in the cure room to ensure corrosion did not develop in areas with exposed metal before the specimens were placed in the exposure tank. The dowels were fabricated and placed in the exposure tank in two batches. The first batch was placed in the tank on June 18, 2024, and consisted of the following specimens: FN1, FN2, FN3, G1G1, G1G3, G1P, and SN3. The SECOND batch was placed in the tank on June 25, 2024, and consisted of the following specimens: C4Z1, C4Z2, C4Z3, C2G1, C2G2, C2G3, C2P1, C2P2, C2P3, G1G2, G1P1, G1P2, SN1, and SN2. The placement of the batches into the tank was staggered by one week to allow for sufficient time each week to evaluate the corrosion development on each sample.

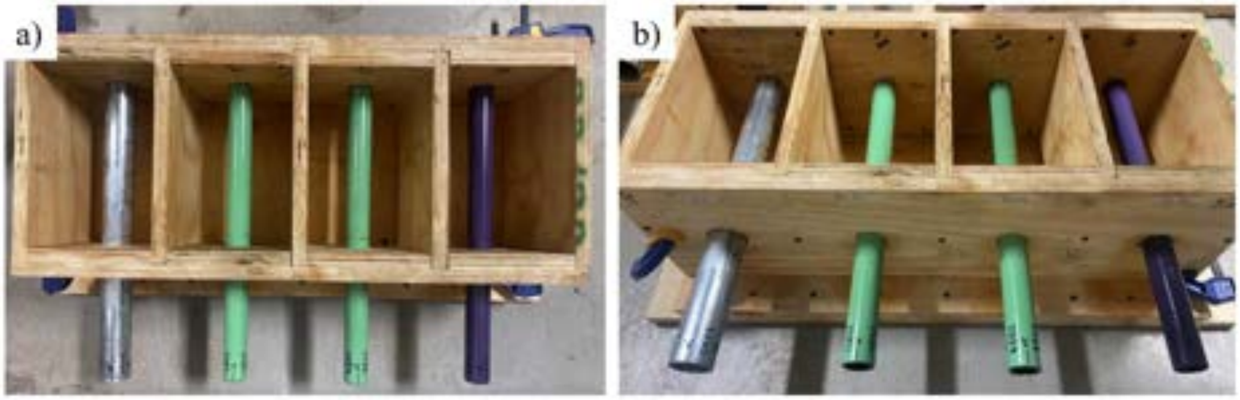

Figure 21. Forms with dowels installed prior to casting.

Table 9. Mixture design used for casting specimens.

Material	Weight (lb/cy)	Volume (cft/cy)	Vol. fraction
Coarse aggregate	1918	11.34	0.42
Fine aggregate	1078	6.59	0.24
Cement	630	3.21	0.12
Water	265	4.24	0.16
Air content (6%)	-	1.62	0.06
Superplasticizer, Sikament SPMN	2.7 oz per 100 lbs cement		
Water reducer, Sika ViscoCrete-1000	2.3 oz per 100 lbs cement		
Air entrainer, Sika AIR-260	1.5 oz per 100 lbs cement		

4.2.5 Corrosion Resistance

The main component of this laboratory investigation is the novel accelerated corrosion setup developed for this study. This test setup consists of an exposure tank and a storage reservoir that were designed so that the 21 specimens (7 different dowel designs with 3 replicates each) tested could be simultaneously exposed to the same solution, thereby minimizing variability between specimens. It also has the capability of cycling between wet and dry periods. The accelerated corrosion setup is shown in Figure 22 - Figure 24. The exposure tank contains approximately 200 gallons of a solution of water and 5% NaCl (wt%). The solution is aerated by a bubbler consisting of a compressor feeding air through a 1/8-in diameter plastic line fixed at a height of approximately 4 in in the center of the tank. The solution is constantly agitated using two submersible pumps fixed at a height of approximately 4 in and 5 ft away, each on opposing sides of the aerator. Both the bubbler and agitators are used to ensure the solution is consistently aerated and that the salt concentration is uniform throughout the test solution. A top view of the location of the bubbler and agitators is provided in Figure 23 with a side view shown in Figure 24.

Each specimen is placed on the support frame in the exposure tank with the dowel oriented vertically towards the bottom of the tank. The specimens are subjected to wetting/drying cycles, which is achieved by raising and lowering the solution level within the exposure tank. Wetting is achieved by raising the solution level to fully submerge the dowel and approximately the first 1 in of the beam. Drying is achieved by pumping approximately 120 gallons of the solution from the exposure tank to the storage reservoir, thereby lowering the solution level and exposing approximately 5 in of the dowel to air. The duration of the wetting period is 30 minutes, and the duration of the drying period is 150 minutes (2 hours and 30 minutes). The pumps are wired into timers to continuously cycle between wetting and drying in an automated fashion. The pump schedule is shown in Table 11. The pump runs for 3 minutes to transfer the solution from the exposure tank to the storage reservoir, and for 4 minutes to transfer the solution from the reservoir back to the exposure tank during each cycle. The reservoir tank is covered with insulation to ensure the solution temperature remains relatively constant throughout the duration of the testing and to slow water evaporation.

After 20 weeks of salt exposure, a significant drop in the solution level was observed. This drop in solution level is attributed to evaporation even though the exposure tank was covered. A sudden rise in the laboratory air temperature due to construction activity was measured during Week 12 for the first batch of samples and Week 11 for the second batch of samples. The rise in temperature likely caused an increase in the rate of surface water evaporation and decreased the solution level. As a result, the beams were not fully saturated throughout the entire duration of the 20-week testing period. The progression of water loss was estimated by evaluating weekly photographs of the specimens taken throughout the duration of the testing. Sediment remaining on the dowel and corrosion progression on the holidays at the face of the beam and 3 in away from the beam were used to determine at which point the solution level dropped below each holiday. It was determined that the solution level dropped below the holiday at the face of the joint during Week 12 for batch one specimens and Week 11 for batch two specimens. The solution level dropped below the holiday 3 in from the face of the beam during Week 20 for batch one specimens and Week 19 for batch two specimens. The visual analysis, showed that corrosion continued to progress, although at reduced rate, which will be discussed in more detail in Section 4.3.2.3. During Week 20, the tank was refilled with water to bring the total solution back to approximately 200 gallons. The salinity was monitored to ensure it remained at 5%. Based on this, the actual duration of exposure of the bottom most holiday between test week 18-36 was determined, and is summarized in Table 10.

Table 10. Estimated salt exposure duration.

Test Week	**12**	**14**	**16**	**18**	**22**	**24**	**30**	**36**
Exposure Duration (Wks)	12	12	12	12	14	16	22	28

Figure 22.Accelerated corrosion test setup, with a) exposure tank, b) storage reservoir, c) inlet pipe for solution flowing from storage reservoir to exposure tank, d) outlet pipe for solution flowing from exposure tank to storage reservoir, and e) emergency overflow pipe.

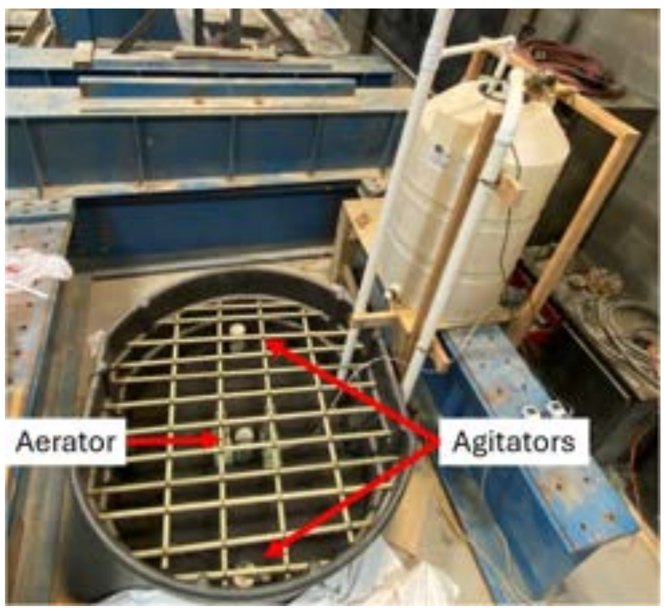

Figure 23. Photo of empty exposure tank and storage reservoir from above, showing the specimen support frame with openings for doweled specimens.

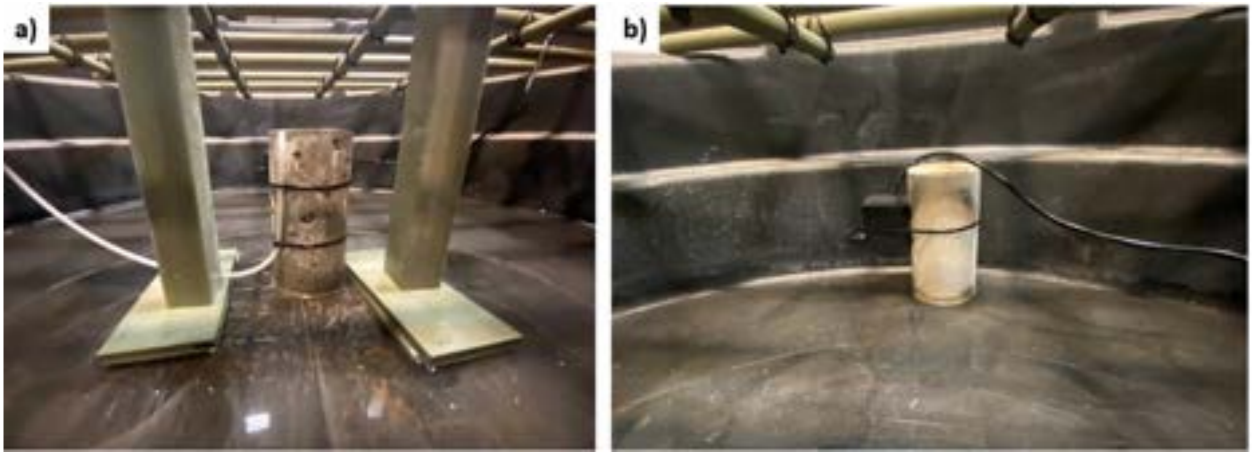

Figure 24. View of the inside of the exposure tank showing a) the center of the tank with the bubbler and verical supports for the specimen frame, and b) one of the two agitators placed near the outer diameter of the tank to maintain constant solution movement throughout testing.

Table 11. Daily pump schedule used to ensure consistent duration of wetting/drying cycles for all specimen.

Fill exposure tank (30 min full)		Drain exposure tank (2 hr 30 min drained)	
Storage reservoir pump		Exposure tank pump	
On	Off	On	Off
12:00 AM	12:04 AM	12:30 AM	12:33 AM
3:00 AM	3:04 AM	3:30 AM	3:33 AM
6:00 AM	6:04 AM	6:30 AM	6:33 AM
9:00 AM	9:04 AM	9:30 AM	9:33 AM
12:00 PM	12:04 PM	12:30 PM	12:33 PM
3:00 PM	3:04 PM	3:30 PM	3:33 PM
6:00 PM	6:04 PM	6:30 PM	6:33 PM
9:00 PM	9:04 PM	9:30 PM	9:33 PM

4.2.6 Simulated joint opening/closing

A byproduct of corrosion is oxidation, which expands from the metal surface. This expansion may result in corroded dowels to seize. Seized dowels require a greater force for the slab to mobilize with temperature changes. To study this behavior, simulated joint movement was periodically conducted on each specimen to measure the bond strength between the dowel and surrounding concrete and joint lock-up potential. The test performed in this study was a modified version of the pullout test described in ACPA T253 [52]. A 5.5-kip actuator was used to apply a load parallel to the axis of the dowel. The actuator was operated in displacement control at a rate of 30 mils/min, and the applied load was recorded throughout the duration of the test. The applied load and displacement were recorded at 12 Hz. A schematic of the simulated joint opening/closing test is shown in Figure 25 and Figure 26.

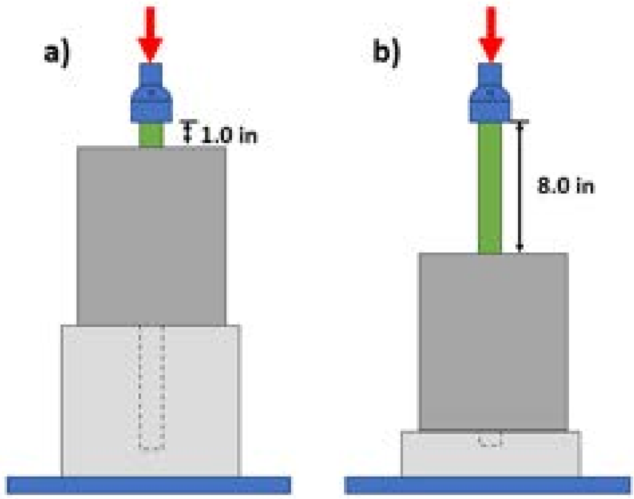

Figure 25. Diagram of simulated joint movement test performed on a) rear end of dowel and b) front end of dowel.

Figure 26. Joint opening simulation test performed on rear end of dowel during shakedown testing.

The joint opening/closing simulation testing was performed both before being exposed to chlorides and throughout the duration of the exposure process. The dowels would not debond without inducing damage to the specimen when simulating opening and closing after 7 days of curing. To prevent this issue and ensure that all dowels were completely debonded, the procedure was revised to include performing initial testing 24 hours after casting and then a second time after 7 days of curing, as shown in Figure 27, to mobilize the dowel just prior to exposing it to the salt solution.

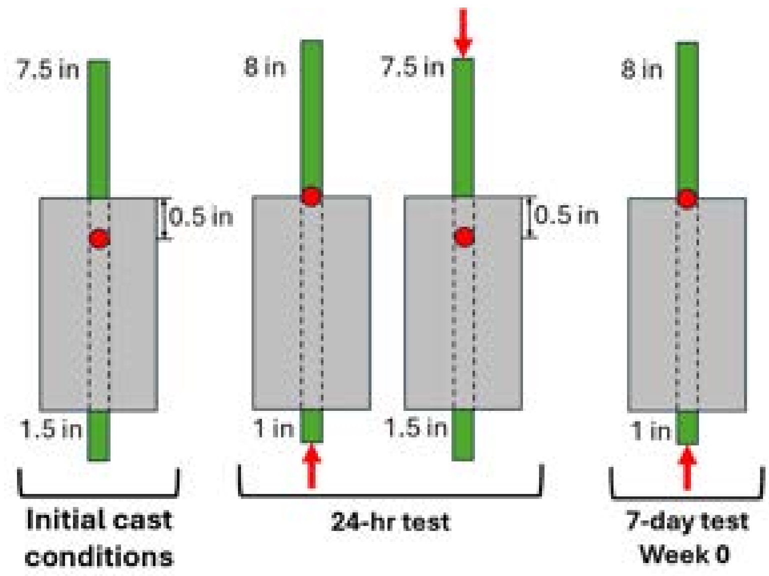

Figure 27. Pre-chloride exposure joint/opening closing simulations. (Direction of load (red arrow), location of holiday nearest to the face of the beam (red circle), and location of bar after each joint opening/closing simulation is applied.)

The beams were cast with the second holiday located 0.5 in from the face of the joint in the interior of the beam. Then, 24 hours after casting, a load was applied at the rear end of the dowel in displacement control at a rate of 30 mils/min as shown in Figure 27. The dowel was pushed such that the second holiday was moved to the face of the beam. The specimen was then flipped 180 degrees so the 8.0-in long segment of the dowel was facing upwards towards the loading head, as shown in Figure 27. The load was applied in displacement control at a rate of 120 mil/min to the front of the dowel test in this orientation so that the holiday was located 0.5 in from the face of the beam in the interior of the beam. The specimens were then cured for an additional 6 days under wet burlap and plastic. After this curing period, simulated joint opening was performed in displacement control at a rate of 30 mil/min in only one direction based on the orientation shown in Figure 27. Upon completion of this test, the holiday was located at the face of the concrete beam and is partially exposed. The dowel was then loaded to assess performance under simulated vehicle loads as described in Section 5.2.3.4. The specimen was then placed in the exposure tank to initiate cycling in the salt solution.

Post-exposure simulated joint open/closing testing was performed periodically after cyclic exposure to the salt solution. The purpose of this was so that any restraint that developed due to expansion of the metal on the surface of the dowel as a result of oxidation could be identified. Simulated joint opening was also performed on FRP specimens to identify the effect of potential swelling of the FRP dowels caused by water intrusion into the dowel.

During weeks 2-16, these tests were performed at 14-day (two-week) intervals during the salt exposure. The test was performed first on the rear of the dowel to simulate joint opening by loading the specimen in the orientation shown in Figure 28 in displacement control at a rate of 30 mil/min. Upon completion of this sequence, the holiday was located 0.5 in away from the face of the joint on the exposed portion of the dowel. The specimen was then rotated 180 degrees and the dowel was loaded from the front in displacement control at a rate of 120 mil/min. Upon completion of this sequence, the holiday was located at the face of the joint and was partially exposed when returned to the exposure tank.

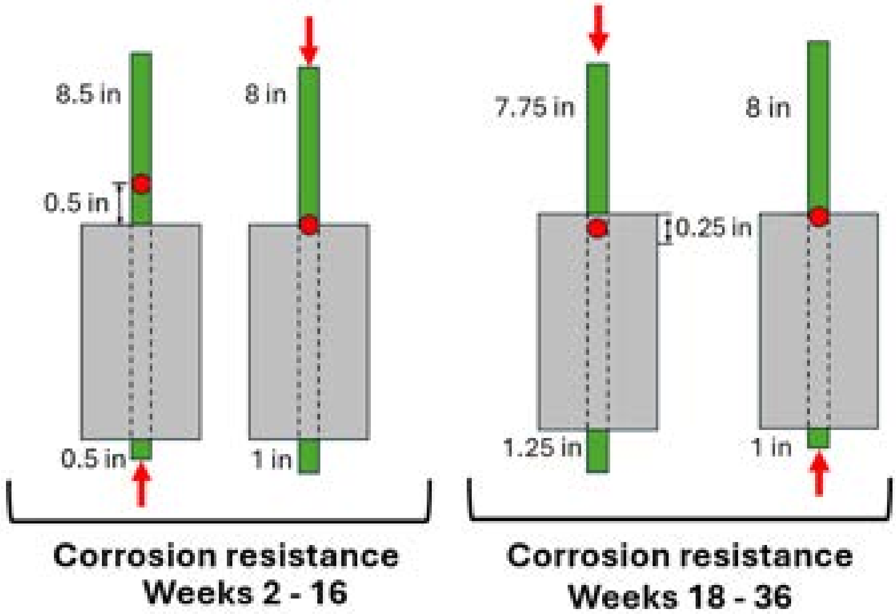

Figure 28. Post-chloride exposure joint opening/closing simulations during Week 2-36. (Direction of load (red arrow), location of holiday nearest to the face of the beam (red circle), and location of bar after each joint opening/closing simulation is applied.)

The samples were tested again at Weeks 18, 22 and 24 and then every 6-weeks through Week 36. While tests conducted in the weeks 0 to 22 focused on the force required for opening the joint, the focus was shifted to the force required for joint closure for testing performed after Week 16. This is reflected in Figure 28. This decision was made so that the effect of the corrosion could be better captured since spalling that occurred during the 24-hr joint closure testing limited the amount of contact between the concrete and the dowel at the location of the second flaw. First, the test was performed by loading the front of the dowel to displace it a total of 0.25 in at a rate of 30 mil/min. Joint opening was than simulated by flipping the specimen 180 degrees and again displacing the dowel 0.25 in at a rate of loading 30 mil/min, as shown Figure 28.

4.2.7 Simulated vehicle loading

A critical component of this laboratory test is the evaluation of the effect of corrosion development on dowel performance. To do so, a novel test setup was developed to test the stiffness of the dowel system. A schematic and photo of the setup is shown in Figure 29. A specimen is placed on supports and a vertical restraint is applied to the specimen. A loading head is positioned to apply vertical loads on the top surface of the dowel at a distance of 5 in from the face of the beam. The loading head consists of a steel fixture with a rounded tip fixed to a rotational knuckle on the end of a 5.5-kip capacity hydraulic actuator. The applied load is equal to 475 lbf. This load was determined based on a bearing stress equivalent to that generated by a 36-kip tandem axle (ML) in the accelerated load test described in Chapter 6 of Donnelly (2025) [59]. The applied load magnitude was determined based on a 1.25-in diameter solid dowel with an assumed modulus of dowel concrete interaction, K, of 1.5×10^6 psi/in.

For each test, two load sequences are applied. The first loading sequence consists of 1,000 cyclic loads applied at 5 Hz. The purpose of these loads is to minimize the effect of microcracking or debris, which may develop while the specimen is subjected to accelerated corrosion. Each load consists of a sinusoidal load pulse applied over 0.05 seconds, followed by a 0.15 second rest period. The applied load and actuator displacement was collected at a frequency of 1024 Hz for the final 10 cycles to ensure the proper loading sequence is being applied. A constant load of 100 lbs is maintained between load pulses to ensure the loading head remains in constant contact with the dowel. The second loading condition consists of applying a 475 lb static load to measure dowel deflection. The load is applied for 30 seconds before deflection measurements are taken to ensure the dowel deflection has stabilized. Deflection measurements are taken with an AccuRange600™ laser profiler produced by Acuity Lasers. The laser is mounted to a linear traverse table. The linear traverse performs three 6-in long passes in the direction parallel to the axis of the dowel. Deflection measurements are recorded every 0.1 in along each pass. Each pass is offset from the adjacent pass by 0.1 in perpendicular to the axis of the dowel. The deflection measurements are compiled to establish the deflection profile of the dowel.

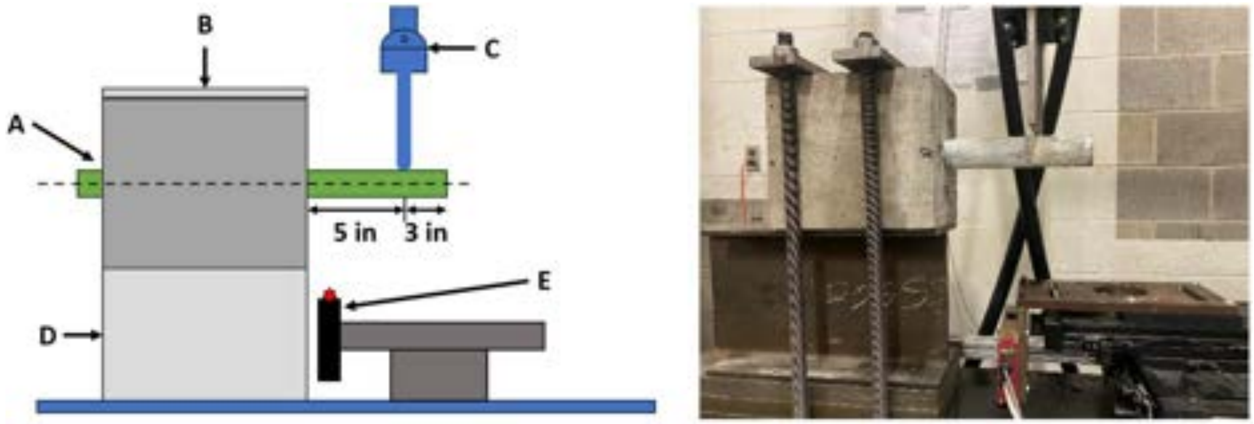

Figure 29. Photo and schematic of vertical load test, with a) the doweled specimen, b) a vertical restraint, c) actuator load head, d) steel supports, and e) AR600 laser scanner mounted to an xy-table.

4.2.8 Corrosion assessment

The degree to which corrosion developed at the localized flaws is measured every two weeks throughout the duration of the accelerated corrosion program, with the exception of a four week period between Week 8 and Week 36. The specimens are removed from the exposure tank, and simulated joint opening/closing testing is performed and then the surface of each specimen is scanned. The surface of each specimen is scanned using the Quantum Max FaroArm® 3D laser scanner [60] starting Week 0 (prior to the dowels being placed in the salt exposure tank) and continuing through subsequent weeks, as previously described. The laser scanner measures points with a minimum spacing of 0.0012 in and an accuracy of 0.001 in. The FaroArm® model used in this study is shown Figure 30. The face of the concrete beam adjacent to the dowel and the dowel itself is manually scanned with several passes to fully capture the corroded features along the length of the dowel. An example of a specimen with a 1.25-in diameter green epoxy coated steel dowel evaluated during shakedown testing is shown in Figure 31. The seven holidays placed in the epoxy coating prior to testing can be seen in the scan.

Figure 30. Quantum Max FaroArm® used to scan dowel specimens.

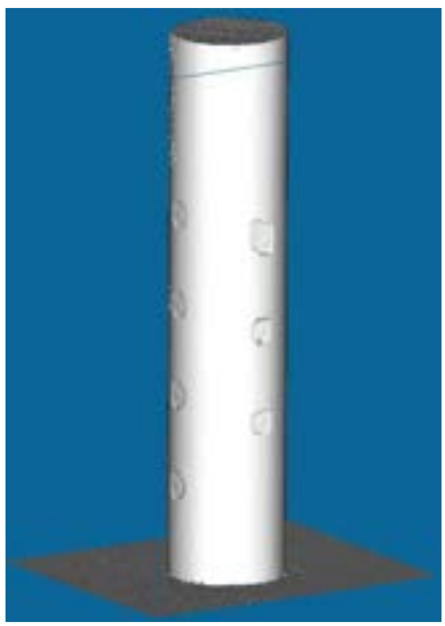

Figure 31. Surface generated from a dowel specimen with a 1.25-in diameter green epoxy-coated dowel prior to placement in corrosion tank.

To quantify the temporal progression of the corrosion, focus was placed on the 2% holiday furthest from the beam face. The surface of each specimen is scanned using the Quantum Max FaroArm® (See Figure 31.) with the initial scan beginning in week 0 (prior to the dowels being placed in the salt exposure tank) and continuing throughout the duration of the time the specimens were in the exposure tank. The scan performed at Week 0, prior to the development of corrosion on the dowel bar, serves as the reference scan. Each scan includes the entire surface of the dowel bar and a portion of the concrete face, generating a large point cloud. A triangular mesh is generated from the point cloud using Geomatic Studio, providing the surface of the dowel bar and concrete in an STL file format. The vertices of the triangular mesh are converted back into point clouds for further analysis. The process of meshing the point cloud and then converting the meshed image back into a point cloud reduces the amount of unnecessary data (overlapping points, etc.) while maintaining the critical information defining the geometry of the object. Additional data processing performed on all scanned data after Week 0 includes manually adjusting the orientation and position of the point cloud to align with the point cloud from Week 0. This facilitates the ability to make direct visual comparisons between the holidays as the development of corrosion progresses. To do this, the center of the exposed 2% holiday (3 in from the beam surface) is identified manually and defined as the reference point between scans. The point clouds for all scans generated in subsequent weeks are manually aligned to this reference point from the point cloud generated in Week 0. Additional processing of each point cloud is then performed to better observe corrosion development around this reference holiday (2 percent holiday located furthest from the beam). First, a 0.2-in radius filter is applied to the surface of the 2 percent holiday for each scan based on the location identified as the "center" of the holiday. The section of the point cloud within this radius is extracted and the density is resampled into a uniform 100 x 100 grid. The process maps scattered 3D points into a regular grid in the X-Z plane using cubic interpolation to estimate missing Y coordinates. This adjusts the distribution of points by filling sparse areas and thinning dense ones. The final product is a uniformly sampled point cloud with a 2% holiday surface for each scan. The results of the scans are discussed below with a library of photos and scans taken incrementally throughout the salt exposure, included as Appendix C.

4.3 Results

This corrosion testing described in Section 4.2 was used to evaluate the dowel bars described in Section 4.2.2. This section presents the results from the corrosion testing. First, the coating durability assessment portion of the study is presented in Section 4.3.1. This includes results from the abrasion resistance test and the impact resistance tests. Second, the results from the accelerated corrosion test are presented in Section 4.3.2.

4.3.1 Coating Assessment

The following section summarizes the assessment of the durability of the coating and presents the key findings. Detailed results and photographs are provided in Appendix A. This section first presents a discussion of the results from the abrasion resistance testing followed by a discussion of the impact resistance testing.

4.3.1.1 Abrasion resistance

Abrasion resistance testing was performed on the dowels listed in Section 4.2.1 and the results are summarized in Table 12. The 10,000 double-strokes resulted in minimal coating wear on the epoxy coated dowels, as seen in the images in Appendix A, as well as in the summary date provided in Table 12. The full compilation of data collected is provided in Table A1 in Appendix A. Typically the wear observed was localized to linear wear paths parallel to the length of the dowel. An example of a purple epoxy-coated dowel before and after testing is shown in Figure 32. The abrasion wear was likely localized due to slight variations in coating thickness throughout the diameter of the dowel. During testing, regions where the coating is thicker extended outward more from the bar, thereby creating contact points with the abrasion block resulting in areas with increased wear. Despite areas of localized wear, there were no locations where the epoxy coating was compromised to the point that the bare metal was exposed. Therefore, all epoxy coated dowels passed the abrasion resistance test. The uncoated dowels (stainless steel, zinc-clad, FRP) exhibited negligible wear. Although slight wear was visible on the stainless steel and zinc clad dowels, the average loss of metal for both types was approximately 1 mil. No measurable wear was observed for the FRP dowels. The FRP dowels tested are very smooth due to the resin contained in the dowels, which minimizes friction. The lack of friction likely contributes to the resistance to wear. The variability in wear observed in the green epoxy-coated zinc galvanized and zinc-clad tubular dowels is likely due to nonuniformity in the dowel surface. It was observed that some of the dowels did not have perfectly circular cross-sections. This causes uneven contact between the abrasion block and the dowel surface that results in localized areas of abrasion. Regardless, none of the barriers were damaged to the extent that corrosion developed in these regions.

Figure 32. Specimen G1P3 a) before testing and b) showing channelized abrasion wear after testing.

Table 12. Average coating loss due to abrasion testing performed on three test points per specimen.

Dowel Type	Specified Coating Thickness, mil	Avg. Coating Loss, mil	Stan. dev. of Coating Loss, mil
Solid steel dowel with green epoxy	20	0.4	0.8
Solid steel dowel with purple epoxy	20	1.1	0.8
Galvanized tubular dowel with green epoxy	10[1]	3.1	2.2
Galvanized tubular dowel with purple epoxy	10[1]	1.0	0.3
Zinc-clad tubular steel dowel	35	1.1	1.9
Stainless steel tubular dowel	-	1.3	0.7
Solid FRP dowel	-	0.0	0.0

[1]The galvanized layer is 0.8 mils thick.

4.3.1.2 Impact resistance

Impact resistance testing was performed on the dowels. The majority of the dowels exhibited minimal damage due to the impact testing. The impact from the weighted tup caused negligible surface deformation for the uncoated, metallic dowels (SN and C4Z) and the FRP dowels. The impact caused minimal deformation in the flexible, green epoxy coated dowels (C2G, G1G), however, the underlying steel was not exposed. The results of the impact test, along with an assigned damage rating, is included in Table A2 of Appendix A along with photos of the impact locations.

The only type of dowel that developed impact damage is the 20-mil thick purple epoxy-coated steel dowels. At least one impact resistance test on each of the three specimens resulted in a large depression in the coating. Additionally, the impact from the weighted tup caused cracking in the epoxy coating adjacent to the location of impact. An example of damage that occurred is shown for specimen C2P2 in Figure 33. The coating adjacent to the impact location was damaged but not compromised, resulting in small particles of the coating flaking away. Each of the 20-mil thick purple epoxy coated dowels failed the testing requirements specified in AASHTO T253 [61] due to the degree of damage from impact, but a tup with a larger weight was used in this testing than is defined for use on a purple epoxy in this specification. The damage to the coating was not compromised to the extent that corrosion developed at these locations when exposed to the salt solution, which will be discussed further in the results section.

Interestingly, the 10-mil thick purple epoxy-coated tubular dowels did not exhibit the same degree of damage from the impact testing as compared to the 20-mil thick purple epoxy on the carbon steel dowels. There are two possible explanations. First, the increased coating thickness may have enabled additional deformation, resulting in damage. This is not likely given the 20-mil green (flexible) epoxy coating did not exhibit similar damage. The second, and likely, explanation is the solid steel dowel and tubular dowels were sourced from different manufacturers. Therefore, the materials used to apply the 20-mil thick coating and the 10-mil thick coating are not identical, and the purple epoxy used for the solid steel dowels is more prone to failure. As will be described below, the effects of this minor damage did not compromise the corrosion resistance for any of the dowels.

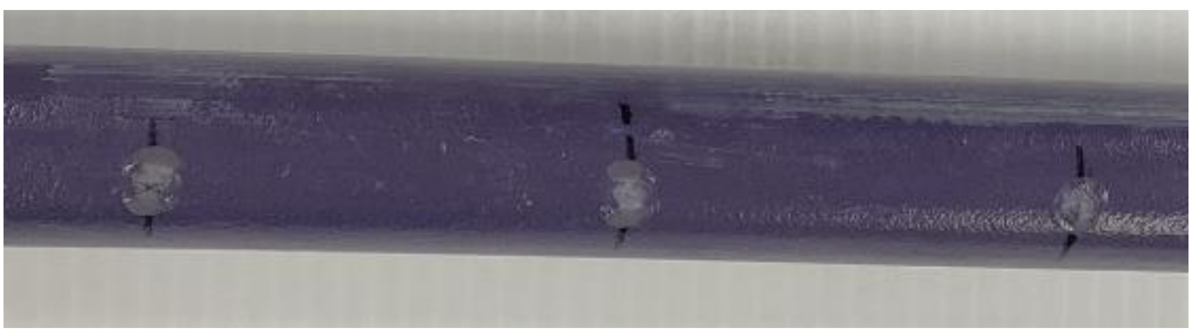

Figure 33. Result of impact resistance testing on C2P2.

Conclusions: All coatings evaluated have sufficient resistance to impact and abrasion and are suitable for use.

4.3.2 Corrosion Assessment

The following section summarizes the corrosion assessment and presents the key findings. Detailed results and photographs are provided Appendices B and C. Section 4.3.2.1 first provides a discussion of the results from the simulated joint opening/closing. Second, in Section 4.3.2.2, a discussion of the simulated vehicle testing is presented. Section 4.3.2.3 provides a discussion on the measurement of increasing corrosion area on the corrodible dowel types using a manual image segmentation method. Lastly, section 4.3.2.3 contains a characterization of the changes in corrosion development of 2% holiday area.

4.3.2.1 Simulated Joint Opening/Closing

This section provides a discussion of the results from the simulated joint opening/closing. The distance the joint was opened and then closed or closed and then opened in the case of Weeks 18-36, is summarized in Table 13. First, the results from the initial joint opening/closing simulation is discussed to evaluate the bond between the concrete and the dowel bar prior to salt exposure. Then a discussion is presented on the results from the simulations performed between Weeks 2 – 36 to establish the effect of salt exposure on joint opening/closing.

Table 13. Distances the joint was opened/closed and closed/opened.

	Opened	**Closed**
24 hrs.	0.5 in	0.5 in
7 days (Week 0)	0.5 in	-
Weeks 2-16	0.5 in	0.5 in
	Closed	**Opened**
Weeks 18-36	0.25 in	0.25 in

Pre-exposure Joint Opening/Closing

The simulated joint opening/closing was performed after 24 hours and 7 days (Week 0) of curing prior to exposing the dowels to the salt solution. This ensures all dowels are completely debonded within the concrete beam prior to exposure to the salt solution and provides an opportunity to evaluate the force required to overcome the initial bond between the dowel surface and the surrounding concrete, in a manner similar to a simulated joint opening/closing test. A summary of the averages and standard deviations is tabulated in Table 14 and shown graphically in Figure 34 and Figure 35 with all measured values provided in Appendix B.

It should be noted that two specimens, one steel bar with green epoxy (C2G3) and one stainless steel bar (SN1), exhibited significantly lower joint opening/closing forces when loaded 24 hours after casting potentially due to an excessive application of debonding agent. For one the green epoxy coated carbon steel rods (C2G3), the 7-day (Week 0) joint movement simulation force was much lower than the other C2G dowels, and the force remained low for all subsequent test weeks (Week 2 – 36). Additionally, one of the stainless steel dowels (SN1) had a low force during the initial joint movement simulation, and by Week 8 became too loose to continue testing. For the purposes of comparing average simulated joint opening/closing forces, these specimens are considered outliers and were excluded when establishing the average and a standard deviation could not be established with only two replicates.

Table 14. Pre-exposure simulated joint opening and closing force and shear stress.

		Mobilization Force, lbs		Mobilization Shear Stress, psi	
Specimen		24-Hour	7 Days (Week 0)	24-Hour	7 Days (Week 0)
C2G	Average	1,977	2,798	55.9	79.2
	St. Dev.	-	-	-	-
C2P	Average	764	577	21.6	16.3
	St. Dev.	192	91	5.4	2.6
C4Z	Average	155	188	3.2	3.9
	St. Dev.	96	66	2.0	1.4
FN	Average	880	523	24.9	14.8
	St. Dev.	401	494	11.3	14.0
G1G	Average	2,930	2,003	77.3	52.9
	St. Dev.	1,736	1,428	45.8	37.7
G1P	Average	3,364	2,894	88.8	76.4
	St. Dev.	546	783	14.4	20.7
SN	Average	3,671	2,909	68.3	54.2
	St. Dev.	-	-	-	-

*Specimens C2G3 and SN1 are considered outliers and are thus omitted from the characterization statistics.

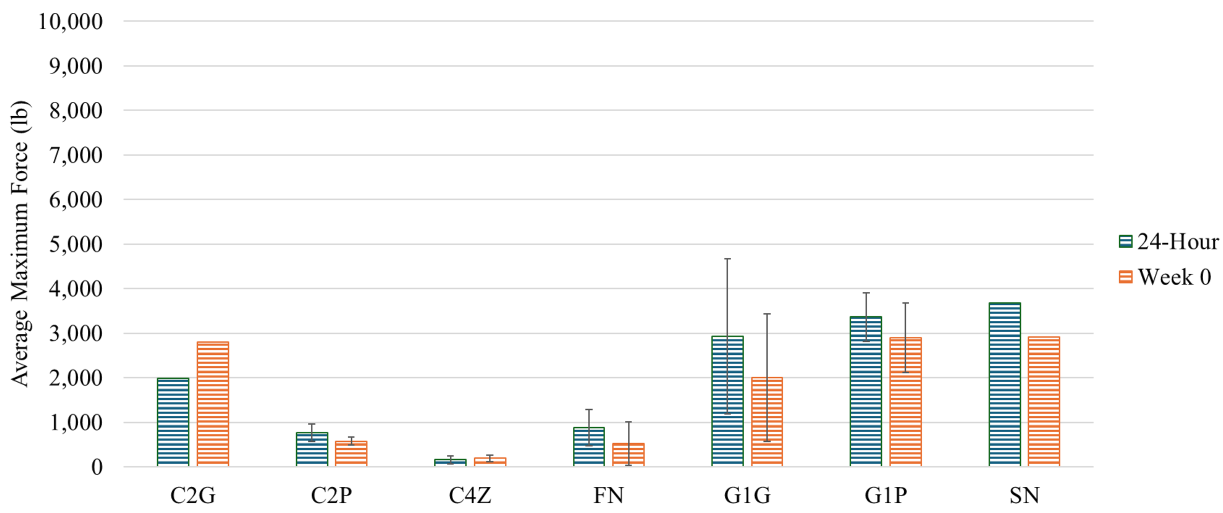

Figure 34. Maximum force when simulating joint opening prior to exposure to the salt solution.

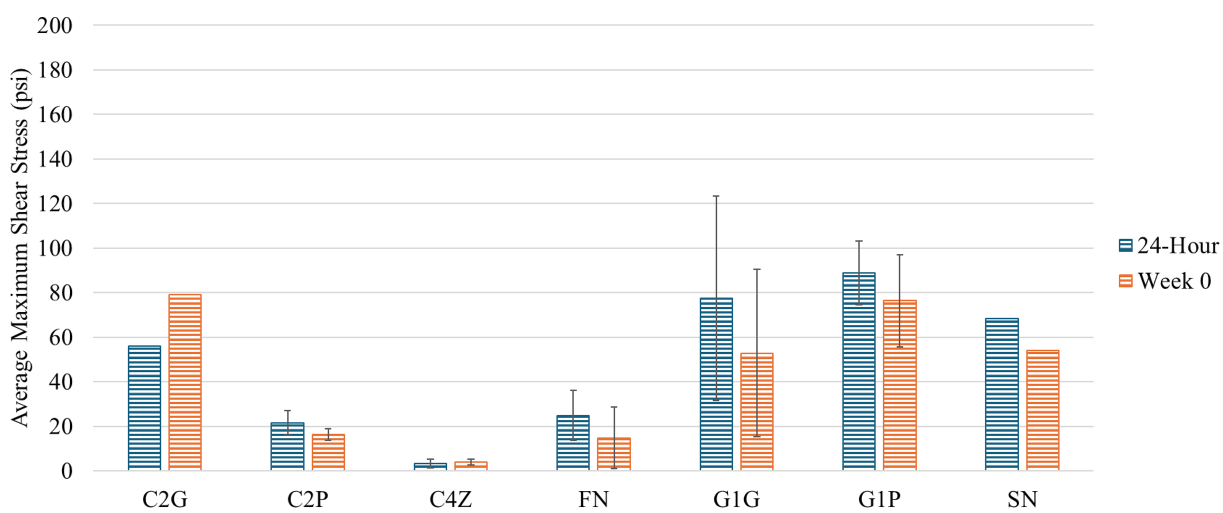

Figure 35. Maximum shear stress when simulating joint opening prior to exposure to the salt solution.

As previously discussed, the simulated joint opening/closing was developed in a manner similar to the pullout test described in AASHTO M254 [62]. The maximum allowable force specified in AASHTO M53 [63] is 3,000 lbs. The forces measured during the initial joint opening are compared to this threshold. On average, the 24-hr. joint opening force measured for the purple epoxy-coated zinc galvanized (G1P) and stainless steel (SN) dowels exceeded the 3,000 lb load limit. The average 24-hr. joint opening force measured for the green epoxy-coated zinc galvanized (G1G) dowel is 2,930 lb, which nearly reaches the 3,000 lbs limit specified. The 24-hr. joint opening force for the other dowel types were below this threshold. Additional differences between this test and the AASHTO M254 [62] test procedure, which would also make this lower threshold less suitable, are described below. It should also be noted that while the average of the 2 specimens for the stainless steel bar is greater than 3,000 lbs, the force for one of the stainless steel dowels was so low it eventually could be moved back and forth by hand.

For all but the steel dowels with green epoxy (C2G), the maximum force to open the joint was higher when the joint was initially opened after 24-hours than after 7 days of curing. The variability in initial joint opening/closing force between dowels may be attributed to differences in the texture of the dowel surface, the surface area of the embedded dowel (dowel diameter), or variation in the thickness of the film of debonding agent. The maximum opening force was the highest for the stainless steel (SN) dowel and it also had the largest diameter dowel. The SN dowel also had just as smooth, if not a smoother surface, as compared to the other dowels. The effects of the texture can be isolated from the diameter but dividing the force by the bonded surface area and comparing the maximum shear stress. This shows the texture of the SN bar to be similar to that of the green epoxy coated dowels (C2G and G1G). It should be noted that the roughest surface was that for the purple epoxy coated dowels (C2P and G1P) yet the maximum shear stress to open the joint was comparable to the green epoxy coated dowels (C2G and G1G). In fact, the maximum shear stress for opening the joint with the C2P dowels appears to be less even less than that for the green epoxy coated dowels.

The high variability between specimens makes it difficult to define a statistical difference between the maximum force and shear stresses between the different dowel types. This high variability can most likely be attributed to differences in the coverage of the debonding agent on the dowel prior to casting. As previously described, the dowel was coated with motor oil prior to being placed in the form. Additional motor oil was applied to account for oil removed while placing the dowel in the well-fit form. It is possible that the reapplication of oil resulted in slight variations in the amount of debonding agent between dowel bars. The primary conclusion made is that all dowels will included in this study will accommodate joint opening and closing if the dowels are adequately lubricated.

Spalling occurred during the simulated joint opening 24-hrs after casting for the majority of specimens. Unlike in the AASHTO M254 [62] test procedure, holidays were created in these dowels prior to casting. This spalling was localized in the area of the concrete adjacent to the side of the dowel with the 2% holiday. During the specimen fabrication, fluid concrete likely filled in the holiday which caused a discontinuity in the otherwise smooth dowel-concrete interface. As shown in Figure 27, the holiday was pushed to the surface of the face of the concrete beam during the initial joint opening/closing. The concrete inside the holiday prevents the dowel from freely moving and causes a stress concentration within the concrete adjacent to the holiday. As a result, the concrete surface adjacent to the holiday spalls when the dowel is pushed 0.5 in out beyond the beam face. The presence of holidays in a dowel close to the joint therefore has the potential to cause spalling at the joint face as the joint opens and closes in the field. Spalling around the dowel may be detrimental to long-term dowel performance for two reasons. First, spalling can introduce looseness around the dowel that may decrease the dowel-concrete stiffness and/or effectively increases the crack width at the dowel both of which result in a reduction in the ability to transfer load. Second, spalling enables further ingression of chlorides along the length of the dowel, which may result in corrosion developing further into the dowel. The spalling was monitored throughout the corrosion test, which is discussed in a subsequent next section.

Joint Opening/Closing After Salt Exposure

Simulated joint opening/closing was performed intermittently throughout Weeks 2 – 36 of exposure to the salt solution to characterize the effect of corrosion development on increases in force required to open or close the joint. This represents joint opening/closing forces required throughout the life of the pavement. The joint opening forces measured at 24-hrs and Week 0 cannot be compared to the joint opening forces measured in Weeks 2-36 because different sections of the dowel are in contact with the surrounding concrete. The location of the holiday relative to the beam face for each testing period is shown in Figure 28. Therefore, the change in joint opening force was evaluated from Week 2 to Week 36 and was not compared to the initial joint opening force from 24-hr and at Week 0 testing.

As previously stated, during the period from Weeks 2 to 16 of exposure, the testing procedure involved joint opening followed by closing. However, for the tests conducted between Weeks 18 and 36, the sequence was reversed, with joint closing performed before opening. Additionally, the joint opening/closing total displacement was changed, which is presented in Figure 28. The average maximum force required to mobilize each dowel type during 36 weeks of testing is presented in Table 15 and Figure 36. A complete set of data for all specimens can be found in Appendix B. The solid bars in the graph represent the maximum force to open the joint while the diagonally hatched bars in the graph and the grey-shaded cells in the table both represent the maximum force to close the joint. The standard deviation between replicates is also indicated using whisker on the bar graph. To eliminate the effect of diameter and further evaluate the effect of only the dowel surface material in contact with the concrete, the average maximum shear stress between the dowel and the surrounding concrete is calculated by dividing the load by the surface area. The results are presented in Table 16 and depicted in Figure 37. Before reviewing the results, it should also be reiterated that it was determined that the solution dropped below the face of the beam shortly after Week 12 testing. While testing was conducted in Week 14, the samples are estimated to have been exposed to solution for 12 Weeks for the samples in batch 1 and 11 Weeks for the samples in batch 2. Following the 14th Week, an adjustment was made, and the actual exposure time to corrosion was determined. Although the dowels were not fully submerged in the solution, corrosion continued to progress at a slower rate, which will be discussed in more detail in Section 4.3.2.3.

Table 15. Simulated joint opening and closing mobilization force.

		Maximum mobilization force (lb)											
	Test Time	Week 2	Week 4	Week 6	Week 8	Week 12	Week 14	Week 16	Week 18	Week 22	Week 24	Week 30	Week 36
	Exposure Duration (Weeks)	2	4	6	8	12	12	12	12	14	16	22	28
C2G	Average	6080	5151	4513	6964	5032	4852	4377	1923	1656	1715	2037	2304
	St. Dev.	-	-	-	-	-	-	-	-	-	-	-	-
C2P	Average	742	747	704	628	665	616	628	268	261	232	250	280
	St. Dev.	108	166	234	126	197	172	170	62	78	67	42	51
C4Z	Average	565	1090	1545	1748	2848	3294	3871	4413	4698	4791	5332	5845
	St. Dev.	295	481	580	796	806	1088	1404	1267	508	660	1073	1166
FN	Average	534	367	819	542	926	971	886	1188	985	1128	1265	2173
	St. Dev.	389	310	819	417	691	809	702	1251	721	818	758	1536
G1G	Average	3499	3020	3175	2883	2835	2624	2509	1621	1191	1159	1910	1104
	St. Dev.	1056	1363	832	523	585	476	504	1395	707	741	2266	839
G1P	Average	4876	4399	4021	4445	3781	3470	3189	1364	965	1067	1017	908
	St. Dev.	1272	1042	791	1171	946	593	662	303	75	275	301	206
SN	Average	9463	8392	6622	6754	6951	5289	4626	552	717	655	1096	1250
	St. Dev.	-	-	-	-	-	-	-	-	-	-	-	-

*Specimens C2G3 and SN1 are considered outliers and are thus omitted from the characterization statistics.
Shaded cells represent joint closing, and all others represent joint opening.

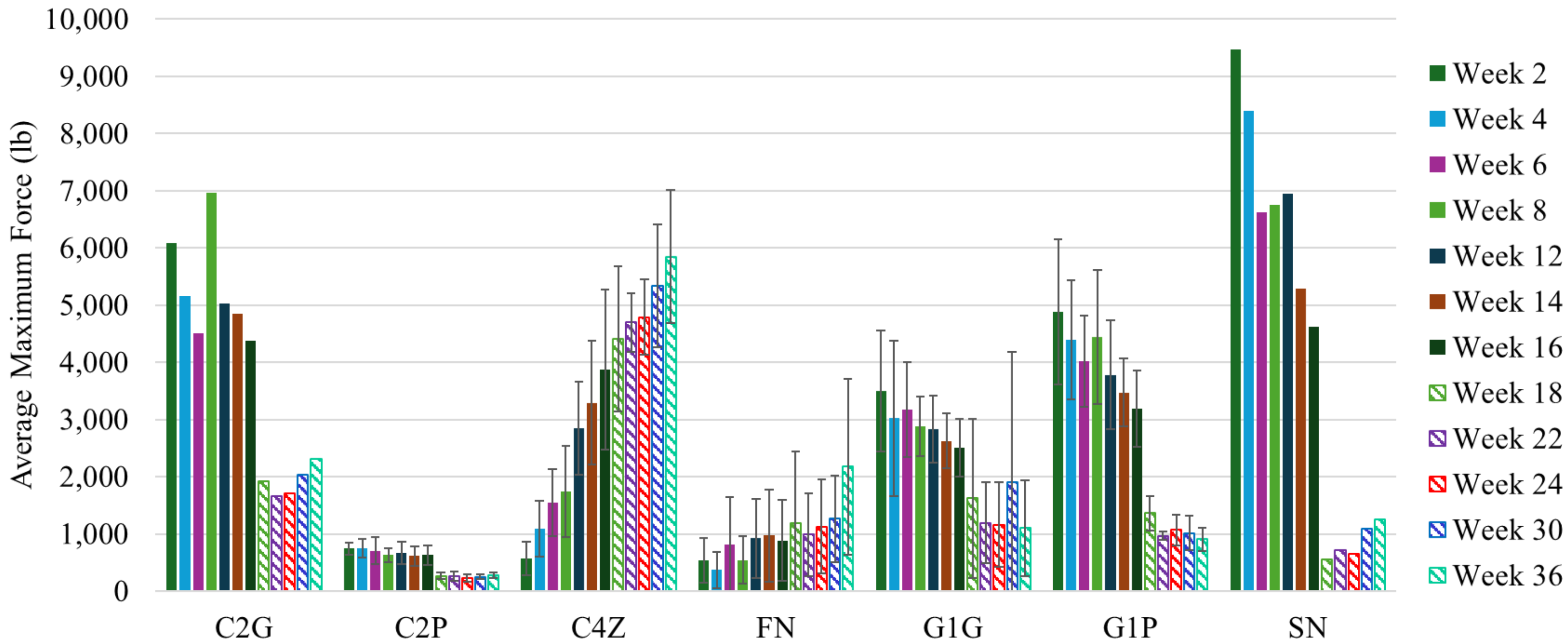

*Diagonal hash marks indicate weeks during which the same portion of the dowel was in contact with the surrounding concrete during loading.

Figure 36. Average maximum mobilization force during each week of testing.

Table 16. Summary of maximum shear stress during joint opening and closing.

		Maximum shear stress (psi)											
	Test Week	Week 2	Week 4	Week 6	Week 8	Week 12	Week 14	Week 16	Week 18	Week 22	Week 24	Week 30	Week 36
	Exposure Duration (Weeks)	2	4	6	8	12	12	12	12	14	16	22	28
C2G	Average	172.0	145.7	127.7	197.0	142.4	137.3	123.8	54.4	46.9	48.5	57.6	65.2
	St. Dev.	-	-	-	-	-	-	-	-	-	-	-	-
C2P	Average	21.0	21.1	19.9	17.8	18.8	17.4	17.8	7.6	7.4	6.6	7.1	7.9
	St. Dev.	3.1	4.7	6.6	3.6	5.6	4.9	4.8	1.8	2.2	1.9	1.2	1.4
C4Z	Average	11.7	22.7	32.1	36.4	59.2	68.5	80.5	91.8	97.7	99.7	110.9	121.6
	St. Dev.	6.1	10.0	12.1	16.6	16.8	22.6	29.2	26.4	10.6	13.7	22.3	24.3
FN	Average	15.1	10.4	23.2	15.3	26.2	27.5	25.1	33.6	27.9	31.9	35.8	61.5
	St. Dev.	11.0	8.8	23.2	11.8	19.5	22.9	19.9	35.4	20.4	23.2	21.5	43.5
G1G	Average	92.4	79.7	83.8	76.1	74.8	69.3	66.2	42.8	31.4	30.6	50.4	29.2
	St. Dev.	27.9	36.0	22.0	13.8	15.4	12.6	13.3	36.8	18.7	19.5	59.8	22.1
G1P	Average	128.7	116.1	106.1	117.3	99.8	91.6	84.2	36.0	25.5	28.1	26.8	24.0
	St. Dev.	33.6	27.5	20.9	30.9	25.0	15.6	17.5	8.0	2.0	7.3	7.9	5.4
SN	Average	176.1	156.2	123.3	125.7	129.4	98.5	86.1	10.3	13.3	12.2	20.4	23.3
	St. Dev.	-	-	-	-	-	-	-	-	-	-	-	-

*Specimens C2G3 and SN1 are considered outliers and are thus omitted from the characterization statistics.
Shaded cells represent joint closing, and all others represent joint opening

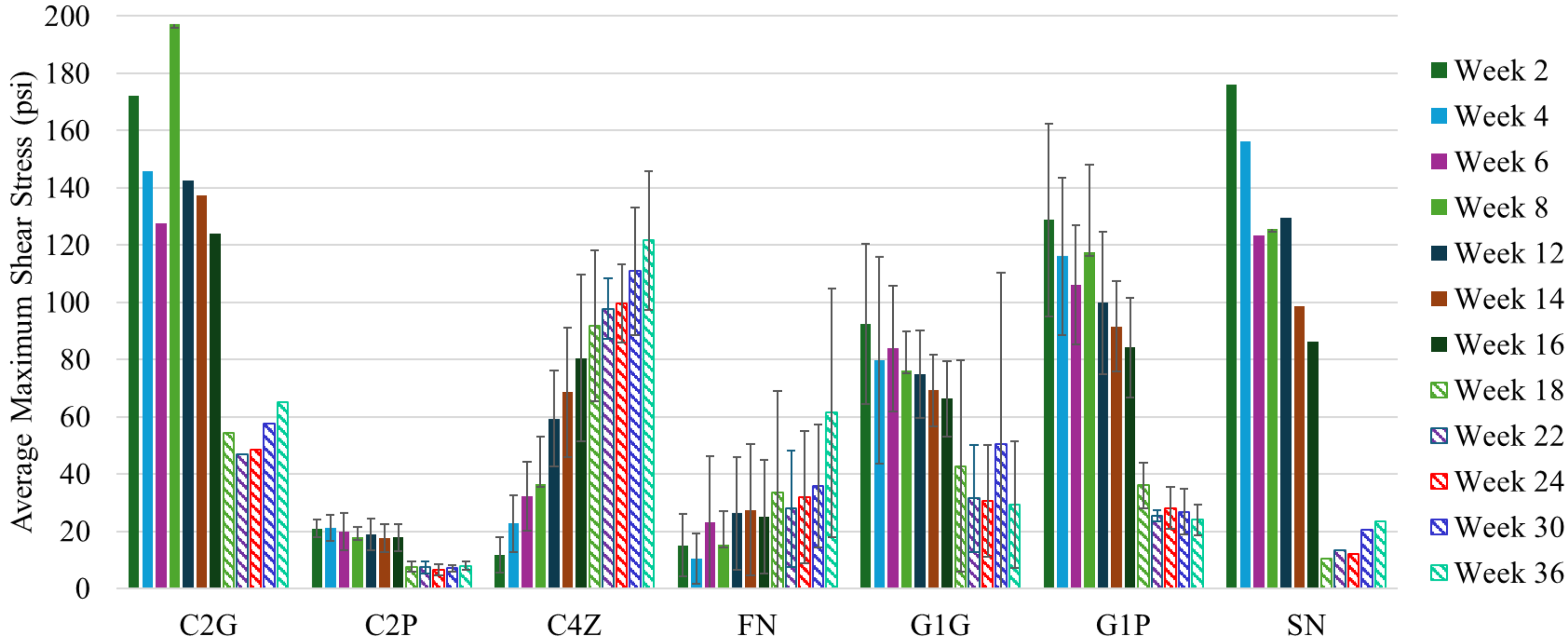

*Diagonal hash marks indicate weeks during which the same portion of the dowel was in contact with the surrounding concrete during loading.

Figure 37. Average maximum mobilization shear stress for each week of testing.

It can be seen that the maximum force to open the joint (Weeks 2-16) was typically greater than that to close the joint (Weeks 18-36) for most dowels. The most significant reductions in maximum force were seen for the stainless steel (SN) dowels and the green epoxy coated steel (C2G) dowels. The magnitude of the increase in the difference between the maximum force for opening to that of closing the joint appears to correspond to increases in the amount of spalling that developed during the 24-hour testing, as will be discussed further below.

It can also be observed that for the galvanized dowels (G1G and G1P) and the stainless steel dowels (SN), the average maximum joint opening/closing force decreased with time. This can be explained by the fact that repeatedly simulating joint movement enabled easier mobilization of the dowel, despite any effects of localized corrosion. The opposite trend was observed for the zinc-clad tubular dowels (C4Z). After 2 weeks of salt exposure the average maximum joint opening force during testing was 565 lbs, which is far below the allowable 3,000 lbs based on AASHTO M54 [64] specifications. The joint opening/closing force continuously increased with time in the corrosion tank. The average force increased from 565 lbs in Week 2 to 5,845 lbs in Week 36. This is a 934% increase. The increase in maximum joint opening/closing force is due to the zinc oxide that formed on the entire length of the dowel due the abundance of readily available zinc in the cladding wrapping around the steel tube. An example of the condition of a zinc clad dowel C4Z1) in Week 36 is shown in

Figure 38. While the initial maximum force/shear stress was initially one of the lowest for all dowel types, it has risen to the largest. It exceeded 3,000 lbs in Week 14. It should be noted that this deleterious effect was not observed in the galvanized dowels for reasons presented under Section 4.3.2.3. An increase in the maximum force required to open/close the joint was also observed in the FRP (FN) dowels. Although, the magnitude of the increase in force is far less with the total force still less than most other dowel designs. It is presumed this increase could be related to swelling of the FRP, as has been reported in previous research for FRP dowels.

Figure 38. C4Z3 in Week 36.

Another observation made was that there is significant variability in the results of the green epoxy coated steel dowels (C2G). This might be the result of the coating being peeled away from the holiday at various times throughout the 36 weeks of data collection. Two factors contributed to this. The softer green epoxy coating is more pliable than the harder purple epoxy and the epoxy coating thickness of the C2G dowels was twice that of the G2G dowels. The thick coating of pliable epoxy might tend to coil or “bunch up” instead of slipping smoothly along the surrounding concrete.

Spalling was monitored throughout the duration of the corrosion testing. As previously discussed, the initial joint opening/closing caused spalling to develop adjacent to the holidays for the majority of dowel types. The spalling was evaluated from Weeks 2 – 12 to determine if corrosion development on the holidays caused additional spalling. It was hypothesized spalling that developed after the first 24-hr test was the result of high shear stresses, which form between the dowel and the surrounding concrete during the simulation joint movement testing. The shear stress may be due to either an increase in friction between the dowel and the surrounding concrete or interlocking of grout in the holiday that causes a stress concentration. To evaluate this, the spalling was measured and compared to the simulated joint movement results. The depth of spalling was measured directly adjacent to the dowel at four locations for each specimen using a set of calipers. Each location corresponds to the location of abrasion testing, impact testing, or holidays placed on the dowel, as shown in Figure 13. The spalling depths measured at each location are shown in Table 17.

The lowest average spall depth was observed around dowels with the lowest shear stress measured during the simulated joint movement testing. Average spall depths are 0.025 in and 0.021 in for purple epoxy coated solid (C2P) and FRP (FN) dowels, respectively. These dowels exhibited the lowest average shear stress, as shown in Figure 37. The average spall depth was higher for dowels that exhibited greater average shear stress during the simulated joint movement testing. The average spall depth is 0.0836 in, 0.0766, 0.0642 in, and 0.0758 in for green epoxy coated carbon steel (C2G), green epoxy coated galvanized tubular (G1G), purple epoxy coated galvanized tubular (G1P), and stainless steel tubular dowels (SN), respectively. As shown in Figure 37, these dowels exhibited greater shear stresses compared to the purple epoxy coated carbon steel (C2P) and FRP (FN) dowels.

Critically, the spalls measured around these dowels are located adjacent to the holidays and did not progress throughout corrosion testing. This indicates the spalling is likely caused by stress concentrations which occur due to grout interlocking in the holiday. The larger holidays allowed for a greater amount of interlocking, which caused a larger buildup of stress when the joint is opened. However, the spalling on the zinc-clad (C4Z) dowel specimens developed around the entire perimeter of the dowels and progressed throughout the corrosion testing. An example of the spalling that developed Week 18 on the face of C4Z2 (zinc-clad tubular dowel) and C4Z3 at Week 36 is shown in Figure 39.

Figure 39. Spalling observed on C4Z2 (zinc-clad tubular dowel) in Week 18 and Week 36.

As previously discussed, this volume of oxidation has the potential to increase the force required to open and close the joint. The increase in shear stress observed throughout the corrosion testing indicates that there could be the potential for seizing to occur in the zinc-clad specimens tested. The measured spall depths indicate that expansion of the zinc cladding during corrosion may also cause spalling when the dowel is mobilized. It should be noted that this was not observed in the galvanized tubular dowels. As observed in this testing, the oxidation of the sacrificial zinc on the zinc-clad dowels not only causes increased shear stress during joint movement but also a greater potential for spalling around the dowel at the face of the joint.

Table 17. Average measured depth of spalling (in).

		Spall depth adjacent to the dowel (in)				
		Abrasion	Impact	2% holiday	1% holiday	Average spall depth (in)
C2G	Average	0.0257	0.0528	0.1465	0.1093	0.0836
	St. Dev.	0.0363	0.0747	0.0220	0.0276	0.0211
C2P	Average	0.0000	0.0673	0.0318	0.0000	0.0248
	St. Dev.	0.0000	0.0952	0.0450	0.0000	0.0351
C4Z	Average	0.4087	0.2323	0.3350	0.3060	0.3205
	St. Dev.	0.0798	0.0825	0.0672	0.1549	0.0511
FN	Average	0.0000	0.0307	0.0513	0.0000	0.0205
	St. Dev.	0.0000	0.0434	0.0381	0.0000	0.0159
G1G	Average	0.0210	0.0277	0.1562	0.1017	0.0766
	St. Dev.	0.0297	0.0391	0.0506	0.0813	0.0426
G1P	Average	0.0312	0.1068	0.1187	0.0000	0.0642
	St. Dev.	0.0441	0.0259	0.0923	0.0000	0.0327
SN	Average	0.1100	0.0600	0.0000	0.1530	0.0758
	St. Dev.	0.1556	0.0000	0.0000	0.0156	0.0280

Conclusions: All dowels, except for the zinc clad dowels (ZN) and to a lesser extent the FRP dowels (FN), did not exhibit a constant increase in joint opening/closing force.

4.3.2.2 Simulated Vehicle Load

The simulated vehicle load data from Weeks 0 to Week 6 was evaluated to determine if the development of corrosion on the dowel corresponded to a measured loss of dowel performance. The average maximum dowel deflection measured 7 in away from the joint face for each type of dowel is presented in Table 18 and Figure 40, with the standard deviations noted with error bars. The results were evaluated to determine if corrosion development results in an increase in deflection throughout the duration of the accelerated corrosion program. As seen in Figure 40, the change in maximum dowel deflection varied throughout testing. The deflection was observed to be greatest at Week 0 compared to subsequent weeks. This is likely due to the concrete having a lower initial strength and stiffness, which allows greater deflection under loading. The deflections decreased in Weeks 2 – 6 as the concrete strength increased.

No discernable trend was observed within each dowel type, indicating that the measured deflection is not indicative of corrosion development for the level of corrosion that developed. The deflections did vary as a function of dowel type. The deflections of the green and purple epoxy coated steel dowels (C2G and C2P), the galvanized tubular green and purple epoxy coated dowels (G1G and G1P), and the zinc clad dowels (C4Z) were observed to have comparable maximum deflections. These dowels have a comparable dowel stiffnesses, as shown in Table 18, therefore the similar performance under loading is expected. On average the FRP dowels (FN) exhibited 95% higher deflections than the green and purple epoxy coated steel dowels (C2G and C2P), the galvanized tubular green and purple epoxy coated dowels (G1G and G1P), and the zinc clad dowels (C4Z). This is explained by the lower stiffness of the FRP dowels, which results in a greater deflection under loading. Lastly, the tubular stainless steel dowel (SN) exhibited the lowest deflections under loading. On average, the deflection of the stainless steel dowels (SN) were 50% lower than the deflection of the green and purple epoxy coated steel dowels (C2G and C2P), the galvanized tubular green and purple epoxy coated dowels (G1G and G1P), and the zinc clad dowels (C4Z). A series of paired t-tests were performed to evaluate if the differences in average Week 6 dowel deflection are statistically significant at a 95% confidence level. The results shown in Table 18 indicate two main trends. First, the differences between the average deflection of the FRP dowels (FN) and all other dowels were found to be significant. Second, the differences between the average deflection of the stainless steel dowels (SN) and all other dowels except the green epoxy-coated stainless steel dowels (C2G) were found to be significant. Significant differences in deflection were only observed between dowels with significant differences in dowel stiffness. These results do not indicate that the progression of corrosion affected the average dowel deflection.

Table 18. Summarized maximum dowel deflection for a simulated wheel load.

			Max Deflection (in)			
	Stiffness (in·lb)	**Metric**	**Week 0**	**Week 2**	**Week 4**	**Week 6**
C2G	3.2×10^6	Average	47.7	34.7	36.5	33.0
		St. Dev.	9.4	8.1	8.5	7.0

C2P	3.2×10^6	Average	58.8	38.0	33.1	34.9
		St. Dev.	9.6	6.5	1.4	5.6
C4Z	3.8×10^6	Average	51.7	46.9	38.3	39.2
		St. Dev.	21.8	2.9	3.4	6.2
FN*	7.5×10^5	Average	93.4	96.7	73.2	72.1
		St. Dev.	11.3	18.1	-	3.2
G1G	3.2×10^6	Average	55.2	44.4	36.3	45.2
		St. Dev.	6.0	11.1	0.6	11.0
G1P	3.2×10^6	Average	65.1	40.3	43.5	36.3
		St. Dev.	15.5	1.0	16.3	2.8
SN	4.9×10^6	Average	16.9	23.4	22.3	22.5
		St. Dev.	17.9	7.1	3.6	3.0

*An erroneous reading was observed for one specimen (FN2) in Week 4 and was removed from the dataset. The average value is reported based on specimens FN1 and FN3

Table 19.Summarized results from the difference in means testing from Week 6 dowel deflection testing.

	C2G	C2P	C4Z	FN	G1G	G1P	SN
C2G							
C2P	0.73						
C4Z	0.31	0.42					
FN	**< 0.01**	**< 0.01**	**< 0.01**				
G1G	0.18	0.23	0.46	**< 0.01**			
G1P	0.49	0.74	0.50	**0.02**	0.26		
SN	0.08	**0.04**	**0.01**	**< 0.01**	**0.03**	< **0.01**	

*Differences that are significant at 95% confidence level in bold.

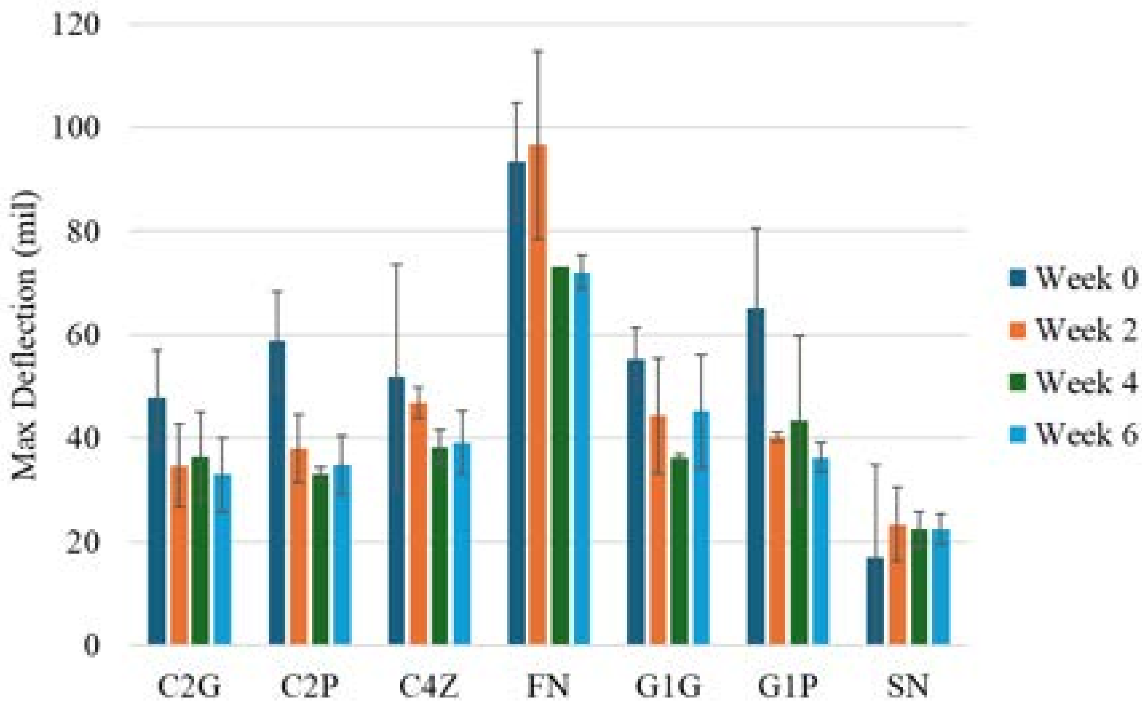

Figure 40. Average maximum dowel deflections for a simulated wheel load.

It was hypothesized that the slope of the dowel throughout testing may be a better indicator of the effect of corrosion on the response of the dowel to loading. An increase in the slope of the dowel throughout testing may indicate an increase in looseness around the dowel caused by loss of dowel diameter due to corrosion development. The slope of the dowel was calculated for each dowel by applying a linear fit to a plot of the deflection vs dowel length plot. The slope of this fit is the slope of the dowel under loading. An example of this is shown in Figure 41. Dowel slope was calculated for each specimen throughout testing, and the results are presented in Table 20 and Figure 42, with the standard deviations noted with error bars. The high initial slope observed for each dowel type is likely due to the low concrete strength at Week 0, as previously noted. It can be seen that dowel slope is consistent within each type of dowel throughout the duration of the accelerated corrosion test. The slope was comparable between the green and purple epoxy coated steel dowels (C2G and C2P), the galvanized tubular green and purple epoxy coated dowels (G1G and G1P), and the zinc clad dowels (C4Z). Similar to the maximum deflection results presented previously, these dowels have relatively comparable dowel stiffnesses, therefore the similar performance under loading is expected. On average the FRP dowels (FN) exhibited 150% higher slopes compared to the green and purple epoxy coated steel dowels (C2G and C2P), the galvanized tubular green and purple epoxy coated dowels (G1G and G1P), and the zinc clad dowels (C4Z). This is explained by the lower stiffness of the FRP dowels, which allow for greater bending, and thus slope, under loading. Lastly, the tubular stainless steel dowel (SN) exhibited the lowest slopes under loading. The average deflection of the stainless steel dowels (SN) were 44% lower than the average deflection of the green and purple epoxy coated steel dowels (C2G and C2P), the galvanized tubular green and purple epoxy coated dowels (G1G and G1P), and the zinc clad dowels (C4Z). The stainless steel dowels (SN) have an outside diameter of 1.9-in, and thus a higher stiffness compared to the 1.25-in (C2G and C2P) and 1.25-in equivalent (G1G, G1P and C4Z) dowels. A series of paired t- tests were performed to evaluate if the differences in average Week 6 dowel slopes are statistically significant at a 95% confidence level. The results shown in Table 21 reflect similar trends observed in the dowel deflection analysis. Only comparisons between dowels with large differences in dowel stiffness were observed to be significant. These results do not indicate that the progression of corrosion affected the average dowel slope.

The results indicate that the corrosion development achieved in the laboratory has not resulted in measurable loss of dowel response to vehicle loading. The corrosion was observed to be localized to the holidays and it is hypothesized that continued corrosion development would begin to measurably affect the response of the dowel to loading. For this reason, simulated vehicle loading was only performed for Weeks 0 to Week 6.

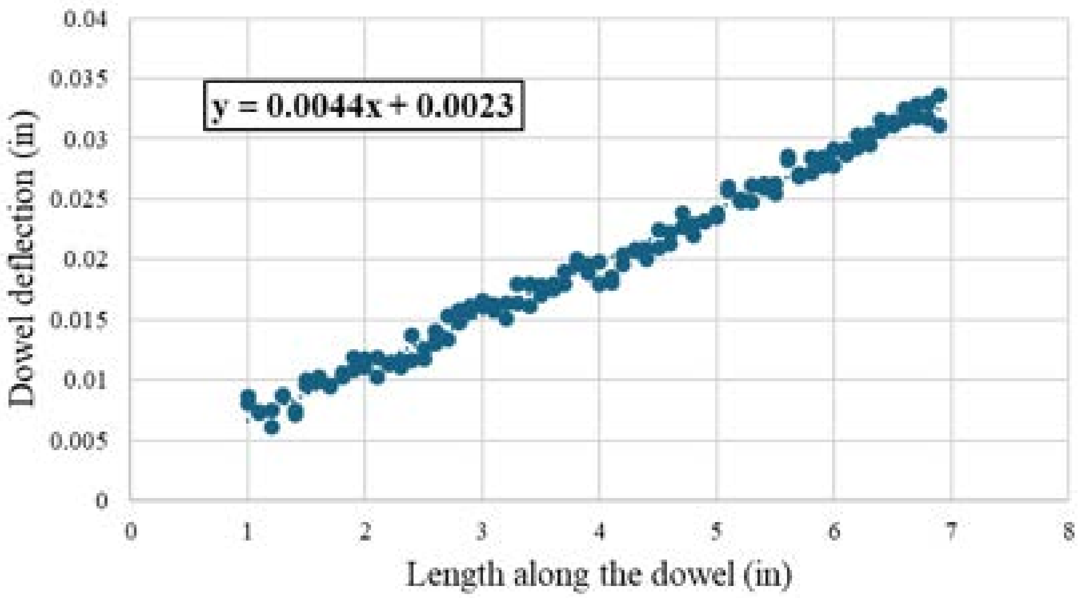

Figure 41. Example deflection plot for G1P2 after 4 weeks of exposure.

Table 20. Summarized dowel slope for a simulated wheel load.

		Dowel Slope (mil/in)			
		Week 0	Week 2	Week 4	Week 6
C2G	Average	6.2	2.6	2.5	2.5
	St. Dev.	1.8	3.1	1.1	1.6
C2P	Average	7.3	5.1	3.6	4.1
	St. Dev.	2.1	2.6	0.7	0.6
C4Z	Average	4.3	1.9	2.5	2.9
	St. Dev.	2.4	1.3	1.2	0.9
FN*	Average	12.7	13.2	6.5	10.7
	St. Dev.	3.6	2.4	5.0	0.4
G1G	Average	7.1	6.0	4.4	5.2
	St. Dev.	0.6	1.5	0.4	1.0
G1P	Average	8.2	5.7	5.3	4.3
	St. Dev.	1.4	2.2	1.6	0.4
SN	Average	3.1	2.4	2.6	2.2
	St. Dev.	0.1	0.5	1.0	0.2

*An erroneous reading was observed for one specimen (FN2) in Week 4 and was removed from the dataset. The average value is reported based on specimens FN1 and FN3

Table 21. Summarized results from the difference of means testing from Week 6 dowel slope testing.

	C2G	C2P	C4Z	FN	G1G	G1P	SN
C2G							
C2P	0.18						
C4Z	0.73	0.13					
FN	**< 0.01**	**< 0.01**	**< 0.01**				
G1G	0.07	0.18	**0.04**	**< 0.01**			
G1P	0.13	0.66	0.07	**< 0.01**	0.22		
SN	0.76	**< 0.01**	0.26	**< 0.01**	**< 0.01**	**< 0.01**	

***Differences that are significant at 95% confidence level shown in bold**

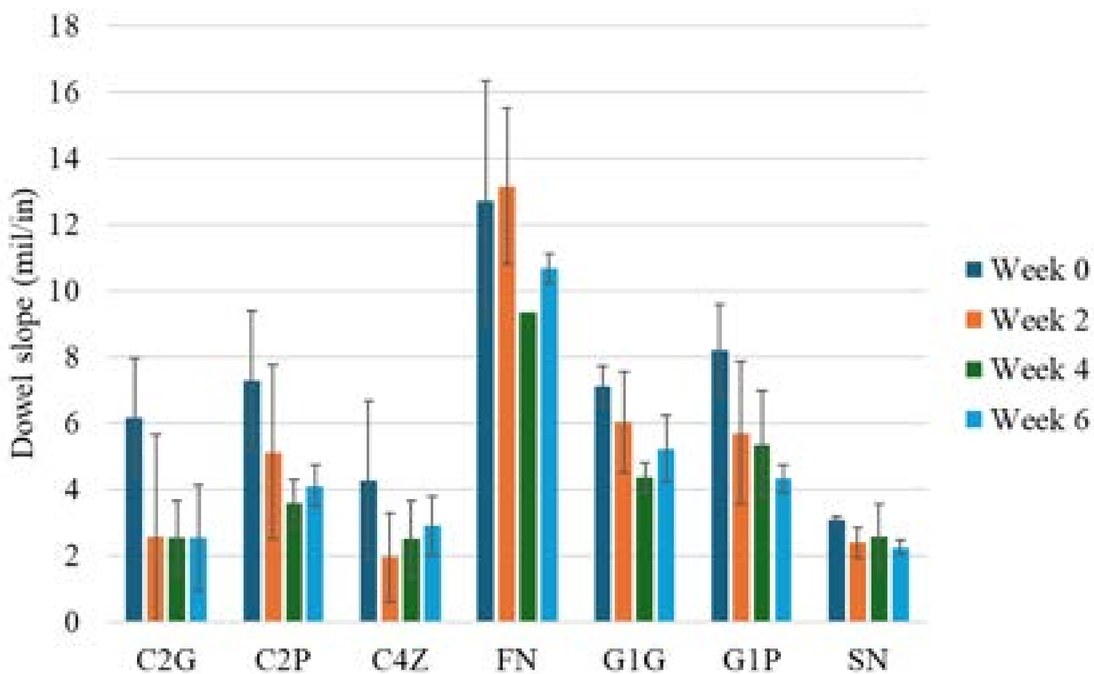

Figure 42. Average dowel slope results.

Conclusions: The results indicate that the corrosion development achieved in the laboratory after Week 6 has not resulted in a measurable loss of dowel response to vehicle loading. The primary factor affecting the deflection performance was dowel stiffness with the largest stiffness (4.9×10^6 psi) provided by the stainless steel tubular dowels having the lowest deflections and the lowest stiffness (7.5×10^5 psi) found with the FRP dowels having the highest deflections. The magnitude of deflections for all other dowel designs were similar.

4.3.2.3 Corrosion Development

The joint opening/closing and vehicle load simulations were used to assess joint performance during the progression of corrosion. This section will discuss the amount of corrosion that developed through Week 36 for each dowel design. As previously described, 3D surface scans were performed on each specimen after joint opening/closing testing. Beginning in Week 8, photos were taken of each dowel as well. The photographs and scans were used to document the progression of corrosion development in the holiday furthest from the beam face in the 2% area cluster. These photos and scans have been included in Appendix A. Initially, the 3D surface scans were used to estimate the volume change in the holiday as corrosion progressed. Due to the limited extent of the corrosion that developed through Week 36, informative volumetric comparisons could not be made. Therefore, it was decided to quantify the early age corrosion development using a 2D approach. The progressive increase in surface area that corroded was defined in each photograph using ImageJ, an image segmentation program [65]. The 2% area holiday 3 in from the face of the concrete was segmented for this analysis. The zinc clad (C4Z) dowels were not included in this analysis because the oxidation of the zinc cladding had completely covered the holidays, making it difficult to discern differences in corrosion development inside the holiday. It should again be noted that the chloride solution dropped below the holiday 3 in from the face of the concrete between test Weeks 18 and 20. Although the holiday was not fully submerged for this 2-week period, visual inspections indicate that corrosion continued to develop, just at a slower rate.

The photograph of the holiday in the 2% area cluster that is 3 in from the concrete face (at exposure Week 8) was uploaded to ImageJ for each specimen. The image is cropped to show the localized area of corrosion around the holiday, as well as the full width of the dowel bar. The width of the dowel bar is used to scale the image based on the known dowel diameter. Once the image is scaled correctly, the freehand selection tool is used to manually encompass the corroded area in and around the holiday. This method was determined to be more reliable than an automatic image segmentation method, because many of the dowels exhibited staining on the surface or oxidation of the galvanized layers, which may not be easily picked up when using an automated method. The ‘measure’ function in ImageJ is then used to approximate the area of the dowel bar that has been corroded. This process is performed for each specimen beginning in test Week 8 through Week 36.

The results of the corrosion surface area analysis are summarized in Table 22 with a complete table of all values provided in Appendix C. The corrosion area analysis results are also shown graphically in Figure 43. Each data point on the graph represents the average measured area of corrosion that developed at each test week with the error bars indicating the standard deviation. Recall, the original area of each holiday comprising the 2% area at Week 0 is 0.05 in^2 and therefore values greater than this reflect corrosion that progressed beyond the boundary of the holiday. It should be noted that the amount of measured corrosion appears to decrease slightly and increase again. This is an artifact of the manual process of selecting the corroded area in each image. For these cases, it can be assumed that the corrosion development has not progressed in those weeks. Overall, it is seen that the epoxy coated carbon steel dowels (C2G and C2P) have a greater measured area of corrosion than the epoxy coated zinc-galvanized dowels (G1G and G1P). This is expected, as the galvanized layer provided extra protection against corrosion propagation. The stainless steel (SN) and FRP (FN) dowels did not exhibit corrosion, although the simulated joint opening/closing testing indicated slight swelling might occurring in the FN dowels.

Table 22. Corrosion surface area for the holiday location furthest from the beam face (2% area holidays).

		Surface area of corrosion (in^2)									
	Test Time	Week 0	Week 8	Week 12	Week 14	Week 16	Week 18	Week 22	Week 24	Week 30	Week 36
Specimen	Exposure Duration (Weeks)	0	8	12	12	12	12	14	16	22	28
C2G	Average	0.00	0.12	0.14	0.17	0.19	0.20	0.21	0.23	0.30	0.36
	St. Dev.	0.00	0.03	0.03	0.04	0.05	0.05	0.05	0.04	0.04	0.04
C2P	Average	0.00	0.10	0.15	0.17	0.18	0.21	0.25	0.27	0.29	0.32
	St. Dev.	0.00	0.02	0.00	0.02	0.01	0.02	0.03	0.03	0.03	0.03
FN	Average	0.00	0.00	0.00	0.00	0.00	0.00	0.00	0.00	0.00	0.00
	St. Dev.	0.00	0.00	0.00	0.00	0.00	0.00	0.00	0.00	0.00	0.00
G1G	Average	0.00	0.07	0.07	0.08	0.09	0.10	0.11	0.12	0.13	0.14
	St. Dev.	0.00	0.02	0.02	0.02	0.03	0.03	0.03	0.03	0.04	0.04
G1P	Average	0.00	0.03	0.03	0.04	0.04	0.04	0.05	0.06	0.06	0.06
	St. Dev.	0.00	0.01	0.01	0.01	0.01	0.01	0.01	0.00	0.00	0.00
SN	Average	0.00	0.00	0.00	0.00	0.00	0.00	0.00	0.00	0.00	0.00
	St. Dev.	0.00	0.00	0.00	0.00	0.00	0.00	0.00	0.00	0.00	0.00

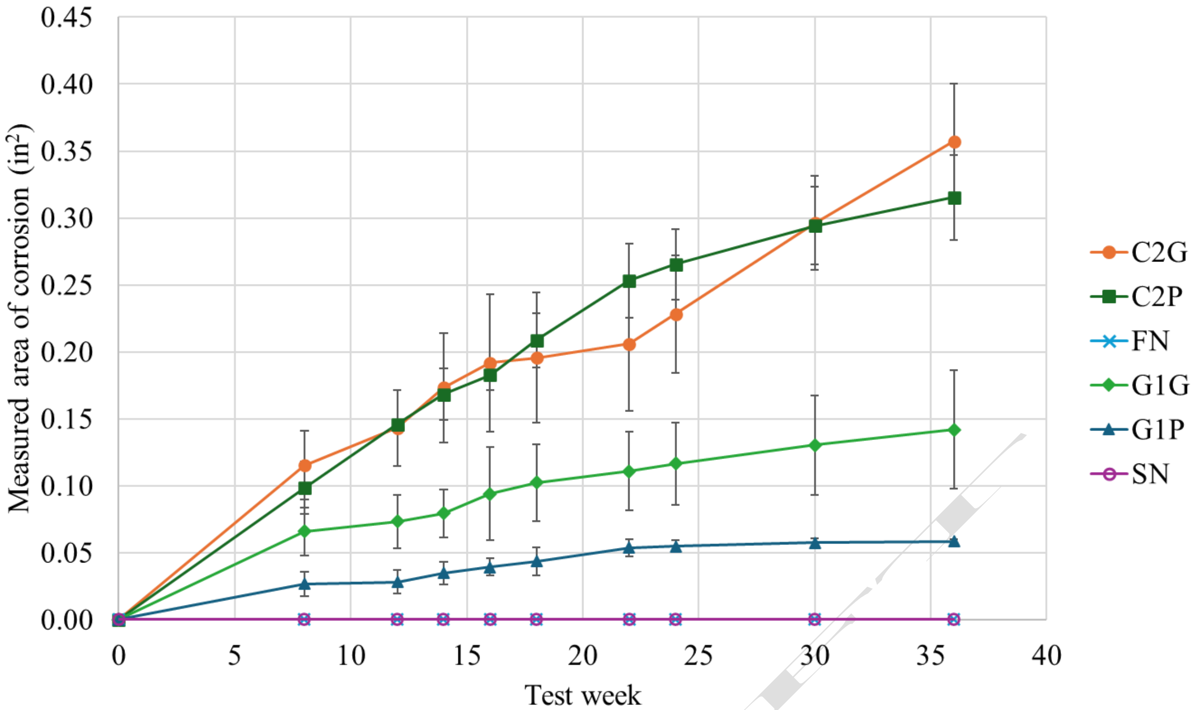

Figure 43.Corrosion surface area for the holiday location furthest from the beam face (2% area holidays).

Steel vs galvanized dowels

The corrosion development of the epoxy coated carbon steel dowels is much greater than that of the epoxy coated zinc galvanized dowels. The size of the corroded area for the C2G dowel was 2.5 greater than the G1G dowel at Week 36 and the C2P was 5.4 greater than the G1P. The corrosion of the G1P dowels was approximately 6.0 times less than that of the C2G dowels, 5.4 times less than that of the C2P dowels, and 2.4 times less than that of the G1G dowels. The carbon steel dowls exhibited an increase in corrosion development of 0.030 in^2/wk and 0.027 in^2/wk for the C2G and C2P, respectively, from Week 8 through Week 36. The epoxy coated zinc galvanized dowels exhibited an increase in corrosion development of 0.010 in^2/wk and 0.004 in^2/wk for the G1G and G1P, respectively. These rates are substantially lower than those for of carbon steel dowels.

These results reveal the benefits of the sacrificial zinc galvanized layer. The preferential corrosion of zinc for the galvanized dowel can be observed in the photos provided in Figure 44 of G1G and C2P dowels in Week 36. It should be noted that the holiday was milled through both the epoxy coating and the galvanized layer as a worst case scenario. The presence of two barriers, the epoxy and galvanized layer, also drastically reduces the probability of developing a holiday that would extend beyond the depth of both the coatings to expose the steel during fabrication or construction. Even if this were to occur, the galvanized zinc in surrounding area would need to be depleted before sacrificial corrosion would cease and corrosion of the steel would begin.

Figure 44. Preferential corrosion of zinc layer for galvanized dowel G1P1 (left) compared to carbon steel dowel C2P2 (right) at Week 36.

Purple vs green epoxy

Although the ultimate corrosion development appears slightly lower for the purple epoxy coated carbon steel dowels (C2P) compared to the green epoxy coated dowels (C2G), the variability in the results makes the difference statistically insignificant. Therefore, no statistical difference can be stated regarding the amount of corrosion development between the green and purple epoxy coated steel dowels. It was observed that the pliable green epoxy coating tended to bunch up and peel during the joint opening/closing simulation testing. This then exposes more steel along the dowel, thereby making it susceptible to additional corrosion. This can be seen in Figure 45 below.

Figure 45. Progression in peeling out epoxy coating during joint opening/closing simulations for carbon steel C2G3 dowel across Week 12 (left), 22 (middle) and 36 (right).

The purple epoxy coated zinc galvanized dowel (G1P) show a substantially slower development of corrosion for the same amount of exposure time compared to the green epoxy coated zinc galvanized dowel (G1G). The area of corrosion on the G1G dowels is 2.4 times greater than that of the G1P dowels. This is believed to be in part due to the greater stiffness of the purple epoxy coating compared to the green epoxy coating, which better prevents chloride ingress.

Zinc clad vs zinc galvanized

The zinc clad dowels oxidized to the point that joint opening/closing was impaired while the zinc galvanized dowels exhibited the least amount of corrosion and performed comparably to the carbon steel dowels in the joint opening/closing. With both dowels containing zinc yet performing in distinctly different manners, further discussion is merited.

Figure 46 shows the structure of the zinc clad and zinc galvanized dowels. For the zinc clad dowels there is a 35 mils thick sheath of 99% zinc that is wrapped around the carbon steel tube. The galvanized bars are produced from galvanized sheet steel (minimum thickness of 0.120 inches) that is formed into a welded tube. The sheet steel is hot-dip galvanized to G90 (0.90 oz galvanizing/s.f., 0.45 oz on each side), which results in a layer that is approximately 0.8 mils thick on the inside and outside of the dowel. The tube weld is re-galvanized after it is ground smooth. The galvanized layer is mostly unalloyed zinc with minimal zinc-iron alloy layers near the steel interface. Unlike with the cladding where the zinc strip is mechanically bonded to the steel substrate, galvanizing produces a stronger metallurgical bond with much harder layers near the steel surface.

Figure 46. The structure of the zinc clad and zinc galvanized dowels.

The role of the zinc in providing corrosion protection is first it creates a barrier between the steel and the environment. It also provides sacrificial protection if the underlying steel is exposed, referred to as galvanic protection. If the epoxy coating is damaged then the zinc (being anodic to iron) will preferentially oxides and sacrificially protect the steel.

There are three stages commonly used for characterizing the corrosion process for galvanized steel. First is the initiation stage. Passivation refers to the thin film of oxides that form over the surface of a steel or zinc dowel in the concrete due to the high alkalinity of the concrete. The presence of deicing chemicals will destroy this layer once a critical threshold of chloride ions is achieved, which is referred to as depassivation. The ion concentration threshold is higher (at least 2.5 times [66] and perhaps as much as 4 to 5 times [67]) for zinc than steel and therefore the passivation layer will break down more quickly for steel. After depassivation, the second stage, referred to as the protection stage, begins. At this point, the zinc coating layer begins to dissolve with the outer pure zinc dissolving more quickly than the inner zinc-iron alloy. In the case of the zinc cladded dowels, the entire zinc sheath is pure zinc. Zinc corrosion product disperses by migrating into the concrete matrix instead of collecting around the bar, as occurs when the steel corrodes. The build-up of corrosion products around the bar results in the development of swelling stresses that causes damage to the surrounding concrete. Once the zinc coating has been completely dissolved in an area and the underlying steel is exposed (or if the galvanized coating was damaged during construction), the zinc will sacrificially protect the steel [68]. The sacrificial protection provided by the galvanized coating surrounding the holiday that was milled through the epoxy and galvanized layer can be observed in the photo on the left of Figure 47. This photo was taken in Week 36. Once the barrier provided by the galvanized layer is dissolved and the zinc providing the sacrificial protection adjacent to the region of exposed steel is depleted, the steel will begin to corrode. This is referred to as the propagation stage. It can be seen that the holiday for the dowel in Figure 47 is in the early part of the propagation stage, as a rust color is just beginning to appear in the central portion of the holiday (farthest away from the boundaries of the zinc source facilitating the sacrificial protection).

Figure 47. Holiday in a galvanized purple epoxy coated and zinc clad dowels in Week 36.

The primary factor contributing to the difference between the superior performance of the zinc galvanized over that of the zinc clad dowels is the availability of pure zinc for forming zinc oxide. The zinc clad dowels consist of 35 mils of pure zinc, while the galvanized layer is only 0.8 mils with the interior portion being a zinc alloy and only the most outer layer consisting of pure zinc. These dowels were also coated with epoxy, so the galvanized zinc was retained until needed for sacrificial protection. It should be noted that both dowel designs successfully deterred the steel from corroding but the additional zinc oxide produced in the zinc clad dowels resulted in a steady increase in the force required to simulate joint opening/closing. This also caused additional spalling to develop around the dowel at the dowel-concrete interface.

Conclusions: The visual corrosion assessment revealed the epoxy coated steel dowels (both purple and green) exhibited a significantly greatest rate of corrosion than all the other dowel designs. This rate was approximately 3 times greater than that for the green epoxy coated galvanized dowels. Both the zinc clad and purple epoxy coated galvanized dowels exhibited very little to no corrosion, although the amount of zinc oxide produced in the zinc clad dowels has the potential to be problematic with respect to the joint opening/closing restraint. Both the stainless steel tubular dowels and FRP dowels also did not exhibit corrosion although there are indications that swelling could be occurring in the FRP dowels. This swelling also has the potential to restrict joint opening/closing.

4.4 Conclusions

The coating assessment and accelerated corrosion testing was performed to evaluate the effect of salt exposure to various types of dowels. The results from the

- Coating assessment testing indicated that all dowel coating types provide sufficient resistance to damage from both impact and abrasion.
- All dowels, except for the zinc clad dowels (ZN) and to a lesser extent the FRP dowels (FN), did not exhibit a constant increase in joint opening/closing force. Significant zinc oxide developed on the ZN dowels and it appears that resulted in a steady increase in force required for joint opening/closing. The FRP dowels appear to be starting to exhibit swelling with small increases in force being required for joint opening/closing. Continued monitoring will be performed to verify this trend. It should be noted that the opening/closing force for the FRP dowel is still below the 3,000 lb threshold but this force is close to 6,000 lbs for the ZN dowels
- The visual corrosion assessment revealed the epoxy coated steel dowels (both purple and green) exhibited a significantly greatest rate of corrosion than all the other dowel designs. This rate was approximately 3 times greater than that for the green epoxy coated galvanized dowels. Both the zinc clad and purple epoxy coated galvanized dowels exhibited very little to no corrosion, although the amount of

zinc oxide produced in the zinc clad dowels has the potential to be problematic with respect to the joint opening/closing restraint. Both the stainless steel tubular dowels and FRP dowels also did not exhibit corrosion although there are indications that swelling could be occurring in the FRP dowels. This swelling also has the potential to restrict joint opening/closing.

The results from this laboratory study support the literature regarding expected performance life. Based on the durability (probability of damage) of the coating (the multi-coating system in the case of the epoxy coated galvanized bars) and the corrodibility of the material, the results from this laboratory analysis is used to incorporate the susceptibility to corrosion development as a function of dowel type and exposure, in a faulting prediction model. This is described in the next section.

5.0 JOINT FAULTING MODEL DEVELOPMENT

5.1 Introduction

This section details the development of the updated JPCP faulting model. The first section presents the updated faulting framework which incorporates damage development to the concrete surrounding the dowel caused by repeated vehicle loading. The predictive dowel damage equations which were developed using the results from a study performed by Donnelly and Vandenbossche [59]. A sensitivity analysis is performed using the revised dowel damage model.

The second section of this chapter contains the updated faulting model that accounts for loss of performance due to corrosion development. First, the proposed updates to the faulting model, which incorporate the effect of corrosion are presented. Second, a recalibration of the faulting model is presented. Lastly, the model adequacy checks are presented to demonstrate the performance of the updated model.

5.2 Incorporation of Dowel Damage in Faulting Model

This section is focused on the incorporation of a novel dowel damage model into the existing faulting model framework. The current faulting model framework accounts for loss of dowel performance in the form of dowel damage through an incremental increase in the damage parameter *DOWDAM*. For each month of the iterative analysis, the increase in *DOWDAM* is calculated using Equations 4 - 5 below:

$$\Delta DOWDAM_i = C_8 \frac{F}{d{f^*}_c} \tag{4}$$

$$F = J_d(\delta_L - \delta_{UL}) * DowelSpace \tag{5}$$

Where $\Delta DOWDAM_i$ is the increase in dowel damage from an individual load application, C_8 is a calibration coefficient specific to dowelled joints, F is effective shear force (lb), d is the diameter of the dowel (in), ${f^*}_c$ is the compressive strength of the concrete (psi), J_d is the nondimensional dowel stiffness, δ_L and δ_{UL} are corner deflections of the loaded and unloaded slabs (mils), respectively, and *DowelSpace* is the dowel spacing (in). This damage model has several limitations Dowels with varying stiffnesses were considered in this study. To account for difference in material and dowel design, the concept of equivalent dowel diameter is used. The equivalent dowel diameter, d_{eq}, is calculated for a given dowel by determining the diameter of a solid steel dowel spaced at 30.5 cm (12 in), which results in the same bearing stress under an applied load. This is calculated using Equation 6 below, which is based off the work developed by Friberg [69].

$$d_{eq} = \frac{12}{DowelSpace} \sqrt[7]{\frac{d_o^3 * E_{dowel} * [(d_o)^4 - (d_i)^4]}{E_{steel}}} \tag{6}$$

Where d_{eq} is the equivalent dowel diameter (in), $DowelSpace$ is the spacing between dowels in the transverse joint (in), E_{dowel} is the elastic modulus of the dowel (psi), d_o is the outer diameter of the dowel (in), d_i is the inner diameter of the dowel (in), and E_{Steel} is the elastic modulus of steel equal to 29×10^6 psi. This dowel diameter equivalency method is supported by the load testing summarized below in Section 5.21.

To address these limitations, a novel dowel damage model was developed using the results of the laboratory experiment performed by Donnelly and Vandenbossche [59]. In this section, the development of the dowel damage model is first presented.

5.2.1 Dowel Damage Model

The results from the accelerated load testing were used to develop a dowel damage model which accounts for loss of dowel performance due to repeated vehicle loading. The damage parameter developed in the laboratory test, referred to as beam deflection energy (DE_{Beam}), is used as the damage parameter in the damage model. The training dataset consists of DE_{Beam} values obtained from the accelerated loading test for 45 specimens. A summary of the specimens and key parameters included in the dataset are shown in Table 23.

The analysis of the experimental results demonstrated that the parameters significant for $\mathrm{DE}_{\mathrm{Beam}}$ includes dowel diameter, applied load, dowel bending stiffness, and number of load cycles. The load transferred through the dowel is determined based on the load applied in the laboratory. This is calculated assuming that 10% of the load is transferred through the simulated base layer, which is consistent with the current design procedure [70]. Half of the remaining load is assumed to transfer through the dowel, which is equal to 45% of the applied load.

Stiffness is accounted for using the dowel constant, β, developed by Friberg [69], which is calculated using Equations 7 - 8 below:

$$\beta = \sqrt[4]{\frac{\mathrm{K} * deq}{4 * E_{dowel} * I}} \tag{7}$$

$$\mathrm{K} = \frac{E_{PCC}}{h_{PCC}} \tag{8}$$

Where β is the relative stiffness of the dowel embedded in the concrete (in^{-1}), K is the modulus of dowel reaction (psi/in), d_{eq} is the equivalent diameter of the dowel (in), E is the modulus of elasticity of the dowel (psi), I is the moment of inertia of the dowel (in^4), E_{PCC} is the elastic modulus of the dowel (psi), and h_{PCC} is the slab thickness. The concrete elastic modulus for each specimen was measured prior to testing. For each specimen, $\mathrm{DE_{Beam}}$ is calculated at 49 discrete times throughout the loading test, which results in 2,205 total data points. The intervals at which $\mathrm{DE_{Beam}}$ is calculated is presented in Table 24.

Table 23. Specimens considered in the damage model prediction.

Specimen ID	**Outer Diameter (in)**	**Load Transferred through Dowel (lb)**	$\boldsymbol{\beta}$ **(in^{-})**
1EC 6 ML a	1.000	1350	2.99E+11
1EC 6 ML b	1.000	1350	2.77E+11
1EC 6 ML c	1.000	1350	3.05E+11
1EC 6 ML d	1.000	1350	3.19E+11
1EC 8 ML a	1.000	1350	2.63E+11
1EC 8 ML b	1.000	1350	2.37E+11
1EC 8 ML c	1.000	1350	2.52E+11
1EC 8 ML d	1.000	1350	1.81E+11
1.25EC 6 ML a	1.250	1350	1.10E+12
1.25EC 6 ML b	1.250	1350	1.01E+12
1.25EC 8 LL a	1.250	900	7.90E+11
1.25EC 8 ML a	1.250	1350	7.03E+11
1.25EC 8 ML c	1.250	1350	7.03E+11
1.25EC 8 ML d	1.250	1350	7.26E+11
1.25EC 8 ML e	1.250	1350	6.66E+11
1.25EC 8 ML f	1.250	1350	6.58E+11
1.25EC 8 ML g	1.250	1350	7.75E+11
1.25EC 8 ML h	1.250	1350	7.95E+11
1.25EC 8 HL a	1.250	1800	7.36E+11
1.25EC 8 HL b	1.250	1800	7.72E+11
1.25EC 8 HL c	1.250	1800	8.29E+11
1.25FRP 8 ML a	1.250	1350	1.79E+11
1.25FRP 8 ML b	1.250	1350	1.94E+11
1.38OD 8 ML a	1.375	1350	9.41E+11
1.38OD 8 ML b	1.375	1350	9.25E+11
1.25EC 10 ML a	1.250	1350	6.10E+11
1.25EC 10 ML b	1.250	1350	6.00E+11
1.25EC 10 ML c	1.250	1350	5.94E+11
1.25EC 10 ML d	1.250	1350	6.03E+11
1.25EC 10 ML e	1.250	1350	6.14E+11
1.25EC 10 HL a	1.250	1800	6.28E+11
1.25EC 10 HL b	1.250	1800	6.30E+11
1.25EC 10 HL c	1.250	1800	6.14E+11
1.25EC 10 HL d	1.250	1800	5.79E+11
1.25EC 10 HL e	1.250	1800	6.65E+11
1.5EC 10 ML a	1.500	1350	1.46E+12
1.5EC 10 ML b	1.500	1350	1.43E+12
1.5EC 10 ML c	1.500	1350	1.26E+12
1.5EC 10 HL a	1.500	1800	1.34E+12
1.5EC 10 HL b	1.500	1800	1.36E+12
1.5EC 10 HL c	1.500	1800	1.38E+12
1.5EC 10 HL d	1.500	1800	1.17E+12
1.63OD 10 ML a	1.625	1350	1.26E+12
1.63OD 10 ML b	1.625	1350	1.20E+12
1.63OD 10 ML c	1.625	1350	1.35E+12

Table 24. Intervals at which DE_{Beam} was calculated for each beam.

Number of Applied Loads	**Frequency of DE_{Beam}**
0 - 20,000	Every 1,000 applications
20,000 - 50,000	Every 5,000 applications
50,000 - 100,000	Every 10,000 applications
100,000 - 500,000	Every 50,000 applications
500,000 - 1,000,000	Every 100,000 applications
1,000,000 - 1,250,000	Every 250,000 applications

A database of the calculated DE_{beam} for each specimen was constructed. Multiple linear regression (MLR) was used to train a DE_{Beam} prediction model shown in Equation 9.

$$DE_{Beam} = \alpha_1 * \log(x+1) + \alpha_2 * \log(x+1) * \frac{\log(Load)}{\beta} + \alpha_3 * \frac{\log(x+1)}{\beta} \qquad (9)$$

Where DE_{Beam} is the beam deflection basin, x is the number of applied loads, *Load* is the magnitude of the load transferred through the dowel (lb), β is the relative stiffness of the dowel (in^{-1}), and α_1, α_2, and α_3 are coefficients presented in Table 25. The adjusted R^2 is equal to 0.82, and the RMSE is equal to 192. The measured vs predicted DE_{beam} is shown in Figure 48.

Table 25. DE_{beam}model coefficients.

Coefficient	**Value**
α_1	592.8
α_2	353.3
α_3	-1256.5

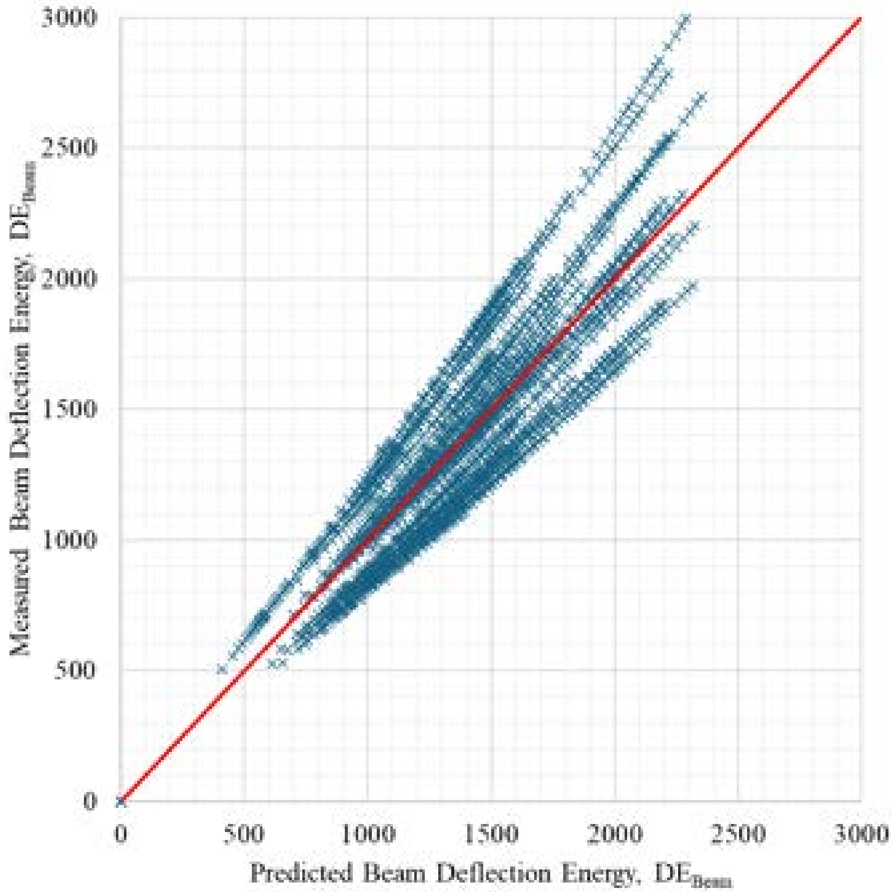

Figure 48. Measured vs predicted DE_{Beam} values.

To ensure that the model did not exhibit bias towards specific load magnitudes or dowel designs, Equation 9 was used to calculate DE_{Beam} across replicates for a given case. The average E_{PCC} measured for each replicate used to determine the average DE_{Beam}. The predicted and measured DE_{Beam} for are presented in Figure 49 - Figure 61 for each case. The predicted DE_{Beam} is comparable to the measured value and do without consistently over or under predicting for any specific parameter. For cases with high variability between replicates, such as those tested with high loads, the model sufficiently predicts within the middle of the range of $DE_{Beam.}$ This demonstrates that the model adequately predicts DE_{Beam} for all cases without exhibiting bias towards specific parameters.

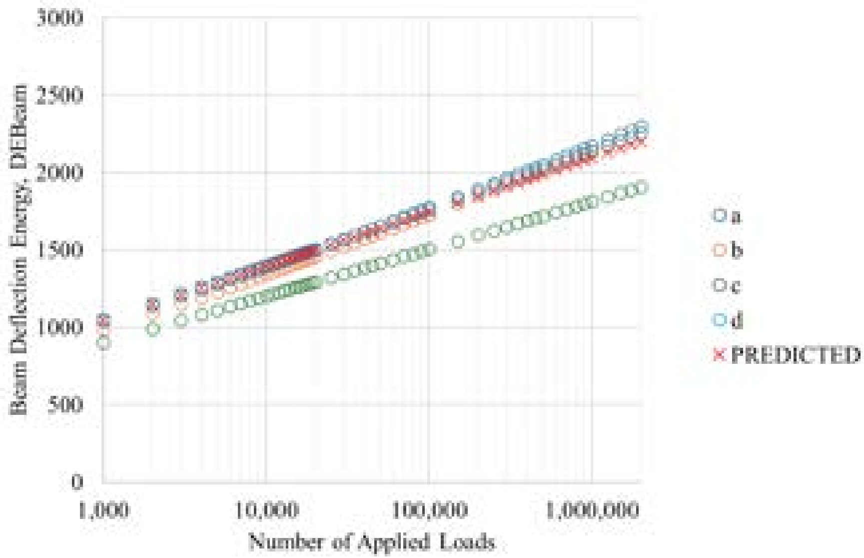

Figure 49. Predicted and actual DE_{Beam} for 1-in EC dowels in 6-in beams with med. load magnitude.

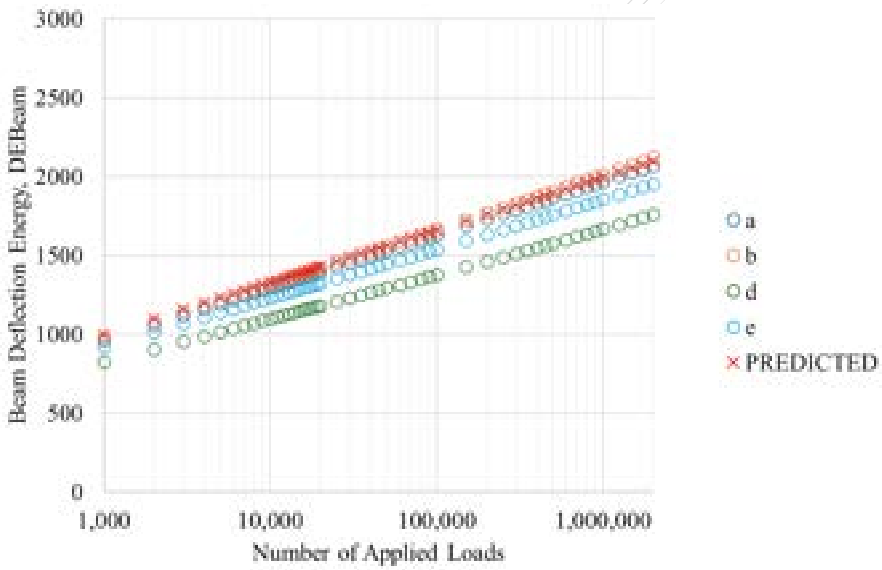

Figure 50. Predicted and actual DE_{Beam} for 1-in EC dowels in 8-in beams with med. load magnitude.

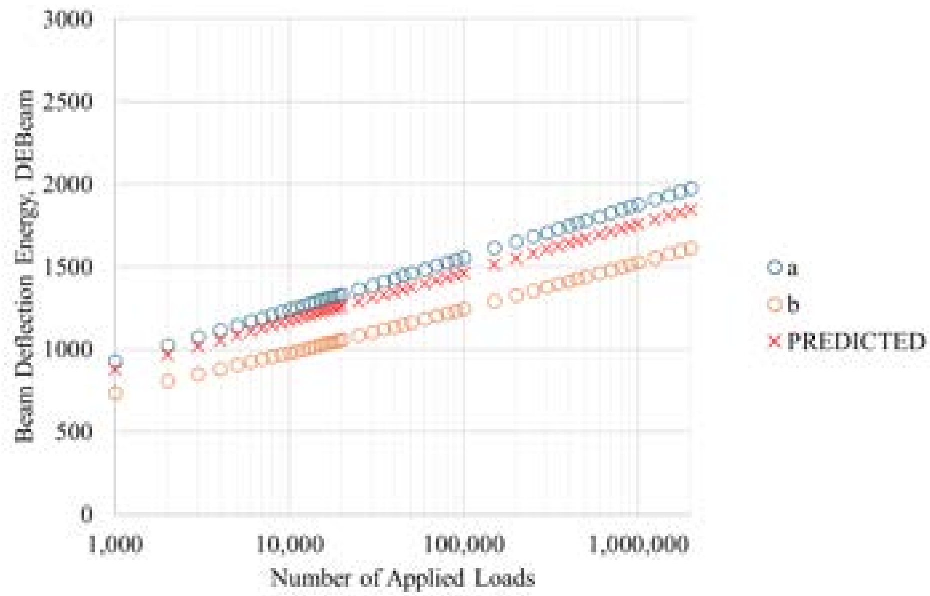

Figure 51. Predicted and actual DE_{Beam} for 1.25-in EC dowels in 6-in beams with med. load magnitude.

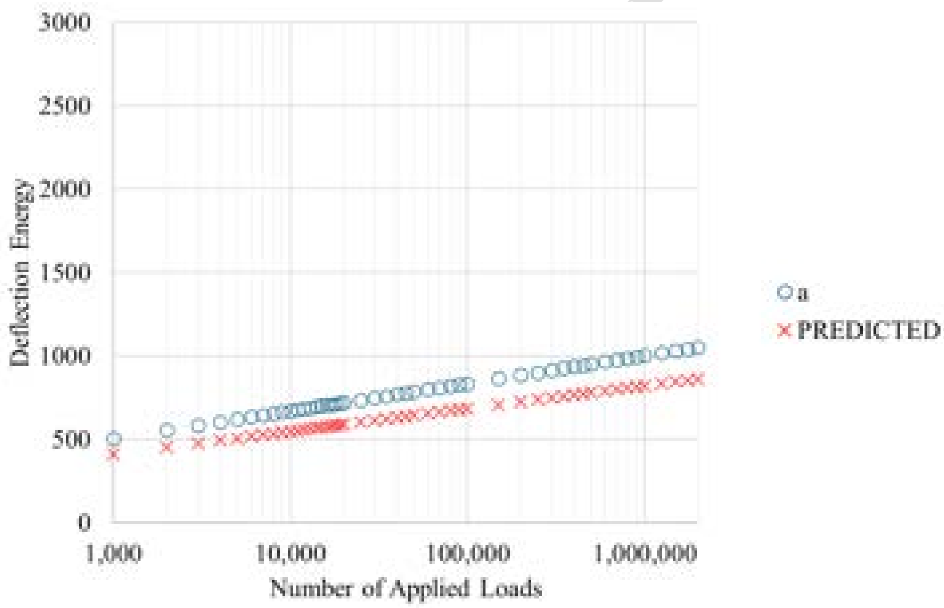

Figure 52. Predicted and actual DE_{Beam} for 1.25-in EC dowels in 8-in beams with low load magnitude.

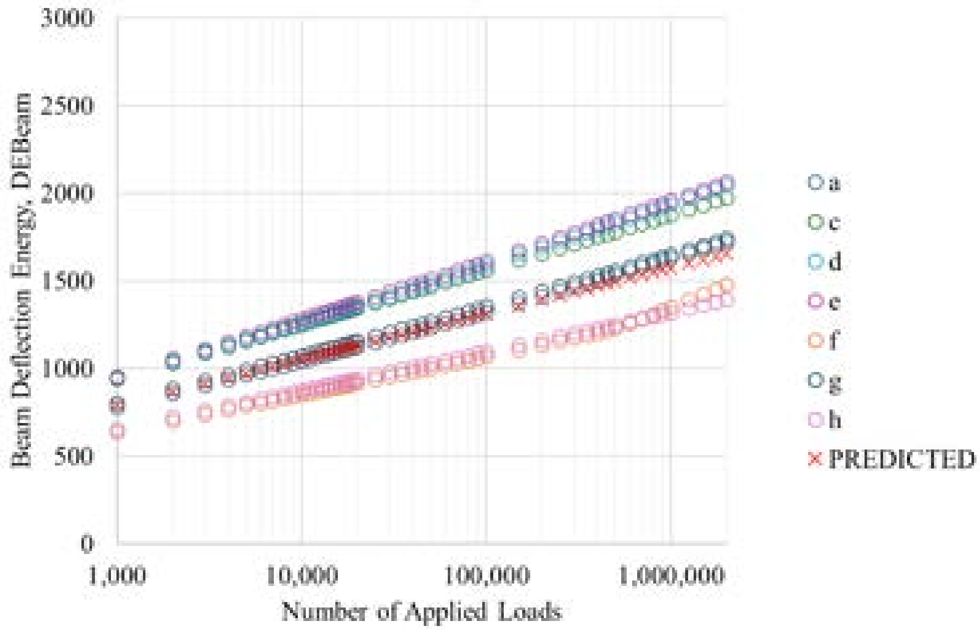

Figure 53. Predicted and actual DE_{Beam} for 1.25-in EC dowels in 8-in beams with med. load magnitude.

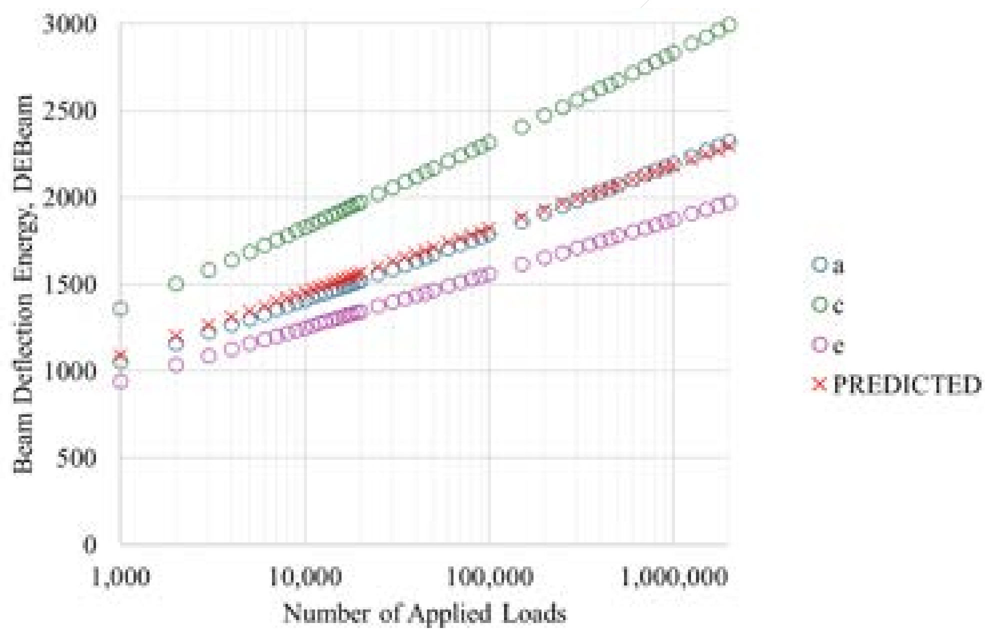

Figure 54. Predicted and actual DE_{Beam} for 1.25-in EC dowels in 8-in beams with high load magnitude.

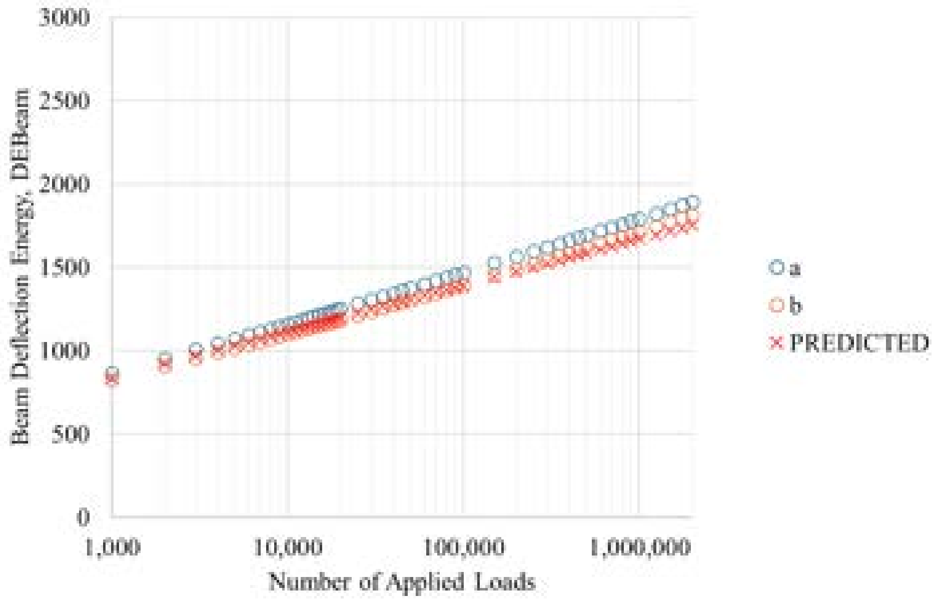

Figure 55. Predicted and actual DE_{Beam} for 1.375-in ET dowels in 8-in beams with med. load magnitude.

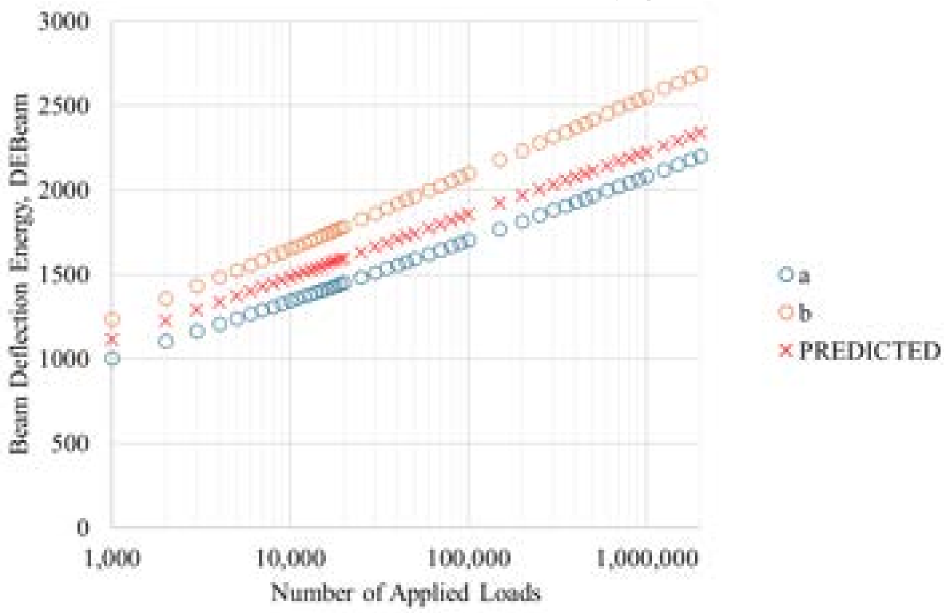

Figure 56. Predicted and actual DE_{Beam} for 1.25-in FRP dowels in 8-in beams with med. load magnitude.

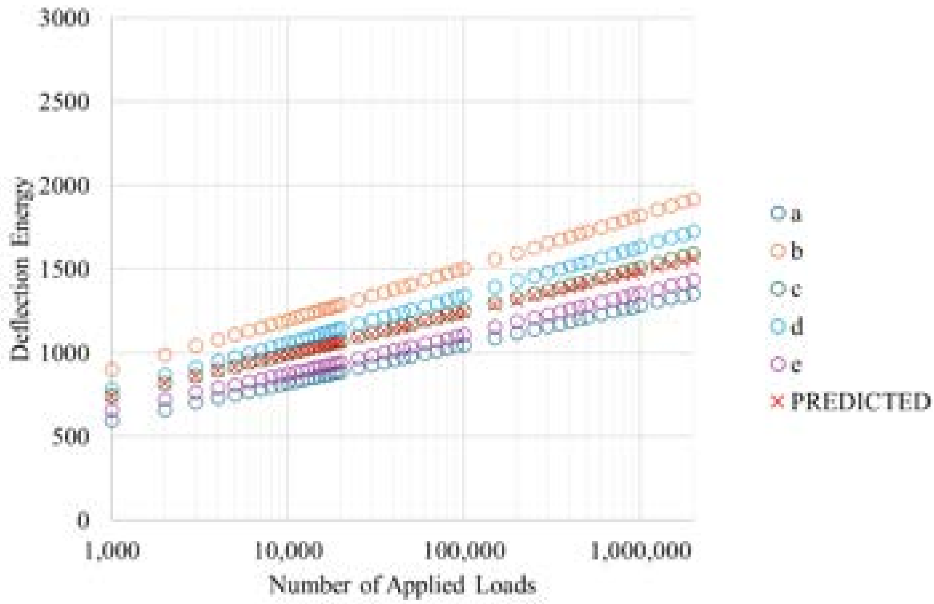

Figure 57. Predicted and actual DE_{Beam} for 1.25-in EC dowels in 10-in beams with med. load magnitude.

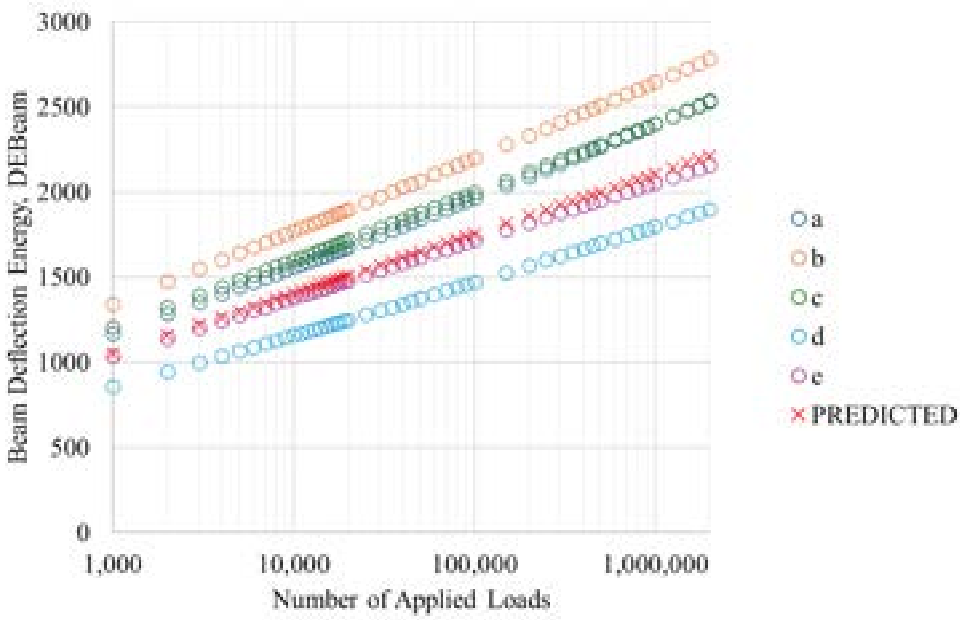

Figure 58. Predicted and actual DE_{Beam} for 1.25-in EC dowels in 10-in beams with high load magnitude.

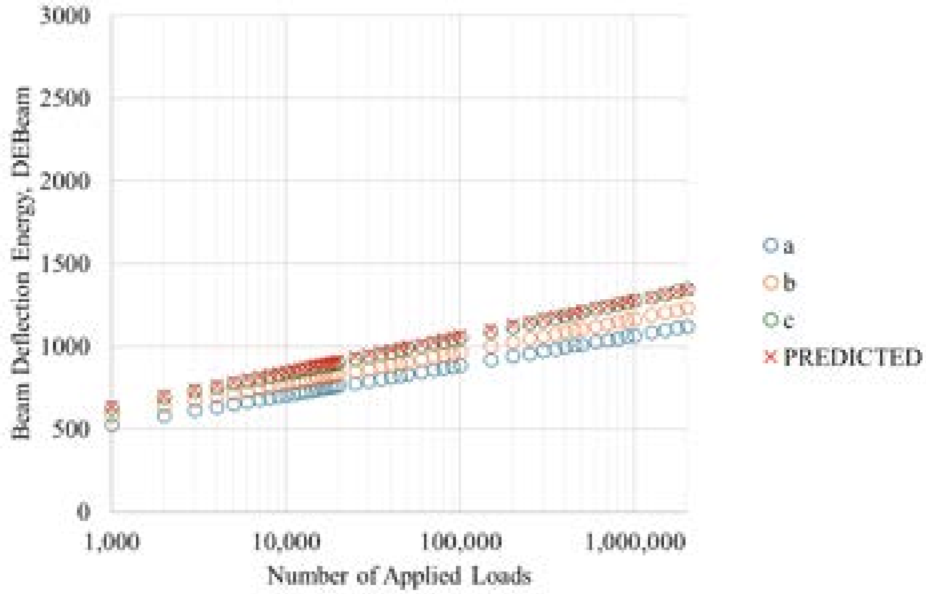

Figure 59. Predicted and actual DE_{Beam} for 1.5-in EC dowels in 10-in beams with med. load magnitude.

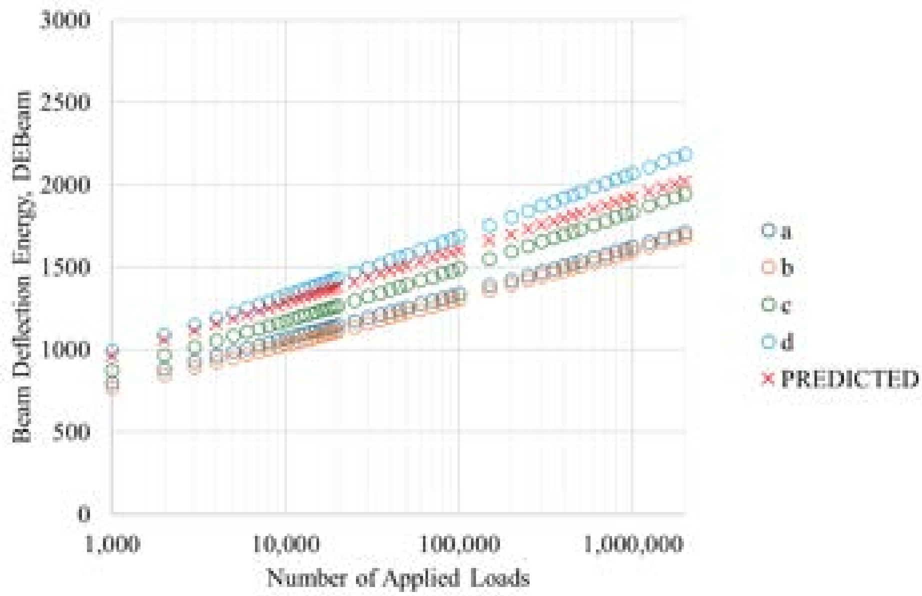

Figure 60. Predicted and actual DE_{Beam} for 1.5-in EC dowels in 10-in beams with high load magnitude.

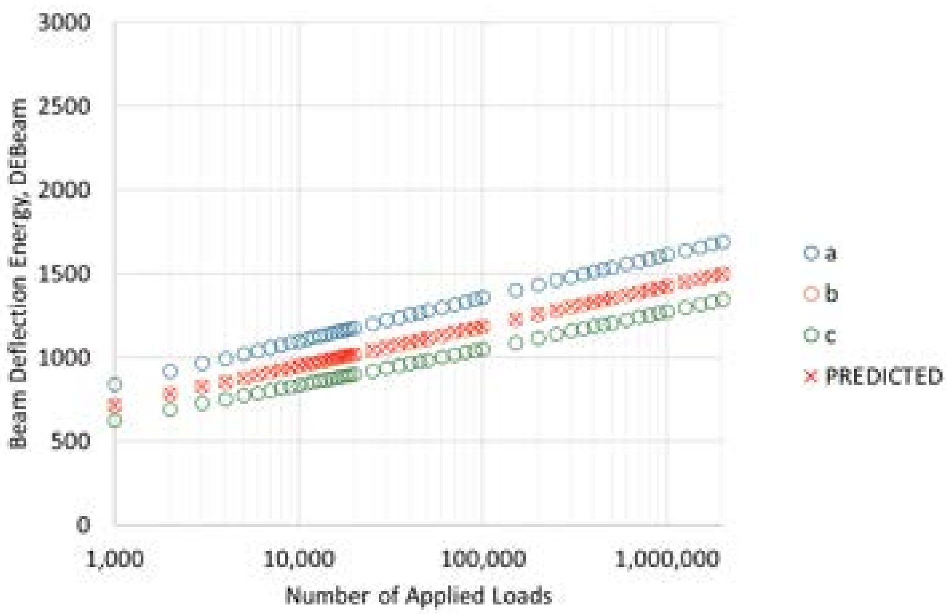

Figure 61. Predicted and actual DE_{Beam} for 1.625-in ET dowels in 10-in beams with med. load magnitude.

The DE_{Beam} prediction equation shown in Equation 9 was adopted into the faulting model framework to predict DOWDAM. It was observed that the original equation predicts negative values for DE_{Beam} for low loads transferred through the dowel. This occurred because the training data did not include low load values since the lowest applied laboratory load is equal to 2,000 lbs, or 900 lbs transferred through the dowel. To remedy this, a stepwise form of the function was developed to ensure a continuous and positive prediction of DOWDAM for all loads. The modified DOWDAM equation is shown below in Equation 10:

$$DOWDAM = \begin{cases} C8 * \sum [\alpha_1 * log(x_i + 1) + \alpha_2 * log(x_i + 1) * \frac{log(Load_i)}{\beta} + \alpha_3 * \frac{log(x_i + 1)}{\beta}] & if\ Load_i \geq 900 \\ C8 * \frac{Load_i}{900} * [\alpha_1 * log(x_i + 1) + \alpha_2 * log(x_i + 1) * \frac{log(900)}{\beta} + \alpha_3 * \frac{log(x_i + 1)}{\beta}] & if\ Load_i < 900 \end{cases} \quad (10)$$

Where $DOWDAM$ is the cumulative dowel damage, x_i is the number of applied loads at the *i*th load magnitude, *Load_i* is the magnitude of load transferred through the dowel at the *i*th load magnitude (lb), β is the relative stiffness of the dowel (in^{-1}), α_1, α_2, and α_3 are coefficients presented in Table 25, and C_8 is the calibration coefficient specific to doweled pavements. Calibration of C_8 is discussed in greater detail in the subsequent sections.

5.2.1.1 Sensitivity Analysis

A sensitivity analysis of the predicted DOWDAM to various parameters included in the model is conducted to ensure sufficient prediction across the range of typical parameters. A baseline set of parameters is presented in Table 26. Each parameter was individually adjusted, while all other parameters remain fixed and DOWDAM is calculated. For the purpose of the sensitivity analysis, the calibration constant, C_8, remained equal to 1. This constant is adjusted through the calibration process, which will be described in a subsequent section.

Table 26. Parameters included in DOWDAM model sensitivity analysis.

Parameter	**Value**
Concrete elastic modulus, psi	4.5×10^6
Slab thickness, in	10
Dowel elastic modulus, psi	29×10^6
Dowel diameter, in	1.25
Dowel type	Solid
Load transferred through dowel, lbs	1,350
Total number of applied loads	10 million

The effect of slab thickness on DOWDAM is shown in Figure 62. Increasing slab thickness results in slight decreases in predicted DOWDAM. This is anticipated since increasing slab thickness reduces K calculated using Equation 8. Similarly, an increase in concrete elastic modulus results in a slight increase in DOWDAM, as seen in Figure 63. Increasing concrete elastic modulus increases K calculated using Equation 8. However, the effect of both of these parameters is observed to be small, which is consistent with the experimental results from the accelerated load testing.

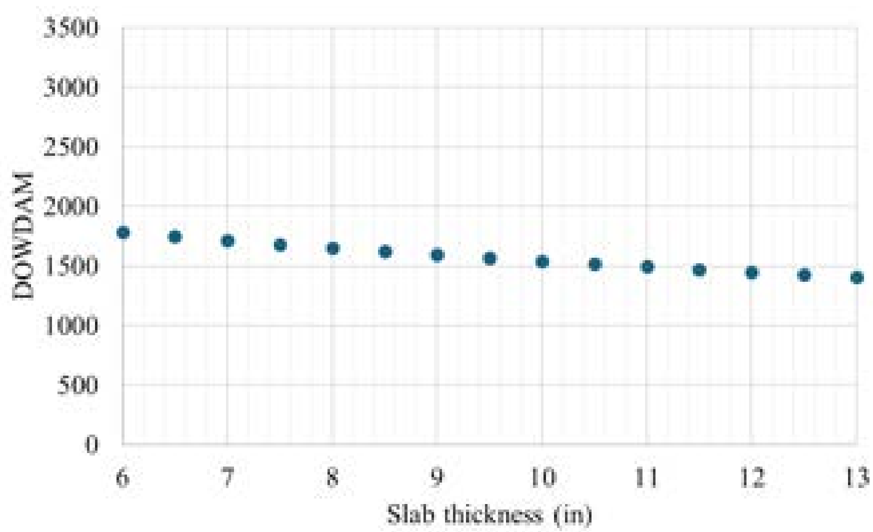

Figure 62. Effect of slab thickness on predicted DOWDAM.

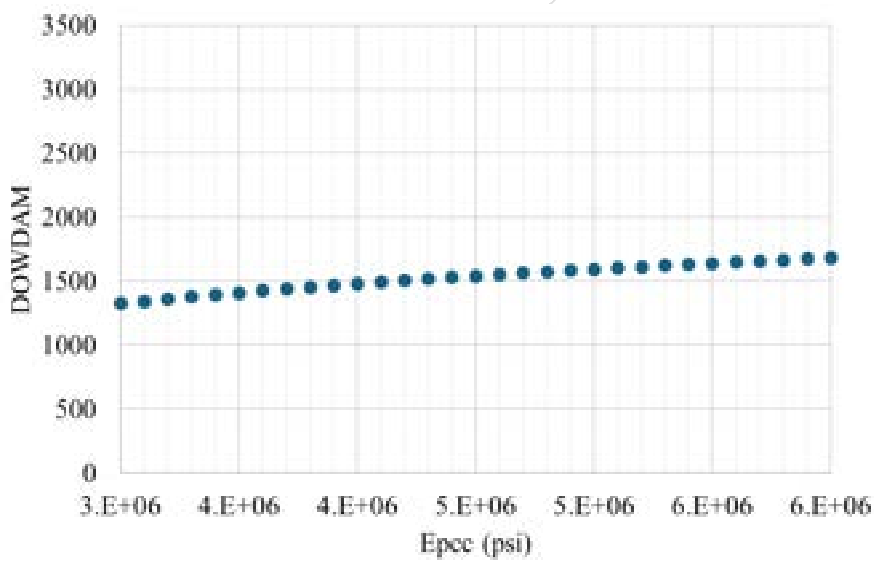

Figure 63. Effect of concrete elastic modulus on predicted DOWDAM.

The effect of the dowel relative stiffness parameter, β, on predicted DOWDAM is shown in Figure 64. An increase in β results in a decrease in predicted DOWDAM. A larger β corresponds to a lower ability for a dowel to resist bending under loading, thus poorer performance as reflected in the sensitivity plot. Increasing dowel diameter decreases β, and the effect of dowel diameter for both solid and tubular dowels on predicted DOWDAM is shown in Figure 65. As expected, increasing dowel diameter results in decreased DOWDAM. Additionally, tubular dowels exhibit greater DOWDAM compared to solid dowels with identical diameters. This can be attributed to the lower bending stiffness of tubular dowels when compared to solid dowels with identical outer diameters. Tubular dowels must have a greater diameter than solid dowels in order to have comparable resistance to bending under loading.

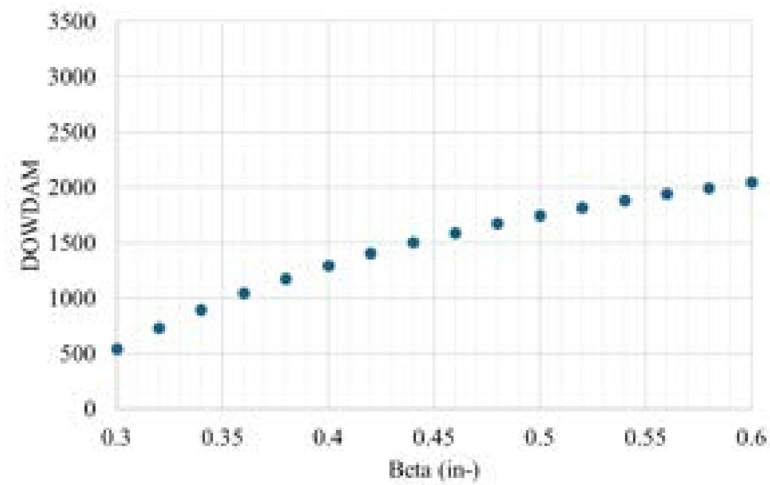

Figure 64. Effect of dowel constant on predicted DOWDAM.

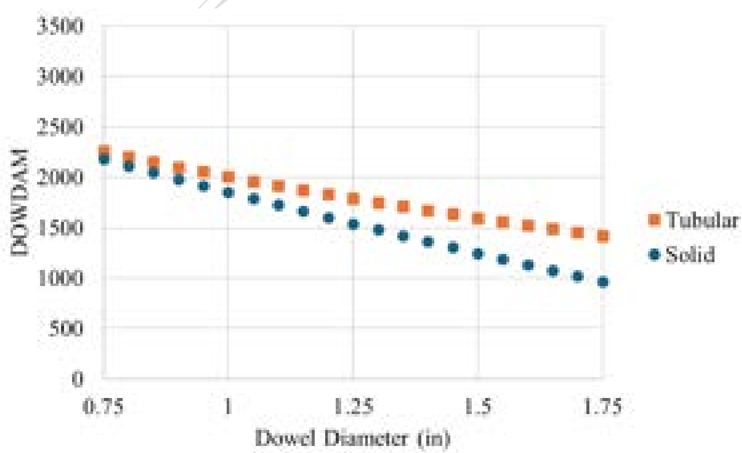

Figure 65. Effect of dowel diameter on predicted DOWDAM.

Lastly, the effect of load on predicted DOWDAM was evaluated. The effect of load magnitude on predicted DOWDAM is shown in Figure 66. As expected, higher loads transferred through the dowel results in higher DOWDAM. Critically, the predicted DOWDAM is a continuous function and is equal to 0 when the load magnitude is 0 lbs. The effect of number of applied loads on predicted DOWDAM for three different load magnitudes is shown in Figure 67. As observed in the accelerated load testing, the increase in DOWDAM has a logarithmic form, therefore Figure 67 is a semi-log plot. As anticipated, the predicted DOWDAM increases as the number of load applications increases. Therefore, an increase in load magnitude or number of load applications increases predicted damage development.

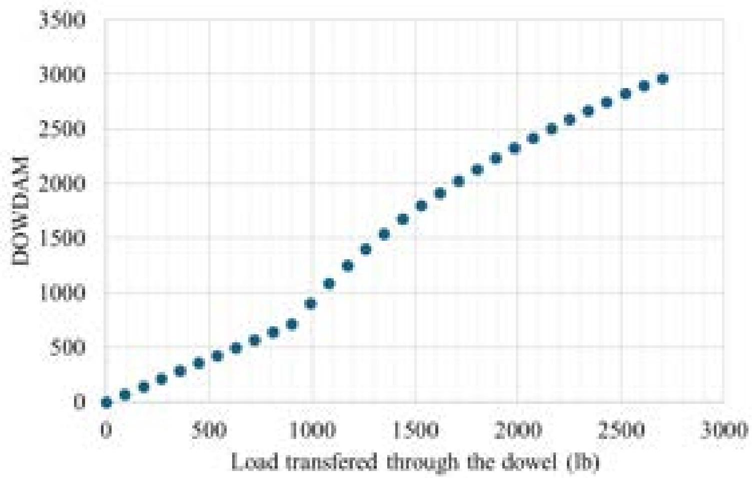

Figure 66. Effect load transferred through the dowel on predicted DOWDAM.

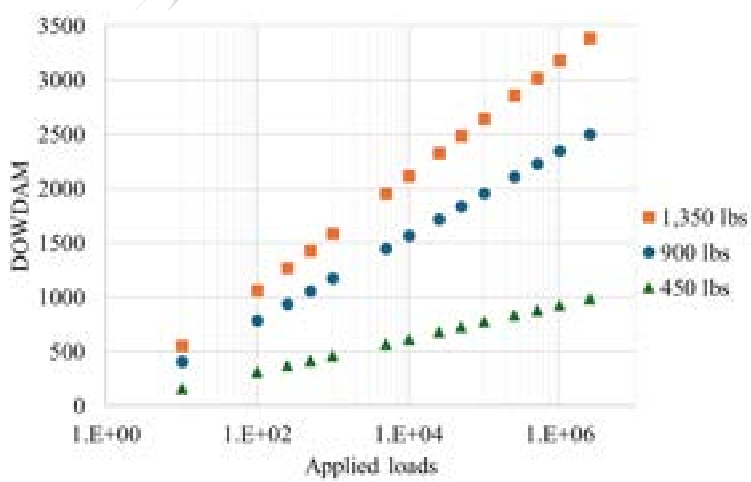

Figure 67. Effect of number of load applications on predicted DOWDAM

5.3 Incorporation of Corrosion in Faulting Model

The faulting model was revised to account for loss of dowel performance due to the development of corrosion on the dowel. The current faulting framework is revised to account for the reduction in dowel diameter due to corrosion development. In the current faulting model framework, dowel diameter is a constant value. The results from the accelerated corrosion study indicate that dowel diameter has the potential to decrease as a function of initial diameter, amount of chloride exposure, coating type, and dowel material. The parameters identified in the accelerated corrosion study align with the critical corrosion parameters identified in the literature. Therefore, the dowel diameter was adjusted in this project to account for a monthly reduction in dowel diameter due to corrosion. The revised dowel diameter equation is presented in Equation 11:

$$d_i = d_0 * \frac{1}{(month_i - CL)^{\frac{WetDays}{365} * C_{EXP} * C_{Coating}}} \tag{11}$$

Where d_i is the monthly dowel diameter (in), d_0 is the initial dowel diameter (in), $month_i$ is the current month, *CL* is the typical coating life in months, *WetDays* is the average number of wet days per year, C_{EXP} is the severity of the salt exposure, and $C_{Coating}$is the resistance of the bar to corrosion development. The coating life parameter, *CL*, is included to account for the delayed development of corrosion achieved through use of coatings. This parameter is informed by the results of the accelerated corrosion study, in which it was observed that corrosion development was delayed as a function of coating type. For standard, epoxy-coated carbon steel dowels it is assumed that the CL is equal to 240 months (20 years). Corrosion initiation was delayed for galvanized dowels, therefore, *CL* is equal to 600 months (50 years) for these dowels.

WetDays is included to account for the climatic effect of precipitation that carries chlorides into the joint. The exposure parameter is introduced to capture the range of exposure conditions throughout various regions. Corrosion potential is greatest where high quantities of deicing salts enter the joint, which occurs in regions with frequent snowfall events and frequent freeze-thaw cycling. Corrosion potential is lower in regions with mild winters with little freezing or in regions with hard winters in which the pavement structure remains below freezing and thus deicing salts are not carried into joints. The exposure parameter is determined as a function of the freezing index (FI), which is calculated by comparing the average annual cumulative difference in mean daily temperature to 32°F. The magnitude of FI determines the value for C_{EXP} using Table 27. Note that at extreme FI values the magnitude of C_{EXP} becomes asymptotic. This is due to the potential for extended durations of freezing and fewer freeze thaw cycles, thus fewer opportunities for deicing salts carried by melted snow to penetrate the joint and corrode the dowel. before being plowed off the roadway during snow removal. The FI is a output parameter calculated in Pavement ME as it is incorporated into the International Roughness Index (IRI) prediction model [70].

Table 27. Range of $\mathbf{C_{EXP}}$ values included in model.

FI (°F day)	$\mathbf{C_{EXP}}$
< 100	0
100 - 400	0.15
400 - 600	0.2
600 - 1000	0.25
> 1000	0.25

The value for $C_{Coating}$is determined as a function of the type and diameter of dowel being evaluated. Larger diameter dowels have greater surface area in the open joint exposed to chlorides, therefore $C_{coating}$ is calculated using Equation 12:

$$C_{coating} = \alpha * (\pi * d) * jw \quad (12)$$

Where $C_{coating}$ is the coating parameter used in Equation 12, α is selected based on the dowel coating or material, d is the outer dowel diameter (in), and jw is the joint width (in). The sections included in the calibration dataset were all constructed with the standard, solid steel epoxy-coated dowels. For standard, epoxy-coated carbon steel dowels, α is equal to 0.15. The results from the accelerated corrosion study were used to estimate the α values for alternative dowel materials. Dowels which do not exhibit corrosion, such as stainless-steel dowels (SN), are assumed to have an α equal to 0 because no corrosion was observed in the laboratory investigation. This would negate the effect of corrosion in the model, and the only loss of dowel performance would be the result damage in the concrete around the dowel due to bearing stresses calculated through the DOWDAM portion of the framework. Galvanized dowels (G1G and G1P) exhibited minor corrosion development in the laboratory investigation, therefore α for galvanized dowels is estimated to be 0.075 for the green epoxy coated galvanized dowels (G1G) that exhibited 1/3 the surface corrosion of the standard epoxy coated steel. An α of 0.01 is recommended for the purple epoxy coated galvanized bars (G1P) as it only exhibited 1/7 of the surface corrosion of the standard epoxy coated steel. These values were adjusted during /calibration, which is described in Section 5.3.1.

5.3 Faulting Model Recalibration

5.3.1 Calibration Database

AASHTOWare Pavement ME Design v2.6.2 was used for performing the calibration. The climatic and performance databases used to calibrate the JPCP faulting model was the same as that constructed and used for the national calibration performed under NCHRP Task 327 project [71, 72]. The database consists of 120 sections from 26 states, 1 province of Canada, and 6 sections at the Minnesota Road Research Facility (MnROAD). The number of sections and datapoints obtained from each region are shown in Table 28, and a map of the calibration site locations is shown in Figure 68.

Table 28. Calibration database geographical details.

Location	Number of Sections	Number of Calibration Datapoints
Alabama	1	3
Florida	2	6
Georgia	4	23
Idaho	1	8
Indiana	4	11
Iowa	3	10
Kentucky	1	4
Michigan	8	50
Mississippi	1	14
Nebraska	2	5
Nevada	2	7
New Mexico	1	19
North Carolina	11	76
North Dakota	2	9
Ohio	5	24
Arizona	10	79
Oklahoma	2	10
Pennsylvania	1	6
South Carolina	1	1
South Dakota	3	14
Texas	1	9
Utah	3	14
Arkansas	9	57
Washington	10	62
Wisconsin	10	24
California	4	23
Colorado	8	50
Quebec	4	21
MnROAD	6	5

Figure 68. Map identifying sections included in calibration database. Background map from Google Maps [73].

5.3.2 Model Calibration

Calibration of the faulting model involves iteratively adjusting the calibration coefficients $C_1 – C_7$ in the faulting transfer functions and C_8 in Equation 10 to minimize the error between the predicted and actual faulting values [70]. Error is calculated using Equation 13. The following calibration process was adopted. First, the calibration constant C_8 was estimated by comparing DOWDAM values calculated using Equation 10 to DOWDAM values calculated in previous recalibrations. The objective of this is to ensure the DOWDAM values were predicted to be a reasonable magnitude so as to minimize the adjustment of the other calibration constants. The estimated C_8 value was implemented into the faulting model framework, and the monthly differential energy (DE) calculated by the artificial neural networks (ANNs) were obtained. The monthly DE values were placed in a macro driven excel spreadsheet developed to calibrate the faulting model. Several calibration parameters were fixed, while the other parameters are varied. The combination of the parameters varied, which yielded the lowest error, were identified. These parameters remain fixed, while the parameters that were previously fixed were varied to find the new combination of parameters that yield the lowest error. The entire process was repeated with several adjustments made to C_8 until the lowest error was achieved. This method does not necessarily guarantee the lowest global error, however, it does provide reasonable results. Throughout the process, both the error and model bias are minimized to ensure sufficient model performance. The error between the predicted and measured faulting was minimized using the following function:

$$ERROR(C_1, C_2, C_3, C_4, C_5, C_6, C_7, C_8) = \sum_{i=1}^{N} (\mathrm{FaultPredicted_i} - \mathrm{FaultMeasured_i})^2 \qquad (13)$$

Where ERROR is the error function (in), C_1 – C_8 are the calibration coefficients, $\mathrm{FaultPredicted_i}$ is the predicted faulting for the i^{th} observation in the dataset (in), and $\mathrm{FaultMeasured_i}$ is the measured faulting for the i^{th} observation in the dataset (in).

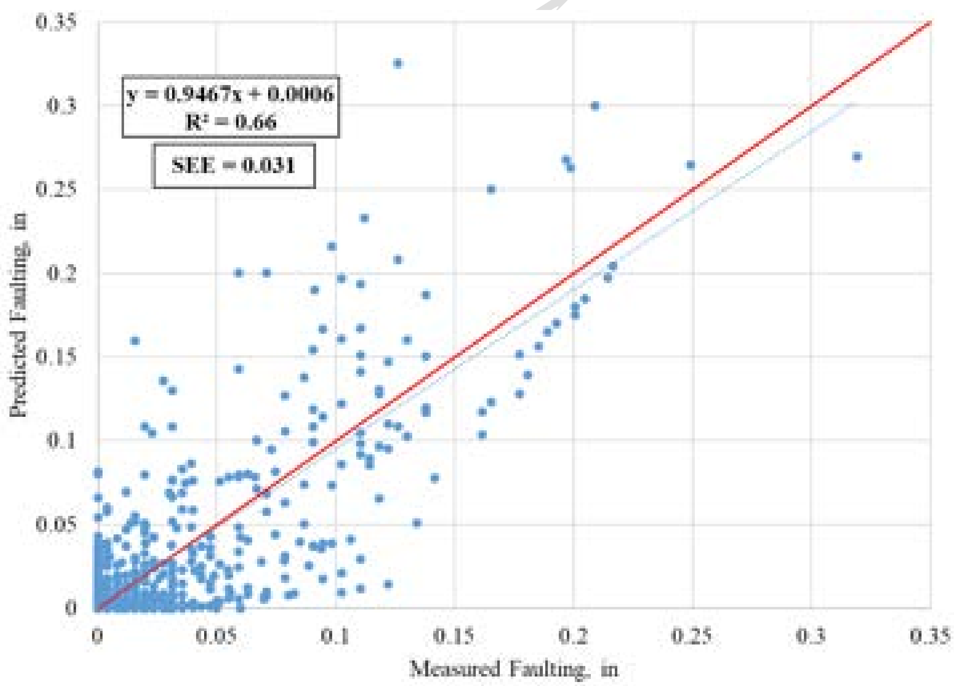

Figure 69. Predicted vs. measured faulting. The red line is a reference line.

Table 29. JPCP transverse joint faulting calibration coefficients

Calibration Coefficient	**Original Pavement ME model (2004)**[1]	**Task 327.7 (2014)**[2]	**Pitt Fault (2025)**
C_1	1.29	0.595	0.55
C_2	1.1	1.636	1.27
C_3	0.001725	0.00217	0.0015
C_4	0.0008	0.00444	0.0022
C_5	250	250	230
C_6	0.4	0.47	0.67
C_7	1.2	7.3	10.6
C_8	400	400	100

[1][70]
[2][72]

5.3.3 Model Adequacy Checks

Model adequacy checks were performed to ensure bias was eliminated from the model. The procedure developed by Mallela et. al was adopted for this analysis [74].Table 30 - Table 31. The null and alternative hypothesis tests outlined in Table 30 are shown in Table 31. A significance level of 0.05 was assumed for all hypothesis testing. Based on Table 31, the null hypothesis is rejected for each of the three hypotheses. Therefore, it is concluded that the model does not exhibit bias and is acceptable.

Table 30. Null and Alternative hypothesis tested for JPCP faulting.

Hypothesis 1	Null hypothesis H_o: Linear regression model intercept = 0
	Alternative hypothesis H_a: Linear regression model intercept ≠ 0
Hypothesis 2	Null hypothesis H_o: Linear regression model slope = 1.0
	Alternative hypothesis H_a: Linear regression model slope ≠ 1.0
Hypothesis 3	Null hypothesis H_o: Mean predicted faulting = Mean measured faulting
	Alternative hypothesis H_a: Mean predicted faulting ≠ Mean measured faulting

Table 31. Results from transverse joint faulting model hypothesis testing

Hypothesis Testing and T-Test			
Test Type	Value	95% CI	P-value
Hypothesis 1: Intercept = 0	0.0006	(0.0013, 0.0025)	0.639
Hypothesis 2: Slope = 1	0.947	(0.89, 1.01)	0.638
Paired t-test	-	-	0.632

5.3.4 Faulting Reliability Model

The faulting reliability model was determined using the same method adopted for Pavement ME [70], Section 5.2.2.2. The model is shown in Figure 70, and the data used to develop the model is presented in Table 32. The reliability model is shown in Equation 14. The R^2 of the reliability model is equal to 0.99.

$$Stdev(Fault) = 0.00594 + 0.0766 * (Fault^{0.318}) \tag{14}$$

Where Stdev(Fault) is the faulting standard deviation (in), and Fault is the average transverse joint faulting (in).

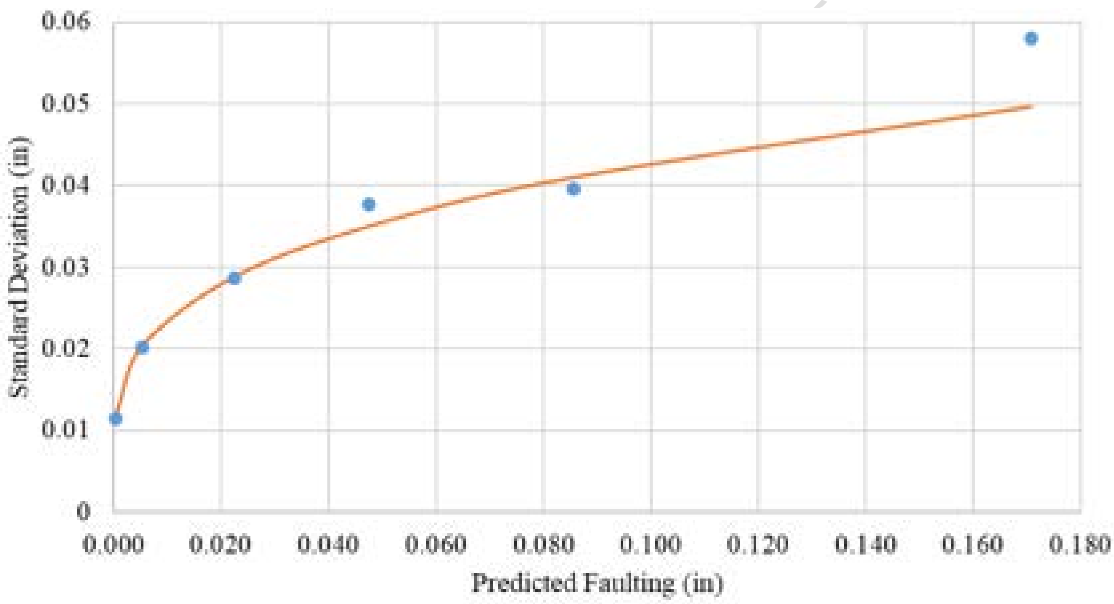

Figure 70. Faulting standard deviation vs. predicted faulting used to fit faulting standard deviation model.

Table 32. Predicted faulting data used to develop faulting standard deviation model incorporating the corrosion model.

Group	Mean Predicted Joint Faulting, in	Std. dev. of Predicted Joint Faulting, in
1	0.0004	0.0115
2	0.0054	0.0202
3	0.0224	0.0287
4	0.0475	0.0377
5	0.0856	0.0396
6	0.1707	0.0580

5.4 Sensitivity Analysis

A sensitivity analysis of the predicted faulting is presented to evaluate the response of the model to key design, loading, and climatic parameters. A baseline structure was used for sensitivity analysis. All parameters remained fixed with one parameter varied at a time to evaluate the effect of the parameter on predicted faulting. The baseline pavement structure parameters are shown in Table 33, and the sensitivity plots are shown in Figure 71 - Figure 83.

Table 33. Baseline structure examined in the sensitivity analysis.

Parameter	Value
PCC thickness	10 in
PCC 28-day MOR	600 psi
PCC CTE	5.0x10^{6}/°F
Slab width	12 ft
Joint spacing	15 ft
Dowel bar	1.25-in diameter, solid epoxy-coated steel
Shoulder type	HMA
Base type	6 in granular
EROD	4
P200 of base	8.7%
Subgrade	A-4
Climate	Wet-freeze (Pittsburgh)
One-way AADTT	3,000
Built-in gradient	-10˚F
Reliability	50%

The effect of PCC thickness on predicted faulting is shown in Figure 71 and Figure 72 for 1.25-in and 1.5-in solid EC dowels. Increasing PCC thickness causes a decrease in the ratio of dowel cross-sectional area to PCC thickness, thus lowering the non-dimensional dowel stiffness. Faulting is not sensitive to thickness with small variations in pavement thickness, however, there is a significant increase in predicted faulting for 1.25-in EC dowels when the pavement thickness is 12 in. If the pavement thickness is 10 in or greater, then a 1.5-in dowel is typically used, therefore, this sensitivity is reasonable.

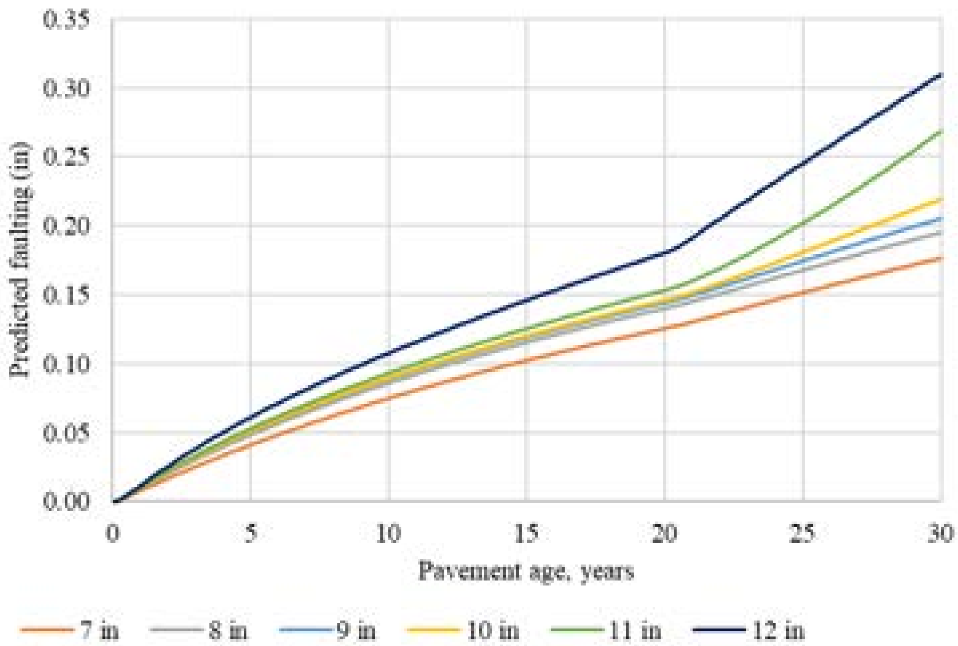

Figure 71. Effect of PCC thickness on predicted faulting for 1.25-in diameter EC dowel.

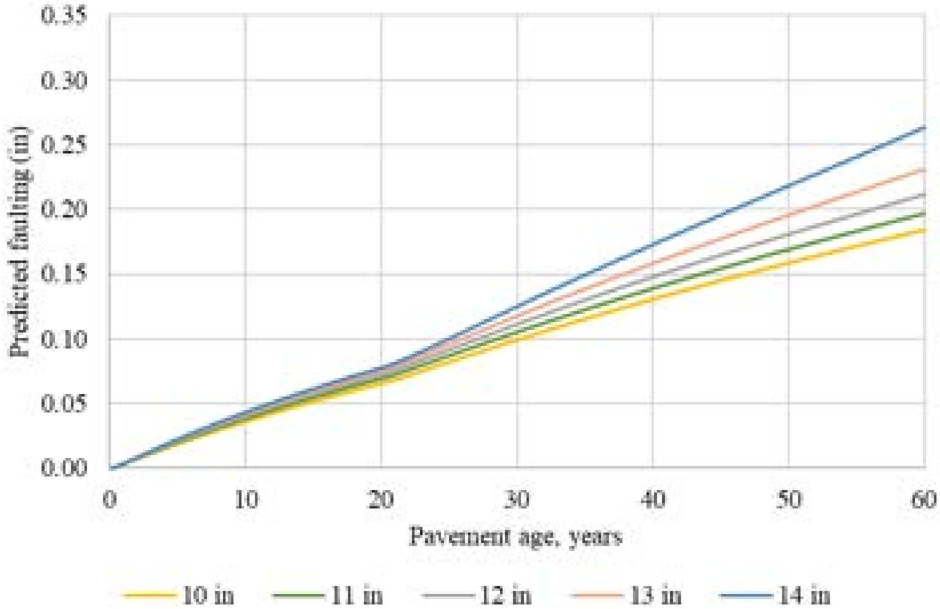

Figure 72. Effect of PCC thickness on predicted faulting for 1.5-in diameter EC dowel.

The effect of joint spacing on predicted faulting is shown in Figure 73. Increasing joint spacing results in an increase in the DE predicted from the structural response model. This results in an increase in the predicted faulting.

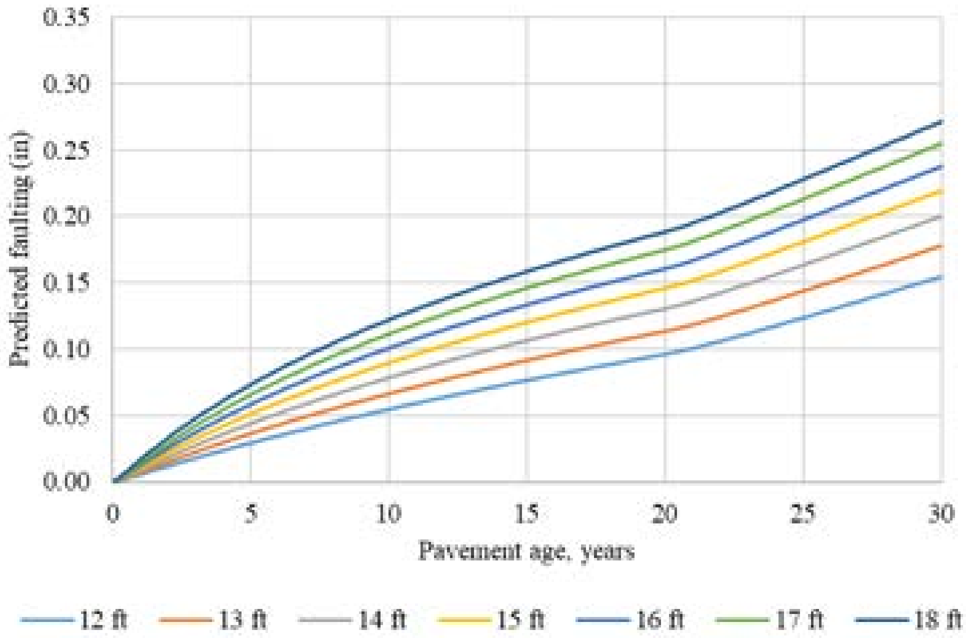

Figure 73. Effect of joint spacing on predicted faulting.

The effect of traffic volume on predicted faulting is shown in Figure 74 and Figure 75 for 1.25-in and 1.5-in solid steel EC dowels, respectively. The one-way AADTT volume is varied for each case. It should be noted that the one-way AADTT indicated in the legend was further reduced when predicting faulting by multiplying by a lane distribution factor. The portion of trucks in the design lane was assumed to be 95%. Increasing the traffic is shown to cause an increase in predicted faulting due to the increase in DE calculated with the structural response model. The revised dowel damage model accounts for the loss of dowel performance due to vehicle loads. Therefore, greater traffic volumes result in greater loss of dowel performance over time.

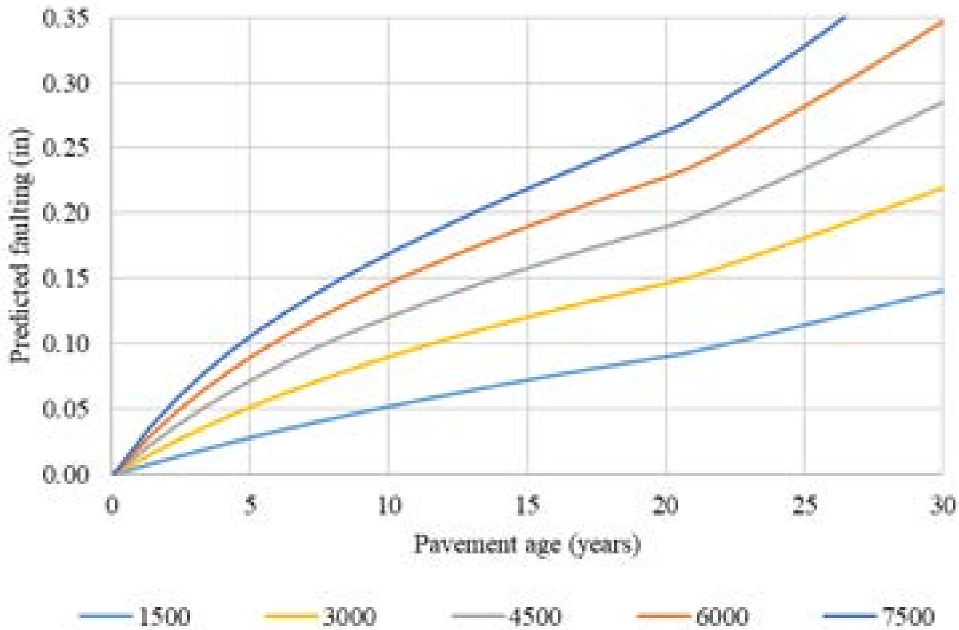

Figure 74. Effect of one-way AADTT on predicted faulting for 1.25-in diameter EC dowels.

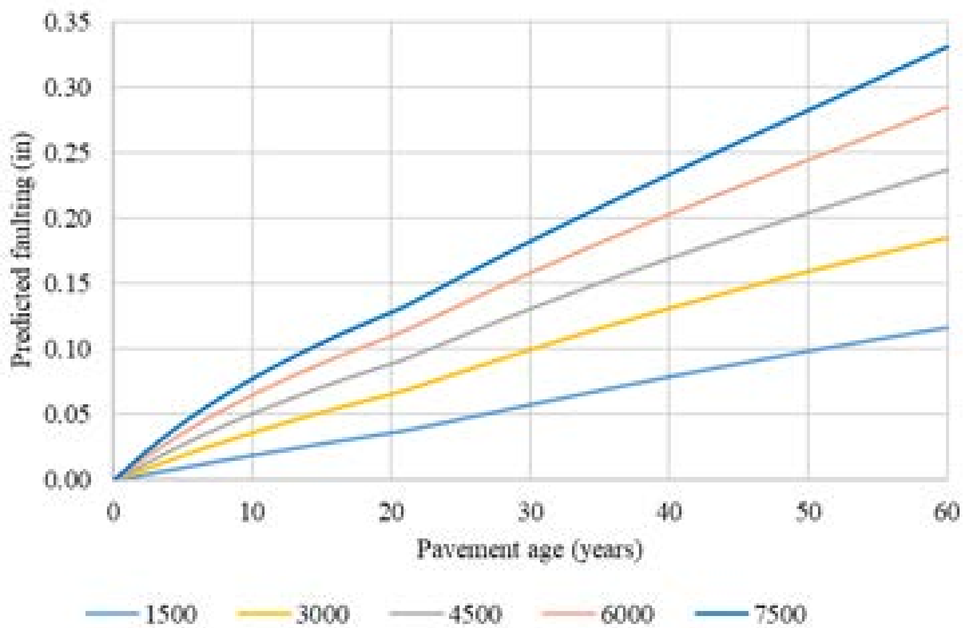

Figure 75. Effect of one-way AADTT on predicted faulting for 1.5-in diameter EC dowels.

The effect of climate on predicted faulting is shown in Figure 76. The predicted faulting is lowest for Arizona due to the high temperatures, lack of freeze-thaw cycles, and dry climate. The predicted faulting for Atlanta, GA, is slightly higher due to the higher amount of precipitation present, which increases the mobility of fines and hence the potential for the development of faulting. Faulting for Pittsburgh, Chicago, and Madison are similar due to their climates having similar precipitation and freeze-thaw cycles. The increase in faulting after 20 years can be seen for these regions. This is due to the effect of the corrosion model, which accounts for loss of dowel performance at the end of the life of the dowel coating.

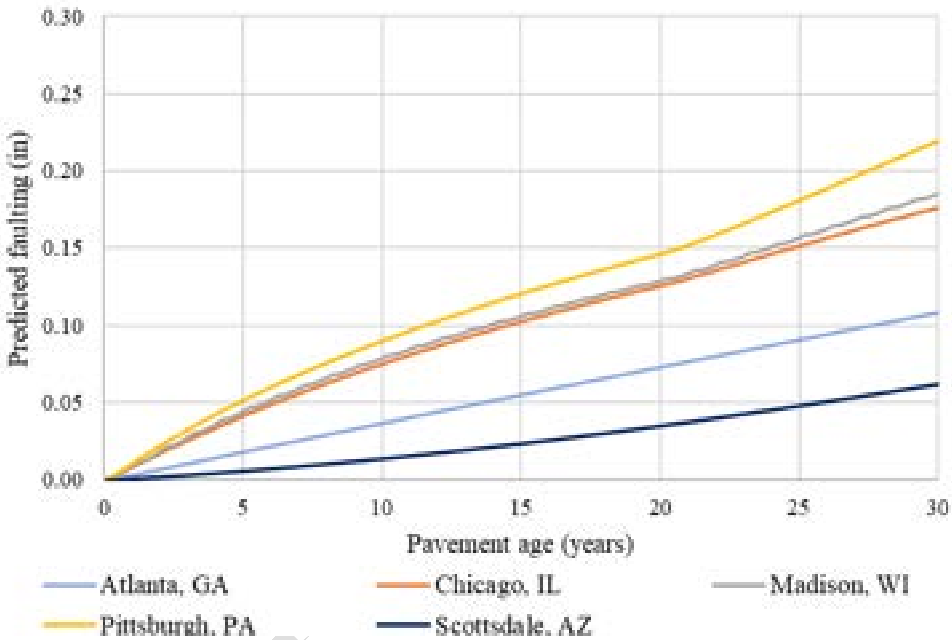

Figure 76. Effect of climate on predicted faulting.

The rate at which the corrosion model affects predicted faulting is a function of the $C_{coating}$ factor, WetDays, and FI. As shown in Figure 77, increasing $C_{coating}$ results in an increase in the predicted faulting. This parameter is calculated using Equation 12 and varies as a function of coating type and dowel diameter. Use of more corrosion-resistant coatings, such as zinc-based galvanization, results in a lower $C_{coating}$ compared to standard epoxy-coatings. The effect of corrosion is also a function of the climatic parameters WetDays and FI. This is shown in Figure 78 and Figure 79. Increasing WetDays causes more not only increases the mobility of fines and hence the potential for the development of faulting but also helps to mobilize deicing salts into the transverse joint, thus accelerating corrosion development on the metallic dowel. The FI accounts for the amount of snowfall that is likely to occur. Increasing FI causes greater amounts of deicing salts to be applied, thus increasing the effect of corrosion on predicted faulting. However, it was observed in the calibration dataset that the effect of FI on predicted faulting became asymptotic. It is hypothesized that at a certain threshold of FI there are fewer freeze-thaw cycles that allow for deicing salts to mobilize into the joint. Therefore, an upper limit on the effect of FI is applied.

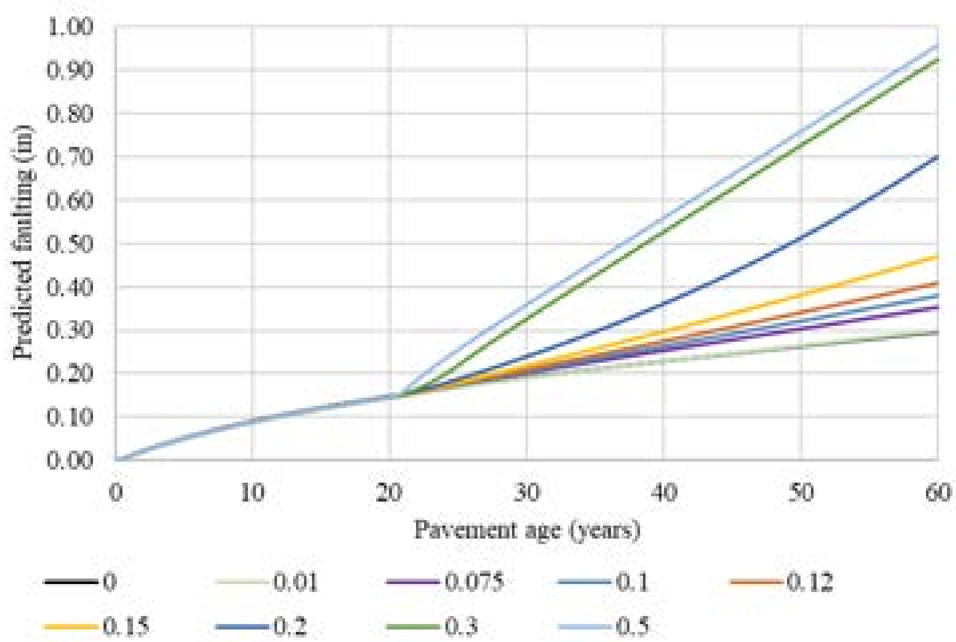

Figure 77. Effect of $C_{coating}$ on predicted faulting.

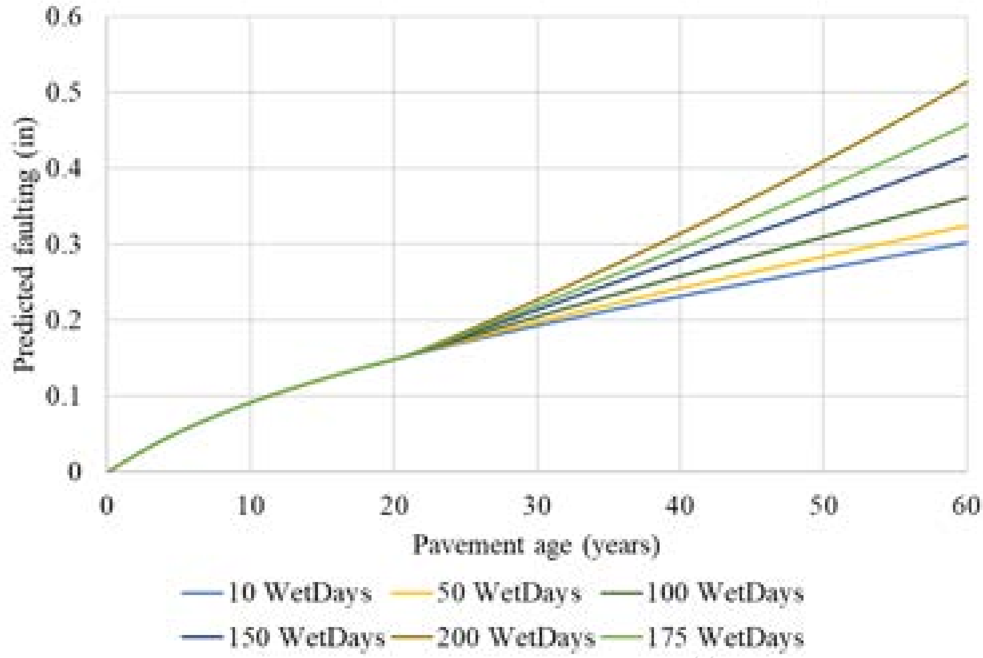

Figure 78. Effect of WetDays on predicted faulting.

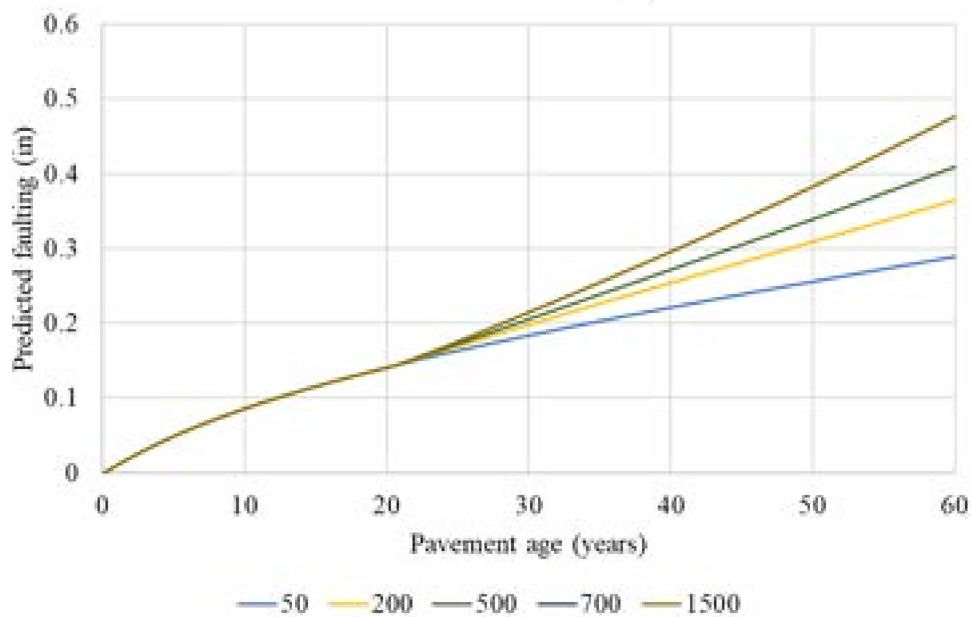

Figure 79. Effect of FI on predicted faulting.

The effect of dowel bar diameter and design on predicted faulting is shown in Figure 80 - Figure 82. First, increasing dowel diameter for solid steel, EC dowels is shown to reduce the predicted faulting. This is consistent with knowledge of pavement design. Novel to pavement performance modeling is the ability to account for long-life, alternative dowel bars, as shown in

Figure 80 and Figure 81. Predicted faulting is calculated for FRP dowels using the concept of equivalent dowel diameter. As shown in Figure 81 this enables 1.25-in and 1.5-in FRP dowels to be used. It can be seen that 1.5-in FRP dowels have similar performance as 1.25-in EC dowels for the first 20 years of the design life due to similar dowel stiffness values. However, FRP dowels do not corrode, therefore the long-life performance of this dowel compared to the EC dowel is superior. The predicted faulting for standard and galvanized tubular dowels is shown in Figure 82. It can be seen that dowels with similar equivalent diameters have similar predicted faulting for the first 20 years of the design life. Once the coating life of the epoxy steel dowel is reached, however, the predicted faulting increases at a greater rate compared to the more corrosion-resistant galvanized dowel. The larger diameter stainless steel (SS) dowel is observed to have the lowest predicted faulting due to the higher equivalent dowel diameter and ability to resist corrosion. These results indicate that alternative dowels can be considered for long-life paving projects, which was not previously possible.

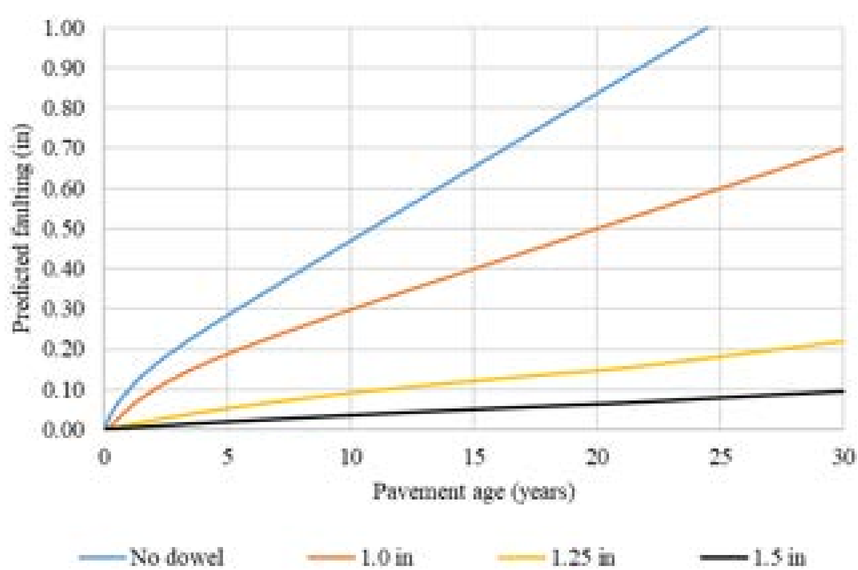

Figure 80. Effect of dowel diameter on predicted faulting.

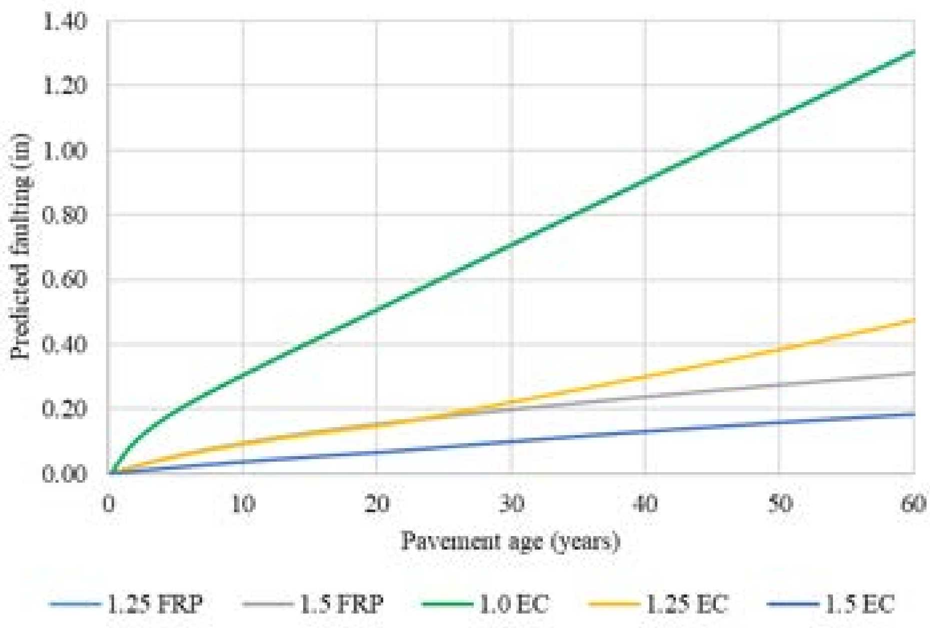

Figure 81. Effect of dowel diameter on predicted faulting for long-life FRP alternative and epoxy coated dowels.

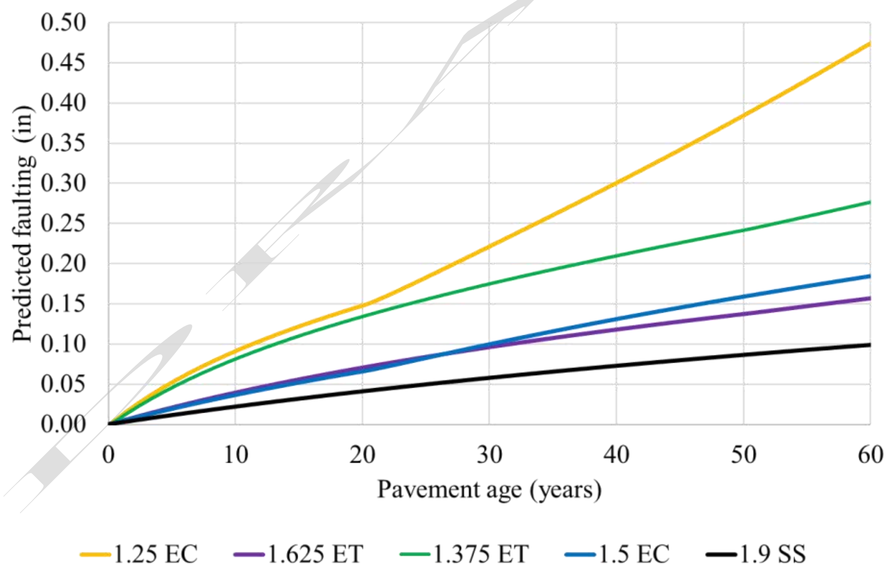

Figure 82. Effect of dowel diameter on predicted faulting for long-life tubular alternative and epoxy coated dowels.

The final factor that is considered is the effect of reliability on predicted faulting. Five levels are examined, from 50% (control) to 99%. As a higher level of reliability is selected, a greater magnitude of faulting is predicted, as shown in Figure 83.

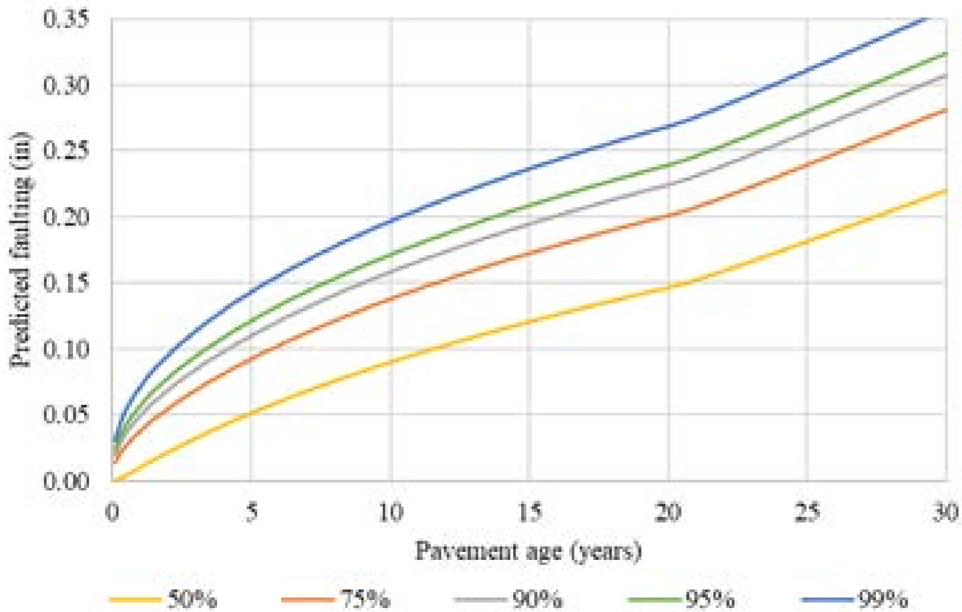

Figure 83. Effect of reliability on predicted faulting.

6.0 CONCLUSIONS

This report presents results from an accelerated corrosion laboratory analysis in which a range of standard and alternative dowel bars were evaluated. The abrasion resistance and impact resistance testing indicated that the majority of the dowels passed the performance requirements with minimal damage to the coating protection systems. Impact testing resulted in significant damage to the coating at several locations on each of the stiff, purple epoxy dowels. This indicates that the stiff epoxy coating may be prone to holiday development prior to paving. It should be noted that the impact test specifications call for a lower impact energy than the impact energy used in this study. Corrosion development was not correlated to increased simulated joint opening/closing force for the epoxy-coated, stainless steel, and FRP dowels. The zinc-clad dowels exhibit increased maximum simulated joint opening/closing force as corrosion developed on the surface of the dowel. This is likely due to seizing of the dowel caused by expansive forces generated by the corrosion by product. Additionally, the green epoxy-coated steel dowels, green and purple epoxy-coated tubular dowels, and stainless steel tubular dowels all exhibit significant simulated joint opening/closing forces. This highlights the need for adequate application of a bond breaker agent, especially for epoxy-coated dowels where the irregular coating surface significantly increases bonding between the dowel and the surrounding concrete.

The results from the accelerated corrosion program indicate that corrosion development is a function of exposure duration, dowel bar material, and dowel coating. For epoxy-coated dowels, corrosion was observed to be localized to holidays placed in the coating. The galvanized dowels were observed to have less corrosion development at the holidays when compared to the carbon steel dowels. Corrosion development was not observed at impact locations for the purple coated epoxy dowels, despite several areas where complete coting failure was observed. No corrosion development is observed on any of the stainless-steel dowels. The zinc-clad dowels exhibited corrosion development on the entire surface of the dowels. The expansive corrosion by product corresponds to the increase in simulated joint opening/closing force measured. Additionally, the FRP dowels do not display any signs of swelling or damage due to moisture intrusion, although it should be noted that the duration of this test was limited with respect to the expected service life of a dowel bar. The results from the laboratory study demonstrate that an epoxy coating is effective in preventing corrosion as long as the coating is free from defects. For this reason, the purple epoxy, which is more prone to impact damage, may be more prone to corrosion development. The dual coating protection system of epoxy coating placed over galvanized steel is found to be superior to plain carbon steel dowels. Although the zinc-clad dowels exhibited excellent corrosion resistance, the effect of these dowels on restricting joint movement should be further investigated for the zinc-clad dowels as an expansive and rapidly forming zinc oxide developed throughout the surface of the bar. It should be noted that the zinc oxide could be easily rubbed off the surface.

Both stainless steel and FRP dowels are found to have superior corrosion resistance compared to the alternatives considered in this study.

A revised faulting model was developed to be implemented in the pavement prediction framework, PavementME. First, a dowel damage model developed in a previous study was incorporated into the existing dowel damage model. Second, a novel corrosion model was introduced, which accounts for a reduction in the dowel diameter due to corrosion development. A recalibration of the revised model is presented, and the model adequacy checks are provided. A sensitivity analysis is provided to evaluate the effect of critical design, loading, and climatic parameters on predicted faulting.

The final product from this model development is an improved dowel damage model, which accounts for key design, loading, and exposure factors. Unlike the existing faulting model, alternative dowels can be directly considered using this model. Moreover, the inclusion of corrosion in the proposed faulting model allows for account for both the loss of performance due to vehicle loading and corrosion development.

7.0 REFERENCES

[1] Broomfield, J., Corrosion of Steel in Concrete, CRC Press, 2000.

[2] Ketcham, S., L. D. Minsk, R. R. Blackburn and E. J. Fleege, "Manual of practice for an effective anti-icing program: a guide for highway winter maintenance personnel (No. FHWA-RD-95-202).," Federal Highway Administration., 1996.

[3] Li, Y., Y. Fang, N. Seeley, S. Jungwirth, E. Jackson and X. Shi, "Corrosion by chloride deicers on highway maintenance equipment: Renewed perspective and laboratory investigation.," Transportation research record, vol. 2361, no. 1, pp. 106-113, 2013.

[4] U.S. Army Cold Regions Research and Engineering Laboratory, "FHWA Test and Evaluation Project No. 28 "Anti-Icing Technology" Field Evaluation Report," Hanover, New Hampshire, 1996.

[5] The Salt Institute, "The Snowfighter's Handbook," 2016.

[6] Casey, P. C., C. W. Alwan, C. F. Kline, G. K. Landgraf and K. R. Linsenmayer., "Impacts of Using Salt and Salt Brine for Roadway Deicing. No. FHWA-ID-14-231," 2014.

[7] Maine Department of Transportation, "Interstate Operating Plan," 2018.

[8] "Michigan Winter Maintenance Manual," Michigan Department of Transportation, 2013.

[9] New Hampshire Department of Transportation, "Winter Maintenance Snow Removal and Ice Control Policy," Montpelier, NH, 2001.

[10] New York Department of Transportation, "Highway Maintenance Guidelines, Chapter 5 Snow and Ice Control," 2012.

[11] Pennsylvania Department of Transportation, "Pub 23 - Maintenance Manual, Chapter 4 Winter Services," Harrisburg, PA, 2019.

[12] South Dakota Department of Transportation, "South Dakota Winter Highway Maintenance Plan 2020-2021," South Dakota Department of Transportation, Pierre, SD, 2020.

[13] The Salt Institute, "The Salt Storage Handbook," Alexandria, VA, 2006.

[14] Larson, R. M. and K. D. Smith., "Evaluation of alternative dowel bar materials and coatings. No. FHWA/OH-2011/19," Ohio. Dept. of Transportation. Office of Research and Development, 2011.

[15] Porter, M. L. and R. L. Braun, "Preliminary Assessment of the Potential Use of Alternative Materials for Concrete Highway Pavement Joints: Final Report.," Iowa State University, Ames, IA., 1997.

[16] ASTM, International, "ASTM C1152: Standard Test Method for Acid-Soluble Chloride in Mortar and Concrete," West Conshohocken, PA, 2020.

[17] Abo-Qudais, S. A. and I. L. Al-Qadi, "Dowel bars corrosion in concrete pavement," Canadian journal of civil engineering, vol. 27, no. 6, pp. 1240-1247, 2000.

[18] Mancio, M., C. Carlos Jr, J. Zhang, J. T. Harvey, P. J. Monteiro and A. Ali, "Laboratory Evaluation of Corrosion Resistance of Steel Dowels in Concrete Pavement," Institute of Transportation Studies, UC Davis, 2005.

[19] ASTM, International, "ASTM C876: Standard Test Method for Corrosion Potentials of Uncoated Reinforcing Steel in Concrete," West Conshohoken, PA, 2022.

[20] Lee, S.-K., "Laboratory evaluation of corrosion resistance of various metallic dowel bars. No. FHWA-HRT-15-079," Federal Highway Administration. Office of Infrastructure Research and Development, 2018.

[21] Isaacs, H. S., "The behavior of resistive layers in the localized corrosion of stainless steel," Journal of the Electrochemical Society, vol. 120, no. 11, 1973.

[22] Frankel, G., "Pitting corrosion of metals: a review of the critical factors," Journal of the Electrochemical society, vol. 145, no. 6, 1998.

[23] Jafarzadeh, S., Z. Chen and F. Bobaru, "Computational modeling of pitting corrosion," Corrosion reviews, vol. 37, no. 5, pp. 419-439, 2019.

[24] Laycock, N. J., S. P. White, J. S. Noh, P. T. Wilson and R. C. Newman, "Perforated covers for propagating pits," Journal of the electrochemical society, vol. 145, no. 1, 1998.

[25] Laycock, N. J. and S. P. White, "Computer simulation of single pit propagation in stainless steel under potentiostatic control," Journal of the Electrochemical Society, vol. 148, no. 7, 2001.

[26] Vagbharathi, A. S. and S. Gopalakrishnan, " An extended finite-element model coupled with level set method for analysis of growth of corrosion pits in metallic structures," Proceedings of the Royal Society A: Mathematical, Physical and Engineering Sciences, vol. 470, 2014.

[27] Duddu, R., "Numerical modeling of corrosion pit propagation using the combined extended finite element and level set method," Computational Mechanics, vol. 54, no. 3, pp. 613-627, 2014.

[28] Krouse, D., N. Laycock and C. Padovani, "Modelling pitting corrosion of stainless steel in atmospheric exposures to chloride containing environments," Corrosion engineering, science and technology, vol. 49, no. 6, pp. 521-528, 2014.

[29] Scheiner, S. and C. Hellmich, "Stable pitting corrosion of stainless steel as diffusion-controlled dissolution process with a sharp moving electrode boundary," Corrosion science, vol. 49, no. 2, pp. 319-346, 2007.

[30] Scheiner, S. and C. Hellmich, "Finite volume model for diffusion-and activation-controlled pitting corrosion of stainless steel," Computer Methods in Applied Mechanics and Engineering , vol. 198, no. 37, pp. 2898-2910, 2009.

[31] Silling, S. A., "Reformulation of elasticity theory for discontinuities and long-range forces," Journal of the Mechanics and Physics of Solids, vol. 48, no. 1, pp. 175-209, 2000.

[32] Chen, Z. and F. Bobaru, "Peridynamic modeling of pitting corrosion damage," Journal of the Mechanics and Physics of Solids, vol. 78, pp. 352-381, 2015.

[33] Jafarzadeh, S., Z. Chen, J. Zhao and F. Bobaru, "Pitting, lacy covers, and pit merger in stainless steel: 3D peridynamic models," Corrosion Science, vol. 150, pp. 17-31, 2019.

[34] De Meo, D. and E. Oterkus, "Finite element implementation of a peridynamic pitting corrosion damage model," Ocean Engineering, vol. 135, pp. 76-83, 2017.

[35] Mai, W., S. Soghrati and R. G. Buchheit, "A phase field model for simulating the pitting corrosion," Corrosion Science, vol. 110, pp. 157-166, 2016.

[36] Chadwick, A. F., S. J. A., E. R. A., S. Du and K. Thornton, "Numerical modeling of localized corrosion using phase-field and smoothed boundary methods," Journal of The Electrochemical Society, vol. 165, no. 10, 2018.

[37] Nguyen, T. T., J. Bolivar, Y. Shi, J. Réthoré, A. King, M. Fregonese, J. Adrien, Jean-Yves Buffiere and M.-C. Baietto, "A phase field method for modeling anodic dissolution induced stress corrosion crack propagation," Corrosion Science , vol. 132, pp. 146-160, 2018.

[38] Tsuyuki, C., A. Yamanaka and Y. Ogimoto, "Phase-field modeling for pH-dependent general and pitting corrosion of iron," Scientific reports, vol. 8, no. 1, 2018.

[39] Ricker, R., "CORR-DATA," National Institute of Standardsa nd Technology, 1997. [Online]. Available: https://researchdata.nist.gov/Materials-Physical-Properties/CORR-DATA-Database/akgq-mt9y.

[40] Thomas, E., K. Lucas and M. Peterson, "Effects of electrolytic chlorination on marine materials," Materials Performance, vol. 27, no. 7, 1988.

[41] Agarwal, D., "Duplex Allow 255 in Marine Applications," Materials Performance, vol. 27, no. 10, 1988.

[42] Wilhelm, S., " Galvanic Corrosion in Oil and Gas Production: Part 1 - Laboratory Studies," Corrosion, vol. 48, no. 8, pp. 691-703, 1992.

[43] Davison, R. and J. D. Redmond, "Practical Guide to Using Duplex Stainless Steels," Materials Performance, pp. 57-62, 1990.

[44] Polar, J. P., "A guide to corrosion resistance: 304, 316, 317, "20", Ni-o-nel," Climax Molybdenum Company, New York City, 1961.

[45] Thyssen Edelstahlwerke AG, "Chemical resistance of the stainless REMANIT steels," Krefeld, Germany.

[46] Malik, A., P. M. Kutty, N. A. Siddiqi, I. N. Andijani and S. Ahmed, "The influence of pH and chloride concentration on the corrosion behaviour of AISI 316L steel in aqueous solutions," Corrosion Science, vol. 33, no. 11, pp. 1809-1827, 1992.

[47] Wang, J., C. Su and Z. Szklarska-Smialowska, "Effects of Cl Concentration and Temperature on Pitting of AISI 304 Stainless Steel," Corrosion, vol. 44, no. 10, pp. 732-737, 1988.

[48] A. A775/A775M-19, "Standard Specification for Epoxy-Coated Steel Reinforcing Bars," ASTM International, West Conshohocken, PA, 2019.

[49] A. A934/A934M-19, "Standard Specification for Epoxy-Coated Prefabricated Steel Reinforcing Bars," ASTM International, West Conshohocken, PA, 2019.

[50] ASTM International, ASTM A653: Standard Specification for Steel Sheet, Zinc-Coated (Galvanized) or Zinc-Iron Alloy-Coated (Galvannealed) by the Hot-Dip Process, West Conshohocken, PA, 2022.

[51] ASTM International, ASTM B69: Standard Specification for Rolled Zinc, West Conshohocken, PA, 2021.

[52] ACPA, Standard Method of test for Dowel Bars for Concrete Street and Highway Pavement, 2021.

[53] AASHTO, T 106M Compressive Strength of Hydraulic Cement Mortar, American Association of State Highway and Transportation Officials, 2019.

[54] ASTM, G14 Standard Test Method for Impact Resistance of Pipeline Coatings, West Conshohocken, PA, 2018.

[55] Pennsylvannia Department of Transportation (PennDOT), Publication 408, Harrisburg, 2020.

[56] ASTM International, ASTM C192: Standard Practice for Making and Curing Concrete Test Specimens in the Laboratory, West Conshohocken, PA, 2015.

[57] ASTM International, ASTM C143: Standard Test Method for Slump Of Portland Cement Concrete, West Conshohocken, PA, 2017.

[58] ASTM International, ASTM C231: Standard Test Method for Air Content of Freshly Mixed Concrete by the Pressure Method, West Conshohocken, PA, 2010.

[59] Donnelly, C. and J. Vandenbossche, "A Novel Small-Scale Beam Test for Evaluating Long-Term Dowel Performance," ACI Structural Journal, vol. In Review, 2024.

[60] [Online]. Available: https://www.faro.com/en/Products/Hardware/Quantum-FaroArms. [Accessed 12 4 2025].

[61] A. T. 253-02, "Standard Method of Test for Coated Dowel Bars," American Association of State Highway and Transportation Officials, Washington, DC, 2020.

[62] AASHTO, "M 254 Standard Specification for Corrosion-Resistant Coated Dowel Bars," American Association of State Highway and Transportation Officials, 2019.

[63] A. M. 5. 53M, "Standard Specification for Deformed and Plain Carbon-Steel Bars for Concrete Reinforcement," American Association of State Highway and Transportation Officials, Washington, DC, 1995.

[64] A. M. 5. 54-22, "Standard Specification for Welded Deformed Steel Bar Mats for Concrete Reinforcement," American Association of State Highway and Transportation Officials, Washington, DC, 2022.

[65] [Online]. Available: https://imagej.net/ij/], . [Accessed 16 04 2025].

[66] Yeomans, S. R., "Performance of black, galvanized and epoxy-coated reinforcng steel in chloride-contaminated concrete.," Corrosion, vol. 50, no. 1, pp. 72-81, 1994.

[67] Tonini, D. E. and S. W. Dean, Chloride corrosion of steel in concrete, ASTM STP 629, Philadephia, PA, USA: American Society for Testing and Materials, 1976.

[68] Yeomans, S. R., "Galvanized Steel Reinforcement in Concrete," Elsevier, 2004.

[69] Friberg, B., "Design of Dowels in Transverse Joints of Concrete Pavements," vol. 64, no. 9, 1938.

[70] Applied Research Associates (ARA), Inc., "Guide for Mechanistic-Empirical Design of New and Rehabilitated Pavement Structures Final Report NCHRP 1-37A," Transportation Research Board of the National Academies, Washington, D.C., 2004.

[71] Sachs, S., J. M. Vandenbossche and M. B. Snyder, "Calibration of National Rigid Pavement Performance Models for the Pavement Mechanistic–Empirical Design Guide," Transportation Research Record, vol. 2524, no. 1, pp. 59-67, 2015.

[72] Sachs, S., J. Vandenbossche and M. Snyder, "Developing Recalibrated Concrete Pavement Performance Models for the Mechanistic-Empirical Pavement Design Guide," NCHRP Project 20-07, Task 327, Transportation Research Board, 2014.

[73] [Online]. Available: https://www.google.com/maps. [Accessed 12 4 2025].

[74] Mallela, J., L. T. Glover, M. I. Darter, H. V. Quintus, A. Gotlif, M. Stanley and S. Sadasivam, "Guidelines for Implementing NCHRP 1-37A M-E Design Procedures in Ohio: Volume 1—Summary of Findings, Implementation Plan, and Next Steps," FHWA Report No. FHWA/OJ-2009/9A, 2009.

APPENDIX A: Dowel Coating Testing

Appendix A contains the summarized results and photos from the dowel coating testing. The results from abrasion resistance testing are presented in Table A1. Table A2 contains the results from impact resistance testing and includes the rating of damage assigned to each dowel based on visual inspection after each test. Finally, a photo library is included. Photographs of each dowel tested is shown in Figure A1 – Figure A84. The photographs document the conditions before and after abrasion resistance testing, before and after and impact resistance testing, and after placement of the holidays.

Table A1. Results from coating abrasion testing.

				Diameters (in)			Avg. coating loss (in)		
Specimen ID	Test date	Test time		D1	D2	D3	D1	D2	D3
C2G1	6/18/2024	8:20 AM	Before	1.294	1.295	1.294	0.001	0.002	0.001
			After	1.293	1.293	1.293			
C2G2	6/18/2024	8:20 AM	Before	1.293	1.294	1.293	0.000	0.000	0.000
			After	1.293	1.294	1.293			
C2G3	6/18/2024	8:20 AM	Before	1.293	1.293	1.293	0.000	0.000	0.000
			After	1.293	1.294	1.293			
C2P1	6/17/2024	5:31 PM	Before	1.293	1.294	1.293	0.001	0.001	0.000
			After	1.293	1.293	1.293			
C2P2	6/17/2024	5:31 PM	Before	1.293	1.294	1.293	0.002	0.001	0.003
			After	1.293	1.294	1.293			
C2P3	6/17/2024	5:31 PM	Before	1.293	1.293	1.293	0.001	0.001	0.000
			After	1.293	1.294	1.293			
G1P1	6/14/2024	9:36 AM	Before	1.334	1.335	1.336	0.001	0.001	0.001
			After	1.333	1.334	1.335			
G1P2	6/14/2024	9:36 AM	Before	1.333	1.336	1.336	0.001	0.002	0.001
			After	1.333	1.333	1.335			
G1P3	5/3/2024	10:47 AM	Before	1.338	1.337	1.338	0.000	0.000	0.002
			After	1.338	1.337	1.336			
SN1	6/17/2024	9:12 AM	Before	1.906	1.905	1.904	0.001	0.002	0.001
			After	1.904	1.904	1.904			
SN2	6/18/2024	9:12 AM	Before	1.906	1.906	1.904	0.002	0.000	0.000
			After	1.905	1.906	1.904			
SN3	5/2/2024	9:35 AM	Before	1.907	1.908	1.908	0.001	0.003	0.002
			After	1.907	1.906	1.906			
G1G1	4/30/2024	12:50 PM	Before	1.334	1.338	1.341	0.004	0.000	0.002
			After	1.330	1.337	1.340			
G1G2	6/17/2024	12:32 PM	Before	1.340	1.338	1.344	0.000	0.001	0.004
			After	1.340	1.337	1.340			
G1G3	4/30/2024	12:50 PM	Before	1.343	1.340	1.338	0.006	0.008	0.003
			After	1.337	1.332	1.334			
C4Z1	6/14/2024	12:17 PM	Before	1.698	1.699	1.699	0.000	0.000	0.000
			After	1.698	1.699	1.699			
C4Z2	6/14/2024	12:19 PM	Before	1.700	1.700	1.700	0.008	0.001	0.001
			After	1.692	1.700	1.699			
C4Z3	6/17/2024	2:05 PM	Before	1.699	1.699	1.700	0.000	0.000	0.000
			After	1.699	1.699	1.700			
FN1	5/1/2024	12:35 PM	Before	1.252	1.252	1.252	0.000	0.000	0.000
			After	1.252	1.252	1.252			
FN2	5/1/2024	12:35 PM	Before	1.252	1.252	1.252	0.000	0.000	0.000
			After	1.252	1.252	1.252			
FN3	5/1/2024	12:35 PM	Before	1.252	1.252	1.252	0.000	0.000	0.000
			After	1.252	1.252	1.252			

Table A2. Results from coating impact testing.

Specimen	Test date	Test time		Diameters (in) Impact 1	Impact 2	Impact 3	Impact rating* Impact 1	Impact 2	Impact 3
C2G1	6/17/2024	3:52 PM	Before	1.289	1.290	1.291	IL, CL	IL, CL	IL, CL
			After	1.286	1.289	1.289			
C2G2	6/17/2024	3:10 PM	Before	1.290	1.290	1.290	IL, CL	IL, CL	IL, CL
			After	1.289	1.286	1.288			
C2G3	6/17/2024	3:45 PM	Before	1.264	1.267	1.267	IL, CL	IL, CL	IL, CL
			After	1.264	1.266	1.267			
C2P1	6/17/2024	2:50 PM	Before	1.268	1.270	1.272	IL, CL	**IH, CH**	IL, CL
			After	1.265	1.266	1.268			
C2P2	6/17/2024	2:54 PM	Before	1.274	1.277	1.276	**IH, CH**	IL, CL	IL, CL
			After	1.271	1.275	1.275			
C2P3	6/17/2024	2:47 PM	Before	1.268	1.271	1.277	IL, CL	**IH, CH**	**IH, CH**
			After	1.267	1.269	1.265			
G1P1	6/13/2024	4:36 PM	Before	1.344	1.342	1.347	IL, CL	IL, CL	IL, CL
			After	1.339	1.338	1.343			
G1P2	6/13/2024	4:40 PM	Before	1.341	1.340	1.343	IL, CL	IL, CL	IL, CL
			After	1.340	1.338	1.343			
G1P3	4/30/2024	4:50 PM	Before	1.337	1.338	1.337	IL, CL	IL, CL	IL, CL
			After	1.330	1.335	1.333			
SN1	6/14/2024	1:50 PM	Before	1.904	1.904	1.904	IL, CL	IL, CL	IL, CL
			After	1.902	1.902	1.902			
SN2	6/14/2024	1:46 PM	Before	1.902	1.902	1.904	IL, CL	IL, CL	IL, CL
			After	1.902	1.902	1.903			
SN3	5/1/2024	11:50 AM	Before	1.909	1.909	1.910	IL, CL	IL, CL	IL, CL
			After	1.907	1.908	1.906			
G1G1	4/30/2024	12:00 PM	Before	1.341	1.341	1.340	IL, CL	IL, CL	IL, CL
			After	1.329	1.337	1.333			
G1G2	6/14/2024	2:38 PM	Before	1.341	1.341	1.342	IL, CL	IL, CL	IL, CL
			After	1.340	1.337	1.338			
G1G3	4/30/2024	12:00 PM	Before	1.339	1.334	1.334	IL, CL	IL, CL	IL, CL
			After	1.329	1.329	1.331			
C4Z1	6/14/2024	12:17 PM	Before	1.700	1.700	1.700	IL, CL	IL, CL	IL, CL
			After	1.699	1.699	1.693			
C4Z2	6/14/2024	12:19 PM	Before	1.705	1.705	1.704	IL, CL	IL, CL	IL, CL
			After	1.701	1.701	1.702			
C4Z3	6/14/2024	2:21 PM	Before	1.701	1.702	1.701	IL, CL	IL, CL	IL, CL
			After	1.700	1.699	1.699			
FN1	5/1/2024	10:50 AM	Before	1.252	1.252	1.252	IL, CL	IL, CL	IL, CL
			After	1.250	1.251	1.250			
FN2	5/1/2024	10:45 AM	Before	1.252	1.251	1.251	IL, CL	IL, CL	IL, CL
			After	1.251	1.251	1.251			
FN3	5/1/2024	10:40 AM	Before	1.253	1.253	1.252	IL, CL	IL, CL	IL, CL
			After	1.251	1.250	1.251			

*The impact ratings highlighted in bold correspond to those with significant damage or substantial coating defects. Impact abbreviations: IL – low impact damage, IH – high impact damage, CL – low coating damage, CH, high coating damage.

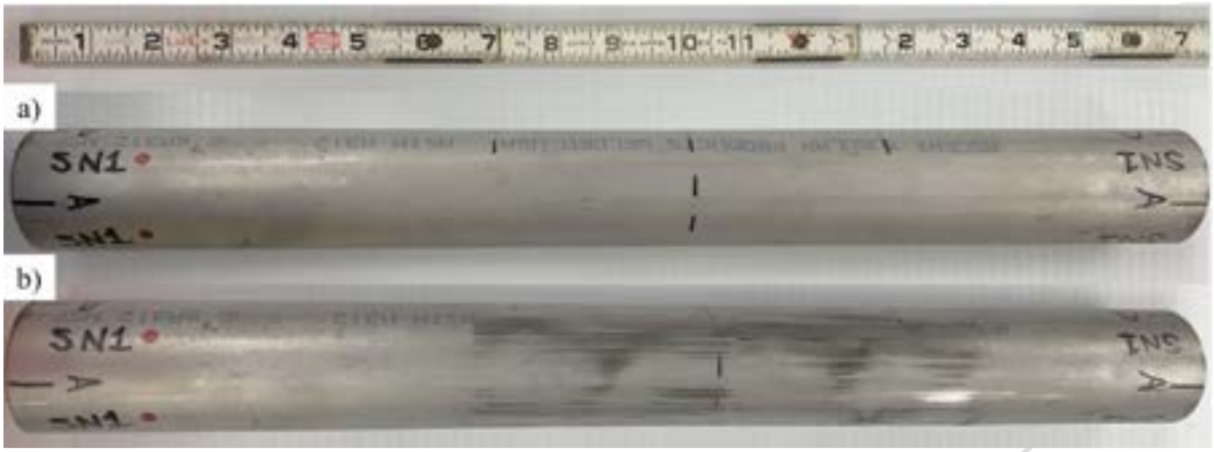

Figure A1. Sample SN1 side A a) before and b) after abrasion.

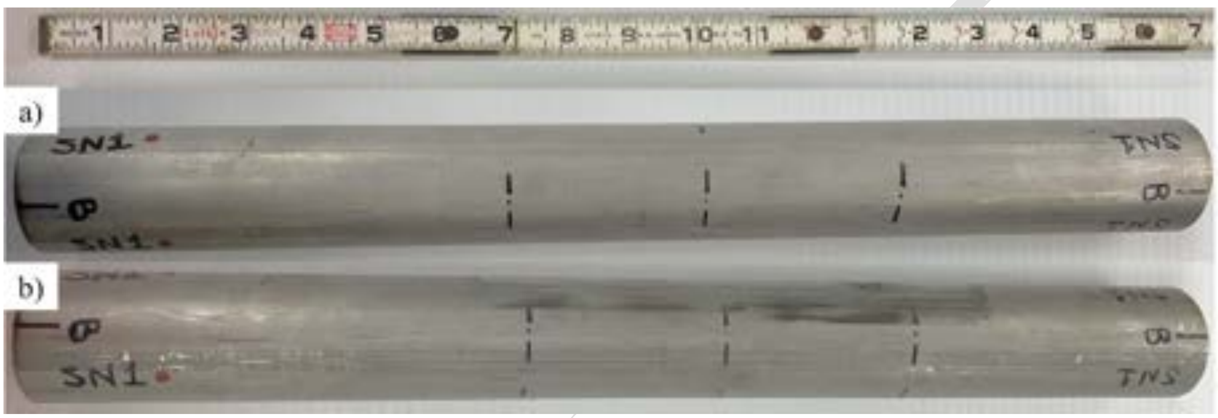

Figure A2. Sample SN1 side B a) before and b) after impact.

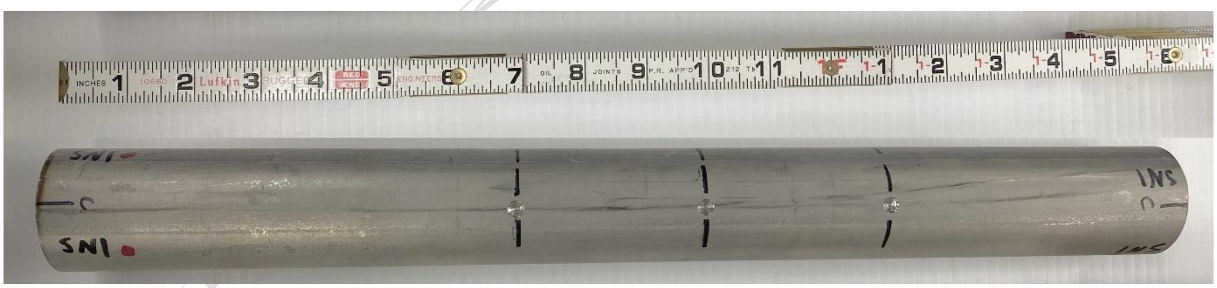

Figure A3. Sample SN1 side C with holidays.

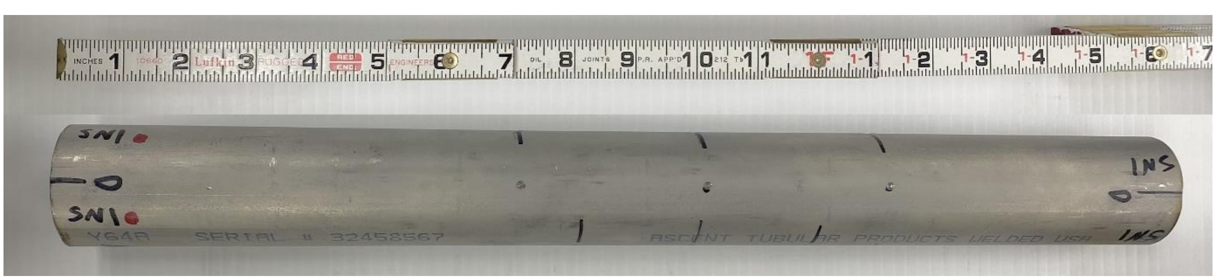

Figure A4. Sample SN1 side D with holidays.

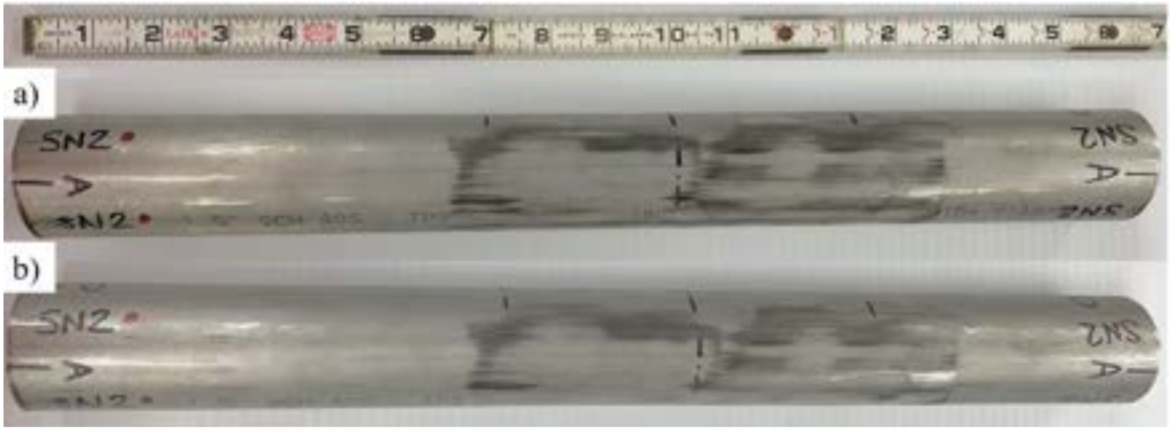

Figure A5. Sample SN2 side A a) before and b) after abrasion.

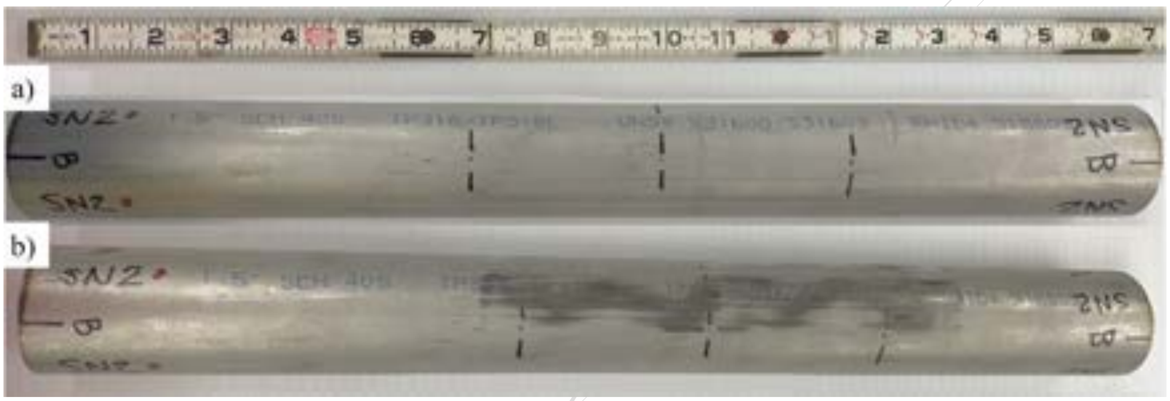

Figure A6. Sample SN2 side B a) before and b) after impact.

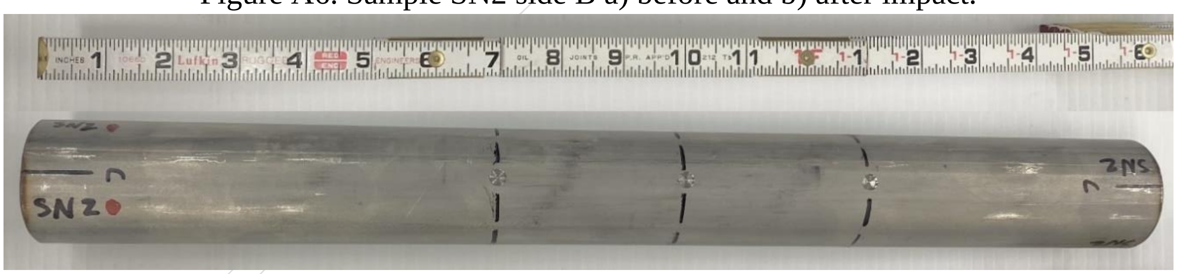

Figure A7. Sample SN2 side C with holidays.

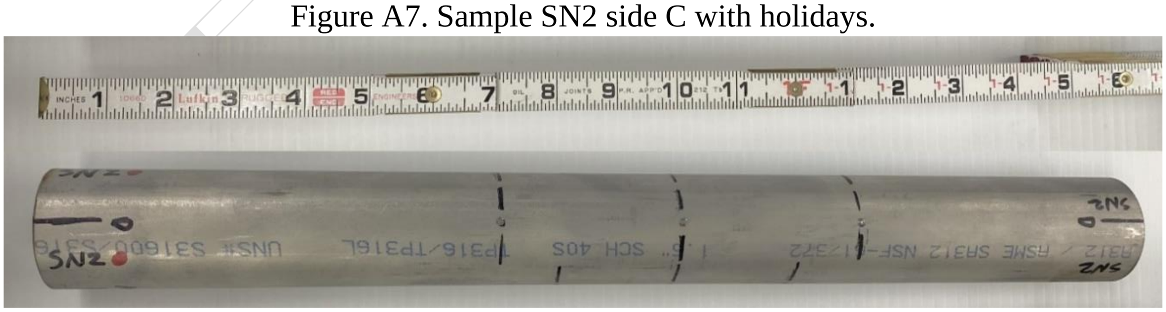

Figure A8. Sample SN2 side D with holidays.

Figure A8. Sample SN3 side A a) before and b) after abrasion.

Figure A9. Sample SN3 side B a) before and b) after impact.

Figure A10. Sample SN3 side C with holidays.

Figure A11. Sample SN3 side D with holidays.

Figure A12. Sample G1P1 side A a) before and b) after abrasion.

Figure A13. Sample G1P1 side B a) before and b) after impact.

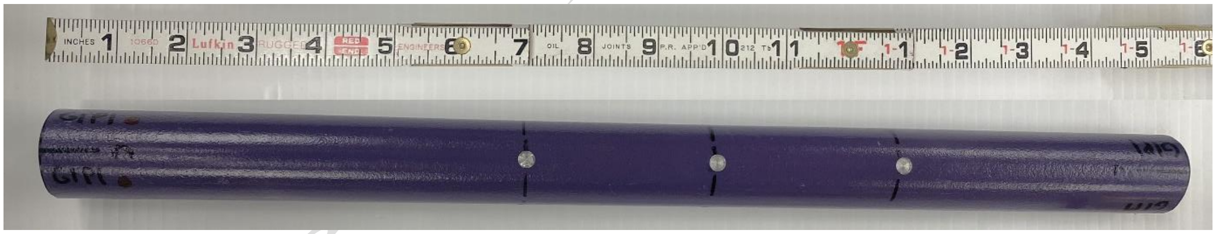

Figure A14. Sample G1P1 side C with holidays.

Figure A15. Sample G1P1 side D with holidays.

Figure A16. Sample G1P2 side A a) before and b) after abrasion.

Figure A17. Sample G1P2 side B a) before and b) after impact.

Figure A18. Sample G1P2 side C with holidays.

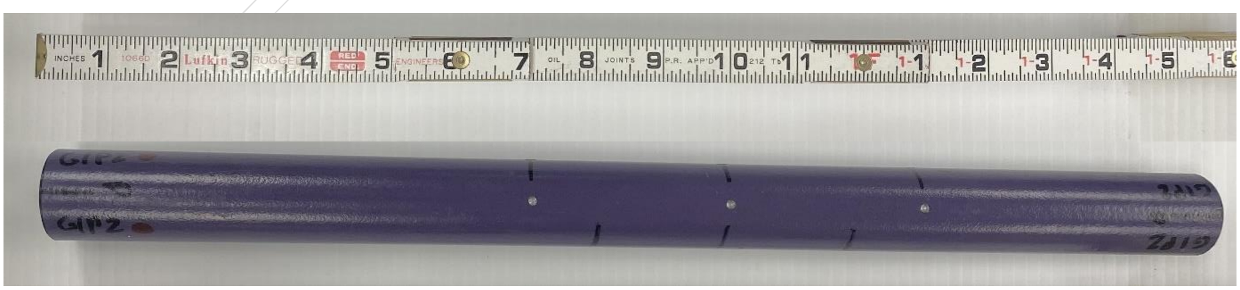

Figure A19. Sample G1P2 side D with holidays.

Figure A20. Sample G1P3 side A a) before and b) after abrasion.

Figure A21. Sample G1P3 side B a) before and b) after impact.

Figure A22. Sample G1P3 side C with holidays.

Figure A23. Sample G1P3 side D with holidays.

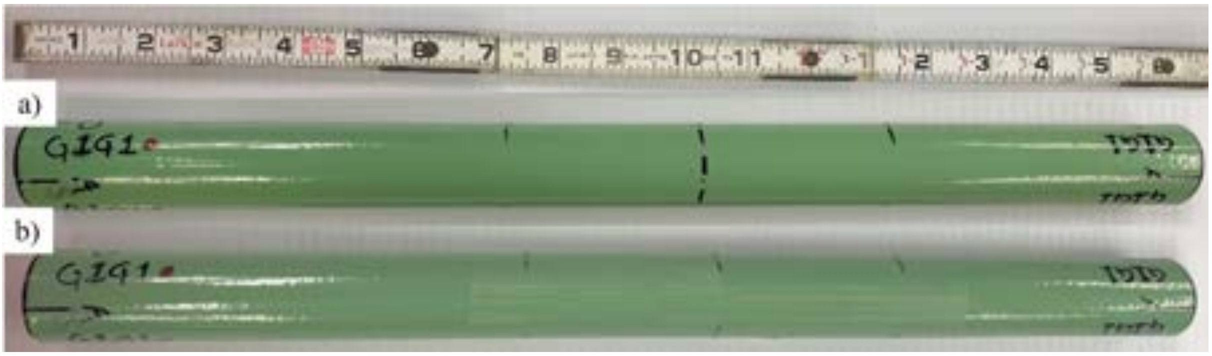

Figure A24. Sample G1G1 side A a) before and b) after abrasion.

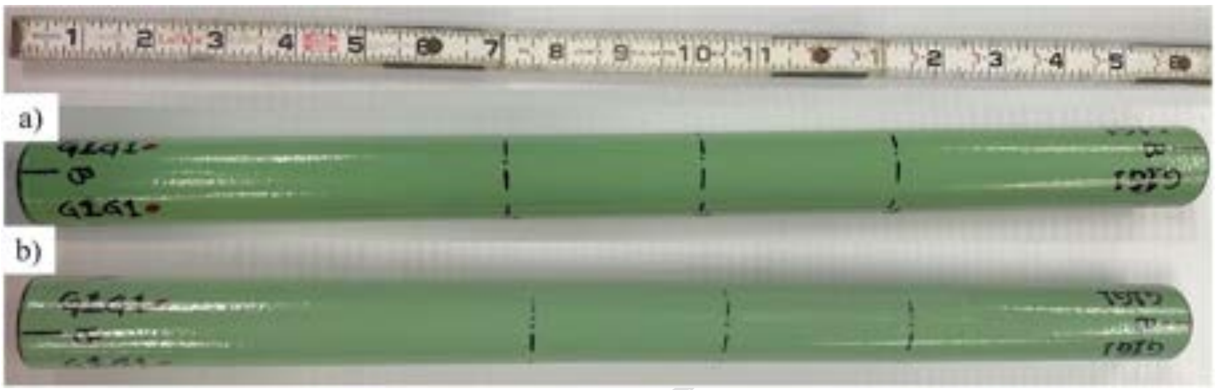

Figure A25. Sample G1G1 side B a) before and b) after impact.

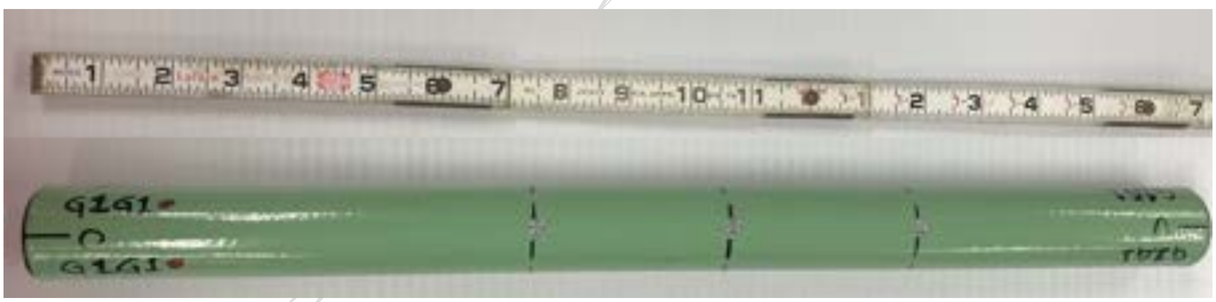

Figure A26. Sample G1G1 side C with holidays.

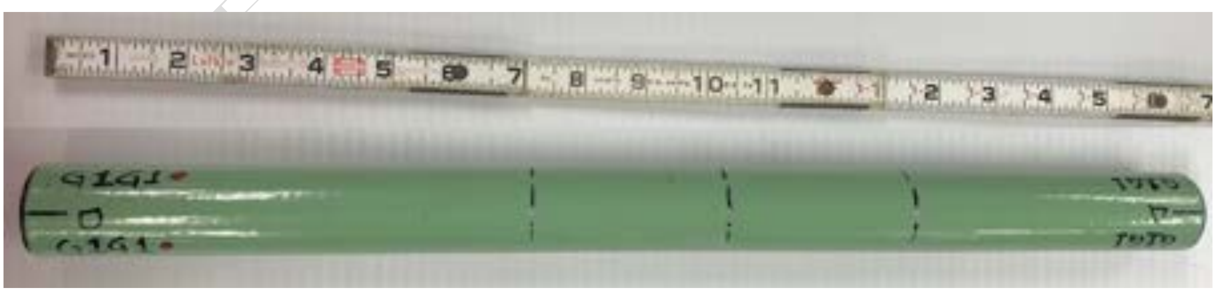

Figure A27. Sample G1G1 side D with holidays.

Figure A28. Sample G1G2 side A a) before and b) after abrasion.

Figure A29. Sample G1G2 side B a) before and b) after impact.

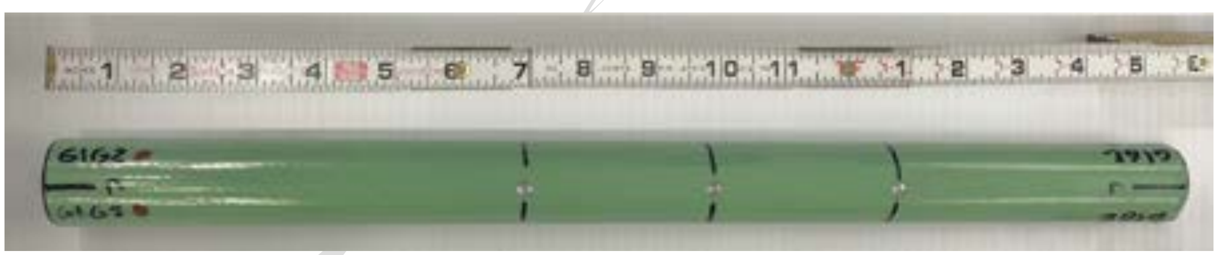

Figure A30. Sample G1G2 side C with holidays.

Figure A31. Sample G1G2 side D with holidays.

Figure A32. Sample G1G3 side A a) before and b) after abrasion.

Figure A33. Sample G1G3 side B a) before and b) after impact.

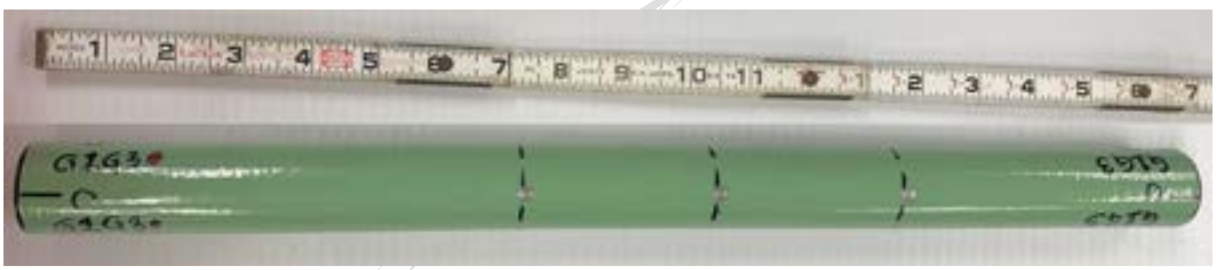

Figure A34. Sample G1G3 side C with holidays.

Figure A35. Sample G1G3 side D with holidays.

Figure A36. Sample FN1 side A a) before and b) after abrasion.

Figure A37. Sample FN1 side B a) before and b) after impact.

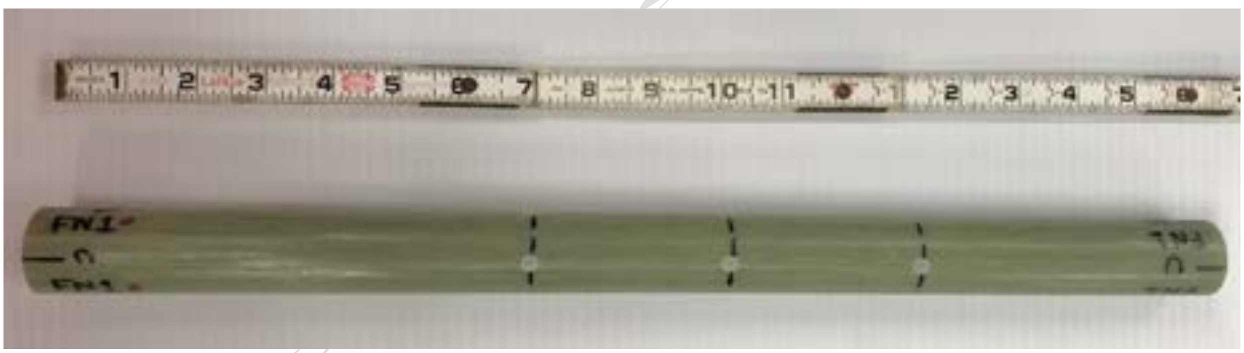

Figure A38. Sample FN1 side C with holidays.

Figure A39. Sample FN1 side D with holidays.

Figure A40. Sample FN2 side A a) before and b) after abrasion.

Figure A41. Sample FN2 side B a) before and b) after impact.

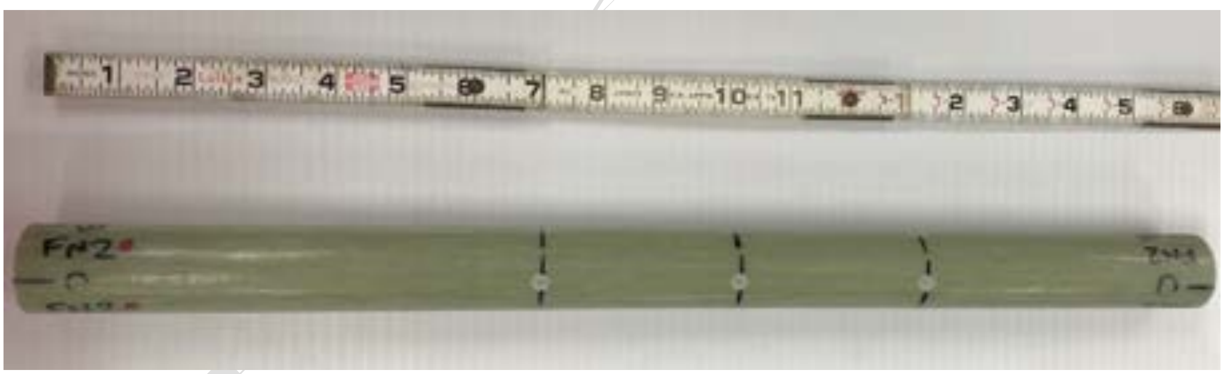

Figure A42. Sample FN2 side C with holidays.

Figure A43. Sample FN2 side D with holidays.

Figure A44. Sample FN3 side A a) before and b) after abrasion.

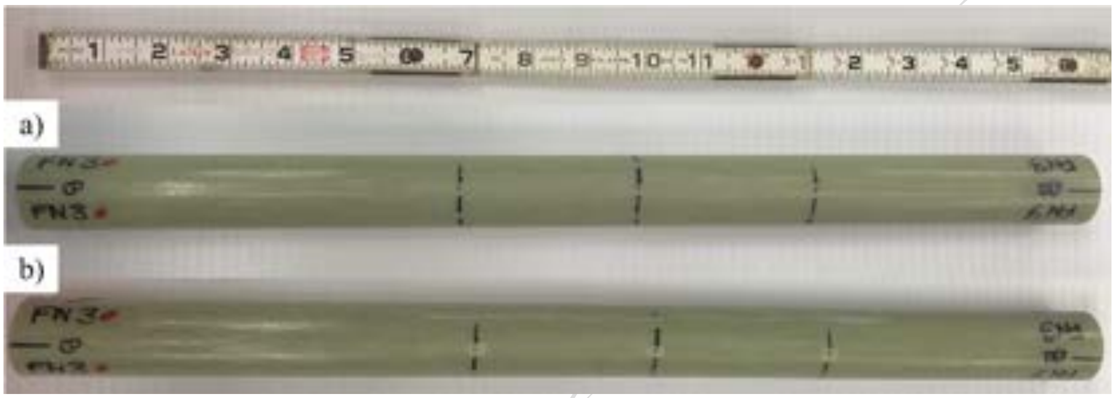

Figure A45. Sample FN3 side B a) before and b) after impact.

Figure A46. Sample FN3 side C with holidays.

Figure A47. Sample FN3 side D with holidays.

Figure A48. Sample C4Z1 side A a) before and b) after abrasion.

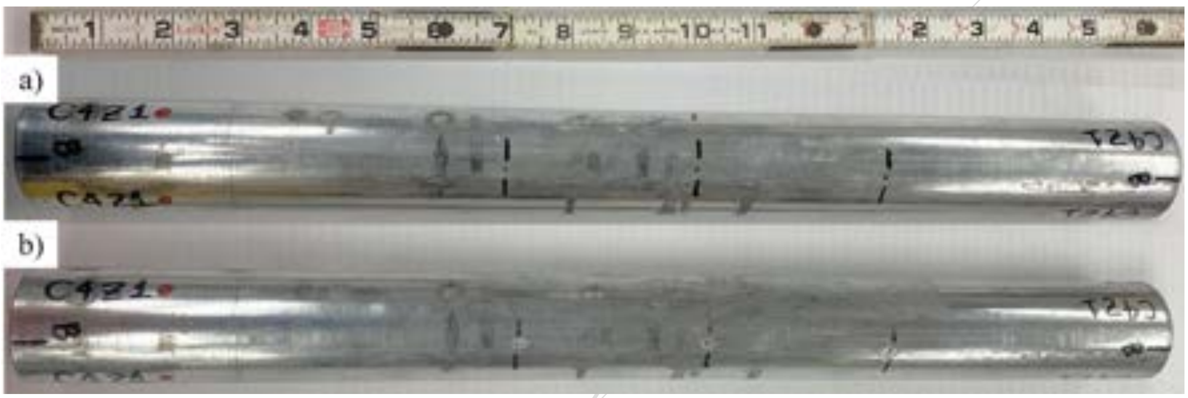

Figure A49. Sample C4Z1 side B a) before and b) after impact.

Figure A50. Sample C4Z1 side C with holidays.

Figure A51. Sample C4Z1 side D with holidays.

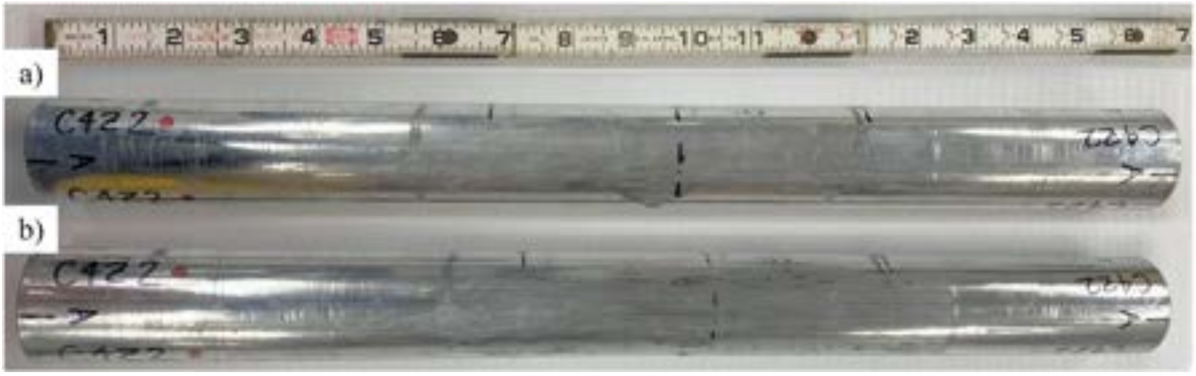

Figure A52. Sample C4Z2 side A a) before and b) after abrasion.

Figure A53. Sample C4Z2 side B a) before and b) after impact.

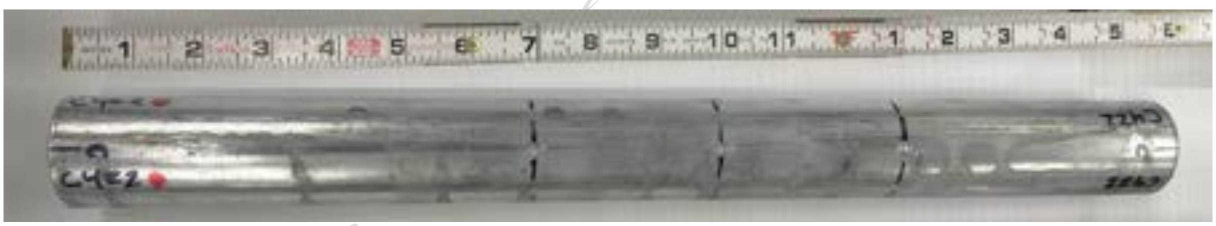

Figure A54. Sample C4Z2 side C with holidays.

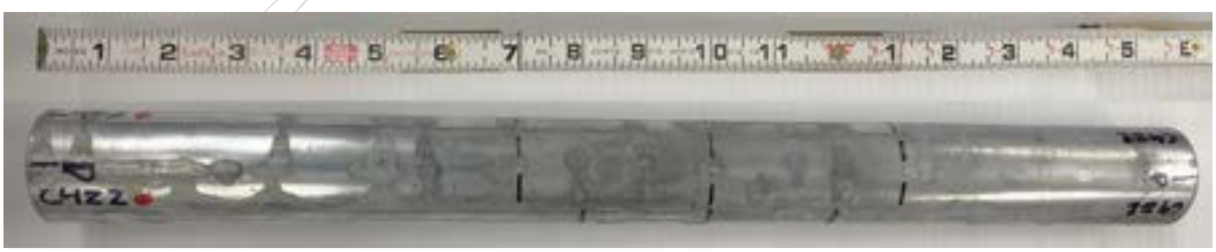

Figure A55. Sample C4Z2 side D with holidays.

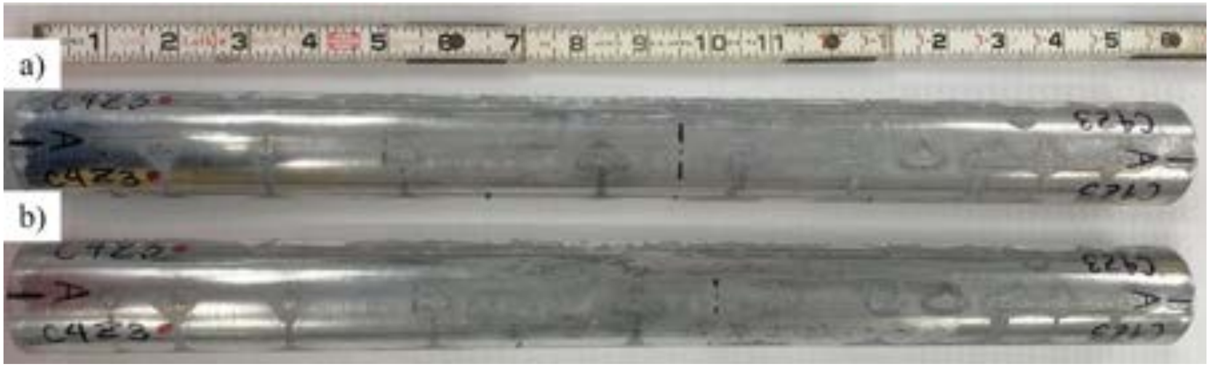

Figure A56. Sample C4Z3 side A a) before and b) after abrasion.

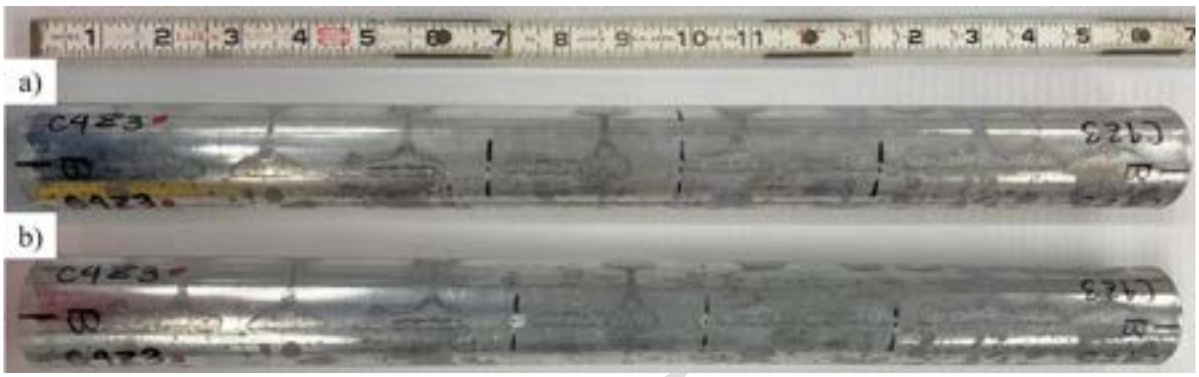

Figure A57. Sample C4Z3 side B a) before and b) after impact.

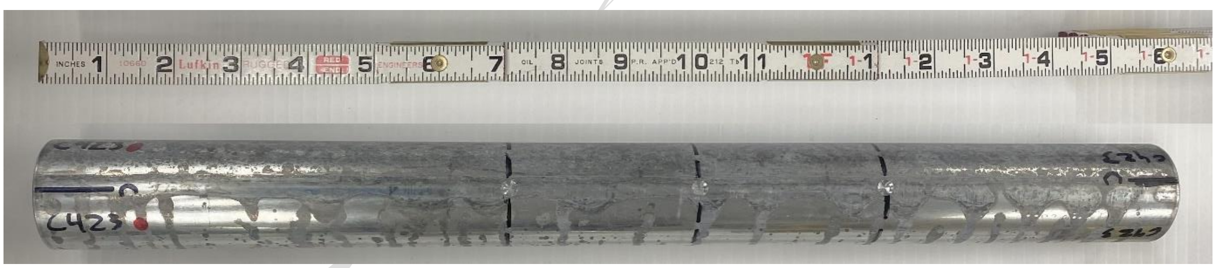

Figure A58. Sample C4Z3 side C with holidays.

Figure A59. Sample C4Z3 side D with holidays.

Figure A60. Sample C2P1 side A a) before and b) after abrasion.

Figure A61. Sample C2P1 side B a) before and b) after impact.

Figure A62. Sample C2P1 side C with holidays.

Figure A63. Sample C2P1 side D with holidays.

Figure A64. Sample C2P2 side A a) before and b) after abrasion.

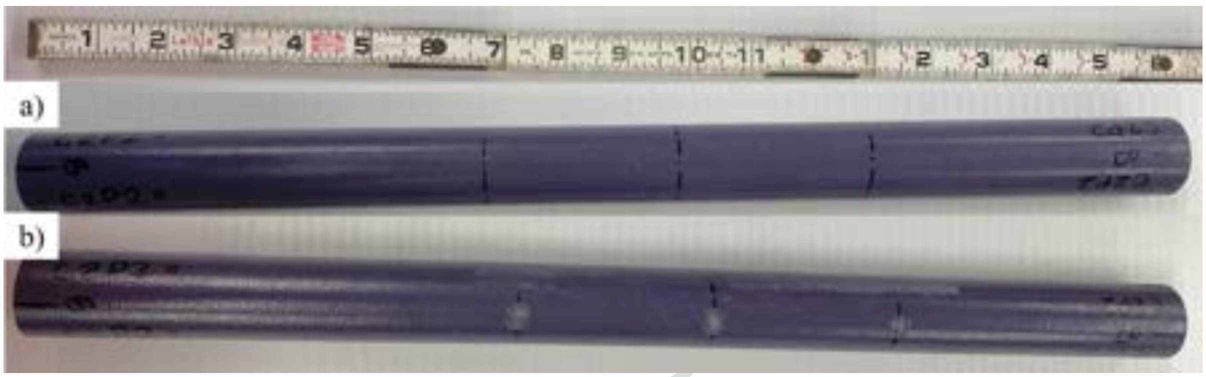

Figure A65. Sample C2P2 side B a) before and b) after impact.

Figure A66. Sample C2P2 side C with holidays.

Figure A67. Sample C2P2 side D with holidays.

Figure A68. Sample C2P3 side A a) before and b) after abrasion.

Figure A69. Sample C2P3 side B a) before and b) after impact.

Figure A70. Sample C2P3 side C with holidays.

Figure A71. Sample C2P3 side D with holidays.

Figure A72. Sample C2G1 side A a) before and b) after abrasion.

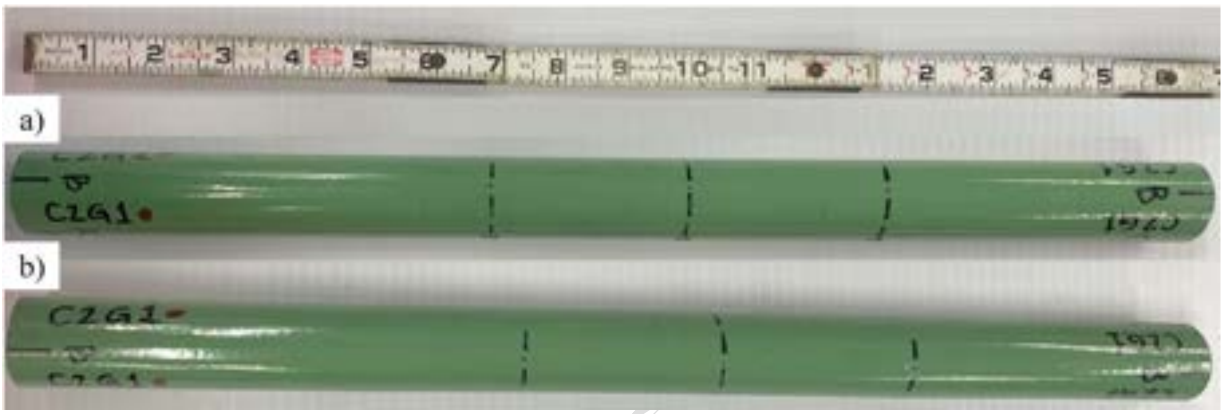

Figure A73. Sample C2G1 side B a) before and b) after impact.

Figure A74. Sample C2G1 side C with holidays.

Figure A75. Sample C2G1 side D with holidays.

Figure A76. Sample C2G2 side A a) before and b) after abrasion.

Figure A77. Sample C2G2 side B a) before and b) after impact.

Figure A78. Sample C2G2 side C with holidays.

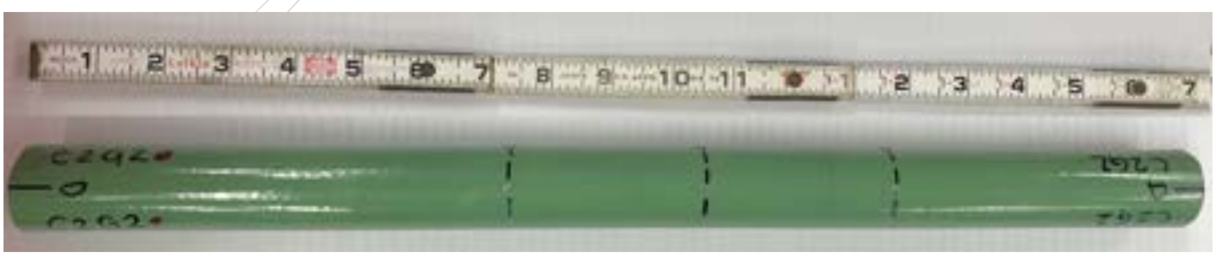

Figure A79. Sample C2G2 side D with holidays.

Figure A80. Sample C2G3 side A a) before and b) after abrasion.

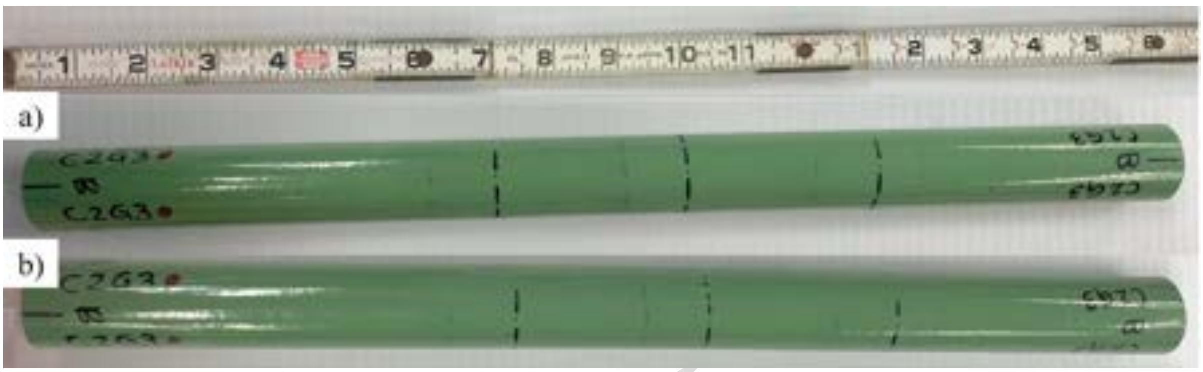

Figure A81. Sample C2G3 side B a) before and b) after impact.

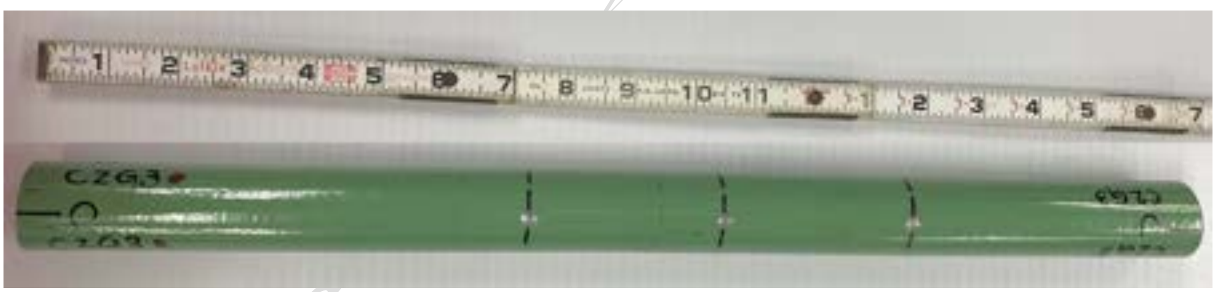

Figure A82. Sample C2G3 side C with holidays.

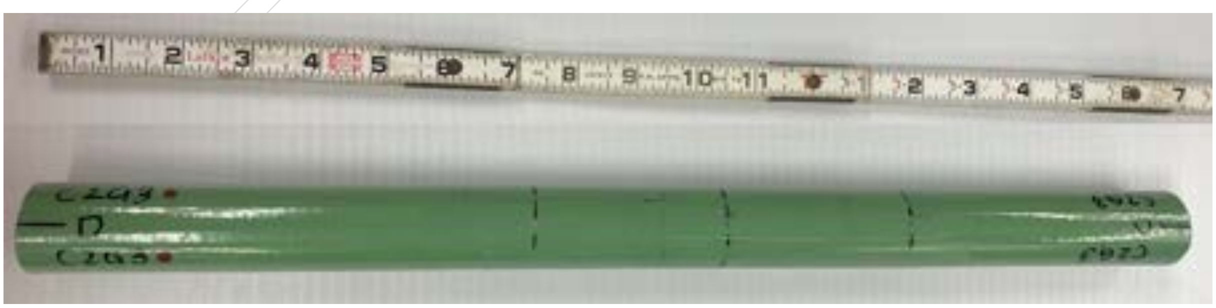

Figure A83. Sample C2G3 side D with holidays.

APPENDIX B: Simulated Joint Opening and Closing and Vehicle Loads

Appendix B contains plots and tables summarizing the results from the accelerated corrosion testing performed. Details pertaining to the test setup and procedure are found in Chapter 4.0. Simulated joint opening/closing test results are summarized in Table B1 and Table B2. Depth of spalling measured for each specimen are summarized in Table B3. Simulated vehicle testing results are summarized in Table B4.

Table B1. Maximum force recorded during joint opening and closing.

Specimen	Maximum force (lb)													
	24-Hour	Week 0	Week 2	Week 4	Week 6	Week 8	Week 12	Week 14	Week 16	Week 18	Week 22	Week 24	Week 30	Week 36
	Exposure Duration (Weeks)	0	2	4	6	8	12	12	12	12	14	16	22	28
C2G1	2085	2908	6504	5422	4731	7189	5348	4812	4626	2078	1747	1807	2146	2164
C2G2	1869	2688	5657	4880	4295	6739	4716	4891	4128	1767	1565	1624	1929	2444
C2G3	162	179	388	419	403	481	407	398	417	177	136	145	197	227
C2P1	591	478	669	656	538	574	500	483	449	246	212	191	212	225
C2P2	971	657	866	938	971	772	883	811	787	338	351	310	295	289
C2P3	730	594	690	647	602	538	610	555	648	219	220	195	242	326
C4Z1	257	238	851	1547	2126	1999	3566	4549	5467	4924	5044	5549	6485	7190
C4Z2	66	113	263	588	967	857	1976	2700	3319	2970	4114	4346	4363	5211
C4Z3	143	213	579	1135	1542	2388	3001	2632	2826	5344	4934	4478	5147	5133
FN1	1267	1088	946	703	1744	978	1513	1815	1592	2616	1805	2062	2113	3912
FN2	905	310	484	305	526	501	1101	895	876	662	702	784	1026	1600
FN3	466	172	173	92	186	146	165	203	189	287	449	538	655	1005
G1G1	2216	894	2646	2108	3678	2580	2705	2389	1929	841	764	662	622	584
G1G2	4910	3614	3172	2366	2215	2582	2326	2311	2762	3231	2007	2010	4526	2072
G1G3	1665	1502	4680	4587	3634	3487	3473	3171	2837	792	802	805	582	657
G1P1	3977	3712	6140	5314	4677	5162	4409	3695	3348	1254	1008	955	1100	939
G1P2	2933	2819	4892	4618	4243	5078	4240	3918	3757	1706	1008	1380	1266	1097
G1P3	3181	2152	3596	3265	3142	3093	2692	2798	2463	1131	878	865	683	689
SN1	42	15	133	79	56	43	-	-	-	-	-	-	-	-
SN2	4833	3351	9650	9616	6714	7705	9329	6977	5996	379	1008	214	205	196
SN3	2509	2467	9275	7168	6529	5802	4574	3601	3256	725	426	1097	1988	2305

*Specimen SN1 was not tested after Week 8 due to low forces.
Shaded cells represent joint closing, and all others represent joint opening.

Table B2. Maximum shear stress during simulated joint opening and closing.

Specimen	Diameter (in)	Embedded area (in^2)	Maximum shear stress (psi)													
			24-Hour	Week 0	Week 2	Week 4	Week 6	Week 8	Week 12	Week 14	Week 16	Week 18	Week 22	Week 24	Week 30	Week 36
			Exposure Week (Duration)	0	2	4	6	8	12	12	12	12	14	16	22	28
C2G1	1.250	35.3	59.0	82.3	184.0	153.4	133.8	203.4	151.3	136.2	130.9	58.8	49.4	51.1	60.7	61.2
C2G2	1.250	35.3	52.9	76.1	160.1	138.1	121.5	190.7	133.4	138.4	116.8	50.0	44.3	45.9	54.6	69.2
C2G3	1.250	35.3	4.6	5.1	11.0	11.8	11.4	13.6	11.5	11.3	11.8	5.0	3.8	4.1	5.6	6.4
C2P1	1.250	35.3	16.7	13.5	18.9	18.6	15.2	16.3	14.2	13.7	12.7	6.9	6.0	5.4	6.0	6.4
C2P2	1.250	35.3	27.5	18.6	24.5	26.5	27.5	21.8	25.0	22.9	22.3	9.6	9.9	8.8	8.3	8.2
C2P3	1.250	35.3	20.7	16.8	19.5	18.3	17.0	15.2	17.3	15.7	18.3	6.2	6.2	5.5	6.9	9.2
C4Z1	1.700	48.1	5.4	5.0	17.7	32.2	44.2	41.6	74.2	94.6	113.7	102.4	104.9	115.4	134.9	149.6
C4Z2	1.700	48.1	1.4	2.4	5.5	12.2	20.1	17.8	41.1	56.2	69.1	61.8	85.6	90.4	90.8	108.4
C4Z3	1.700	48.1	3.0	4.4	12.1	23.6	32.1	49.7	62.4	54.8	58.8	111.2	102.7	93.2	107.1	106.8
FN1	1.250	35.3	35.8	30.8	26.8	19.9	49.3	27.7	42.8	51.3	45.1	74.0	51.1	58.3	59.8	110.7
FN2	1.250	35.3	25.6	8.8	13.7	8.6	14.9	14.2	31.2	25.3	24.8	18.7	19.9	22.2	29.0	45.3
FN3	1.250	35.3	13.2	4.9	4.9	2.6	5.3	4.1	4.7	5.7	5.4	8.1	12.7	15.2	18.5	28.4
G1G1	1.375	38.9	57.0	23.0	68.1	54.2	94.6	66.4	69.6	61.5	49.6	21.6	19.7	17.0	16.0	15.0
G1G2	1.375	38.9	126.3	93.0	81.6	60.9	57.0	66.4	59.8	59.4	71.0	83.1	51.6	51.7	116.4	53.3
G1G3	1.375	38.9	42.8	38.6	120.4	118.0	93.5	89.7	89.3	81.6	73.0	20.4	20.6	20.7	15.0	16.9
G1P1	1.375	38.9	102.3	95.5	157.9	136.7	120.3	132.8	113.4	95.0	86.1	32.3	25.9	24.6	28.3	24.1
G1P2	1.375	38.9	75.4	72.5	125.8	118.8	109.1	130.6	109.1	100.8	96.7	43.9	25.9	35.5	32.6	28.2
G1P3	1.375	38.9	81.8	55.3	92.5	84.0	80.8	79.6	69.3	72.0	63.3	29.1	22.6	22.2	17.6	17.7
SN1	1.900	53.7	0.8	0.3	2.5	1.5	1.0	0.8	-	-	-	-	-	-	-	-
SN2	1.900	53.7	90.0	62.4	179.6	179.0	125.0	143.4	173.7	129.9	111.6	7.0	18.8	4.0	3.8	3.6
SN3	1.900	53.7	46.7	45.9	172.7	133.4	121.5	108.0	85.1	67.0	60.6	13.5	7.9	20.4	37.0	42.9

*Specimen SN1 was not tested after Week 8 due to low forces.
Shaded cells represent joint closing, and all others represent joint opening.

Table B3. Depth of spalling (in) measured for each specimen

	Spall depth adjacent to the dowel (in)				
	Abrasion	Impact	2% holiday	1% holiday	Average spall depth (in)
C2G1	0.000	0.000	0.178	0.143	0.080
C2G2	0.000	0.000	0.129	0.111	0.060
C2G3	0.077	0.159	0.134	0.075	0.111
C2P1	0.000	0.000	0.000	0.000	0.000
C2P2	0.000	0.000	0.000	0.000	0.000
C2P3	0.000	0.202	0.096	0.000	0.074
C4Z1	0.494	0.172	0.288	0.111	0.266
C4Z2	0.302	0.176	0.430	0.317	0.306
C4Z3	0.430	0.349	0.287	0.490	0.389
FN1	0.000	0.000	0.000	0.000	0.000
FN2	0.000	0.092	0.063	0.000	0.039
FN3	0.000	0.000	0.091	0.000	0.023
G1G1	0.000	0.000	0.091	0.000	0.023
G1G2	0.000	0.000	0.215	0.106	0.080
G1G3	0.063	0.083	0.163	0.199	0.127
G1P1	0.000	0.072	0.000	0.000	0.018
G1P2	0.094	0.115	0.131	0.000	0.085
G1P3	0.000	0.134	0.225	0.000	0.090
SN1	0.000	0.060	0.000	0.164	0.056
SN2	0.330	0.060	0.000	0.131	0.115
SN3	0.000	0.060	0.000	0.164	0.056

Table B4. Summary of simulated vehicle testing.

	Max Deflection (in)				Dowel Bending (in/in)			
Specimen	**Week 0**	**Week 2**	**Week 4**	**Week 6**	**Week 0**	**Week 2**	**Week 4**	**Week 6**
C2G1	0.057	0.029	0.031	0.031	0.0080	-0.0009	0.0015	0.0035
C2G2	0.038	0.044	0.046	0.041	0.0044	0.0049	0.0024	0.0007
C2G3	0.047	0.031	0.032	0.027	0.0061	0.0037	0.0037	0.0034
C2P1	0.063	0.044	0.034	0.032	0.0083	0.0072	0.0040	0.0034
C2P2	0.048	0.031	0.034	0.031	0.0049	0.0022	0.0040	0.0043
C2P3	0.066	0.039	0.031	0.041	0.0087	0.0060	0.0028	0.0046
C4Z1	0.074	0.044	0.037	0.037	0.0060	0.0004	0.0012	0.0039
C4Z2	0.052	0.049	0.042	0.035	0.0053	0.0025	0.0032	0.0027
C4Z3	0.030	0.048	0.036	0.046	0.0015	0.0030	0.0031	0.0021
FN1	0.080	0.097	0.067	0.071	0.0086	0.0121	0.0098	0.0105
FN2	0.100	0.079	-0.065	0.076	0.0156	0.0115	0.0008	0.0112
FN3	0.100	0.115	0.079	0.070	0.0139	0.0159	0.0089	0.0104
G1G1	0.053	0.039	0.036	0.058	0.0071	0.0053	0.0039	0.0064
G1G2	0.051	0.037	0.036	0.040	0.0065	0.0050	0.0045	0.0046
G1G3	0.062	0.057	0.037	0.038	0.0077	0.0078	0.0047	0.0047
G1P1	0.081	0.041	0.035	0.033	0.0095	0.0052	0.0044	0.0041
G1P2	0.050	0.040	0.034	0.038	0.0067	0.0039	0.0044	0.0041
G1P3	0.064	0.039	0.062	0.037	0.0084	0.0081	0.0072	0.0048
SN1	0.027	0.031	0.024	0.026	0.0031	0.0026	0.0024	0.0024
SN2	0.028	0.018	0.018	0.020	0.0032	0.0019	0.0017	0.0023
SN3	-0.004	0.021	0.025	0.021	0.0030	0.0027	0.0036	0.0020

APPENDIX C: Corrosion Development in the 1% and 2% Areas Holiday

(INCLUDED AS A SEPARATE FILE TO HELP REDUCE THE FINAL REPORT FILE SIZE.)

Appendix C. Corrosion Development of the 1% and 2% Area Holidays.

Appendix C contains the measured corrosion surface area for the 2% area holidays, as well as a photo library of the 1% and 2% holidays for each dowel specimen from test Week 8 – 36. The corrosion surface area can be seen in Table C1. The following photos are provided for each tested specimen: First, an overall view of the dowel is shown for the side with the 2% area holiday is presented for test Week 8 – 36. This is followed by a closer view of the exposed 2% area holiday for test Week 8 – 36. Next, an overall view of the dowel is shown for the side with the 1% area holiday is presented for test Week 8 – 36, followed by a closer view of the exposed 1% area holiday for test Week 8 – 36. Finally, a 3D visualization of the corrosion progression of the exposed 2% area holiday from Week 0 – 36 is presented.

Table C1. Corrosion surface area for the holiday location furthest from the beam face (2% area holidays).

	Surface area of corrosion (in^2)									
Test Time	Week 0	Week 8	Week 12	Week 14	Week 16	Week 18	Week 22	Week 24	Week 30	Week 36
Exposure Duration (Weeks)	0	8	12	12	12	12	14	16	22	28
C2G1	0.00	0.09	0.18	0.21	0.24	0.23	0.24	0.23	0.29	0.33
C2G2	0.00	0.10	0.11	0.12	0.12	0.13	0.14	0.17	0.26	0.33
C2G3	0.00	0.15	0.15	0.20	0.22	0.23	0.24	0.28	0.34	0.42
C2P1	0.00	0.12	0.14	0.15	0.18	0.18	0.23	0.24	0.28	0.30
C2P2	0.00	0.08	0.15	0.16	0.17	0.22	0.29	0.30	0.34	0.36
C2P3	0.00	N/A	0.14	0.20	0.20	0.23	0.24	0.25	0.27	0.29
FN1	0.00	0.00	0.00	0.00	0.00	0.00	0.00	0.00	0.00	0.00
FN2	0.00	0.00	0.00	0.00	0.00	0.00	0.00	0.00	0.00	0.00
FN3	0.00	0.00	0.00	0.00	0.00	0.00	0.00	0.00	0.00	0.00
G1G1	0.00	0.05	0.05	0.06	0.06	0.08	0.09	0.10	0.13	0.14
G1G2	0.00	0.09	0.10	0.10	0.14	0.14	0.15	0.16	0.18	0.20
G1G3	0.00	0.06	0.07	0.09	0.08	0.09	0.09	0.09	0.09	0.09
G1P1	0.00	0.03	0.03	0.04	0.04	0.04	0.06	0.06	0.06	0.06
G1P2	0.00	0.02	0.02	0.02	0.03	0.03	0.05	0.05	0.05	0.06
G1P3	0.00	0.04	0.04	0.04	0.05	0.06	0.06	0.06	0.06	0.06
SN1	0.00	0.00	0.00	0.00	0.00	0.00	0.00	0.00	0.00	0.00
SN2	0.00	0.00	0.00	0.00	0.00	0.00	0.00	0.00	0.00	0.00
SN3	0.00	0.00	0.00	0.00	0.00	0.00	0.00	0.00	0.00	0.00

Week 8	Week 12	Week 14
		

Week 16	Week 18	Week 22
		

Figure C1. Side with 2% area holidays for G1G1.

Week 24	Week 30	Week 36
		

Figure C2. Side with 2% area holidays for G1G1 continued.

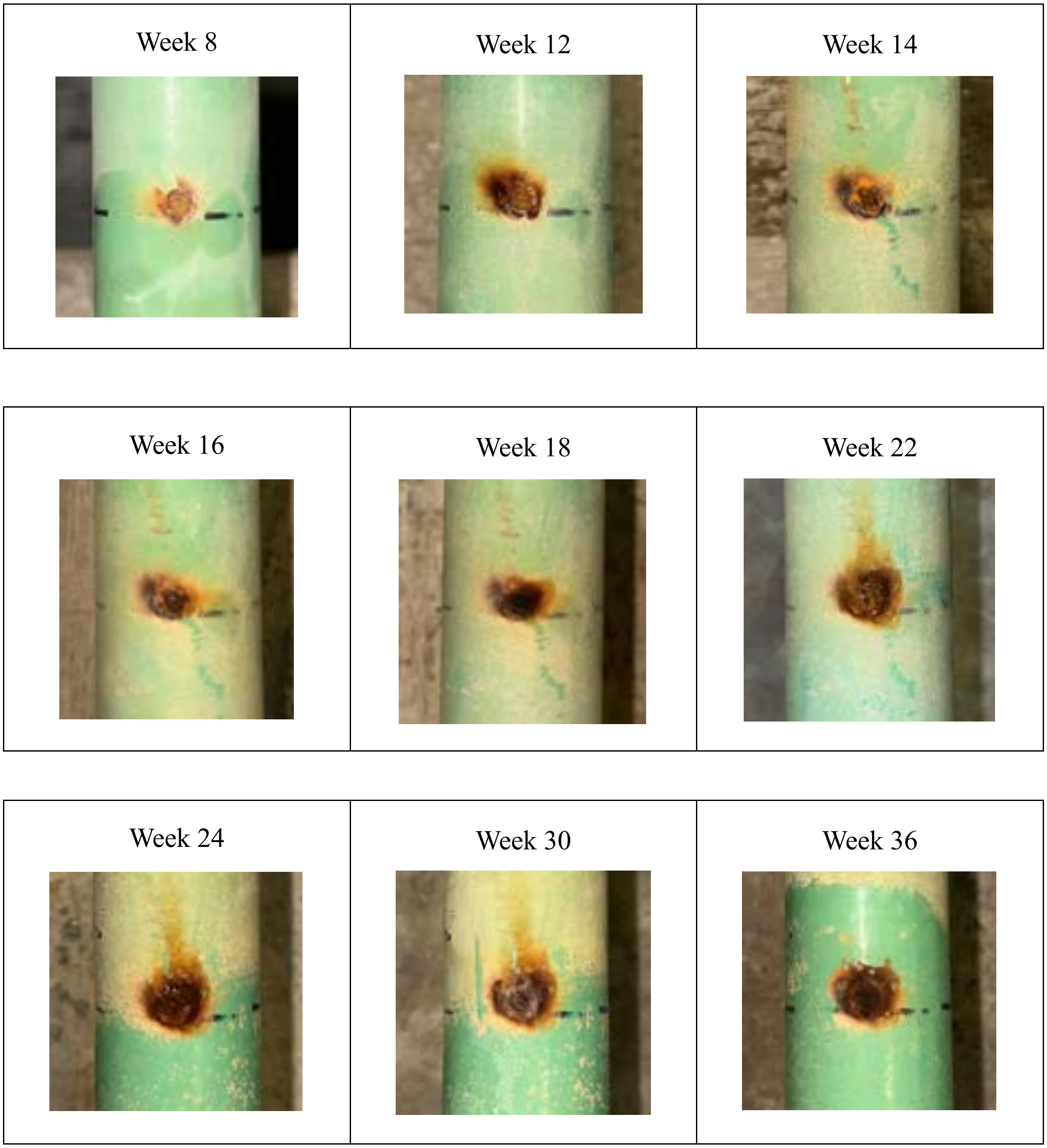

Figure C3. Exposed 2% area holiday for G1G1.

Week 8	Week 12	Week 14
		

Week 16	Week 18	Week 22
		

Figure C4. Side with 1% area holidays for G1G1.

Week 24	Week 30	Week 36
		

Figure C5. Side with 1% area holidays for G1G1 continued.

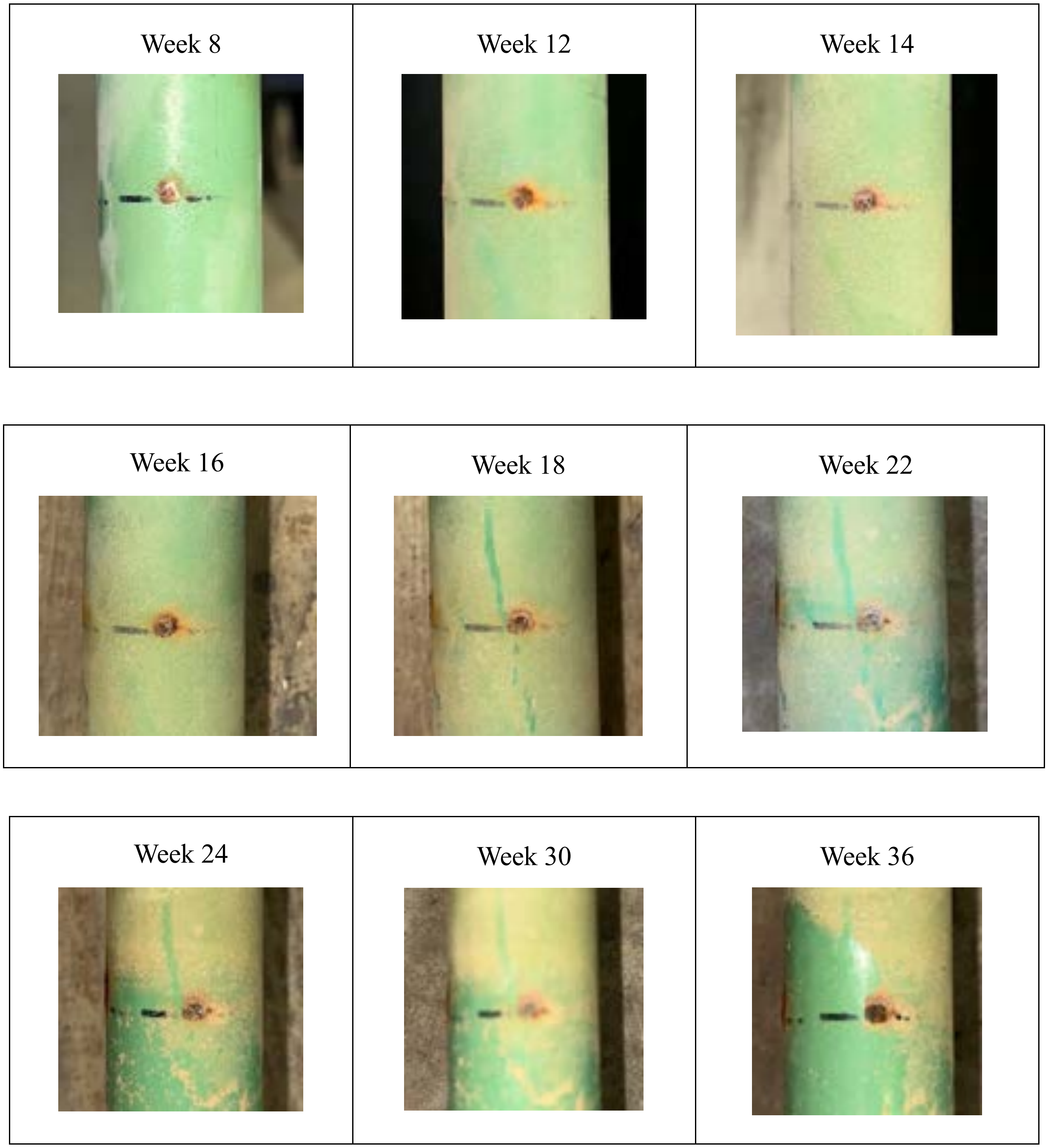

Figure C6. Exposed 1% area holiday for G1G1.

Week 0	Week 2	Week 4
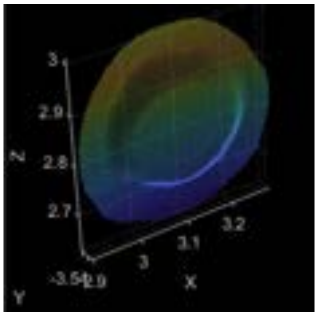	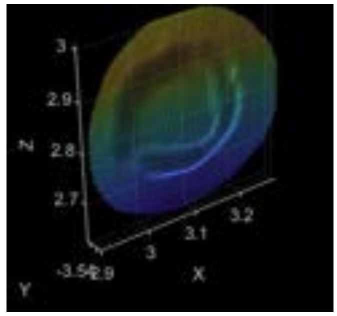	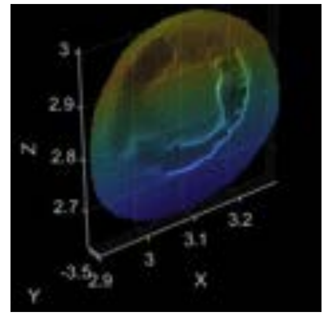
Week 6	Week 8	Week 12
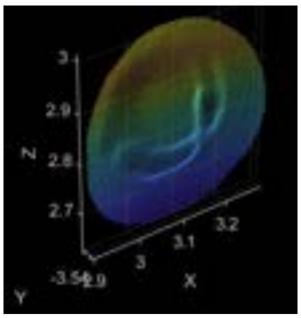	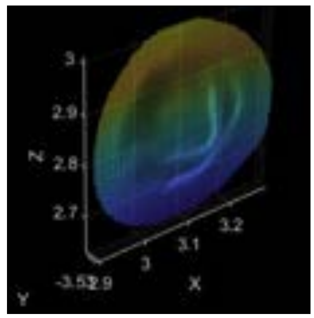	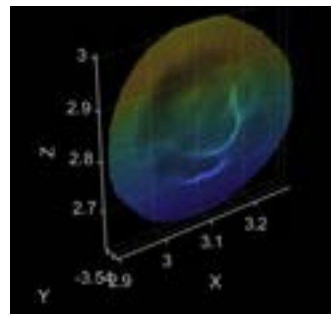
Week 14	Week 16	Week 18
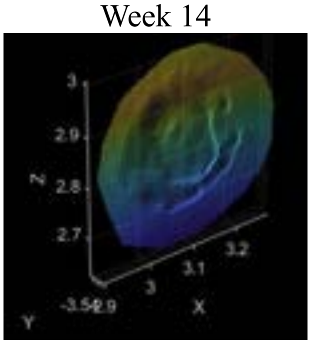	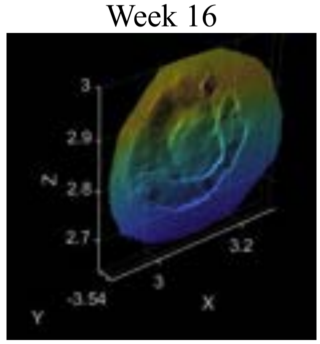	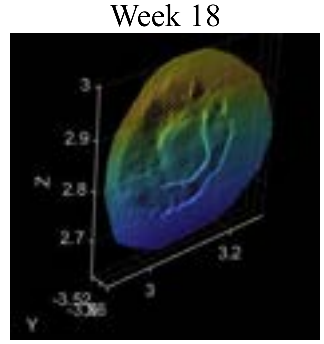

Figure C7. Change in meshed point cloud of exposed 2% area holiday data from Week 0 for G1G1.

Week 22

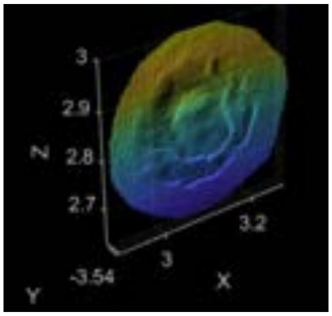

Week 24

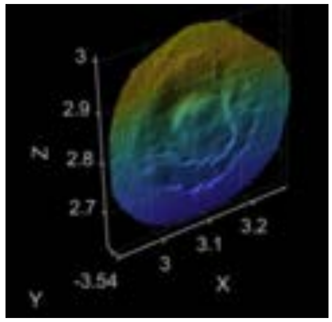

Week 30

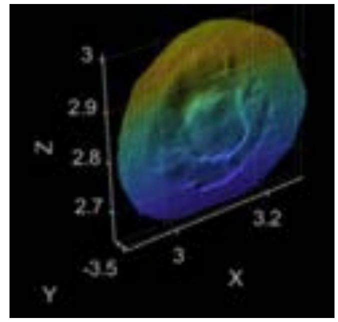

Week 36

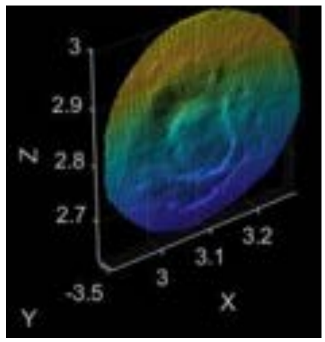

Figure C8 Change in meshed point cloud of exposed 2% area holiday data from Week 0 for G1G1 continued.

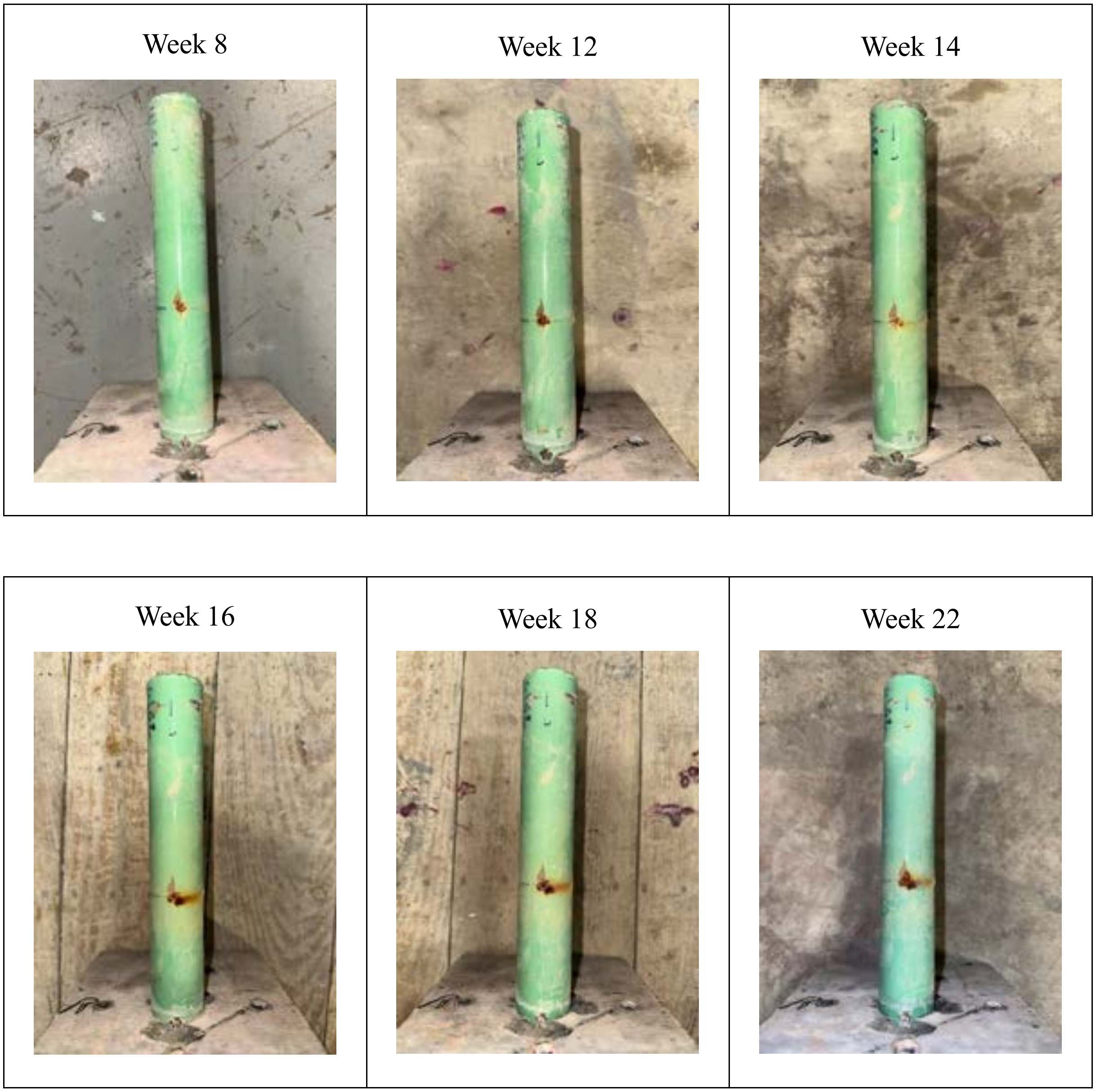

Figure C9. Side with 2% area holidays for G1G2.

Week 24	Week 30	Week 36
		

Figure C10. Side with 2% area holidays for G1G2 continued.

Figure C11. Exposed 2% area holiday for G1G2.

Week 8	Week 12	Week 14
		

Week 16	Week 18	Week 22
		

Figure C12. Side with 1% area holidays for G1G2.

Week 24	Week 30	Week 36
		

Figure C13. Side with 1% area holidays for G1G2 continued.

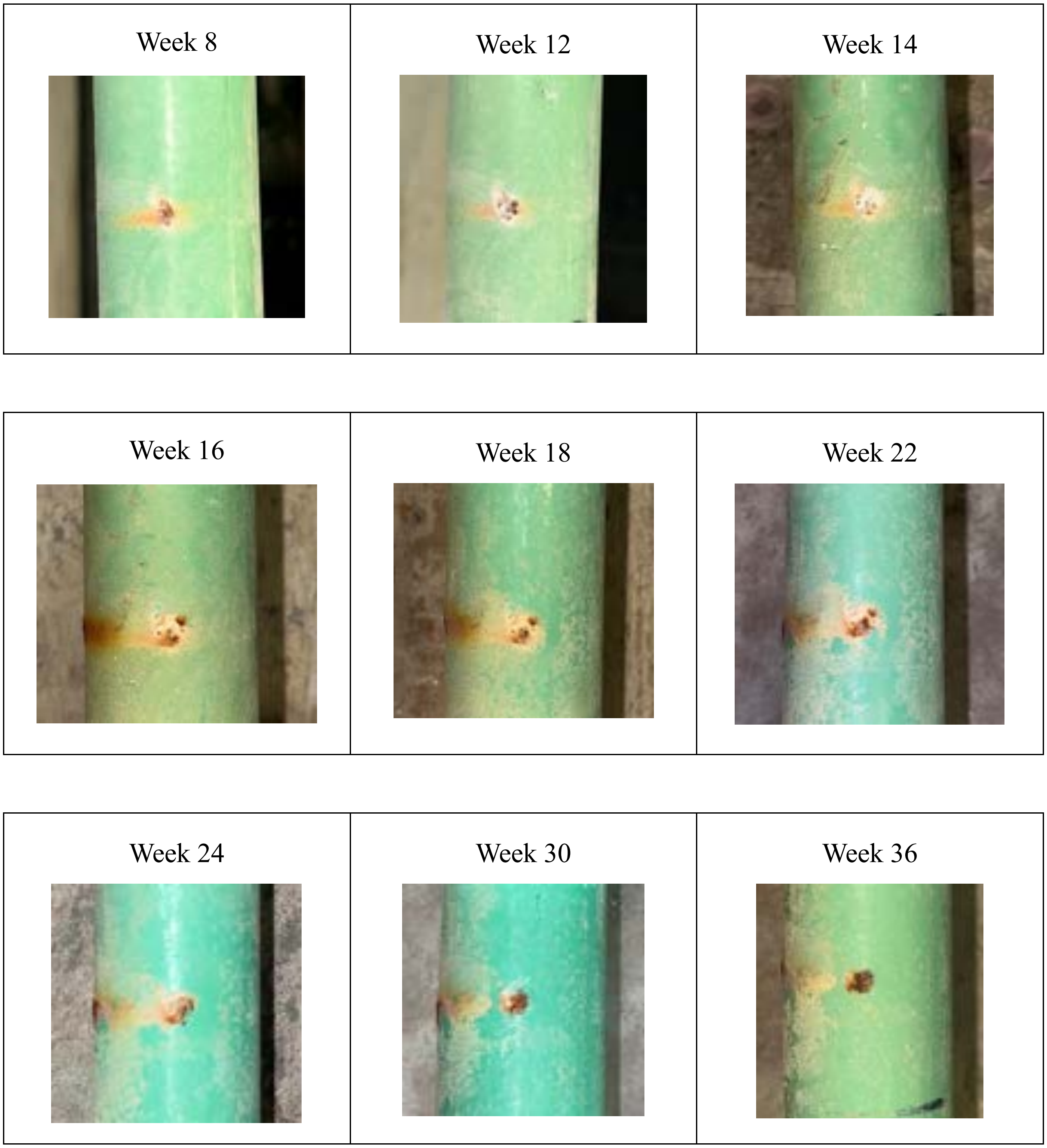

Figure C14. Exposed 1% area holiday for G1G2.

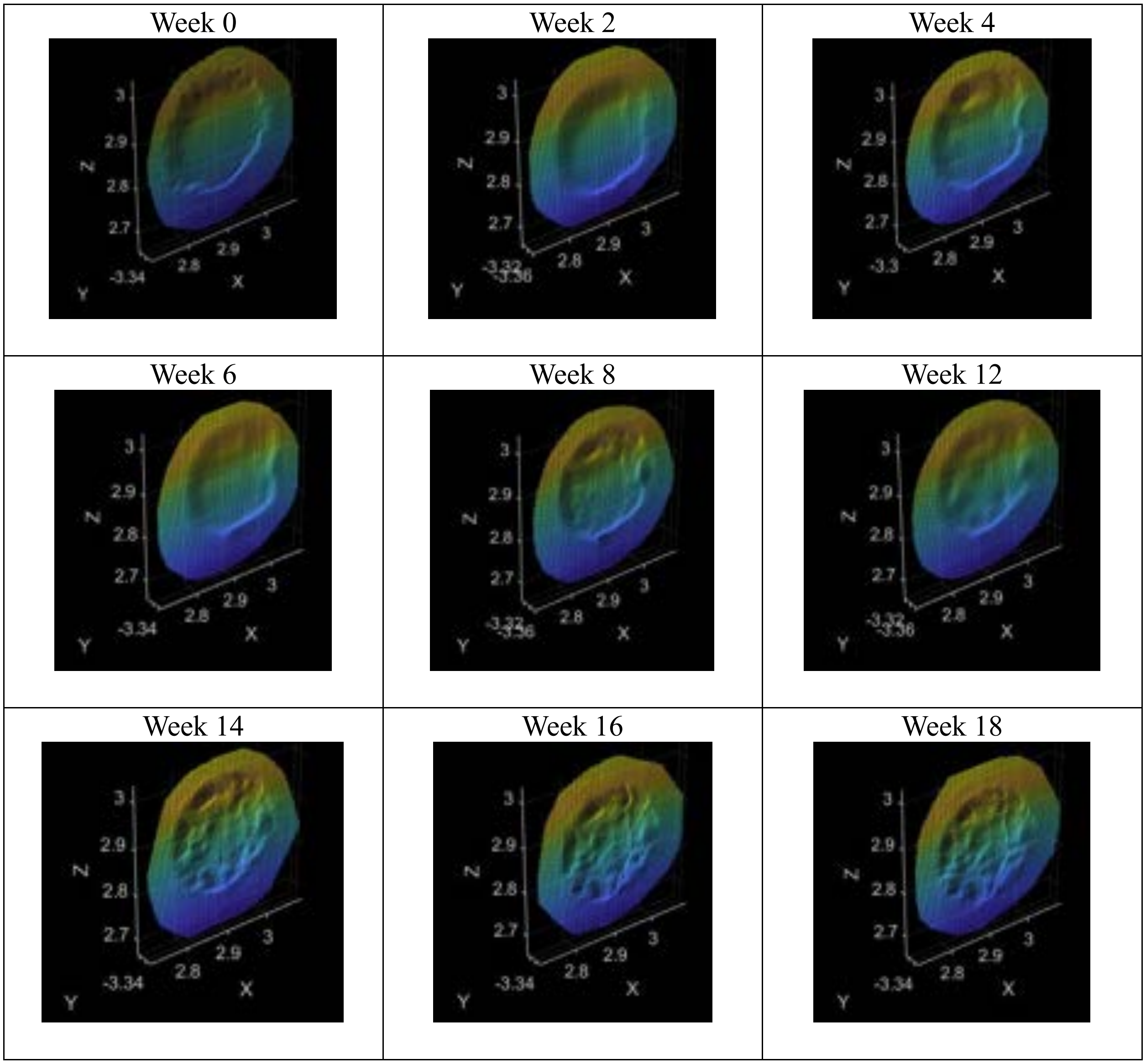

Figure C15. Change in meshed point cloud of exposed 2% area holiday data from Week 0 for G1G2.

Week 22

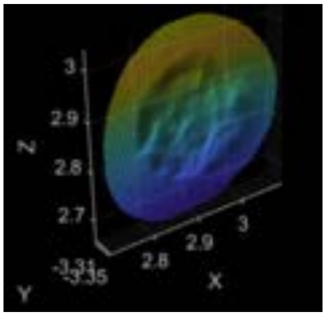

Week 24

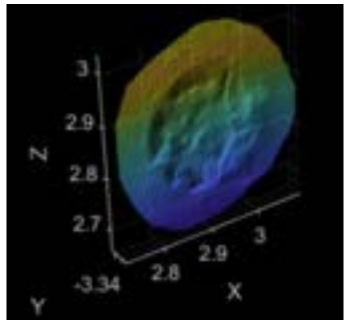

Week 30

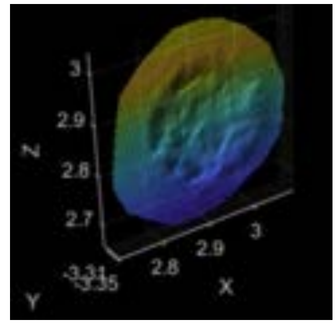

Week 36

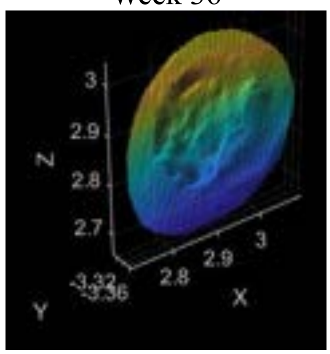

Figure C16. Change in meshed point cloud of exposed 2% area holiday data from Week 0 for G1G2 continued.

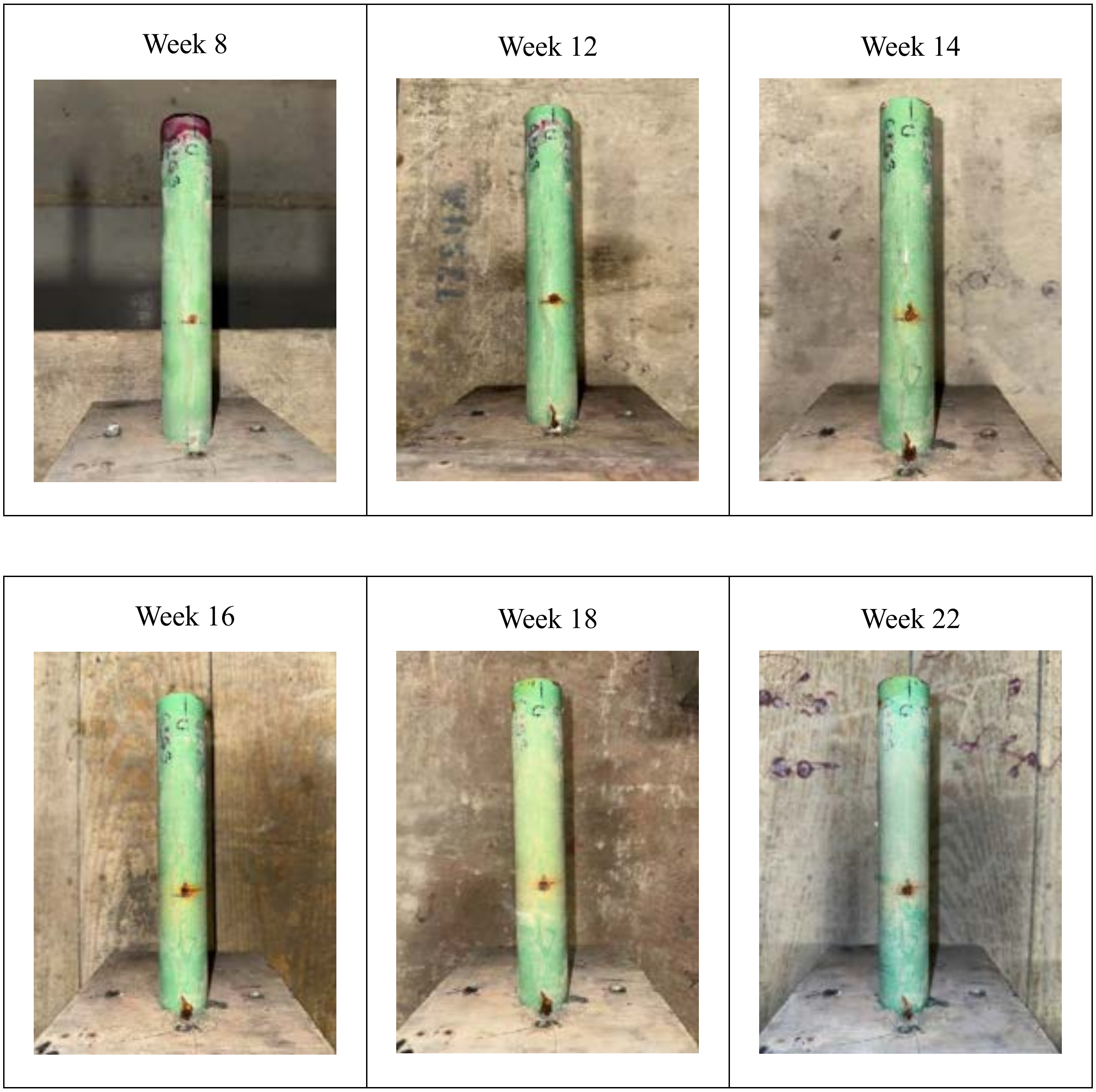

Figure C17. Side with 2% area holidays for G1G3.

Week 24	Week 30	Week 36
		

Figure C18. Side with 2% area holidays for G1G3 continued.

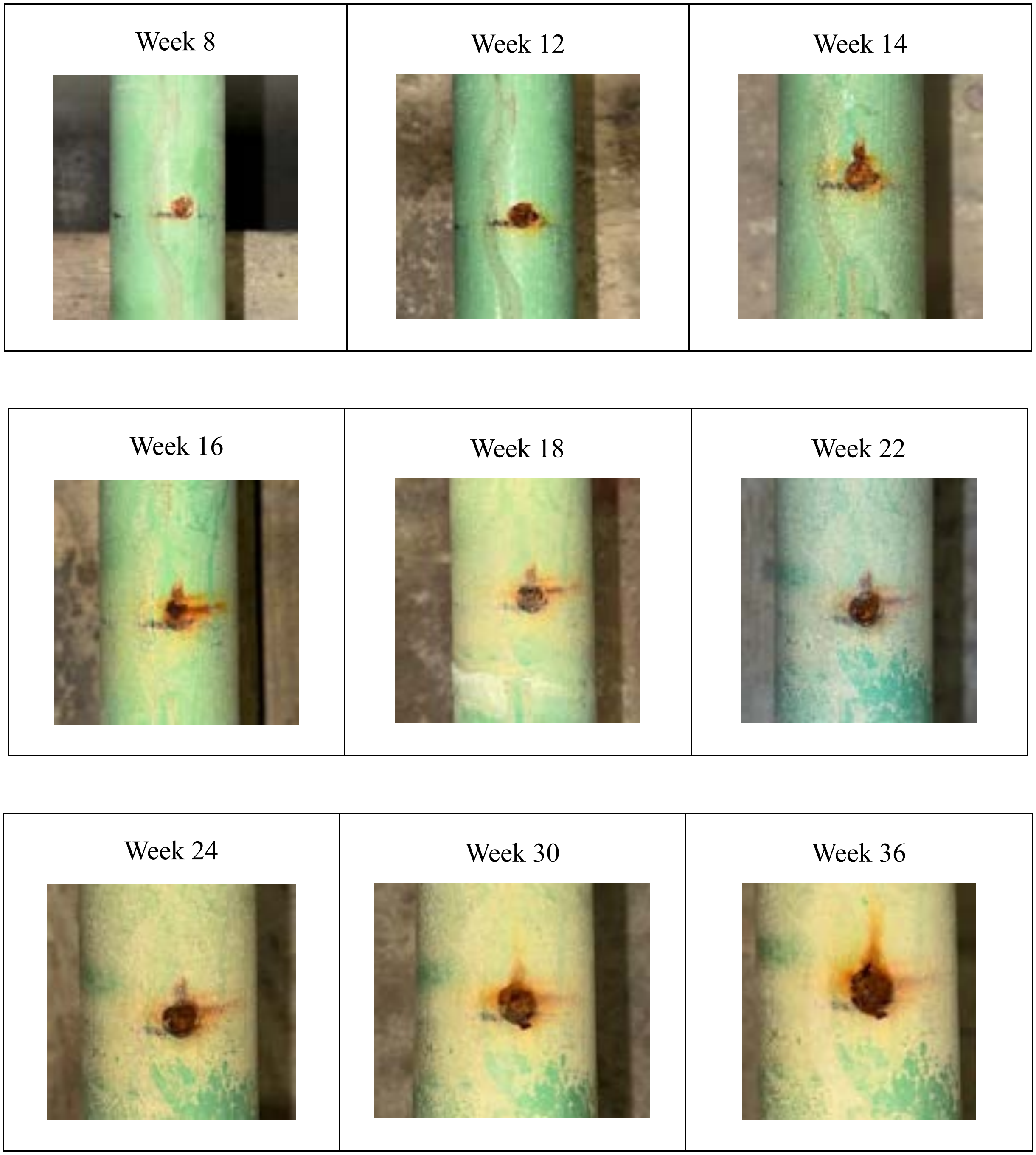

Figure C19. Exposed 2% area holiday for G1G3.

Week 8

Week 12

Week 14

Week 16

Week 18

Week 22

Figure C20. Side with 1% area holidays for G1G3.

Week 24	Week 30	Week 36
		

Figure C21. Side with 1% area holidays for G1G3 continued.

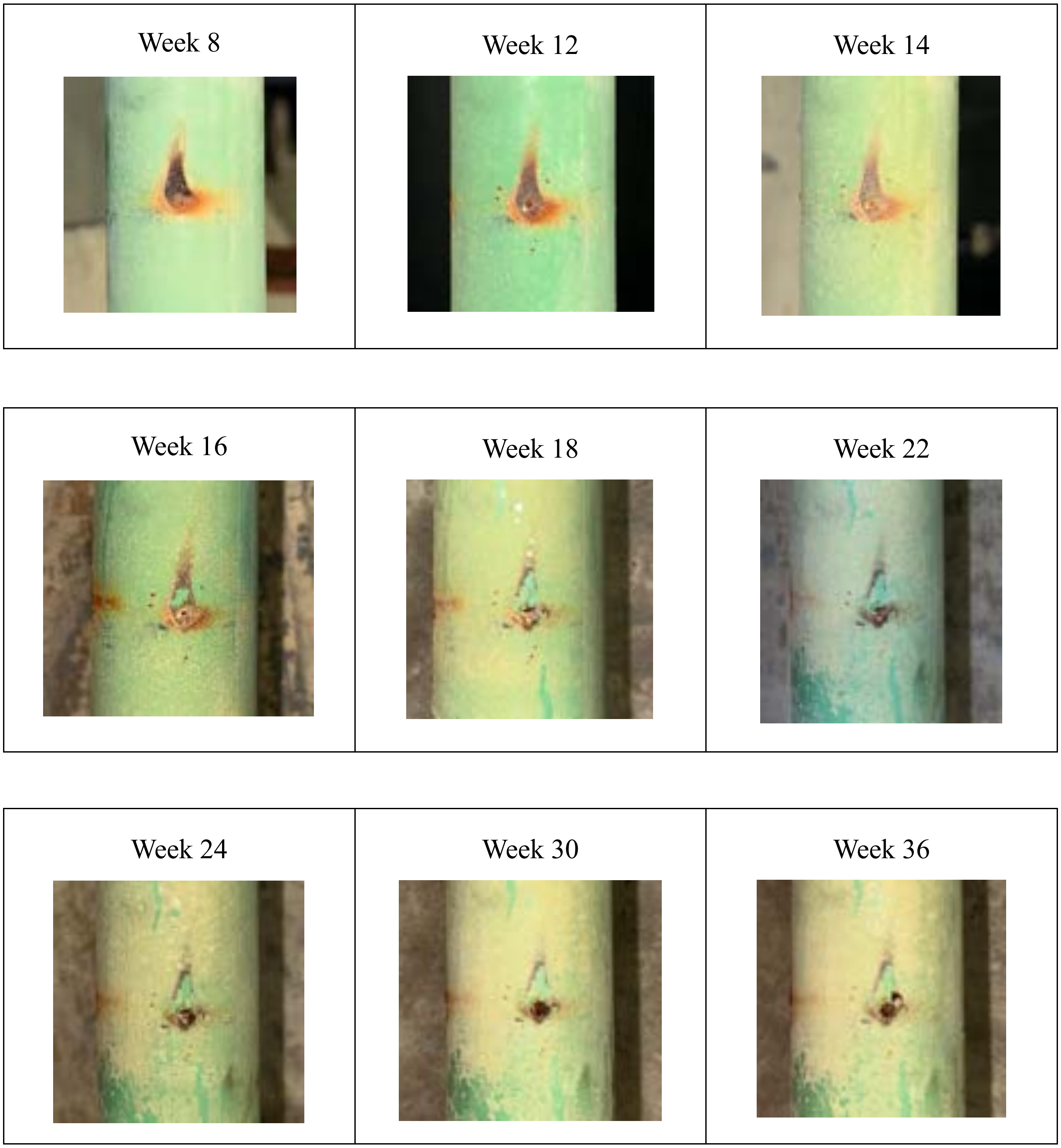

Figure C22. Exposed 1% area holiday for G1G3.

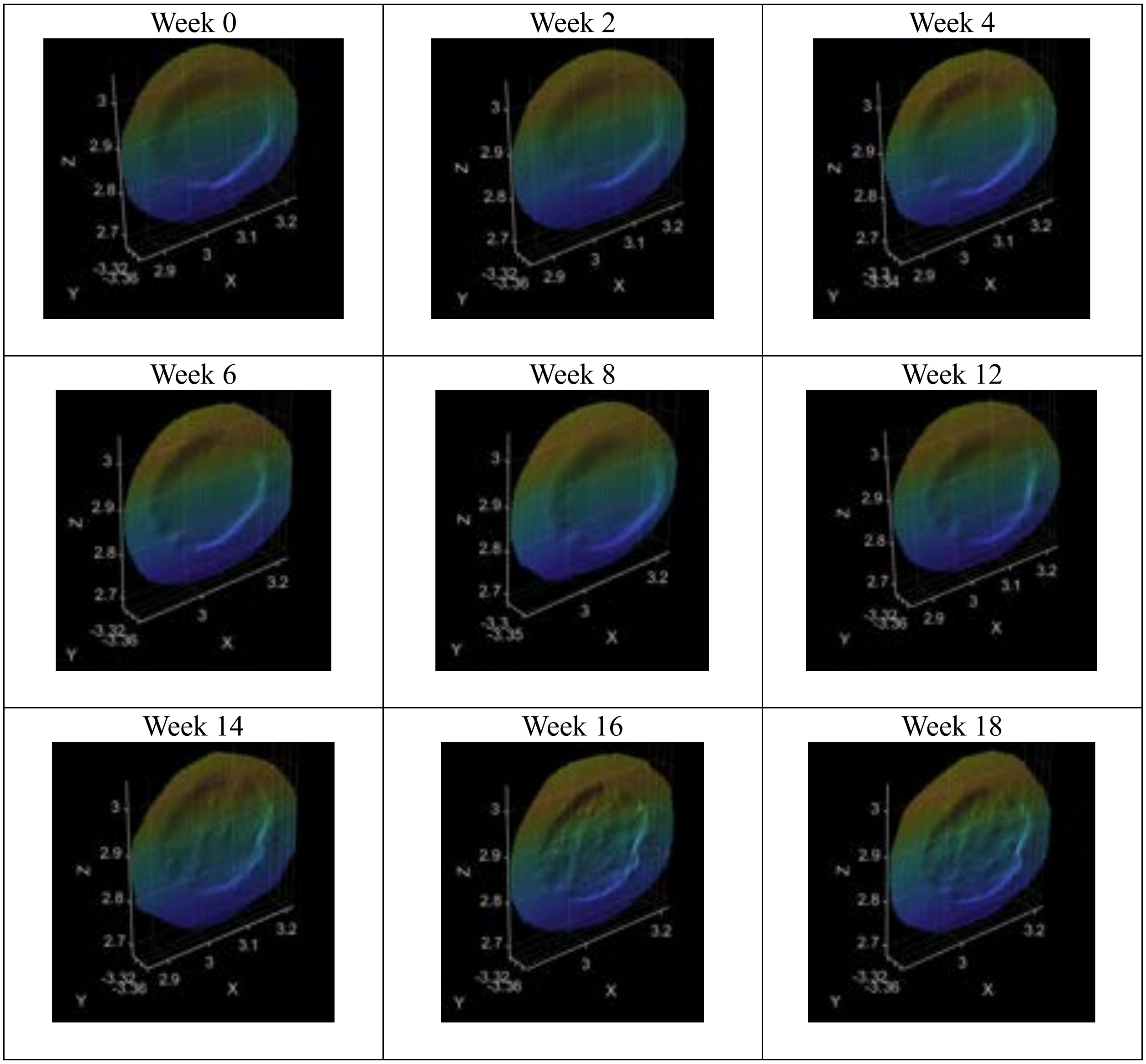

Figure C23. Change in meshed point cloud of exposed 2% area holiday data from Week 0 for G1G3.

Week 22

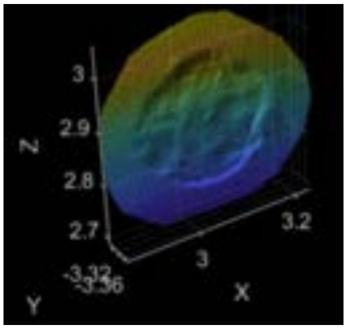

Week 24

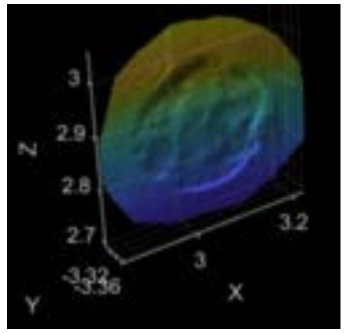

Week 30

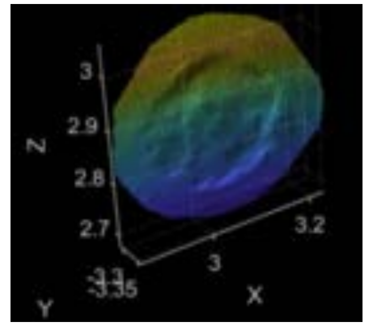

Week 36

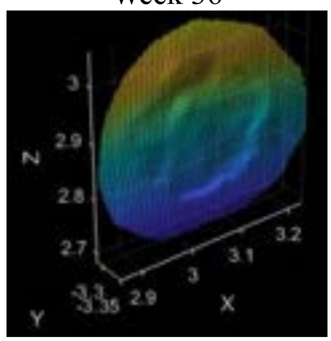

Figure C24. Change in meshed point cloud of exposed 2% area holiday data from Week 0 for G1G3 continued.

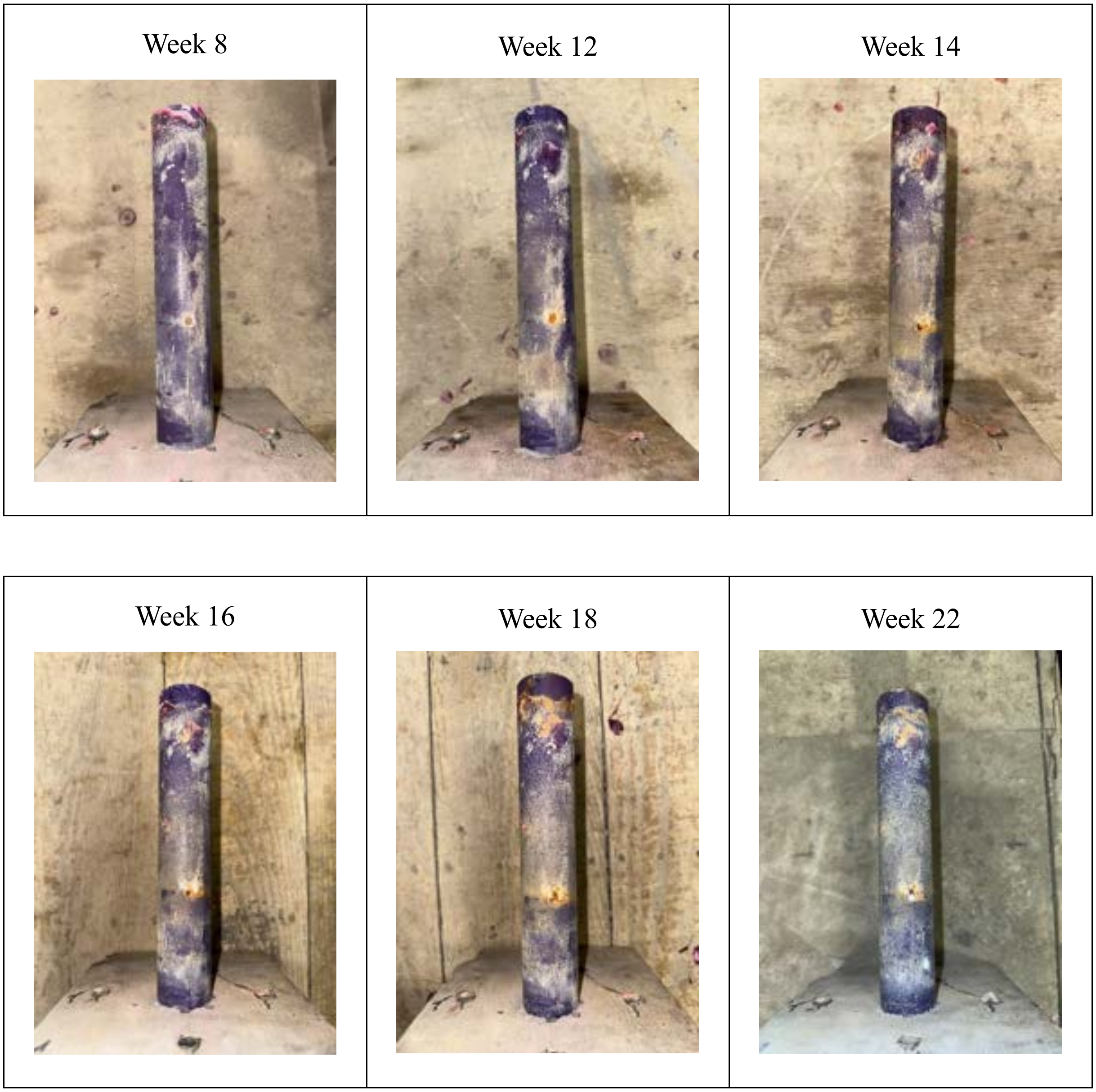

Figure C25. Side with 2% area holidays for G1P1.

Week 24	Week 30	Week 36
		

Figure C26. Side with 2% area holidays for G1P1.

Week 8 	Week 12 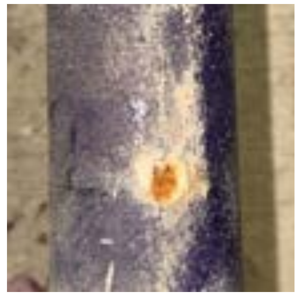	Week 14 
Week 16 	Week 18 	Week 22 
Week 24 	Week 30 	Week 36 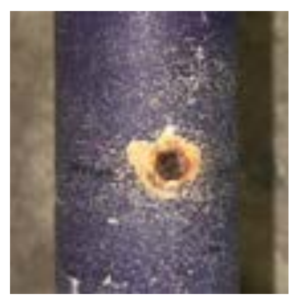

Figure C27. Exposed 2% area holiday for G1P1.

Week 8	Week 12	Week 14
		

Week 16	Week 18	Week 22
		

Figure C28. Side with 1% area holidays for G1P1.

Week 24	Week 30	Week 36
		

Figure C29. Side with 1% area holidays for G1P1 continued.

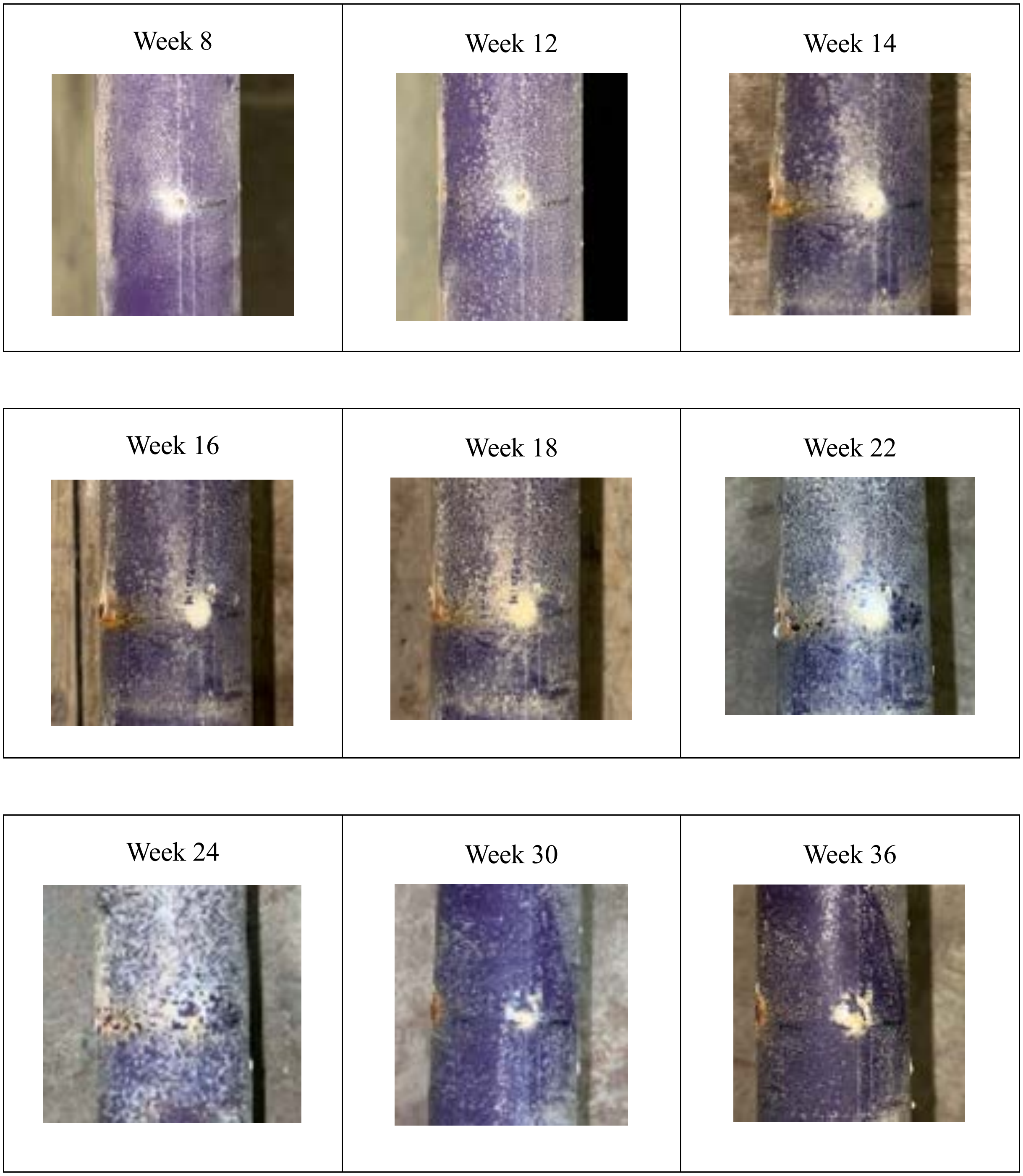

Figure C30. Exposed 1% area holiday for G1P1.

Week 0

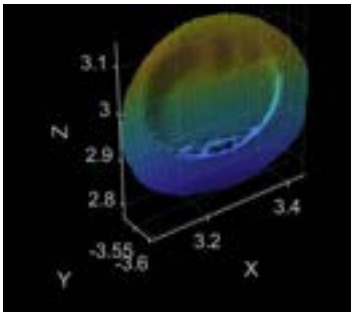

Week 2

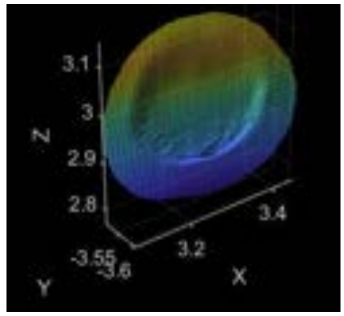

Week 4

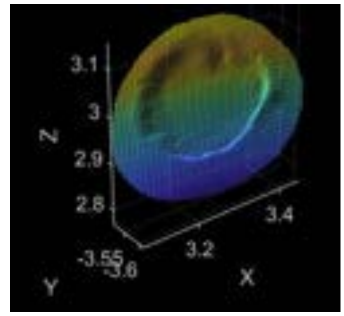

Week 6

Unavailable

Week 8

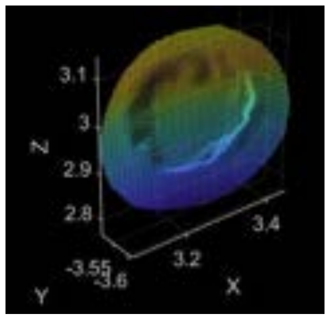

Week 12

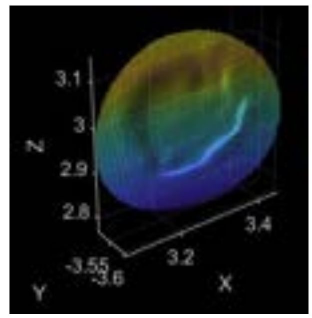

Week 14

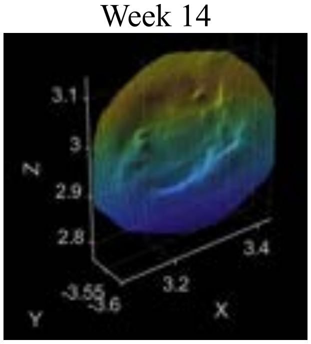

Week 16

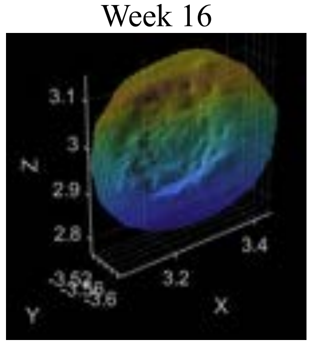

Week 18

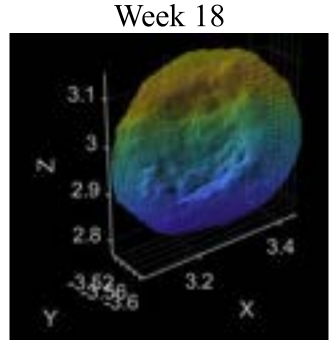

Figure C31. Change in meshed point cloud of exposed 2% area holiday data from Week 0 for G1P1.

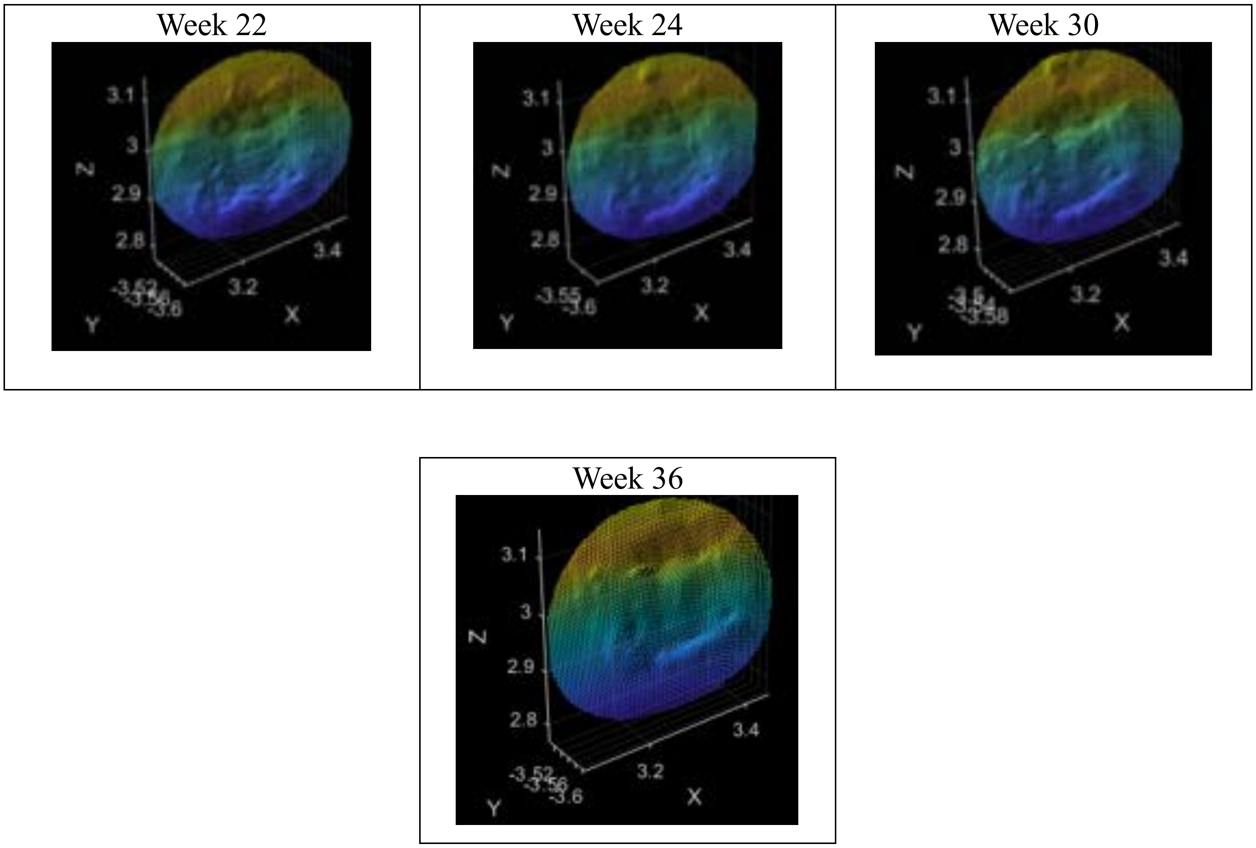

Figure C32. Change in meshed point cloud of exposed 2% area holiday data from Week 0 for G1P1 continued.

Week 8	Week 12	Week 14
		

Week 16	Week 18	Week 22
		

Figure C33. Side with 2% area holidays for G1P2.

Week 24	Week 30	Week 36
		

Figure C34. Side with 2% area holidays for G1P2 continued.

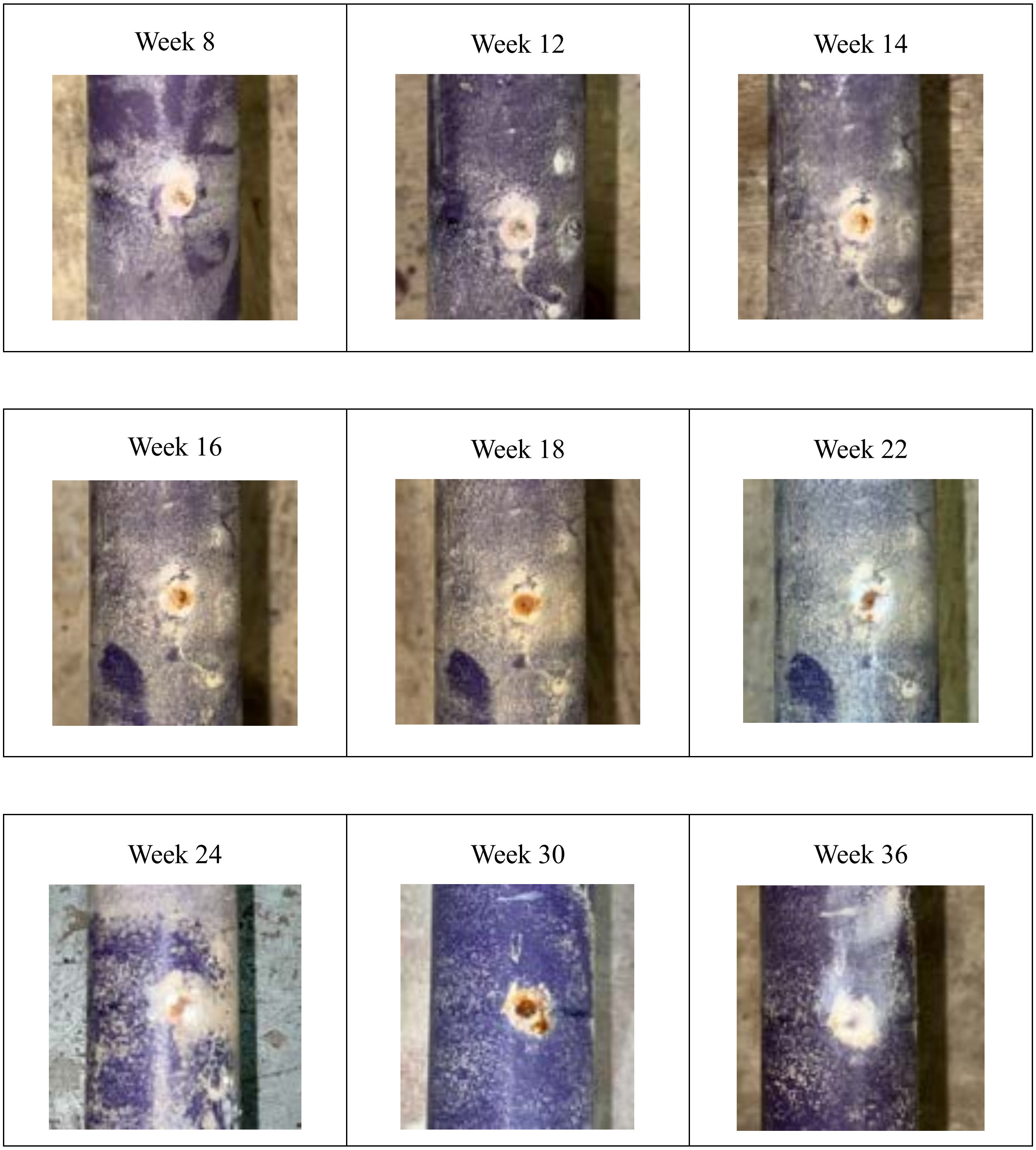

Figure C35. Exposed 2% area holiday for G1P2.

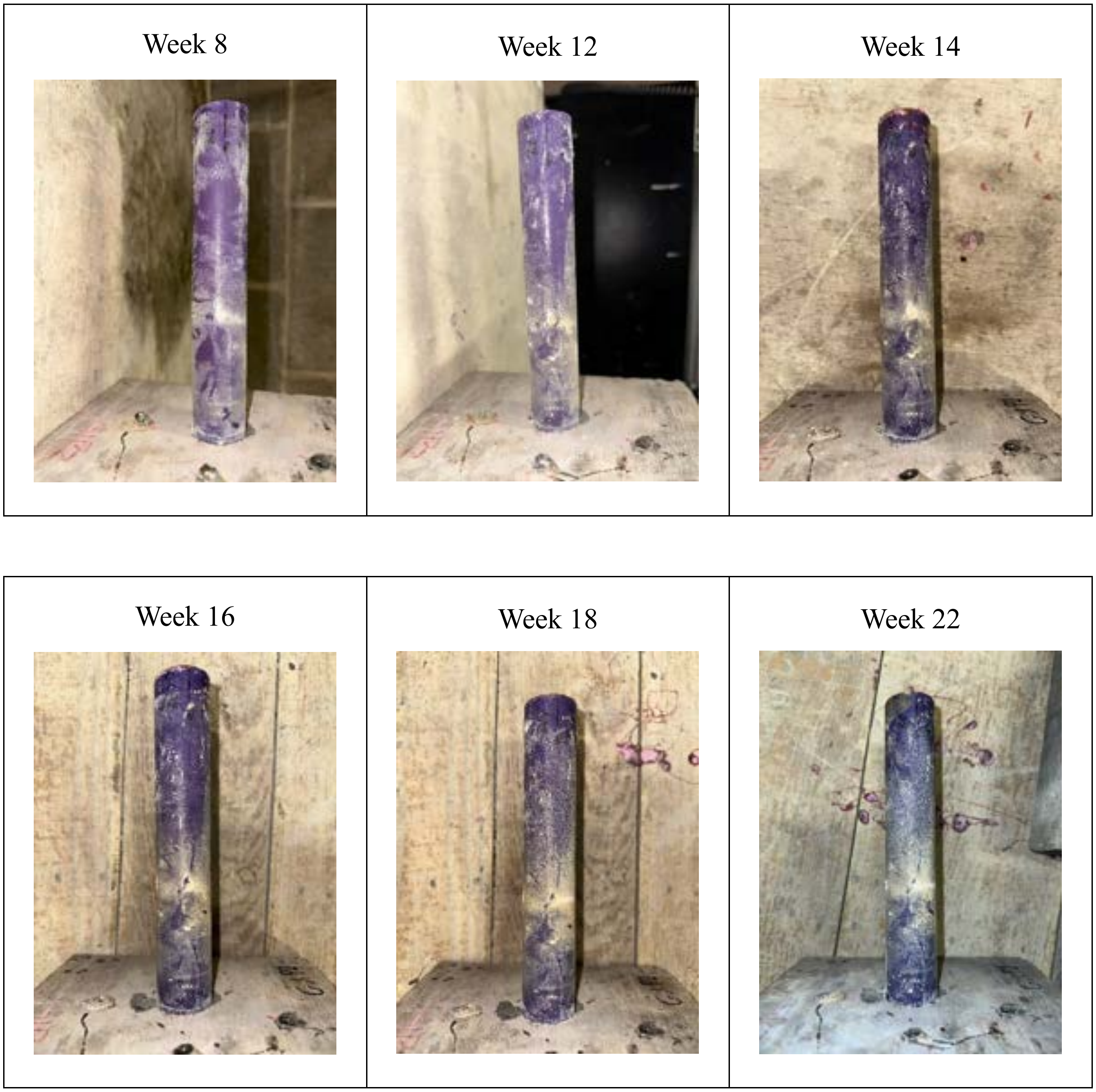

Figure C36. Side with 1% area holidays for G1P2.

Week 24	Week 30	Week 36
		

Figure C37. Side with 1% area holidays for G1P2 continued.

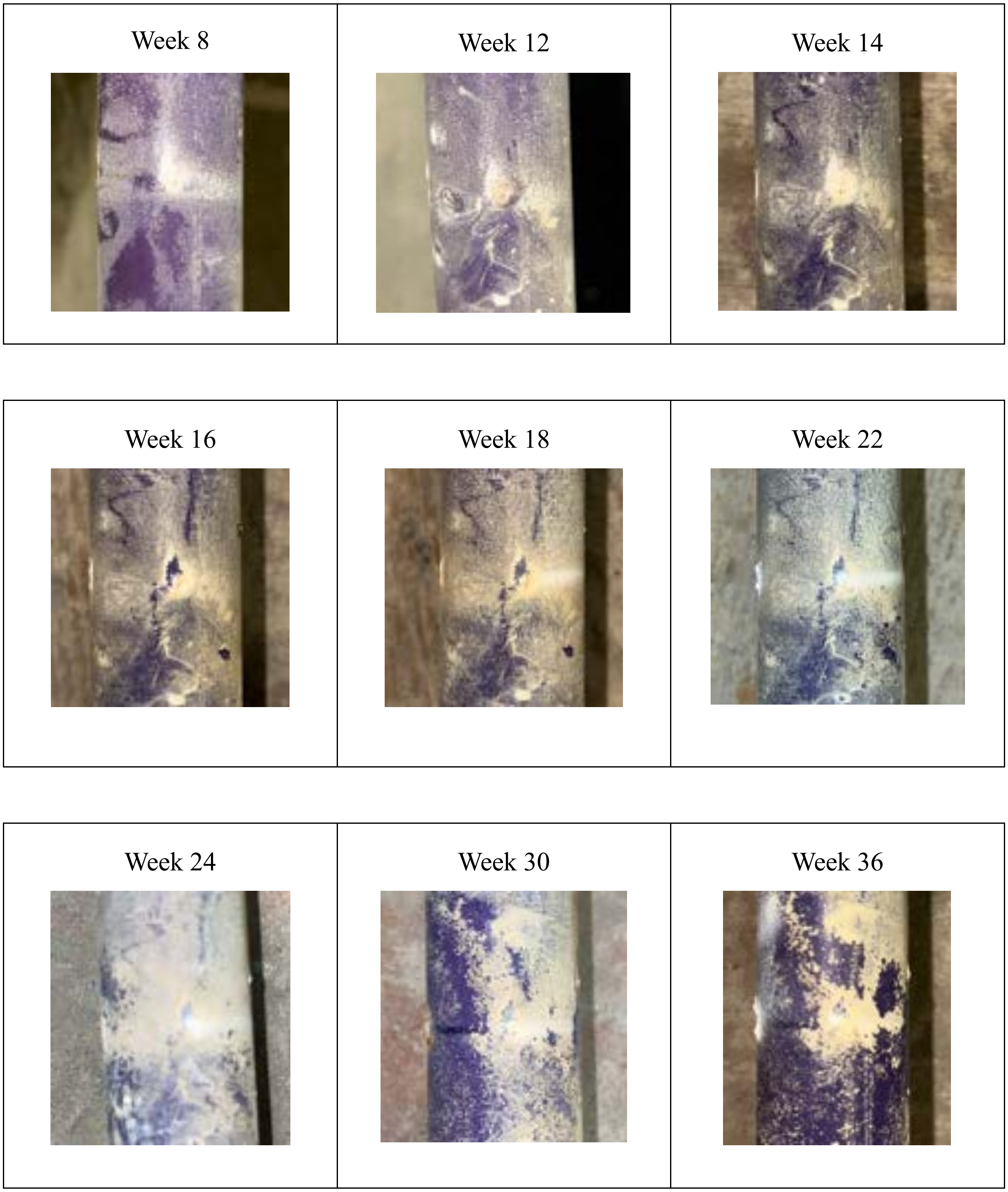

Figure C38. Exposed 1% area holiday for G1P2.

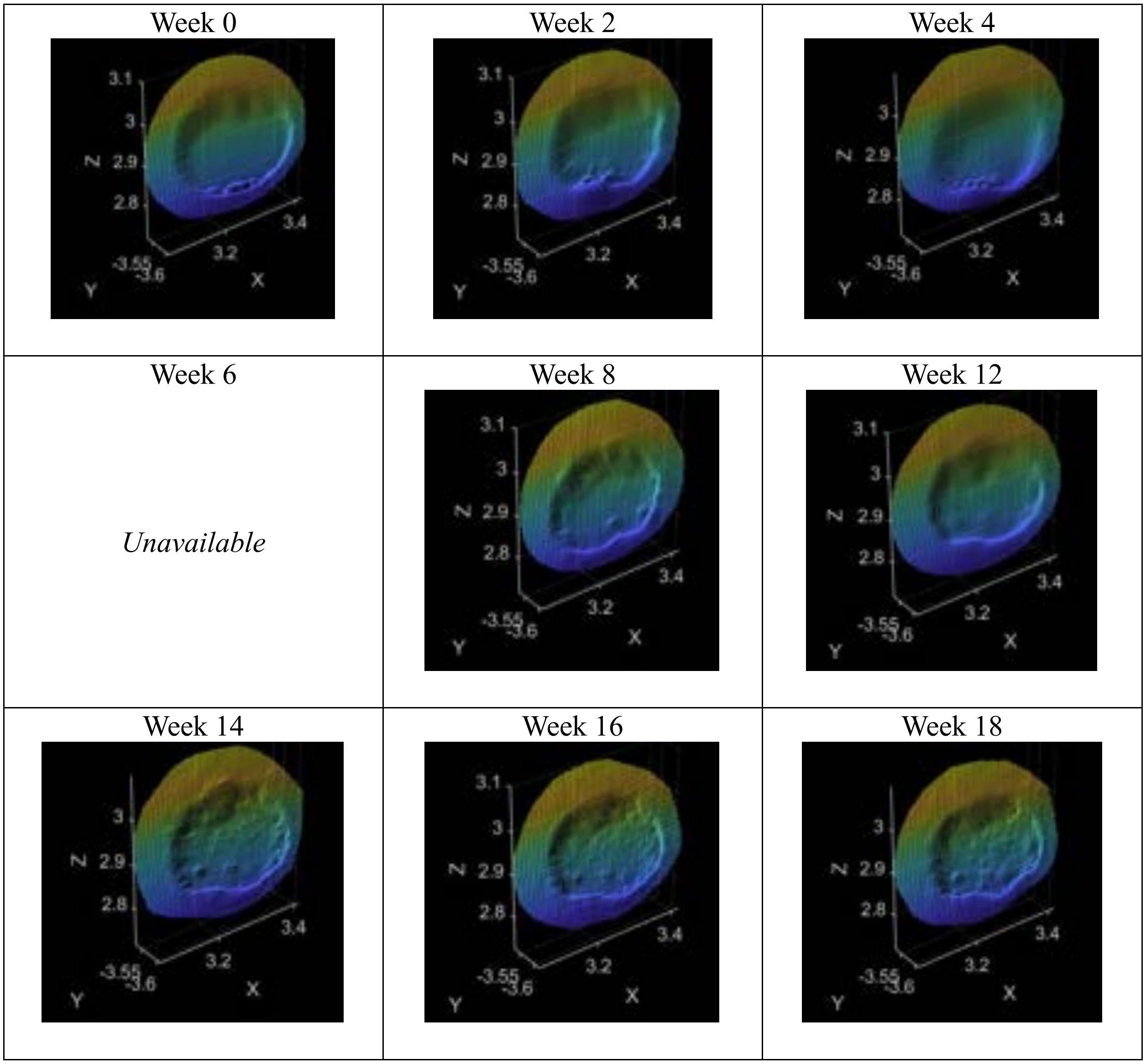

Figure C39. Change in meshed point cloud of exposed 2% area holiday data from Week 0 for G1P2.

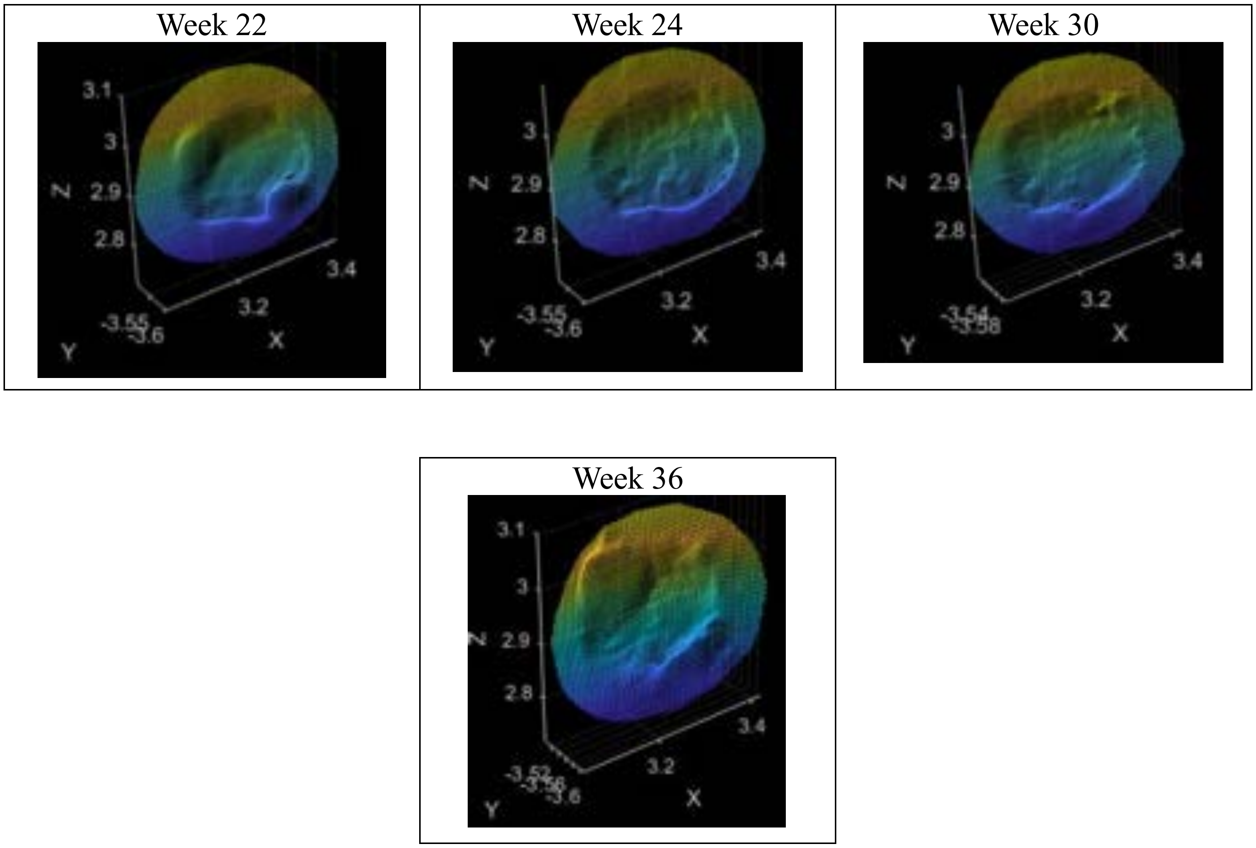

Figure C40. Change in meshed point cloud of exposed 2% area holiday data from Week 0 for G1P2 continued.

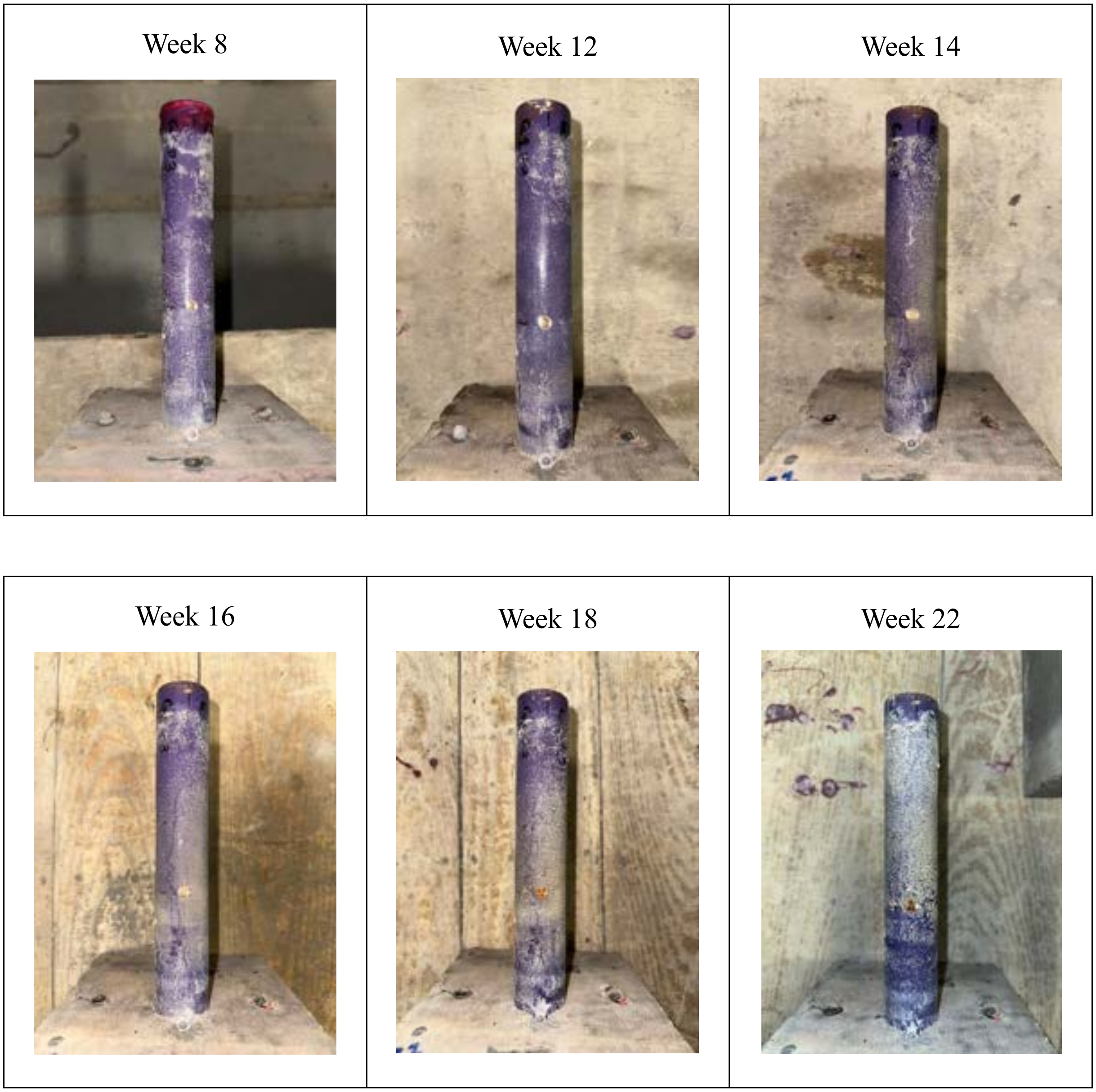

Figure C41. Side with 2% area holidays for G1P3.

Week 24	Week 30	Week 36
		

Figure C42. Side with 2% area holidays for G1P3 continued.

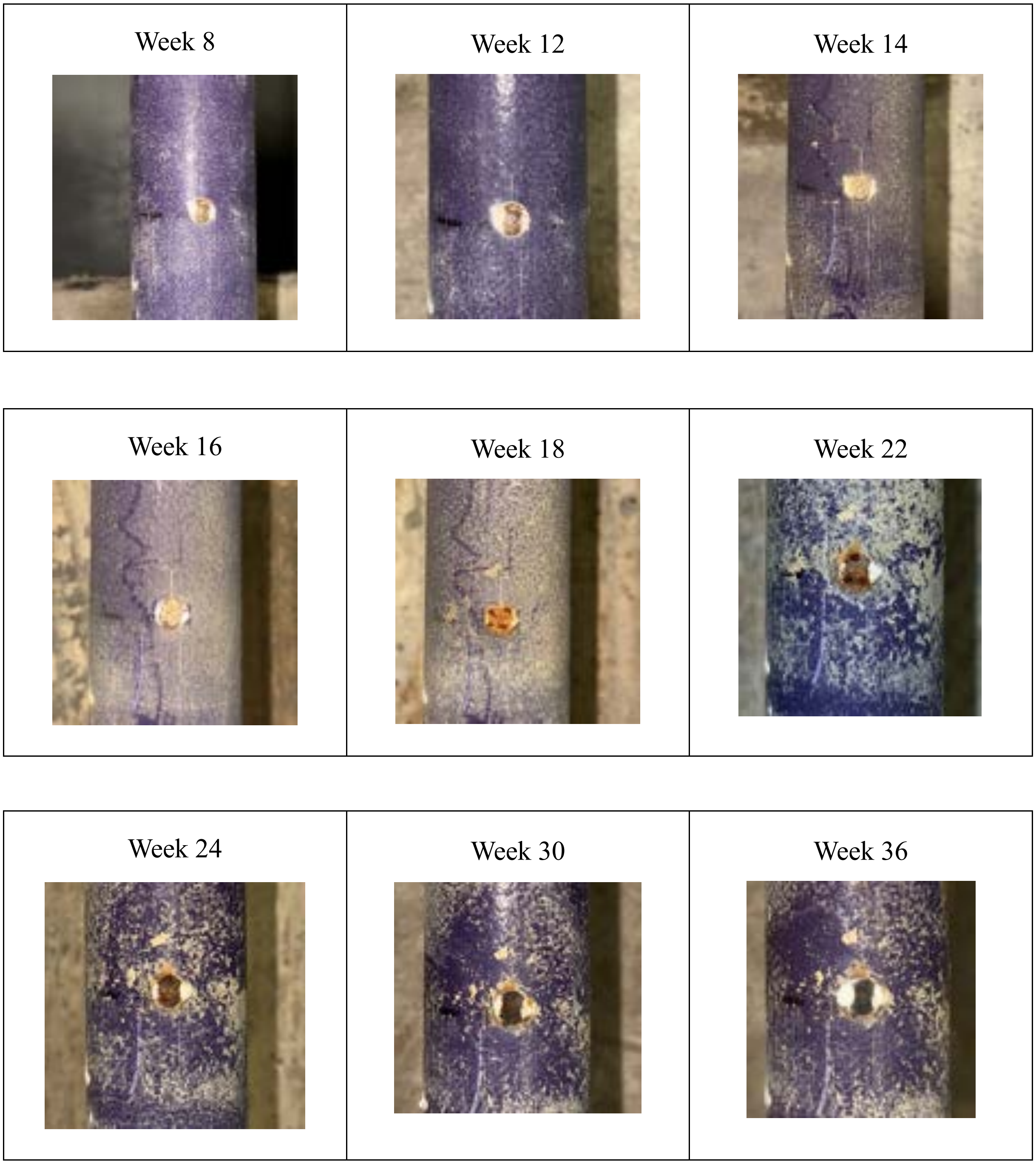

Figure C43. Exposed 2% area holiday for G1P3.

Week 8	Week 12	Week 14
		

Week 16	Week 18	Week 22
		

Figure C44. Side with 1% area holidays for G1P3.

Week 24	Week 30	Week 36
		

Figure C45. Side with 1% area holidays for G1P3 continued.

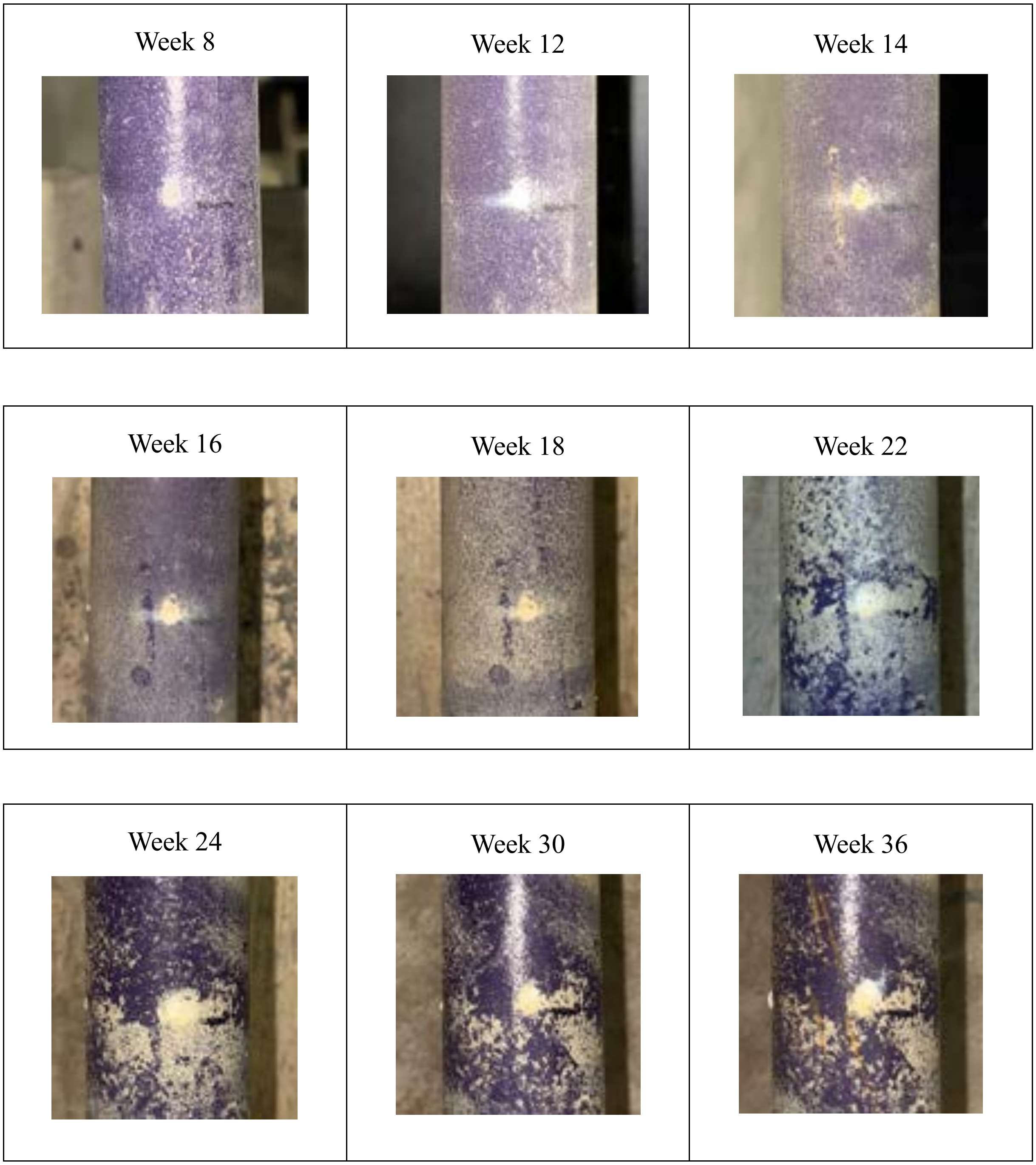

Figure C46. Exposed 1% area holiday for G1P3.

Week 0

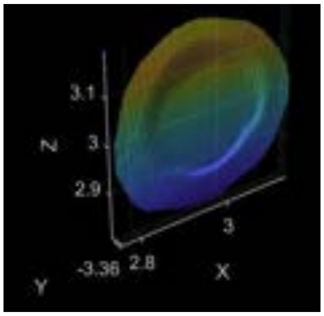

Week 2

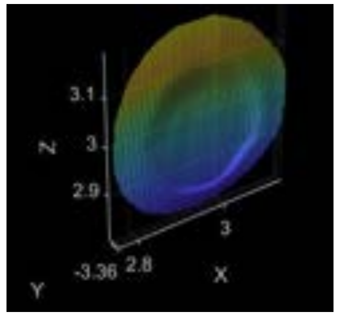

Week 4

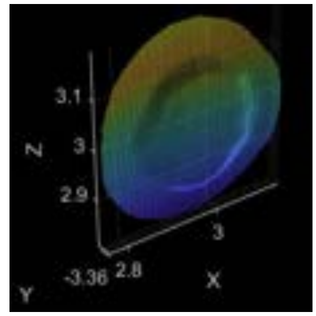

Week 6

Unavailable

Week 8

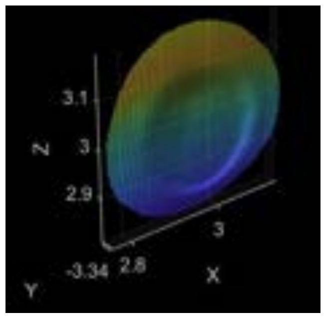

Week 12

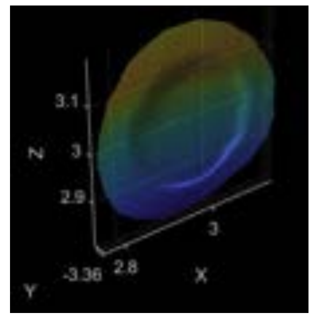

Week 14

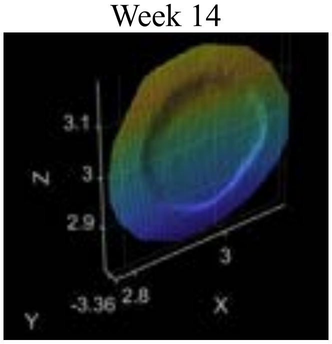

Week 16

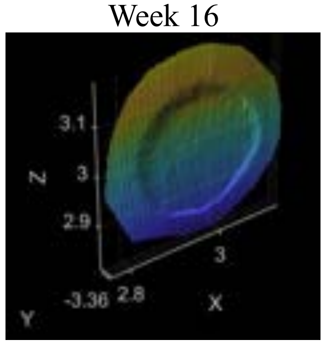

Week 18

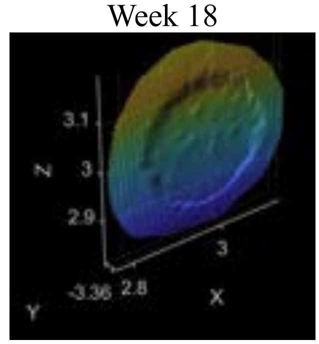

Figure C47. Change in meshed point cloud of exposed 2% area holiday data from Week 0 for G1P3.

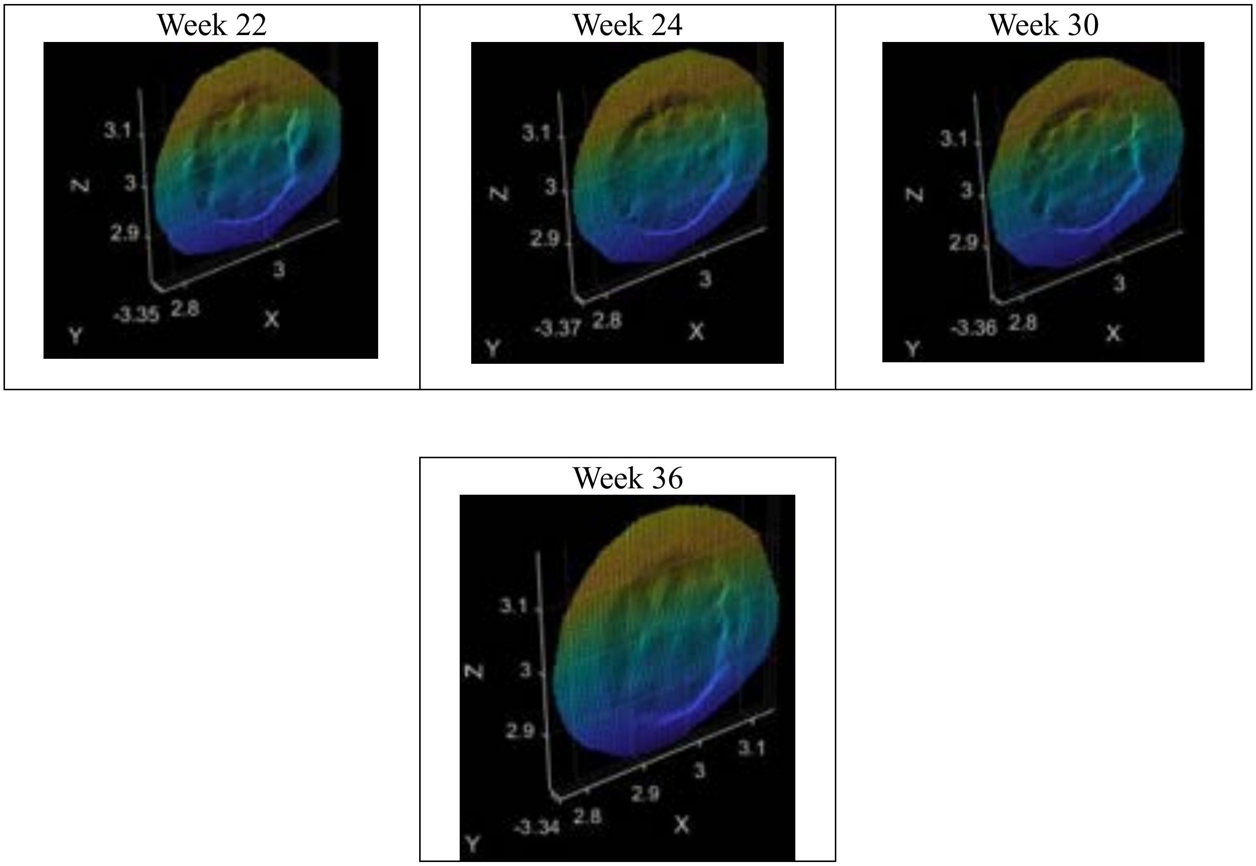

Figure C48. Change in meshed point cloud of exposed 2% area holiday data from Week 0 for G1P3 continued.

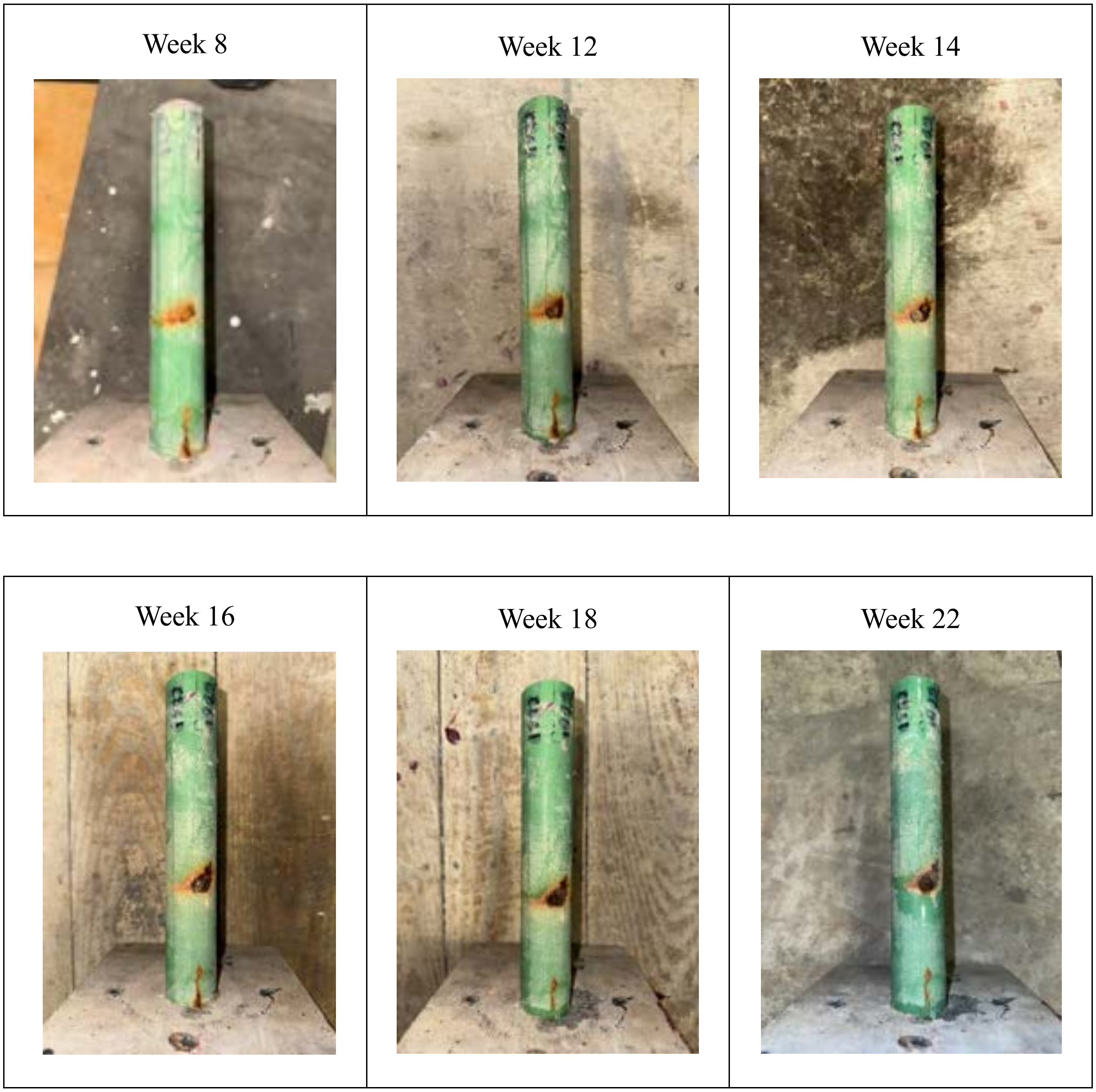

Figure C49. Side with 2% area holidays for C2G1.

Week 24	Week 30	Week 36
		

Figure C50. Side with 2% area holidays for C2G1 continued.

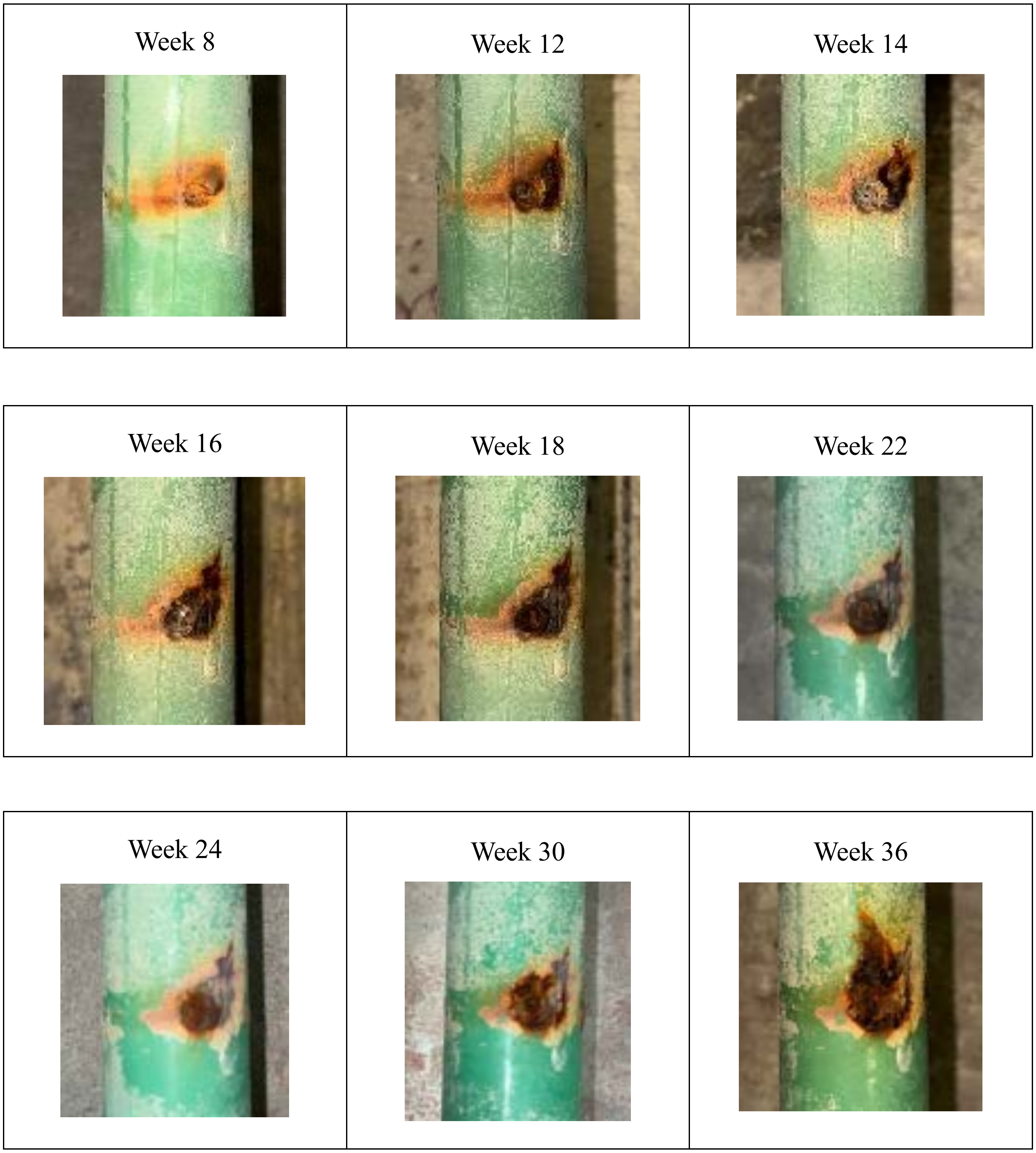

Figure C51. Exposed 2% area holiday for C2G1.

Week 8

Week 12

Week 14

Week 16

Week 18

Week 22

Figure C52. Side with 1% area holidays for C2G1.

Week 24	Week 30	Week 36
		

Figure C53. Side with 1% area holidays for C2G1 continued.

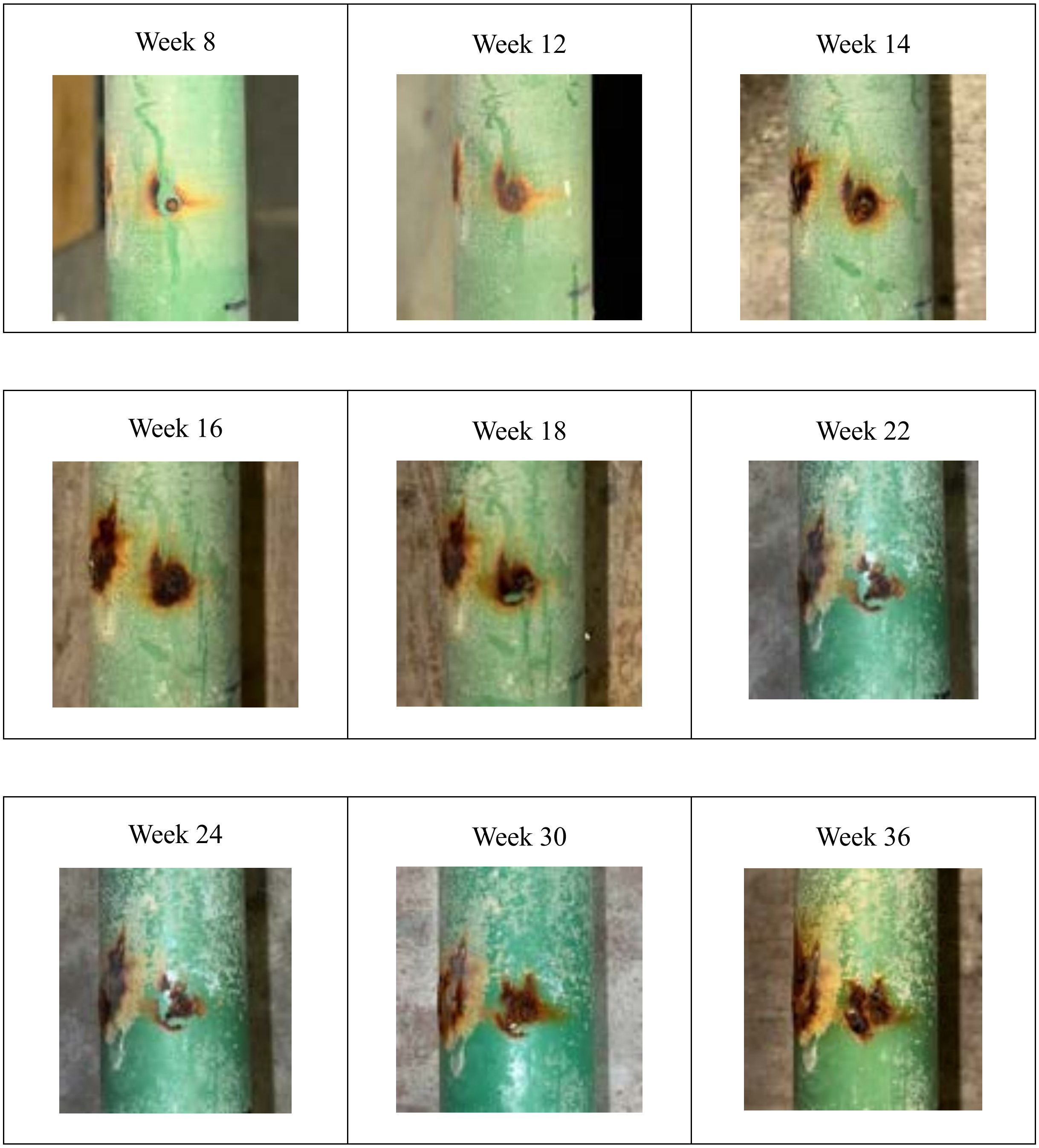

Figure C54. Exposed 1% area holiday for C2G1.

Week 0	Week 2	Week 4
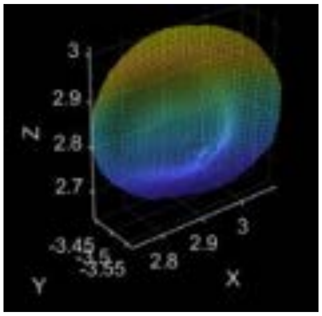	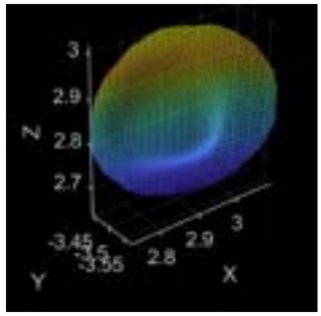	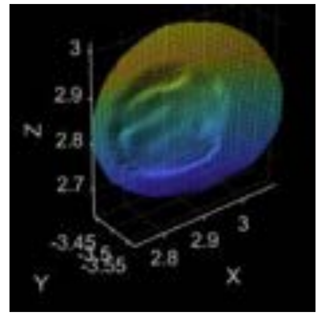
Week 6	Week 8	Week 12
Unavailable	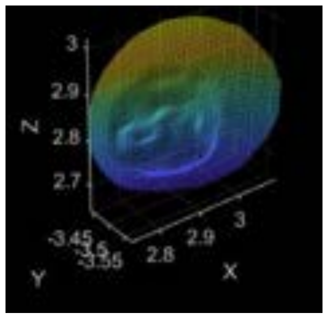	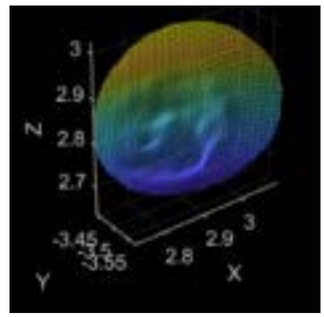
Week 14	Week 16	Week 18
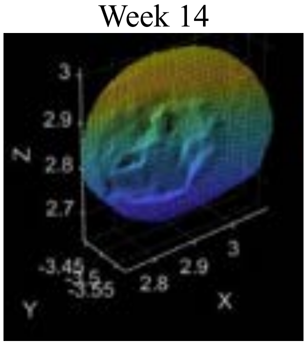	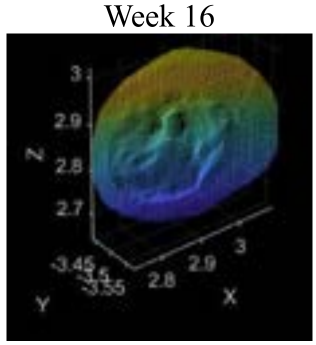	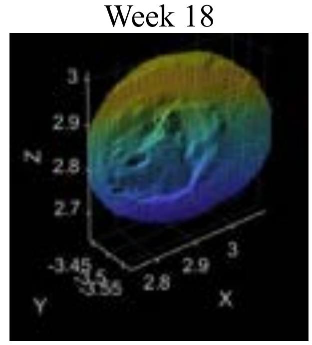

Figure C55. Change in meshed point cloud of exposed 2% area holiday data from Week 0 for C2G1.

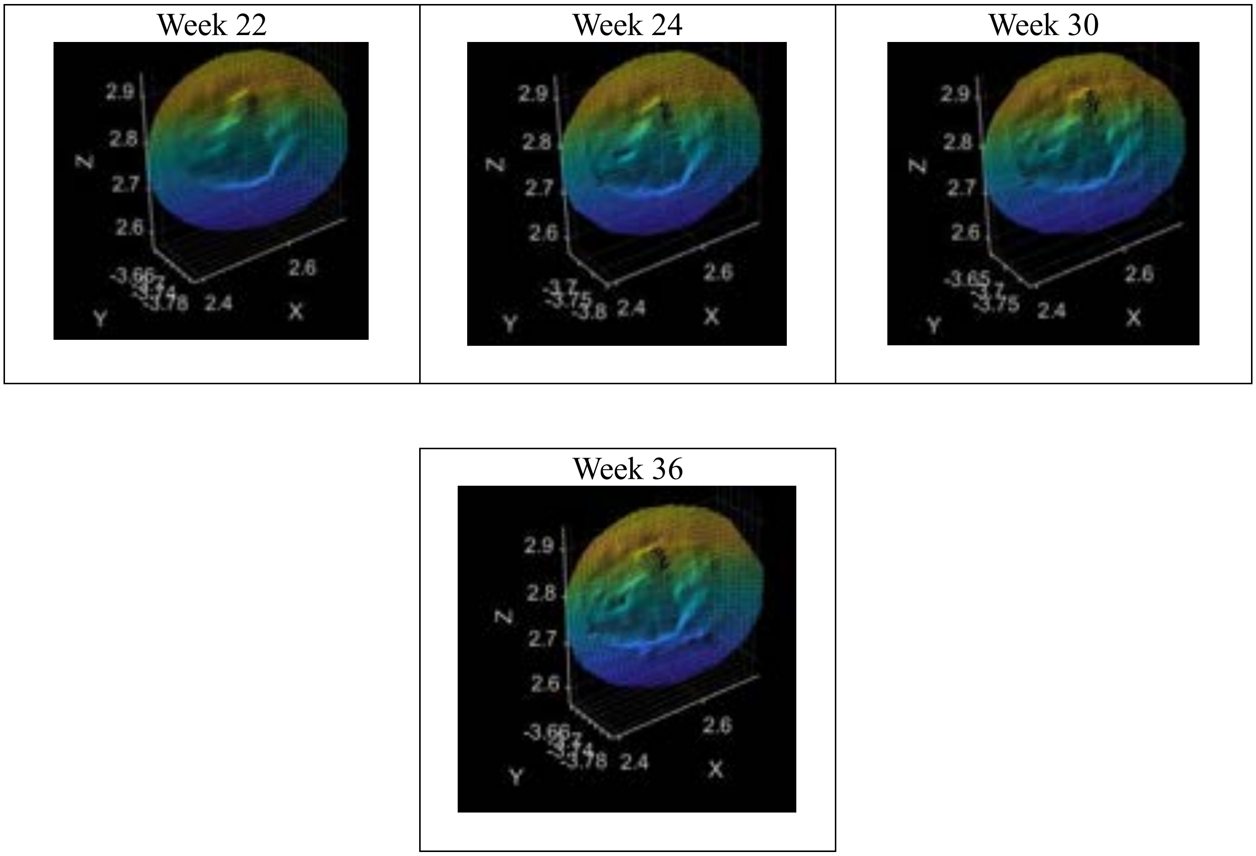

Figure C56. Change in meshed point cloud of exposed 2% area holiday data from Week 0 for C2G1 continued.

Week 8	Week 12	Week 14
		

Week 16	Week 18	Week 22
		

Figure C57. Side with 2% area holidays for C2G2.

Week 24	Week 30	Week 36
		

Figure C58. Side with 2% area holidays for C2G2 continued.

Week 8	Week 12	Week 14
		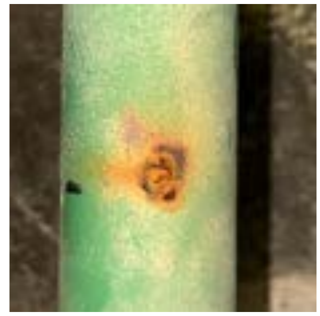
Week 16	Week 18	Week 22
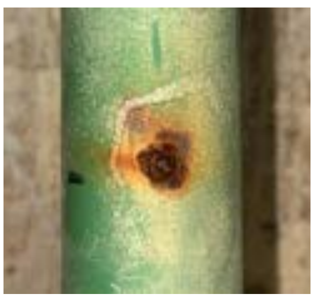	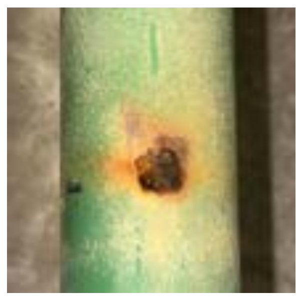	
Week 24	Week 30	Week 36
		

Figure C59. Exposed 2% area holiday for C2G2.

Week 8

Week 12

Week 14

Week 16

Week 18

Week 22

Figure C60. Side with 1% area holidays for C2G2.

Week 24	Week 30	Week 36
		

Figure C61. Side with 1% area holidays for C2G2 continued.

Week 8	Week 12	Week 14
		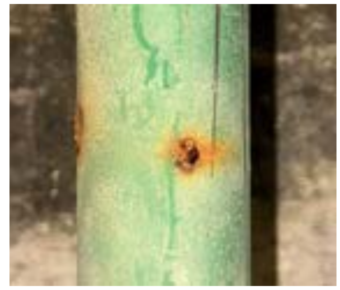
Week 16	Week 18	Week 22
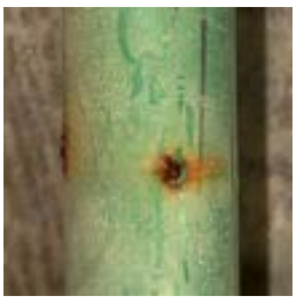	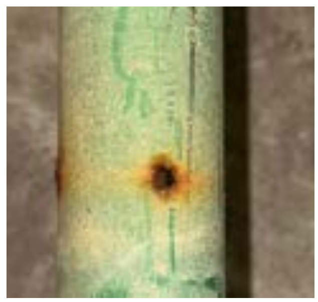	
Week 24	Week 30	Week 36
	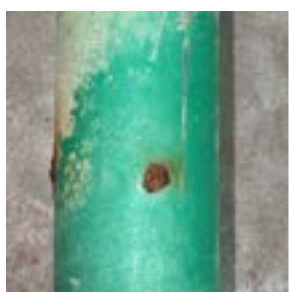	

Figure C62. Exposed 1% area holiday for C2G2.

Week 0	Week 2	Week 4
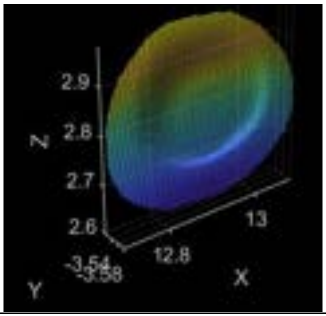	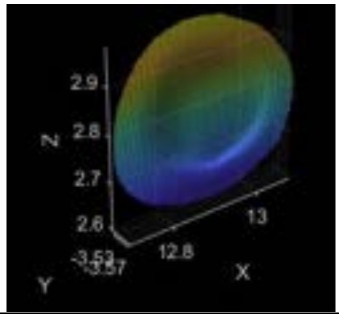	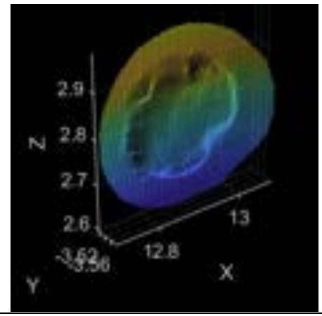
Week 6	Week 8	Week 12
Unavailable	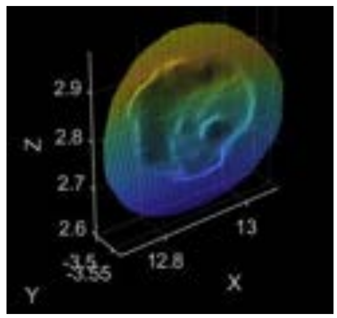	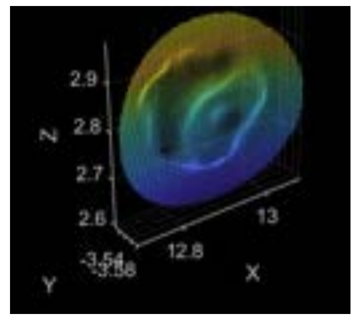
Week 14	Week 16	Week 18
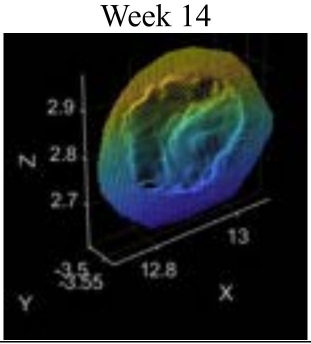	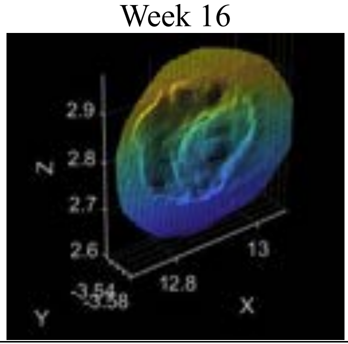	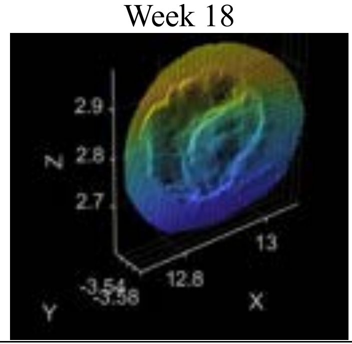

Figure C63. Change in meshed point cloud of exposed 2% area holiday data from Week 0 for C2G2.

Week 22

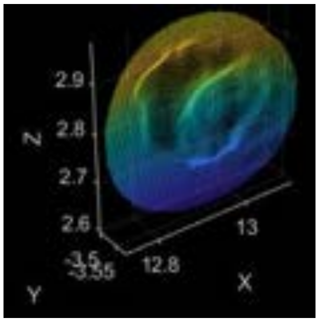

Week 24

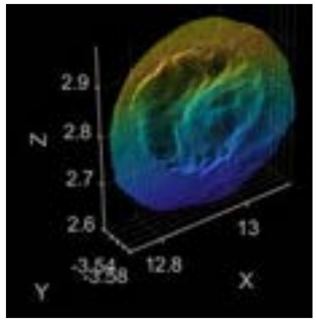

Week 30

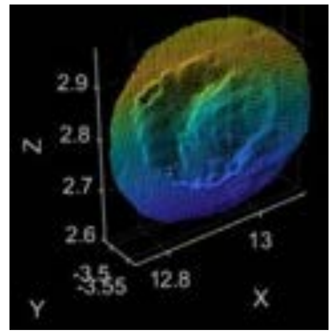

Week 36

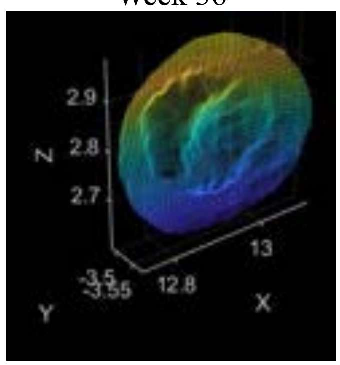

Figure C64. Change in meshed point cloud of exposed 2% area holiday data from Week 0 for C2G2 continued.

Week 8	Week 12	Week 14
		

Week 16	Week 18	Week 22
		

Figure C65. Side with 2% area holidays for C2G2[1].

[1] -corresponds to C2G2X

Week 24	Week 30	Week 36
		

Figure C66. Side with 2% area holidays for C2G21 above[7] continued.

Week 8	Week 12	Week 14
	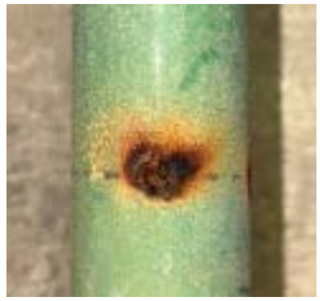	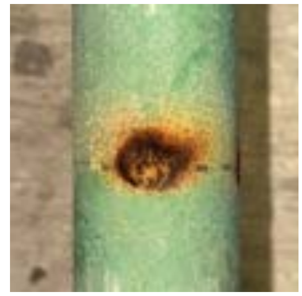
Week 16	Week 18	Week 22
		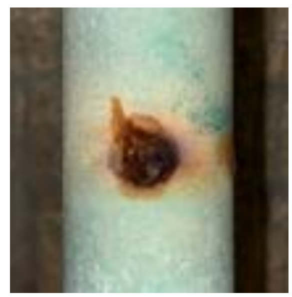
Week 24	Week 30	Week 36
		

Figure C67. Exposed 2% area holiday for C2G2[1].

Week 8	Week 12	Week 14
		

Week 16	Week 18	Week 22
		

Figure C68. Side with 1% area holidays for C2G2[1].

Week 24	Week 30	Week 36
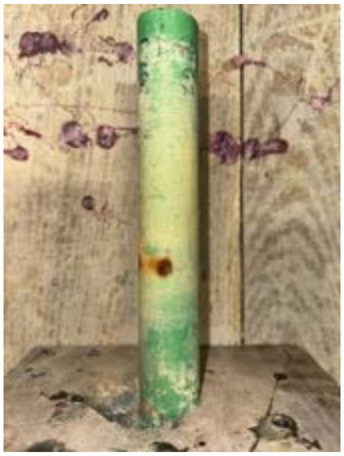		

Figure C69. Side with 1% area holidays for C2G2[1] continued.

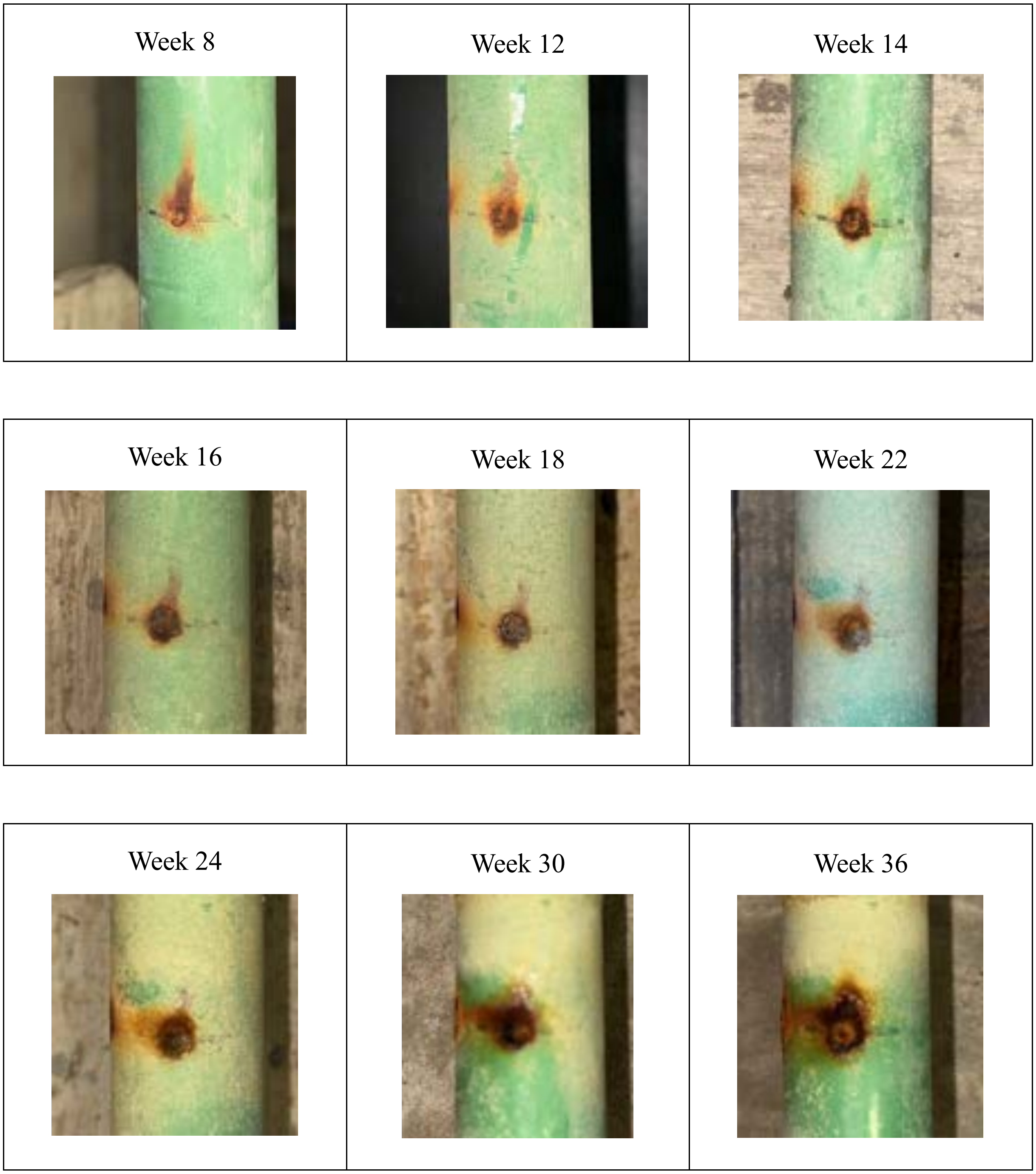

Figure C70. Exposed 1% area holiday for C2G2[1].

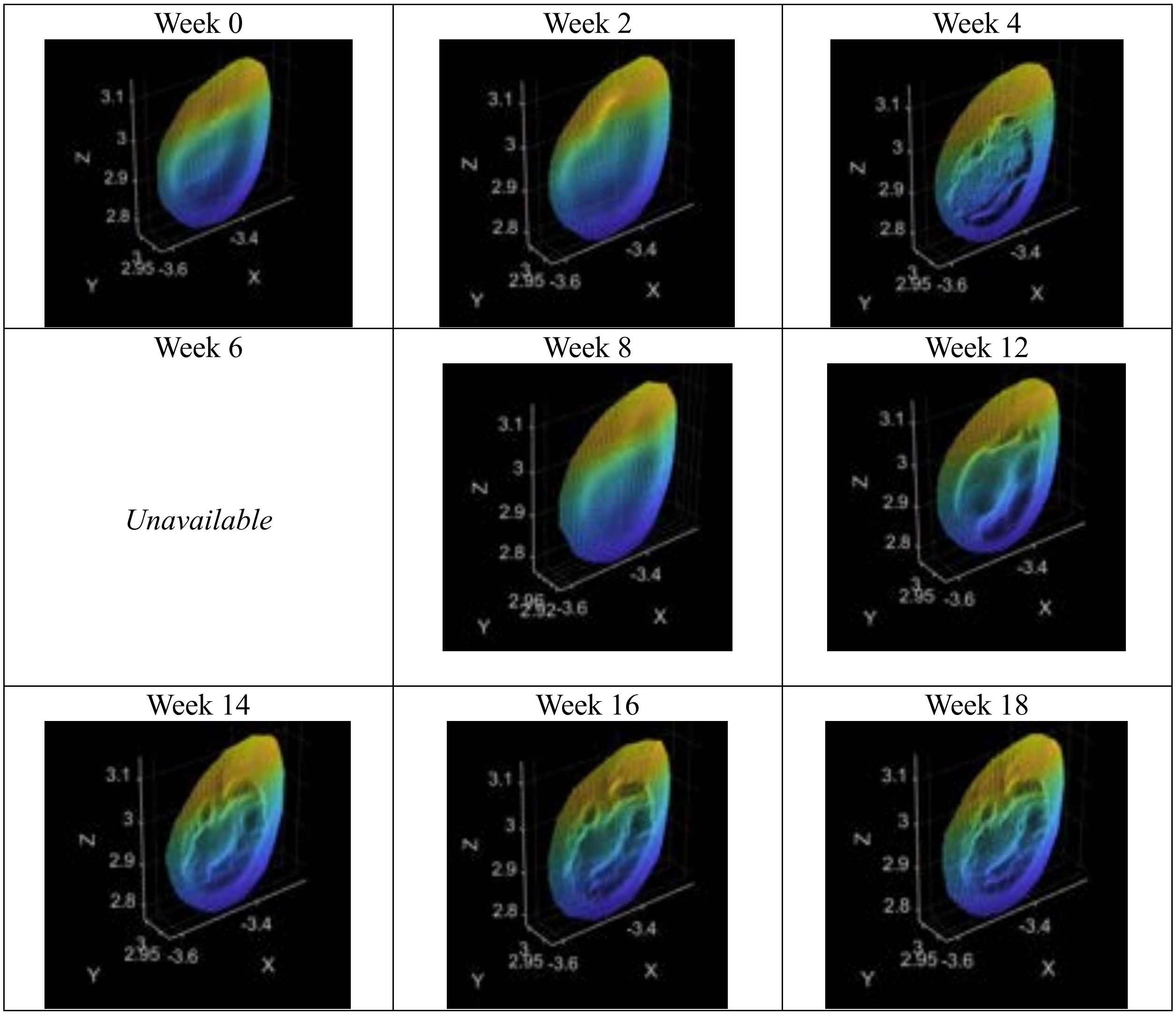

Figure C71. Change in meshed point cloud of exposed 2% area holiday data from Week 0 for C2G2[1].

Week 22

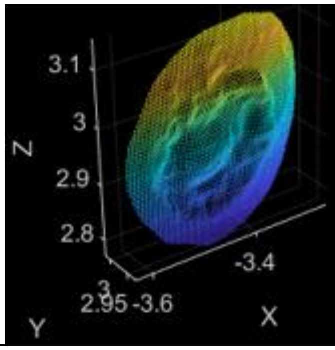

Week 24

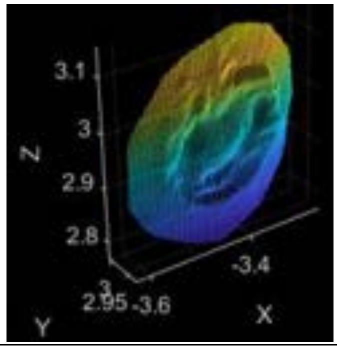

Week 30

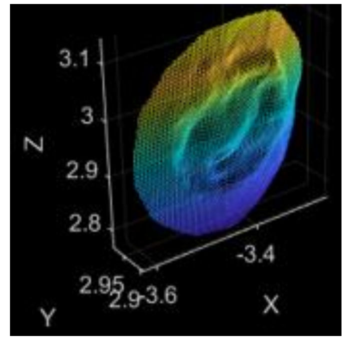

Week 36

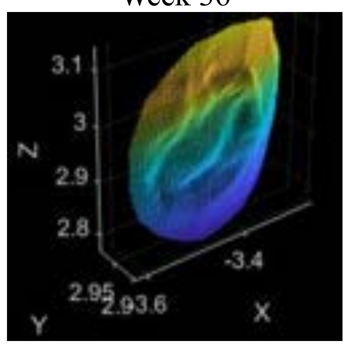

Figure C72. Change in meshed point cloud of exposed 2% area holiday data from Week 0 for C2G2[1] continued.

Figure C73. Side with 2% area holidays for C2G3.

Week 24	Week 30	Week 36
		

Figure C74. Side with 2% area holidays for C2G3 continued.

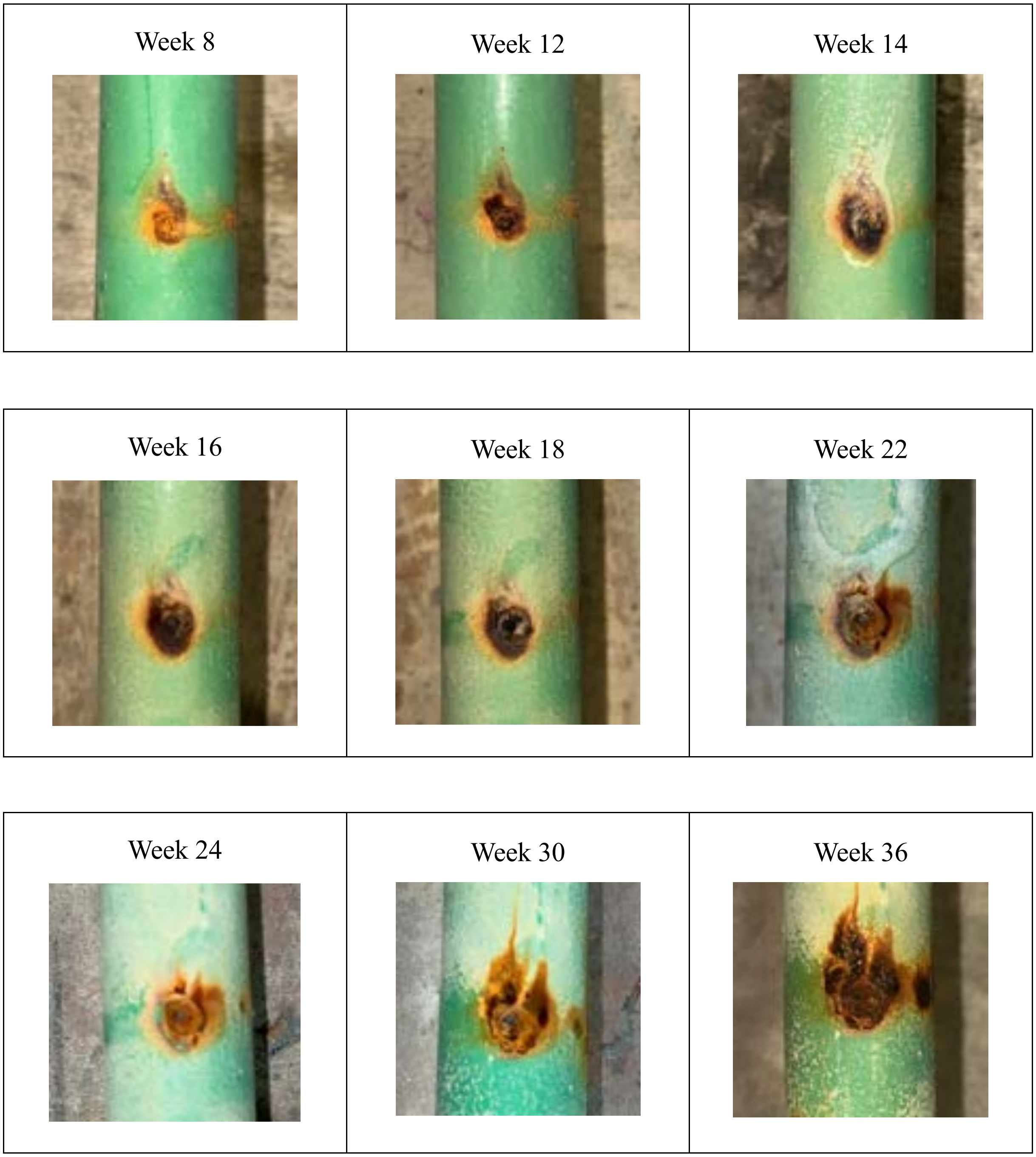

Figure C75. Exposed 2% area holiday for C2G3.

Week 8	Week 12	Week 14
		

Week 16	Week 18	Week 22
		

Figure C76. Side with 1% area holidays for C2G3.

Week 24	Week 30	Week 36
		

Figure C77. Side with 1% area holidays for C2G3 continued.

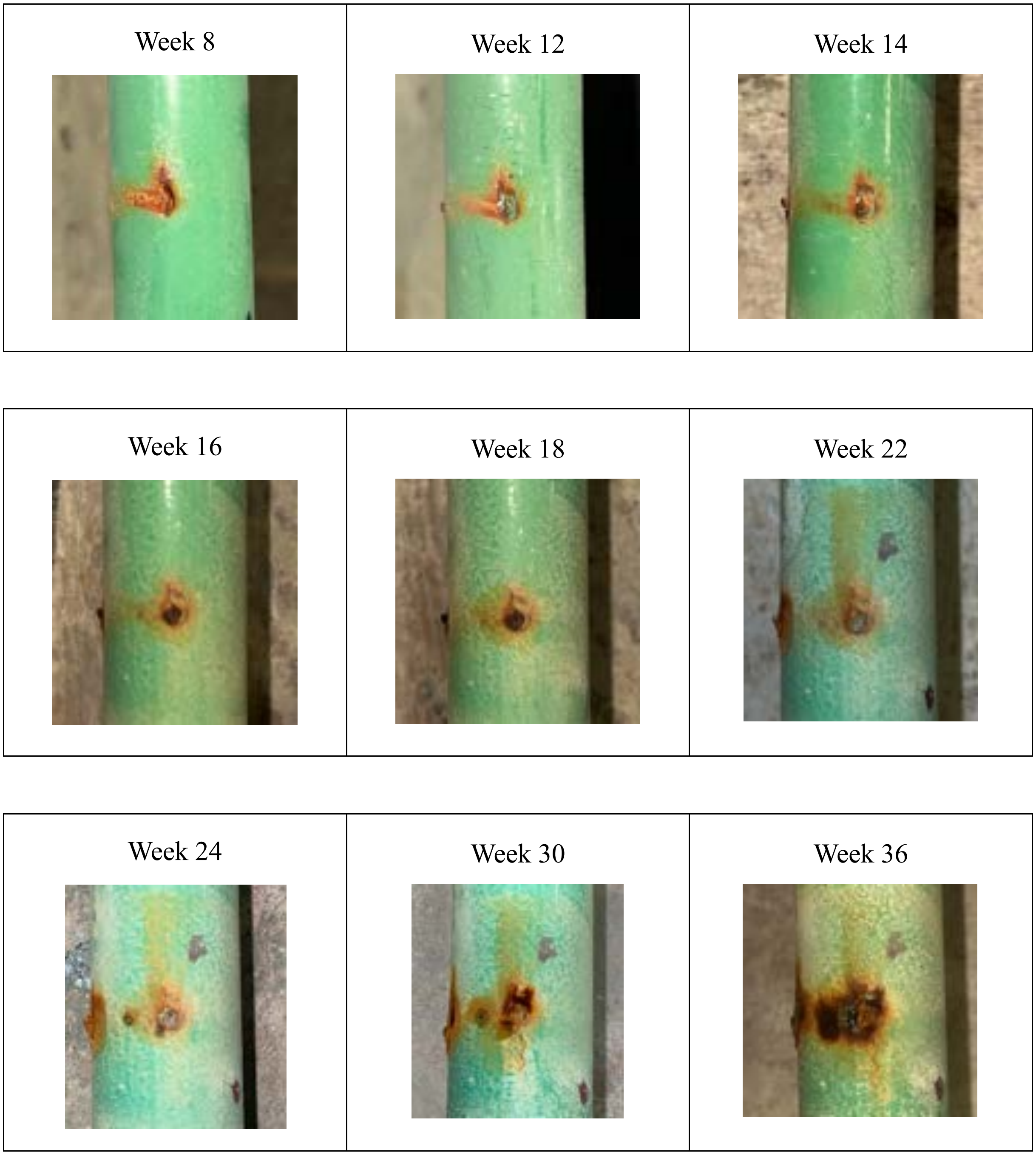

Figure C78. Exposed 1% area holiday for C2G3.

Week 0 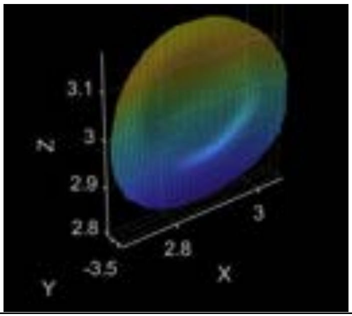	Week 2 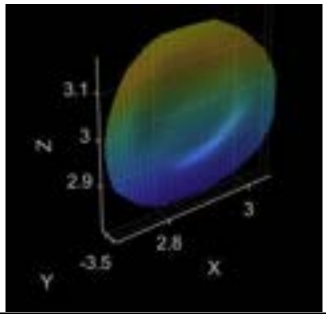	Week 4 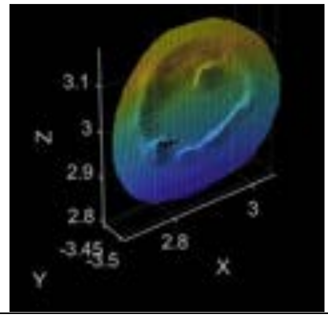
Week 6 *Unavailable*	Week 8 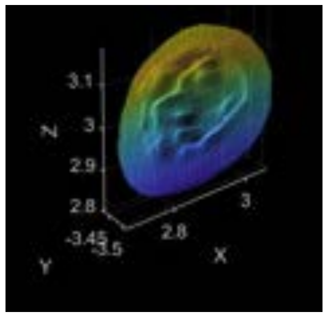	Week 12 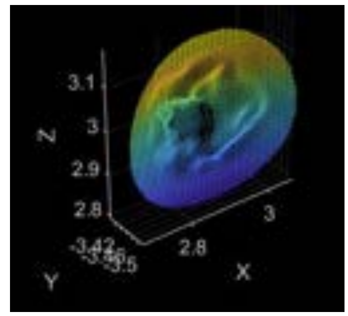
Week 14 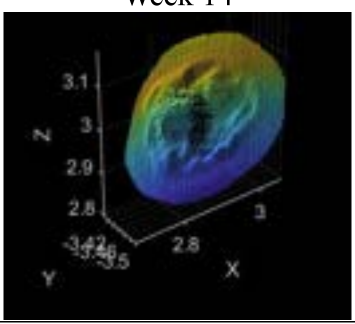	Week 16 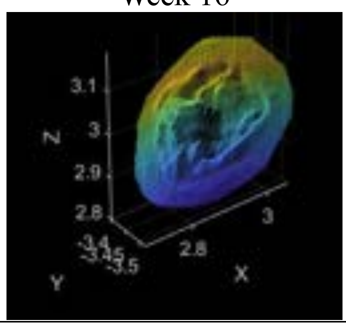	Week 18 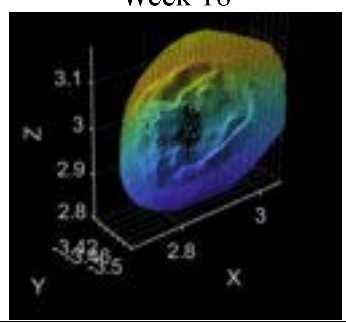

Figure C79. Change in meshed point cloud of exposed 2% area holiday data from Week 0 for C2G3.

Week 22

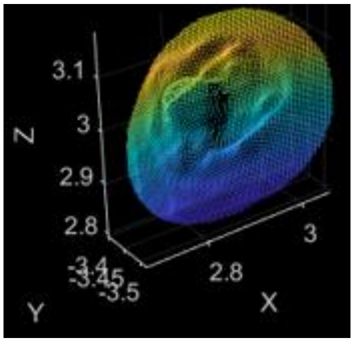

Week 24

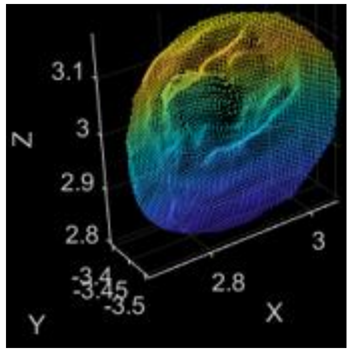

Week 30

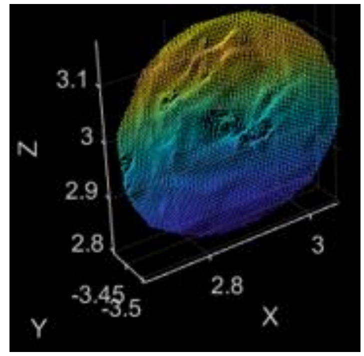

Week 36

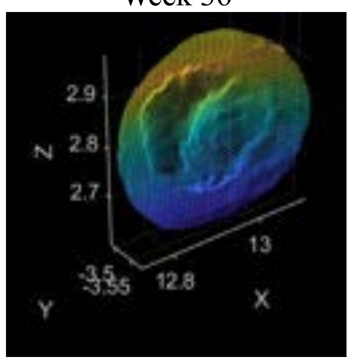

Figure C80. Change in meshed point cloud of exposed 2% area holiday data from Week 0 for C2G3 continued.

Week 8	Week 12	Week 14
		

Week 16	Week 18	Week 22
		

Figure C81. Side with 2% area holidays for C2P1.

Week 24	Week 30	Week 36
		

Figure C82. Side with 2% area holidays for C2P1 continued.

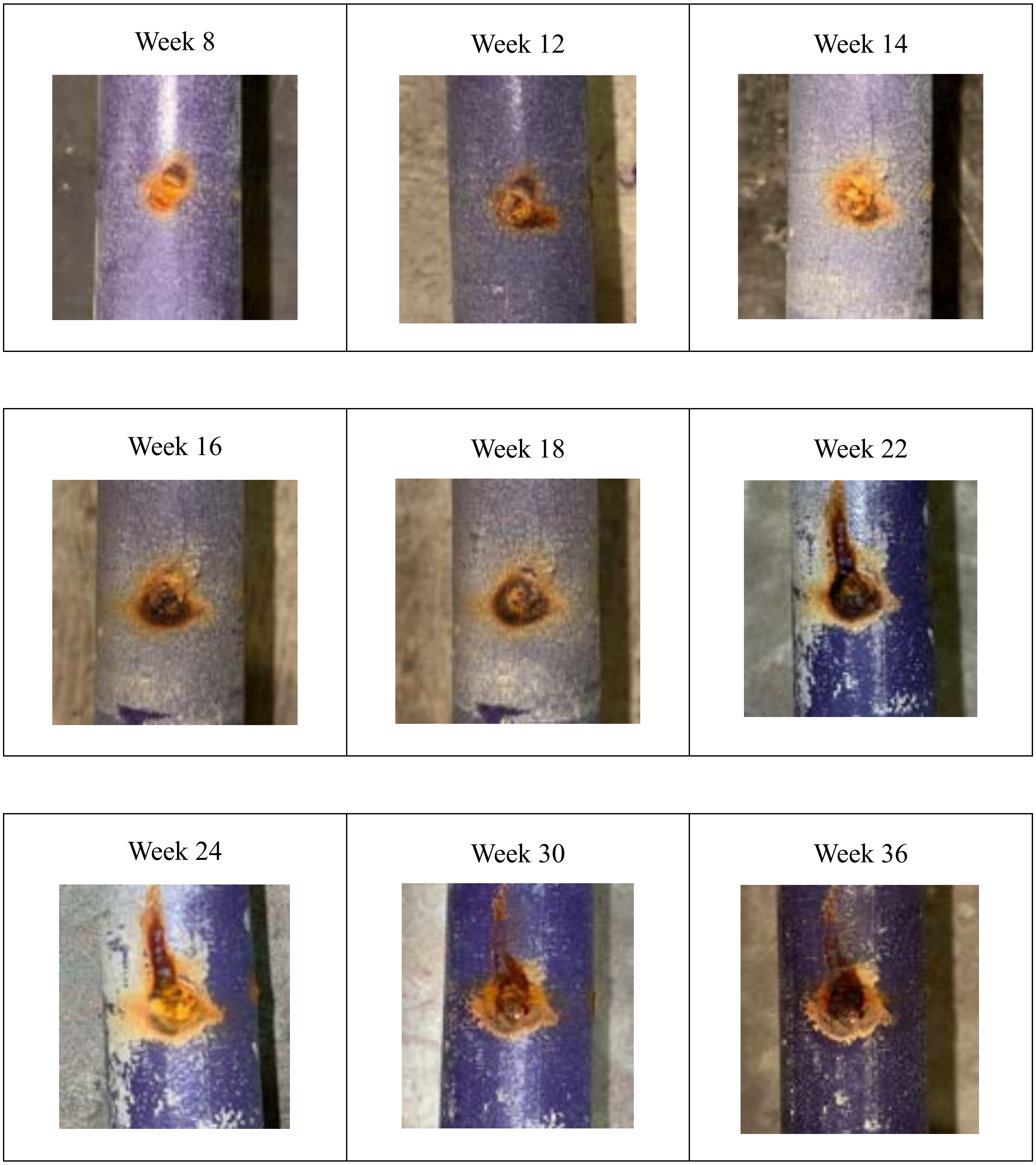

Figure C83. Exposed 2% area holiday for C2P1.

Figure C84. Side with 1% area holidays for C2P1.

Week 24	Week 30	Week 36
		

Figure C85. Side with 1% area holidays for C2P1 continued.

Week 8 	Week 12 	Week 14 
Week 16 	Week 18 	Week 22 
Week 24 	Week 30 	Week 36 

Figure C86. Exposed 1% area holiday for C2P1.

Week 0	Week 2	Week 4

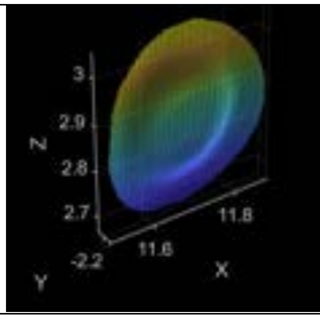

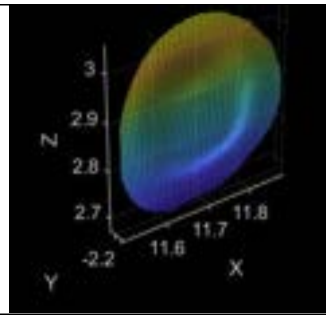

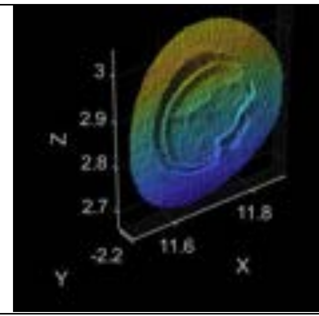

Week 6

Week 8

Week 12

Unavailable

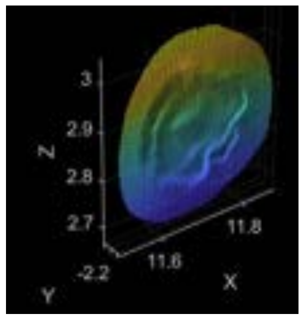

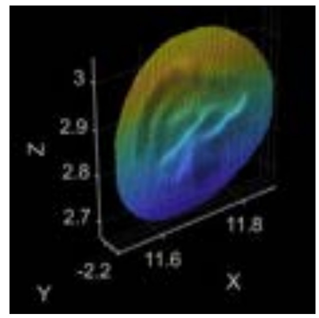

Week 14

Week 16

Week 18

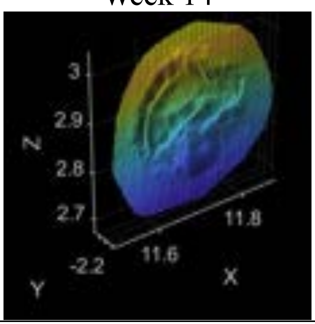

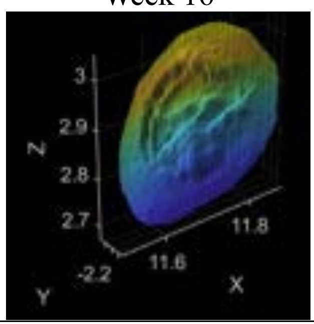

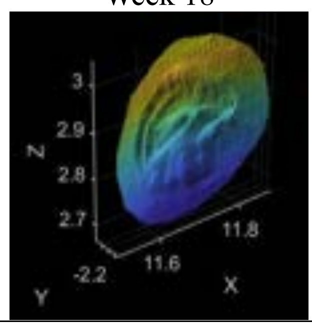

Figure C87. Change in meshed point cloud of exposed 2% area holiday data from Week 0 for C2P1.

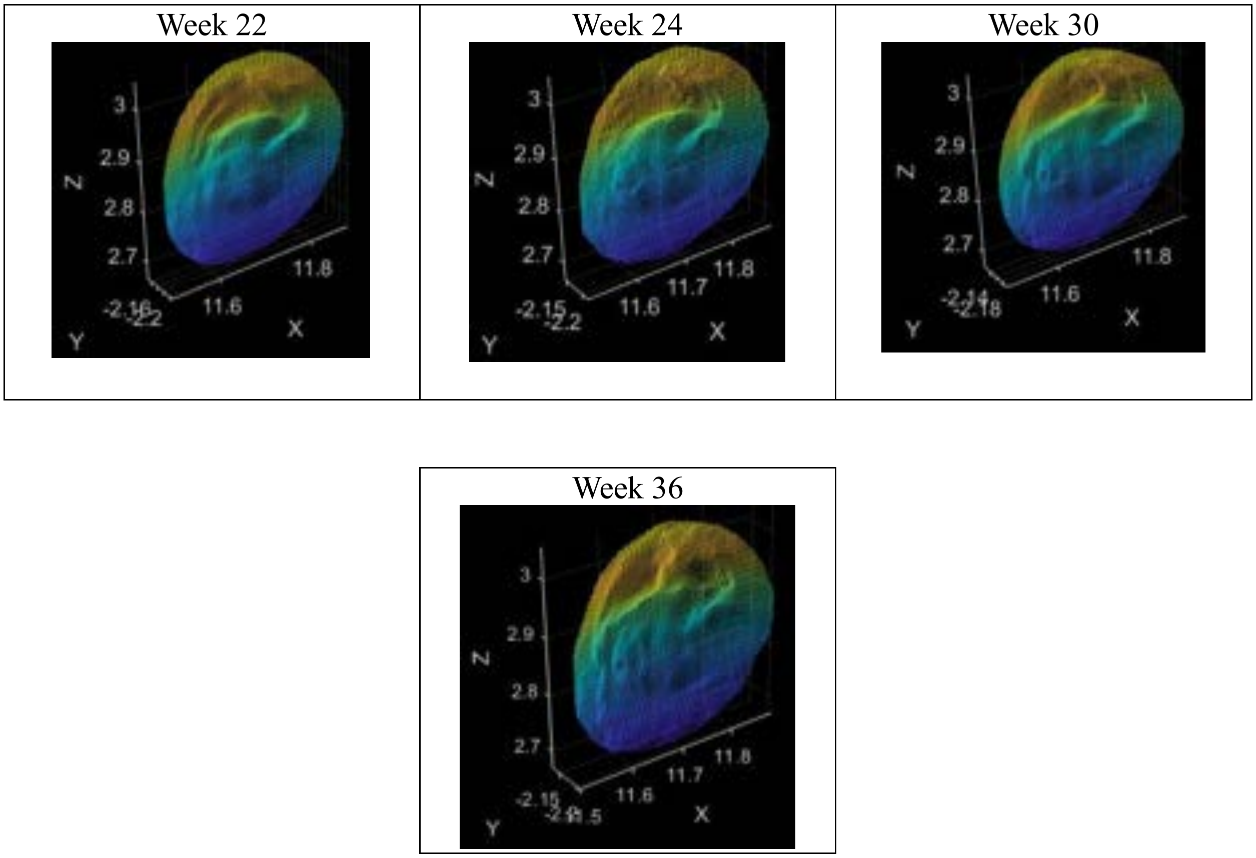

Figure C88. Change in meshed point cloud of exposed 2% area holiday data from Week 0 for C2P1 continued.

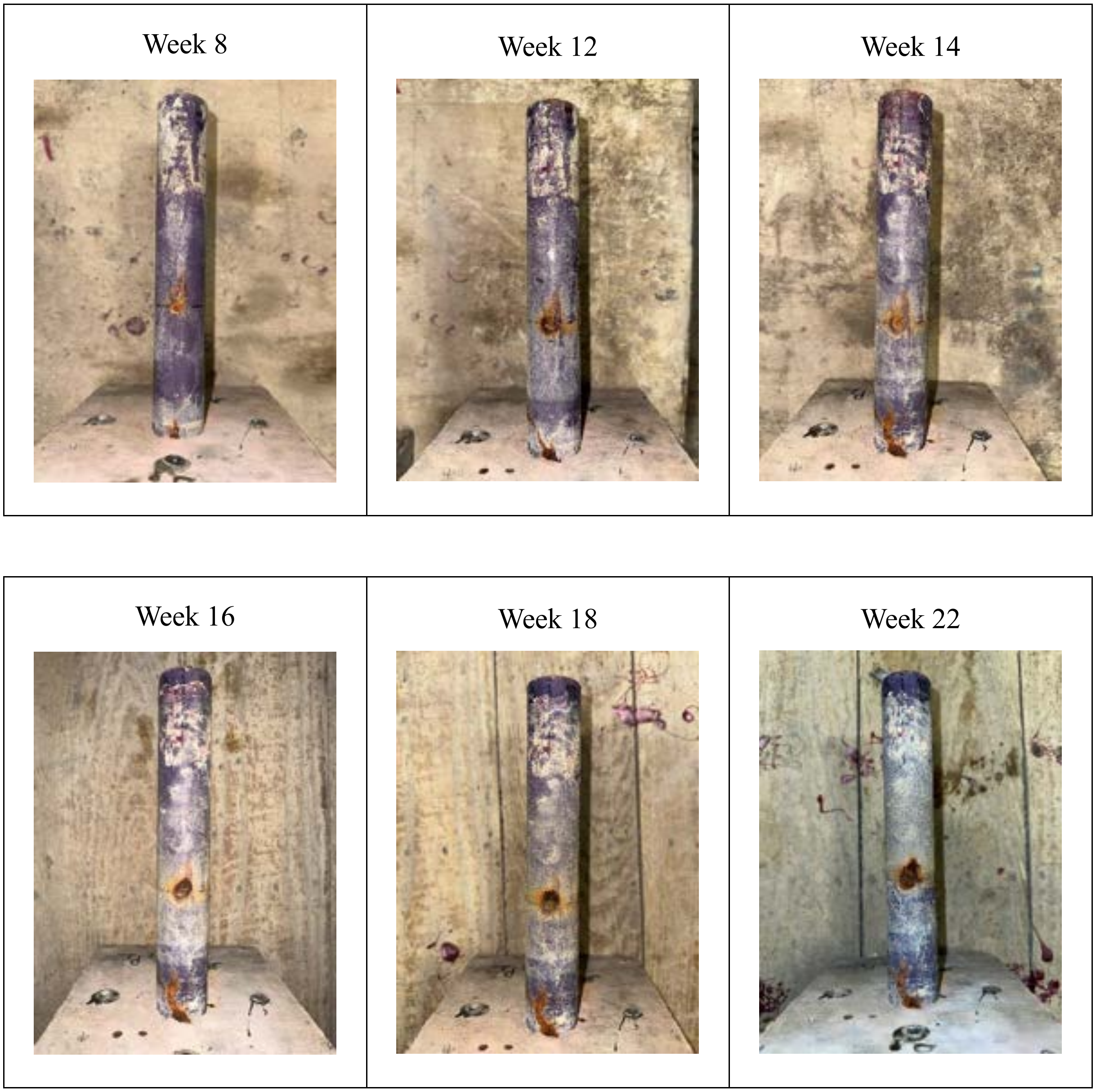

Figure C89. Side with 2% area holidays for C2P2.

Week 24	Week 30	Week 36
		

Figure C90. Side with 2% area holidays for C2P2 continued.

Week 8	Week 12	Week 14
		
Week 16	Week 18	Week 22
		
Week 24	Week 30	Week 36
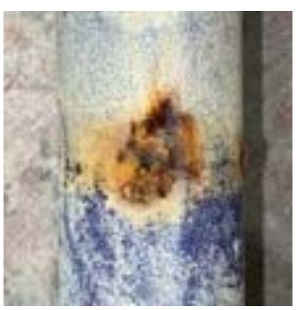		

Figure C91. Exposed 2% area holiday for C2P2.

Week 8	Week 12	Week 14
		

Week 16	Week 18	Week 22
		

Figure C92. Side with 1% area holidays for C2P2.

Week 24	Week 30	Week 36

Figure C93. Side with 1% area holidays for C2P2 continued.

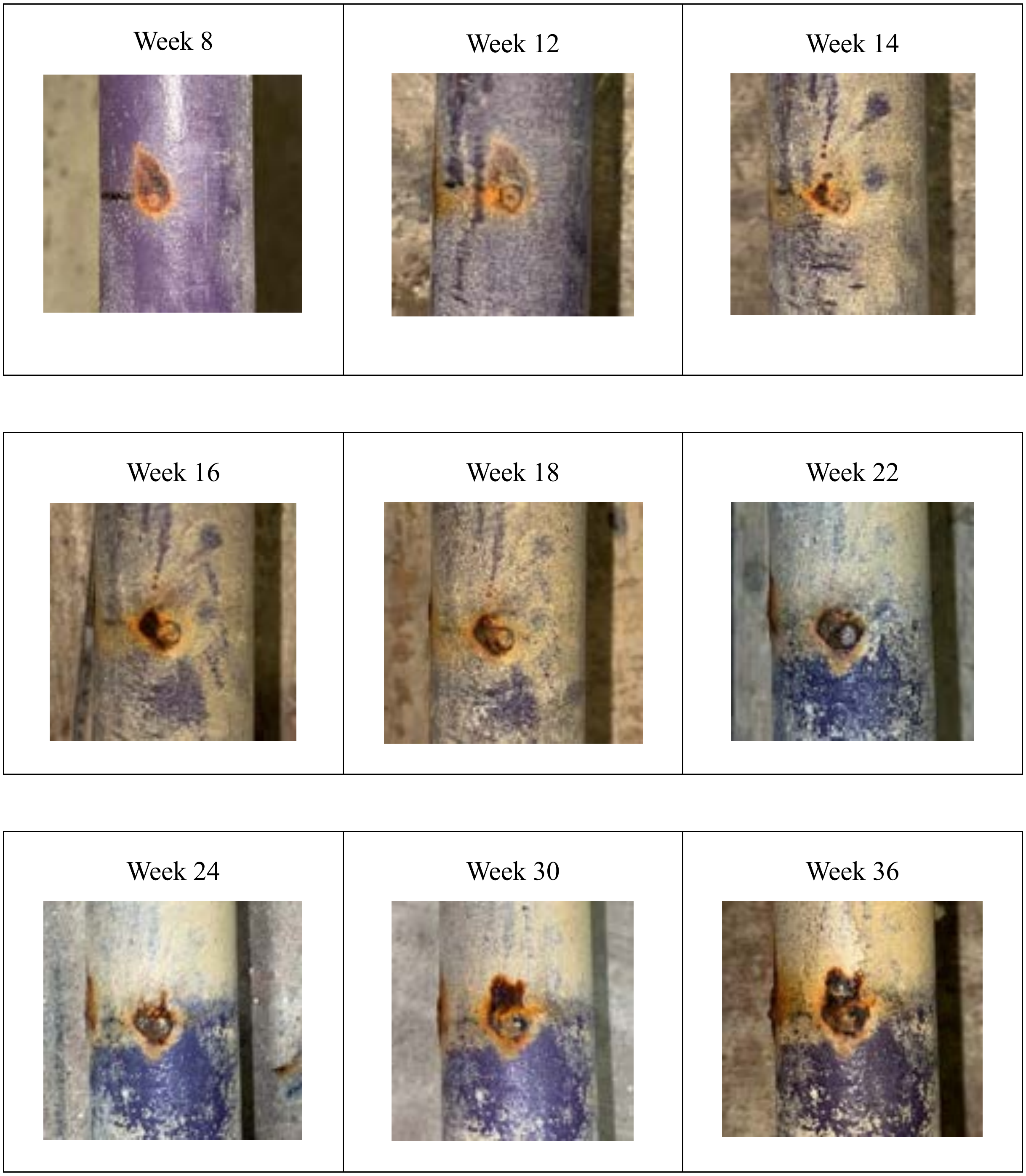

Figure C94. Exposed 1% area holiday for C2P2.

<table>
<tr>
<td>Week 0
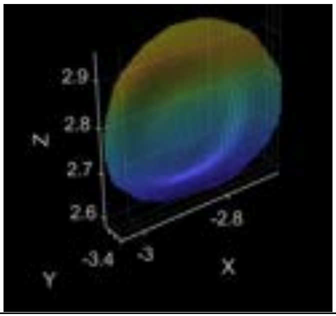</td>
<td>Week 2
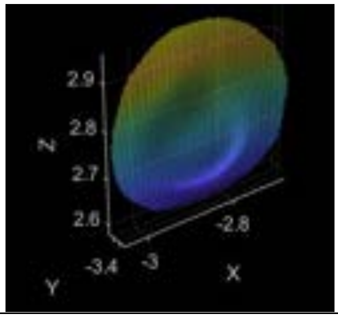</td>
<td>Week 4
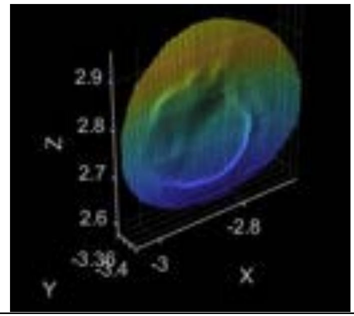</td>
</tr>
<tr>
<td>Week 6
Unavailable</td>
<td>Week 8
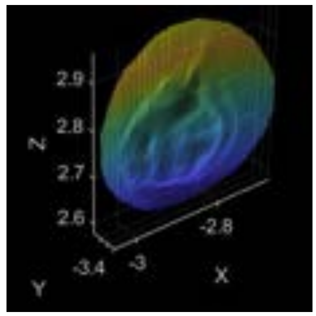</td>
<td>Week 12
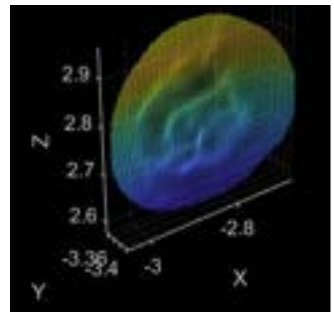</td>
</tr>
<tr>
<td>Week 14
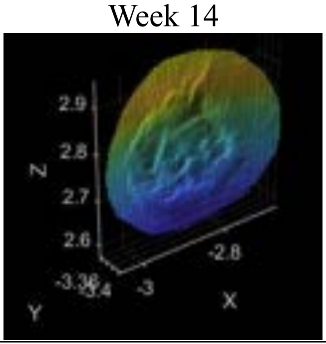</td>
<td>Week 16
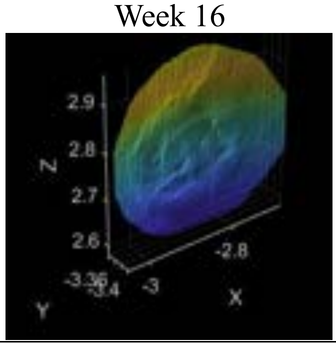</td>
<td>Week 18
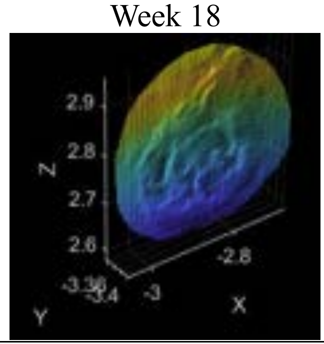</td>
</tr>
</table>

Figure C95. Change in meshed point cloud of exposed 2% area holiday data from Week 0 for C2P2.

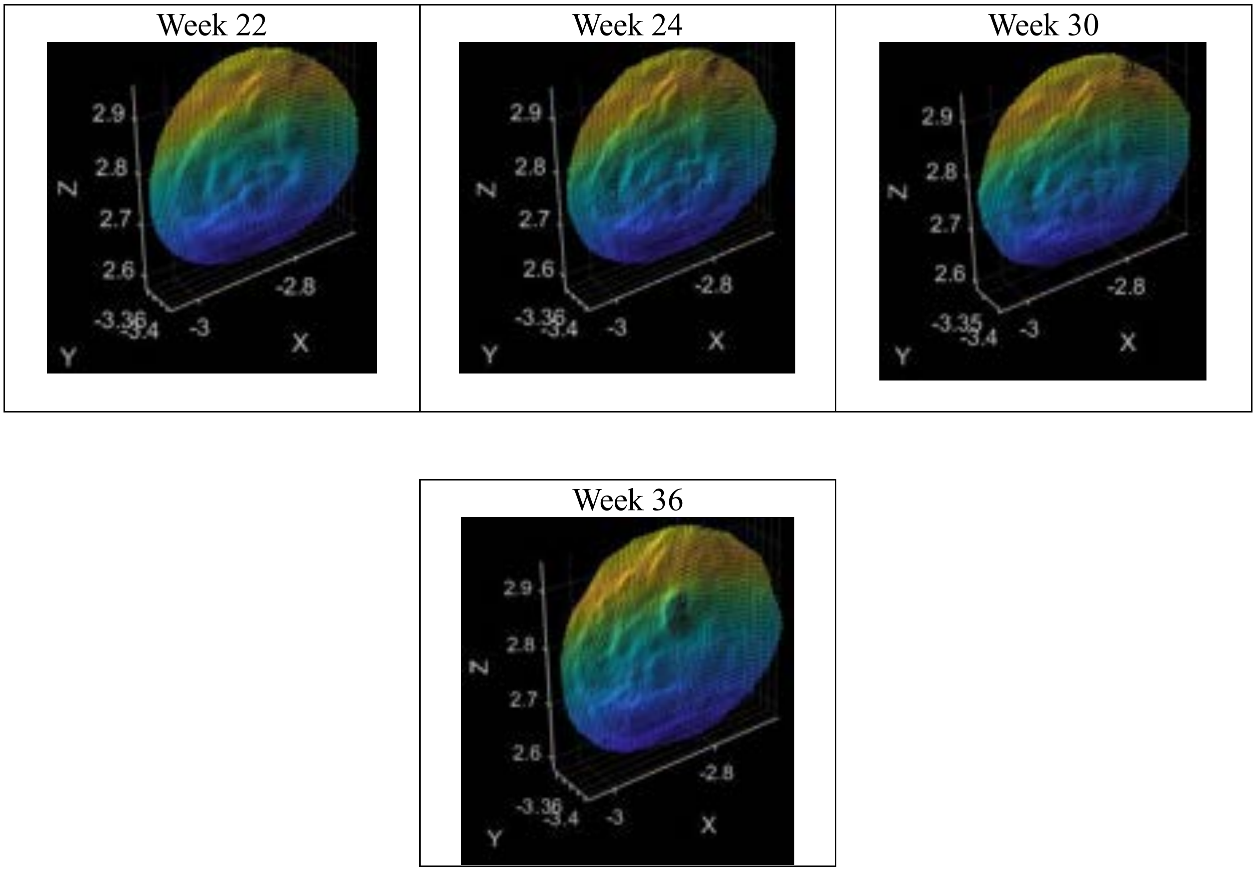

Figure C96. Change in meshed point cloud of exposed 2% area holiday data from Week 0 for C2P2 continued.

Week 8	Week 12	Week 14
		

Week 16	Week 18	Week 22
		

Figure C97. Side with 2% area holidays for C2P2[2].

[2] - corresponds to C2P2X

Week 24	Week 30	Week 36
		

Figure C98. Side with 2% area holidays for C2P2[2] continued.

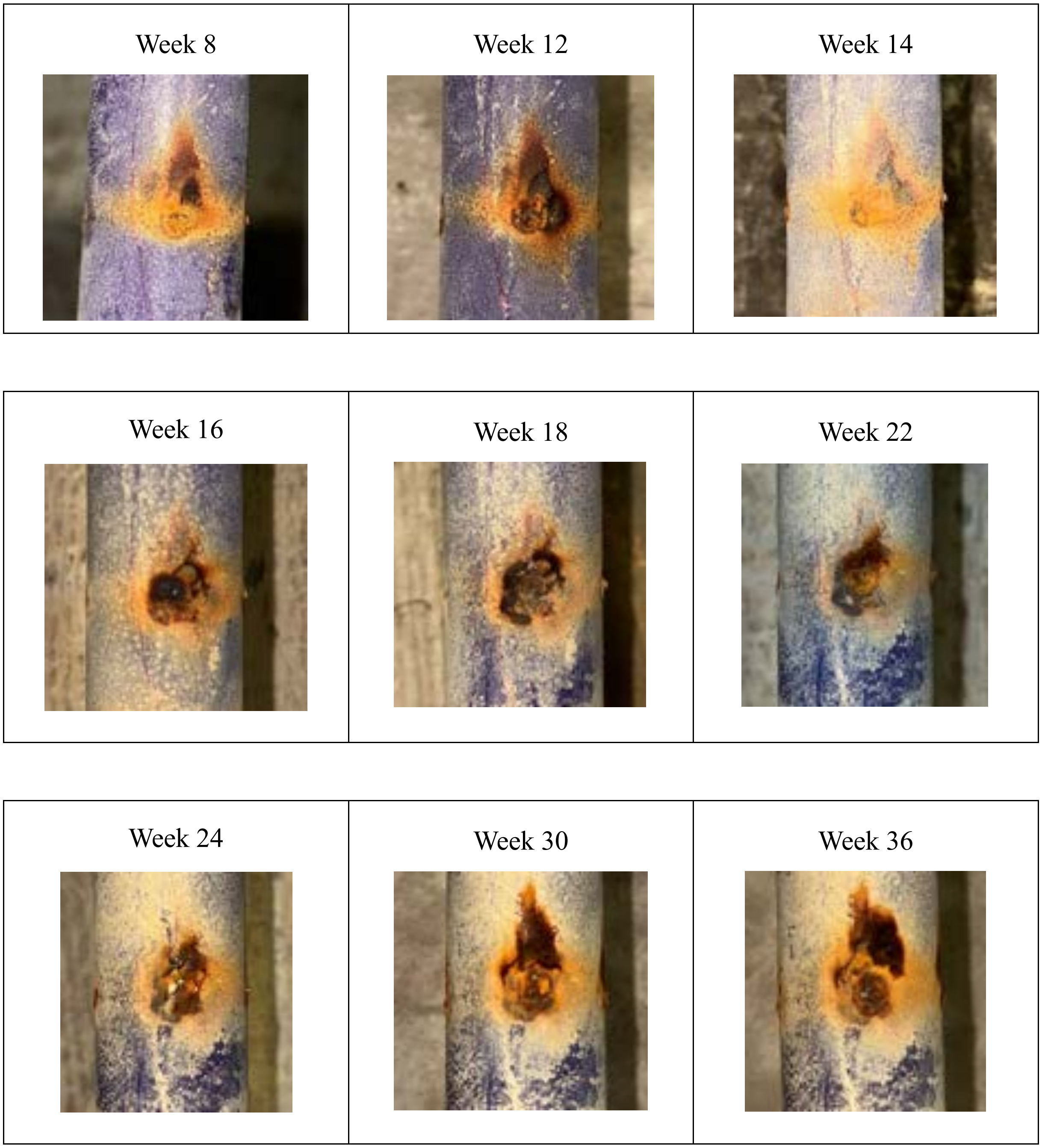

Figure C99. Exposed 2% area holiday for C2P2[2].

Week 8	Week 12	Week 14
		

Week 16	Week 18	Week 22
		

Figure C100. Side with 1% area holidays for C2P2[2].

Week 24	Week 30	Week 36
	*Unavailable*	

Figure C101. Side with 1% area holidays for C2P2[2] continued.

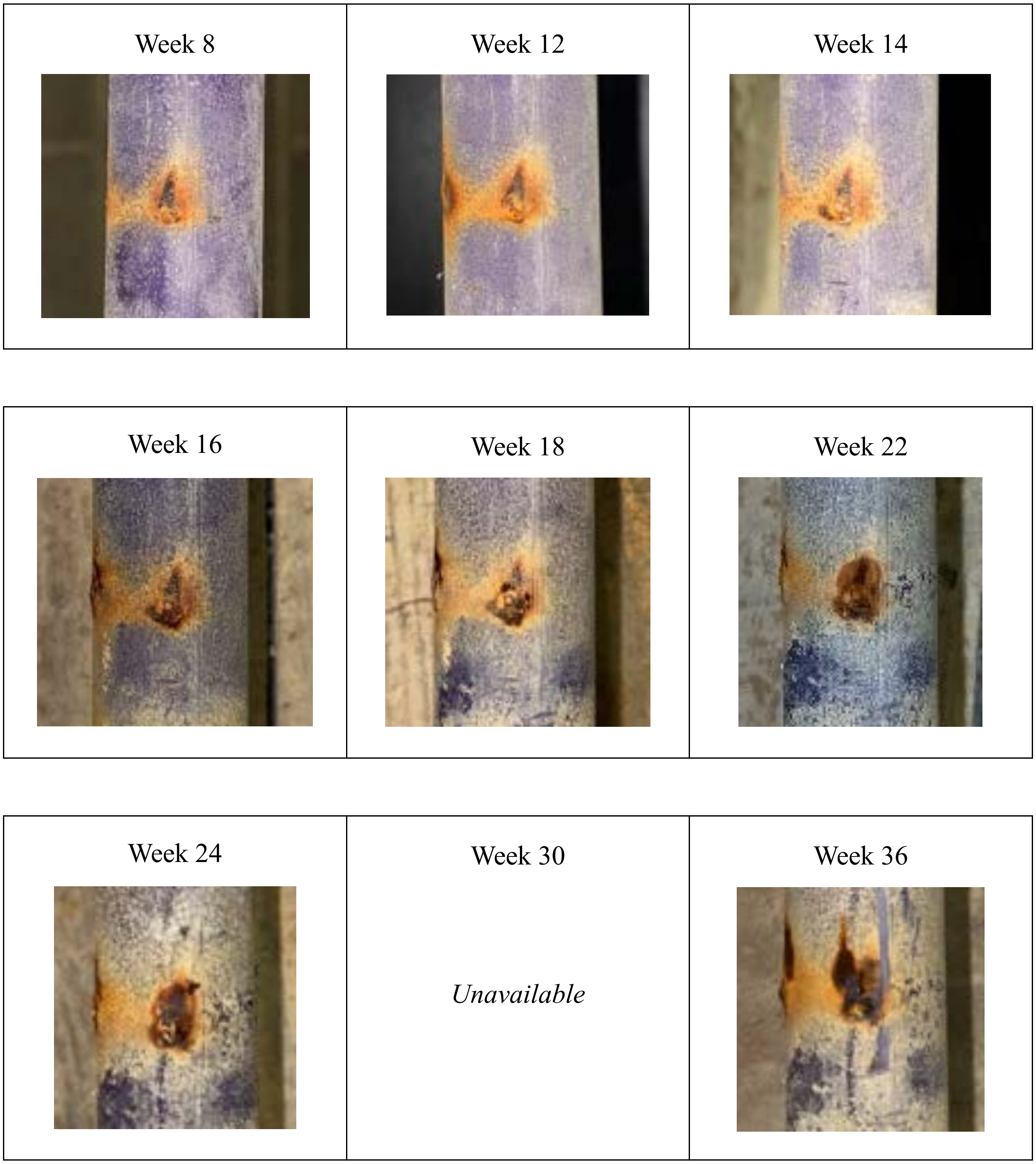

Figure C102. Exposed 1% area holiday for C2P2[2].

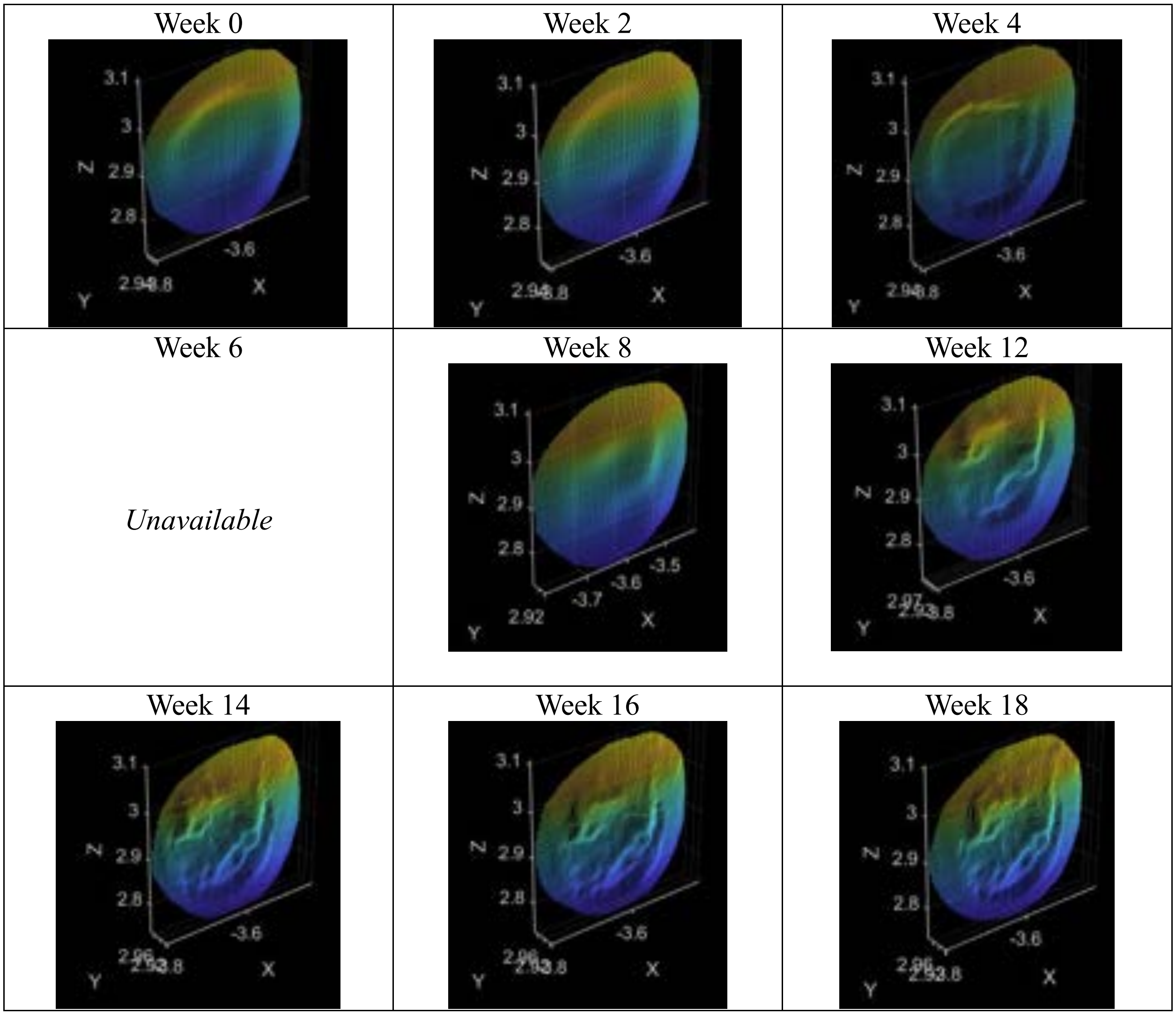

Figure C103. Change in meshed point cloud of exposed 2% area holiday data from Week 0 for C2P2².

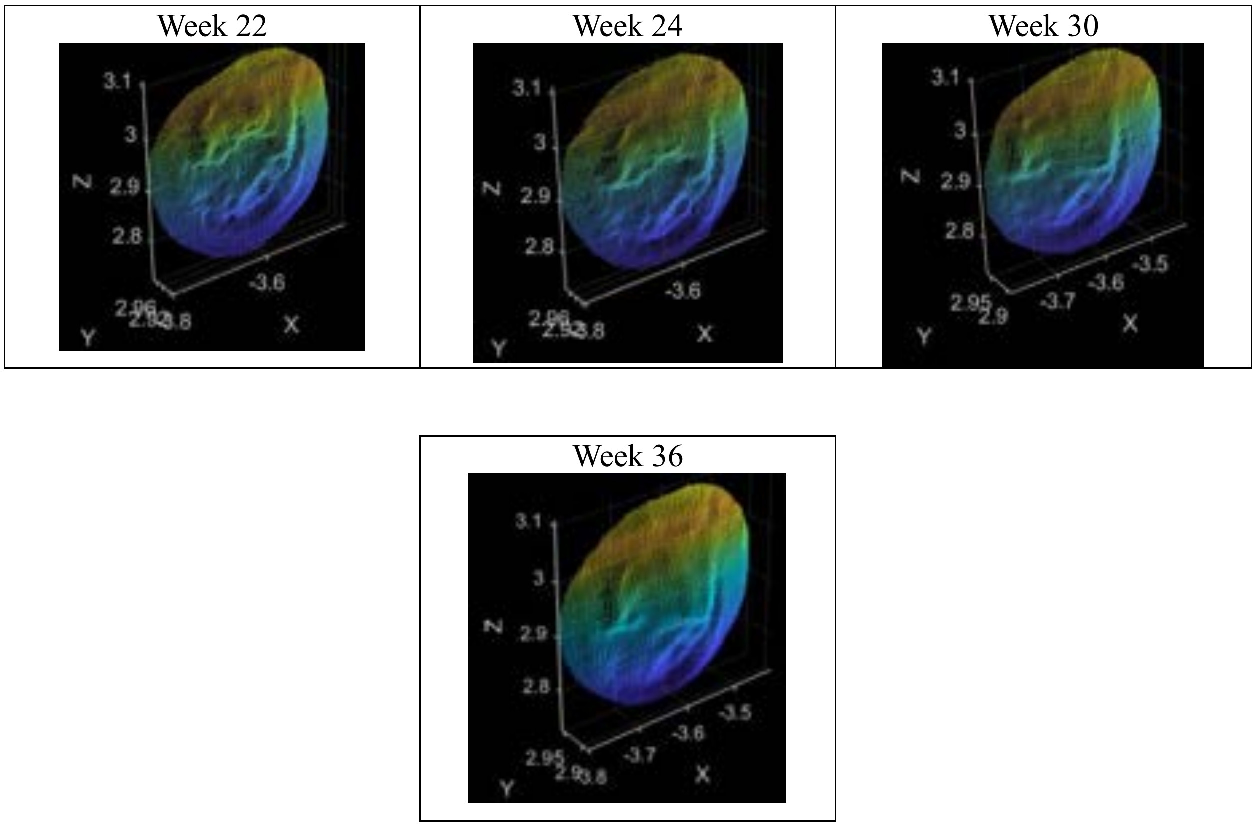

Figure C104. Change in meshed point cloud of exposed 2% area holiday data from Week 0for C2P2[2] continued.

Week 8	Week 12	Week 14
Unavailable		

Week 16	Week 18	Week 22
		

Figure C105. Side with 2% area holidays for C2P3.

Week 24	Week 30	Week 36
		

Figure C106. Side with 2% area holidays for C2P3 continued.

Week 8	Week 12	Week 14
Unavailable		

Week 16	Week 18	Week 22
		

Week 24	Week 30	Week 36
		

Figure C107. Exposed 2% area holiday for C2P3.

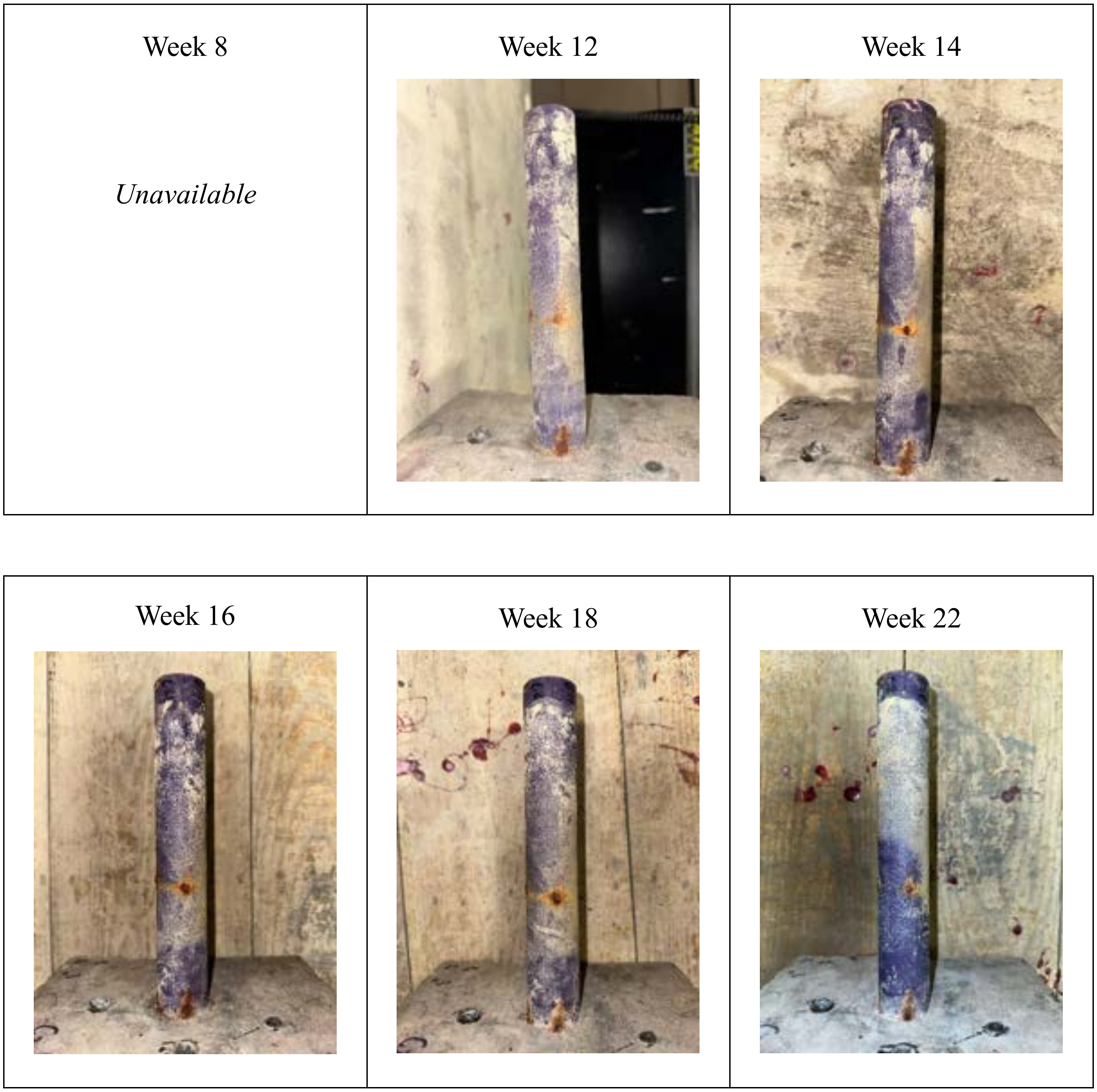

Figure C108. Side with 1% area holidays for C2P3.

Week 24	Week 30	Week 36
		

Figure C109. Side with 1% area holidays for C2P3 continued.

Week 8	Week 12	Week 14
Unavailable		

Week 16	Week 18	Week 22
		

Week 24	Week 30	Week 36
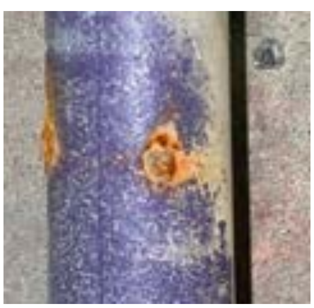		

Figure C110. Exposed 1% area holiday for C2P3.

Week 0	Week 2	Week 4
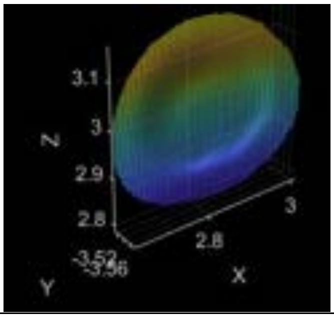	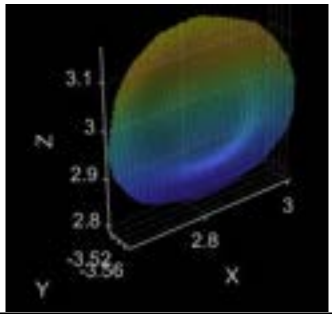	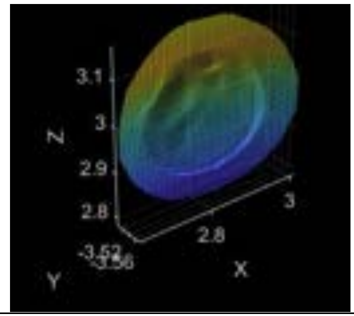
Week 6	Week 8	Week 12
Unavailable	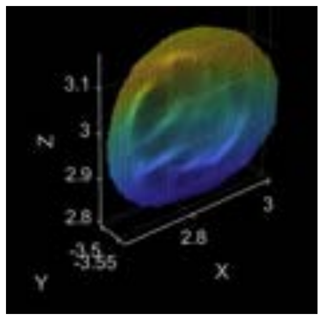	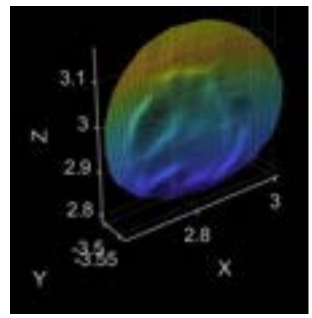
Week 14	Week 16	Week 18
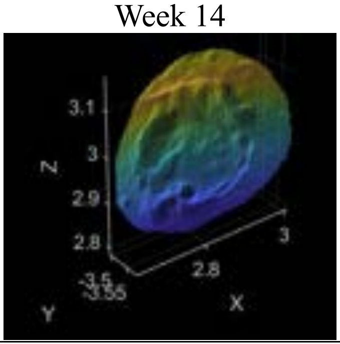	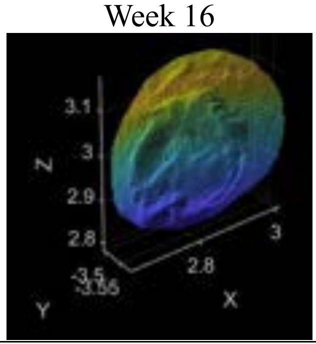	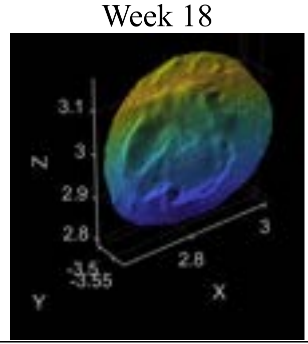

Figure C111. Change in meshed point cloud of exposed 2% area holiday data from Week 0 for C2P3.

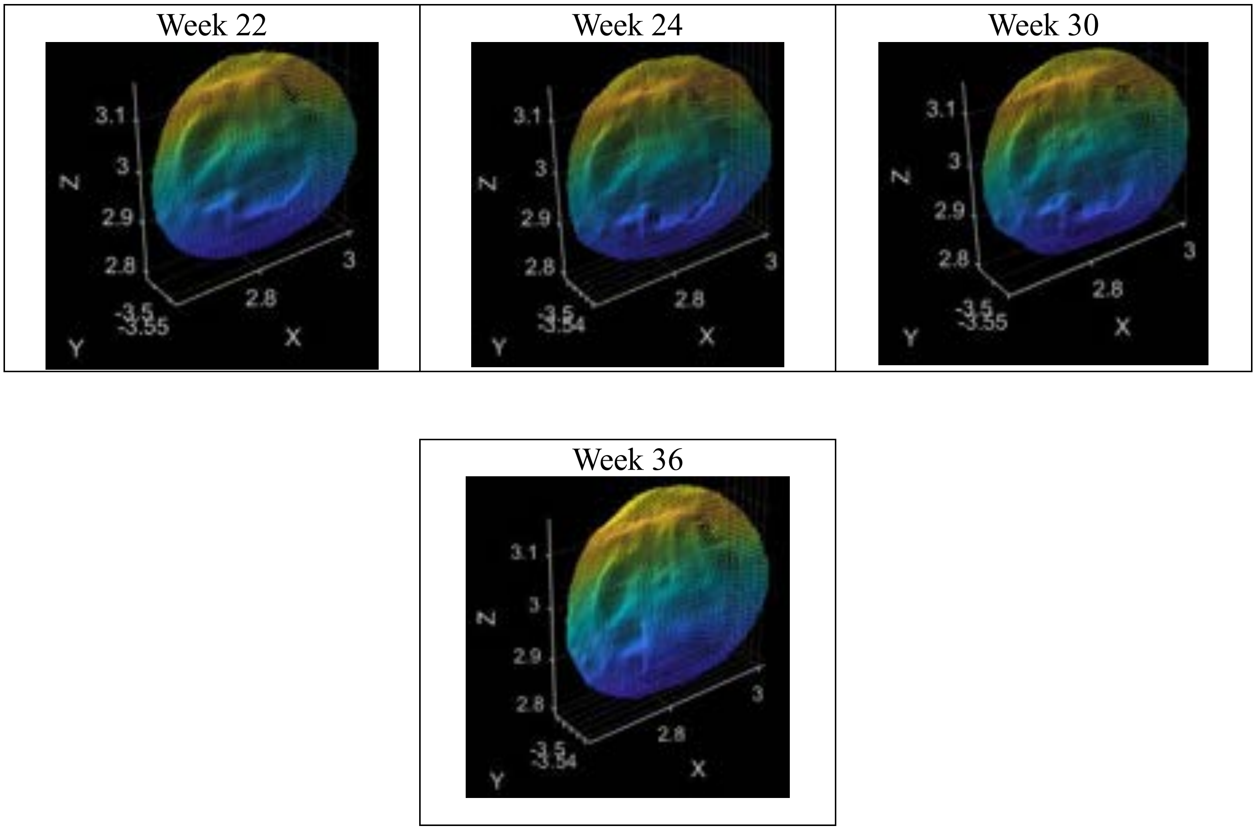

Figure C112. Change in meshed point cloud of exposed 2% area holiday data from Week 0 for C2P3 continued.

Week 8	Week 12	Week 14
		

Week 16	Week 18	Week 22
		

Figure C113. Side with 2% area holidays for C2P3X.

Week 24	Week 30	Week 36
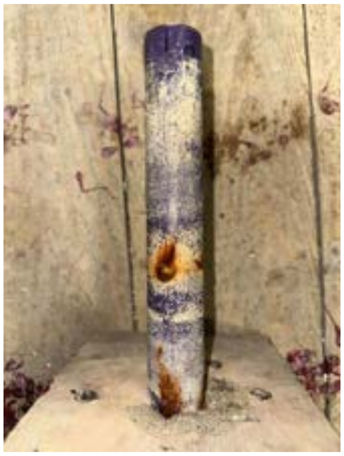		

Figure C114. Side with 2% area holidays for C2P3[3] continued.

[3] -corresponds to C2P3X

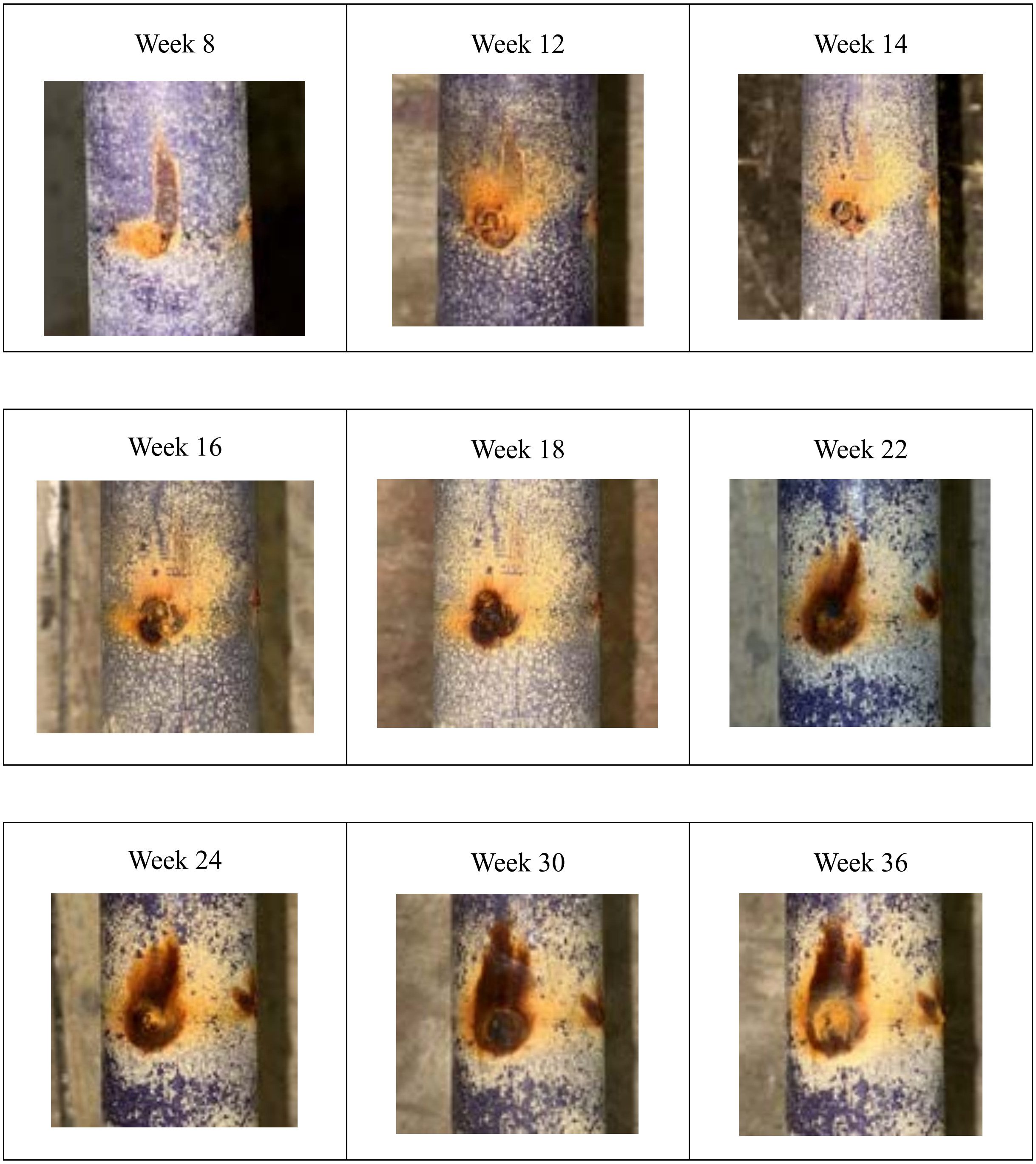

Figure C115. Exposed 2% area holiday for C2P3[3].

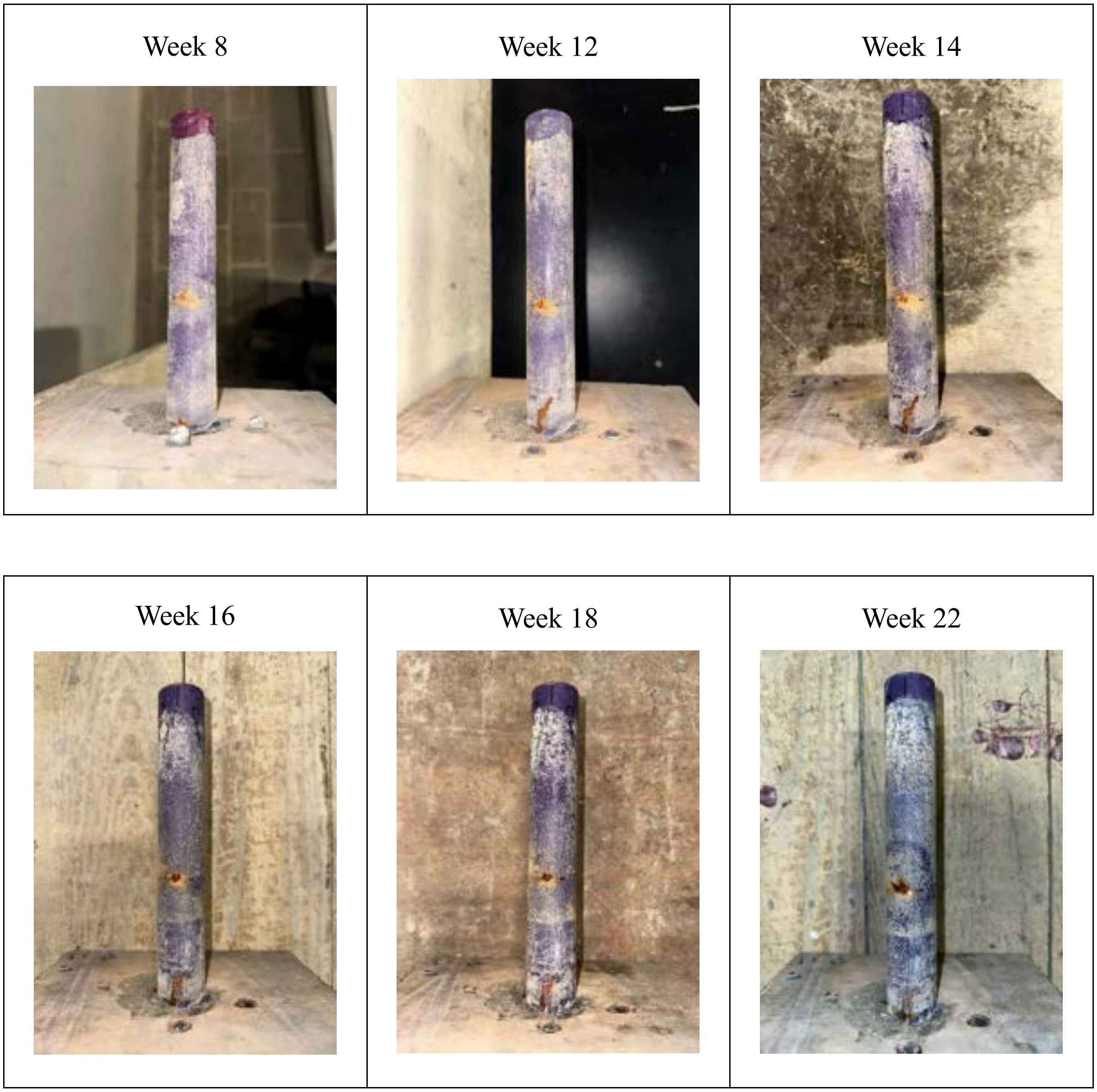

Figure C116. Side with 1% area holidays for C2P3[3].

Week 24	Week 30	Week 36
		

Figure C117. Side with 1% area holidays for C2P3[3] continued.

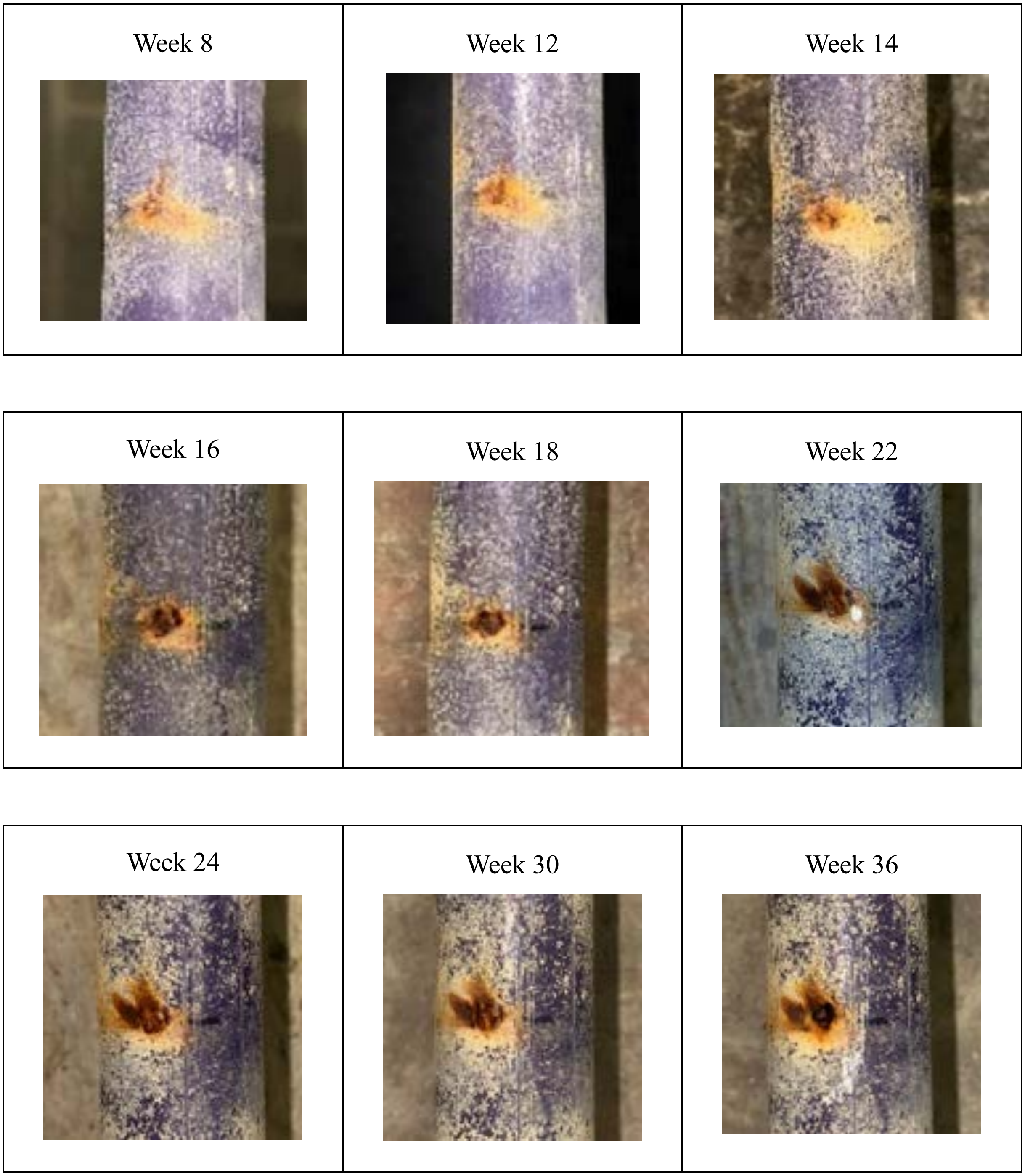

Figure C118. Exposed 1% area holiday for C2P3[3].

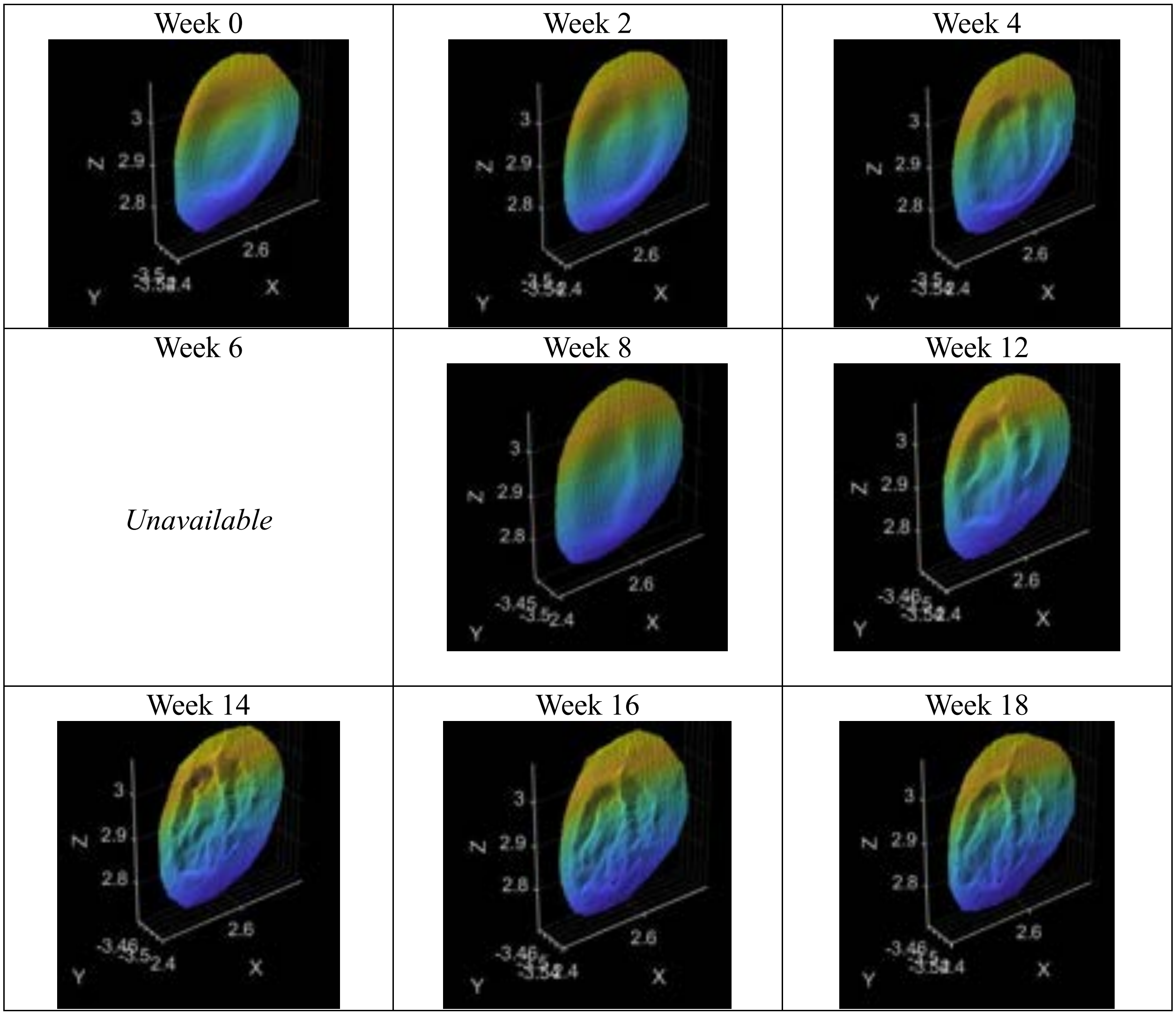

Figure C119. Change in meshed point cloud of exposed 2% area holiday data from Week 0 for C2P3[3].

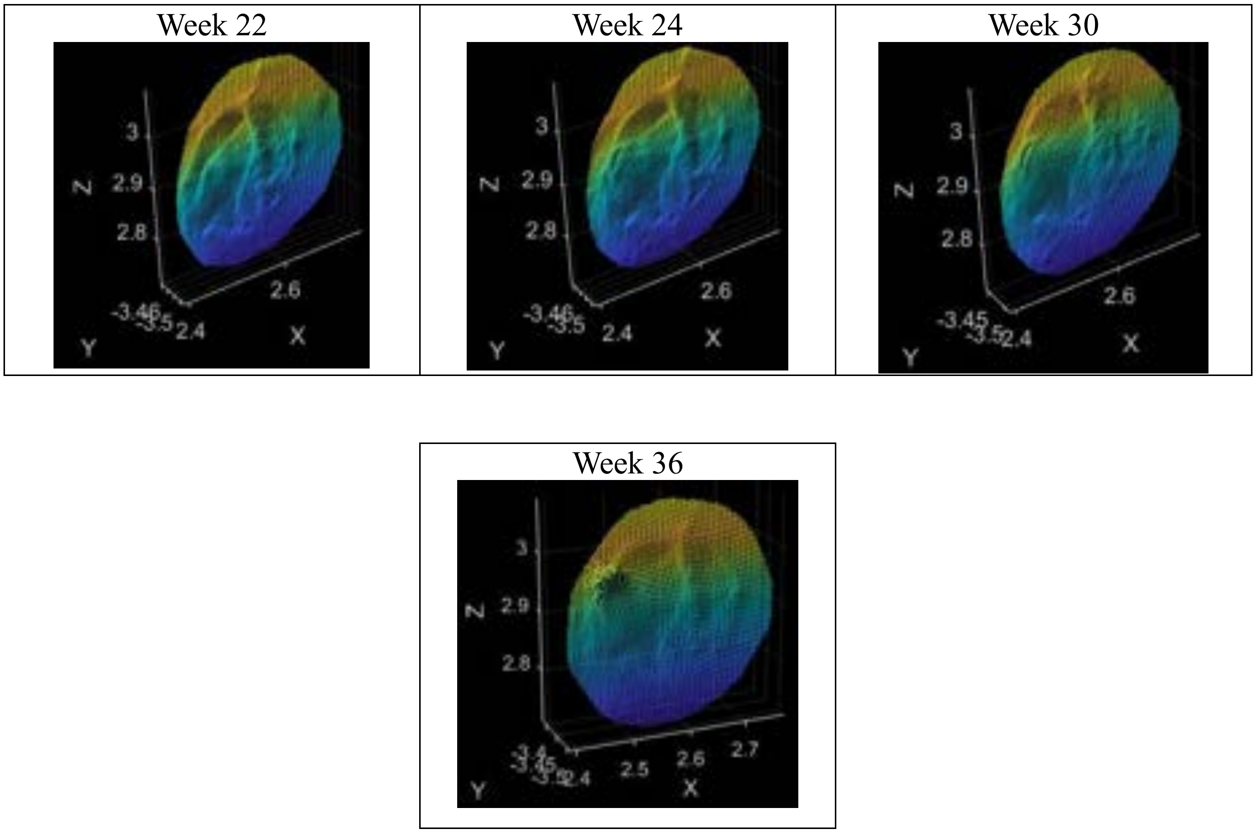

Figure C120. Change in meshed point cloud of exposed 2% area holiday data from Week 0 for C2P3[3] continued.

1- corresponds to C2P2X
2- corresponds to C2P3X

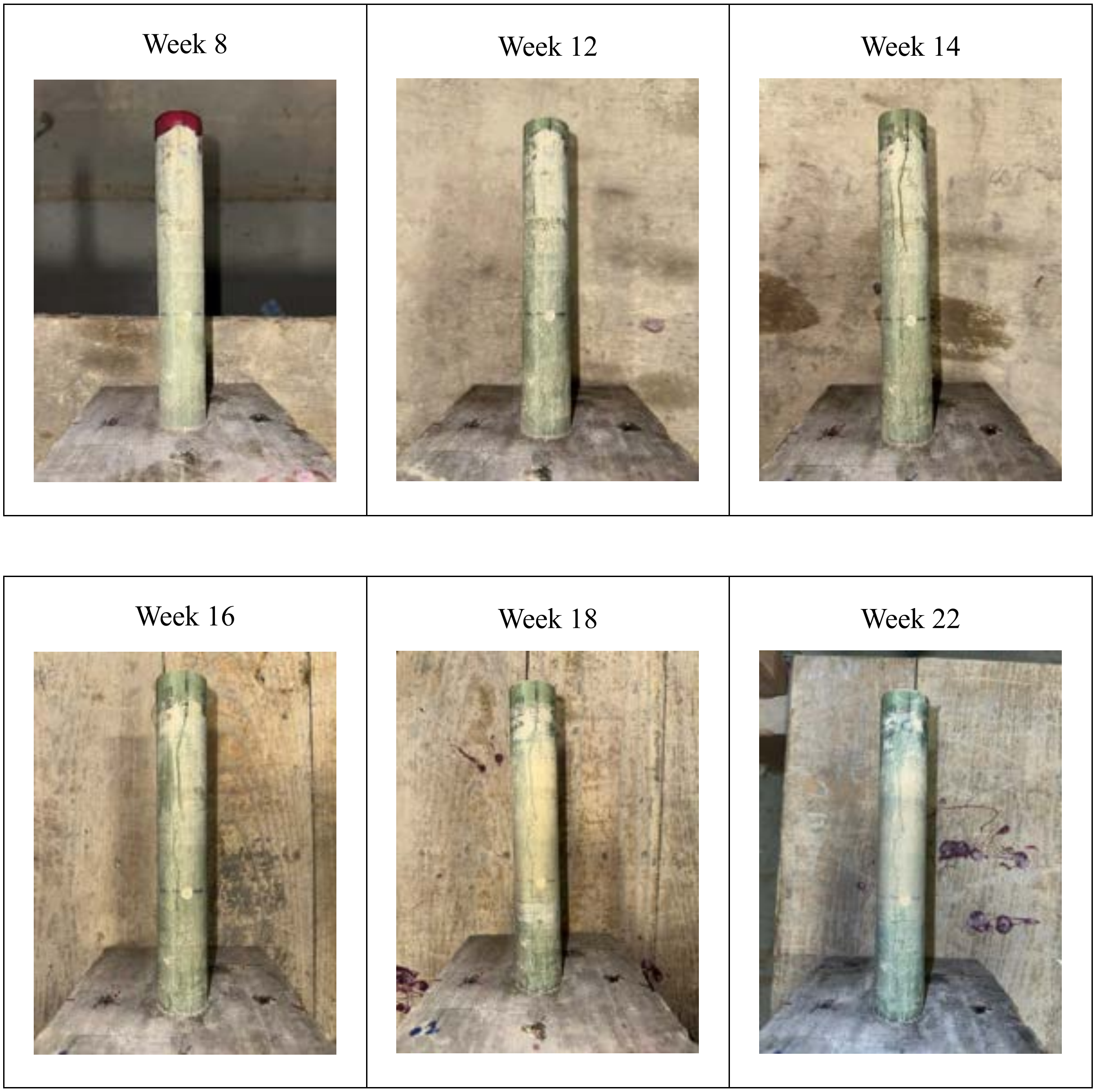

Figure C121. Side with 2% area holidays for FN1.

Week 24	Week 30	Week 36
		

Figure C122. Side with 2% area holidays for FN1 continued.

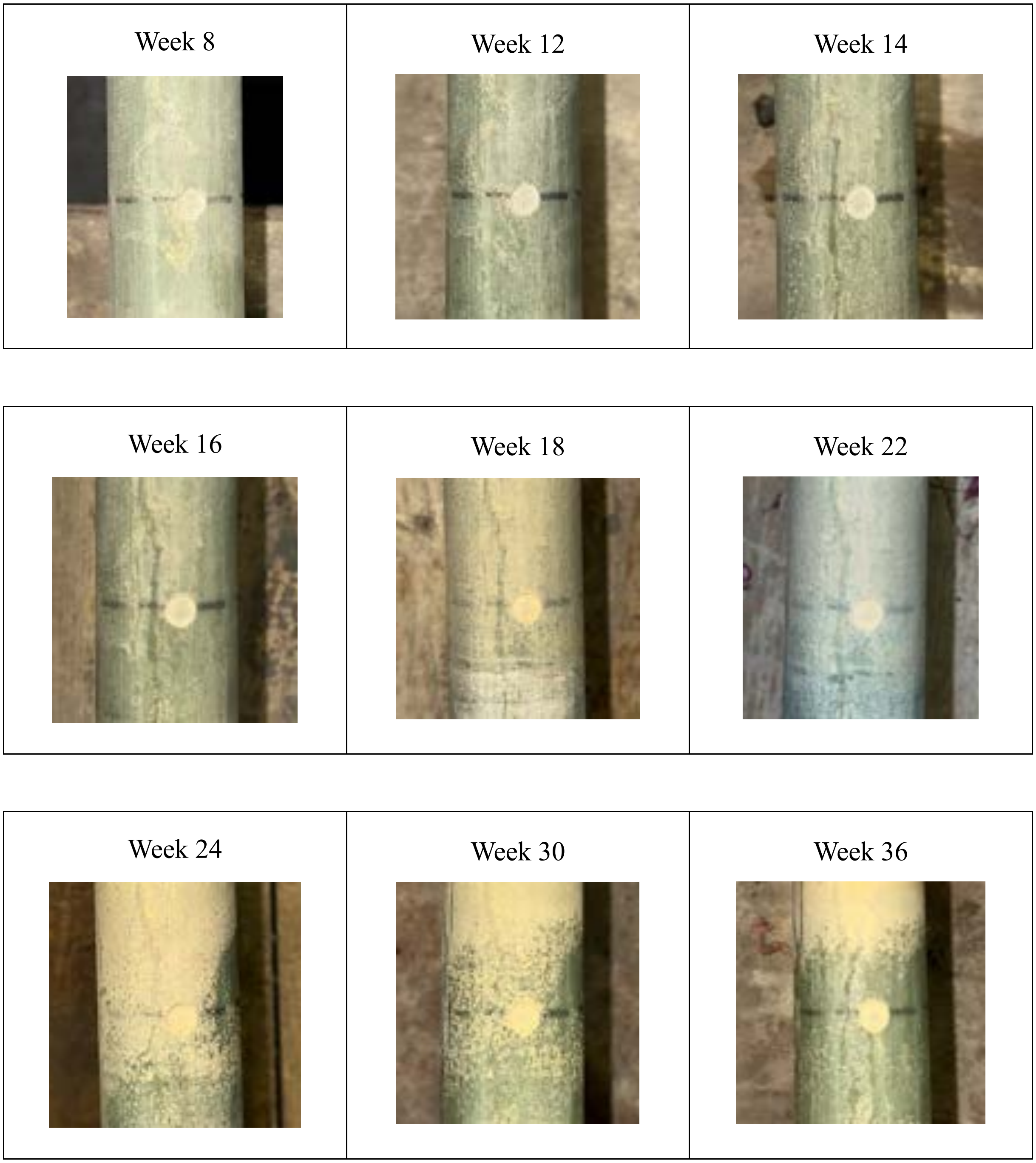

Figure C123. Exposed 2% area holiday for FN1.

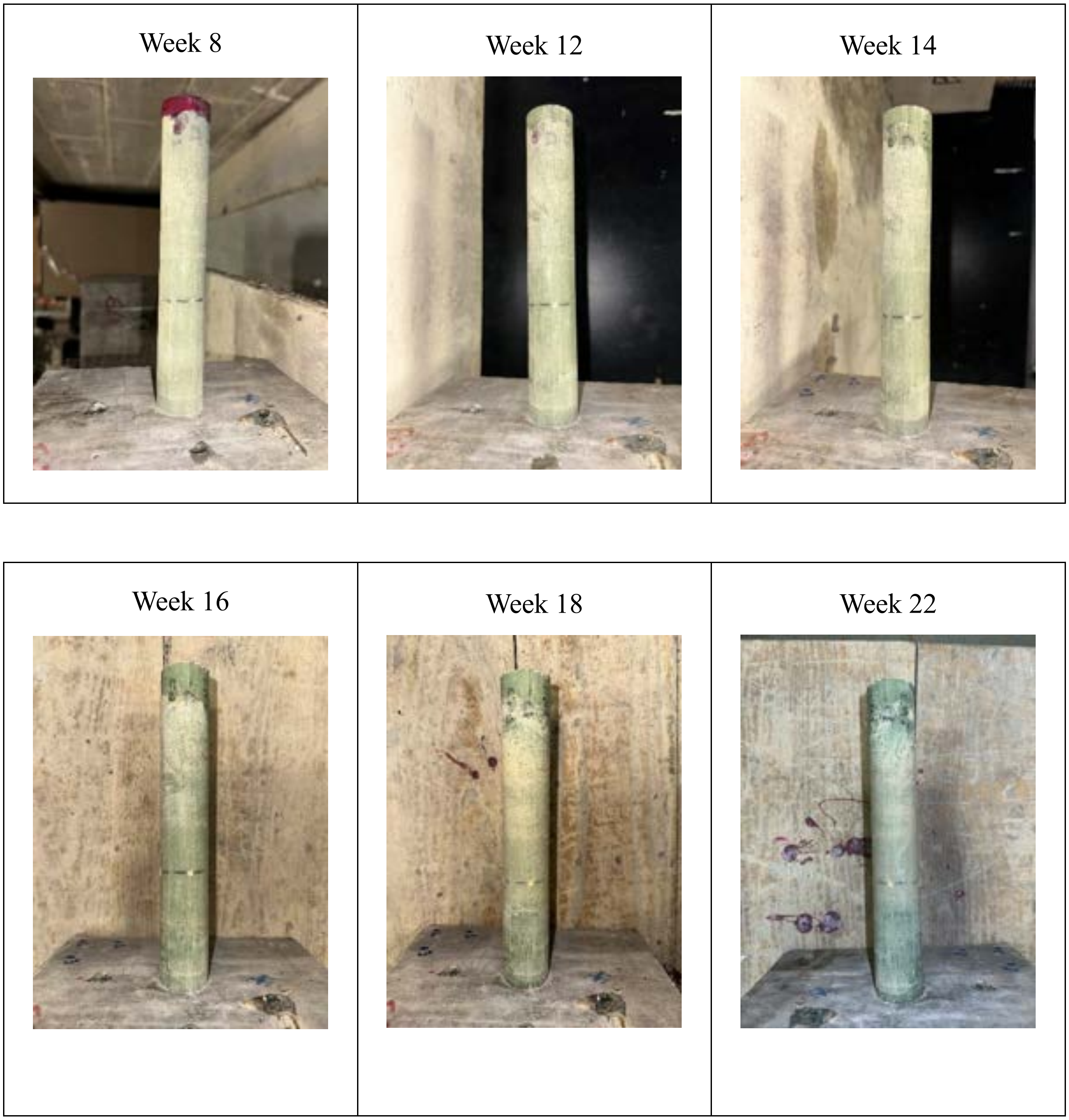

Figure C124. Side with 1% area holidays for FN1.

Week 24	Week 30	Week 36
		

Figure C125. Side with 1% area holidays for FN1 continued.

Week 8

Week 12

Week 14

Week 16

Week 18

Week 22

Week 24

Week 30

Week 36

Figure C126. Exposed 1% area holiday for FN1.

Week 0	Week 2	Week 4
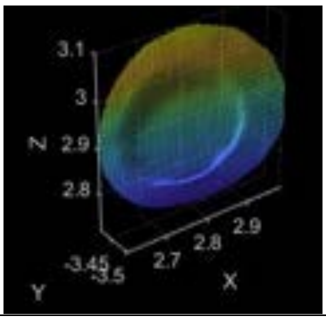	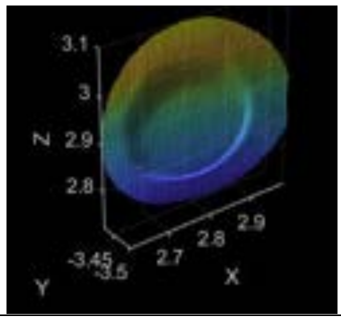	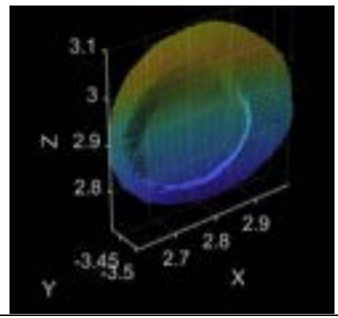
Week 6	**Week 8**	**Week 12**
Unavailable	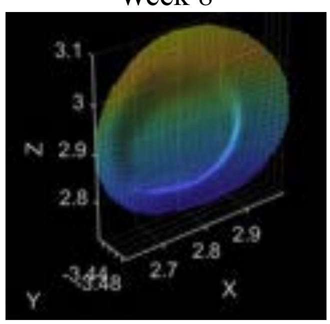	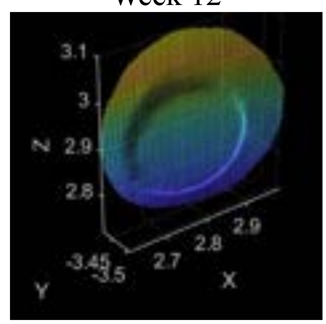
Week 14	**Week 16**	**Week 18**
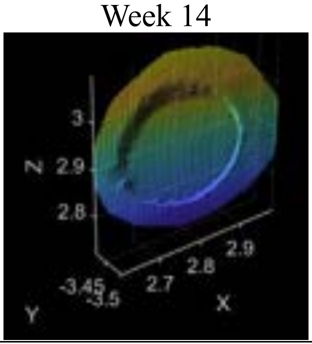	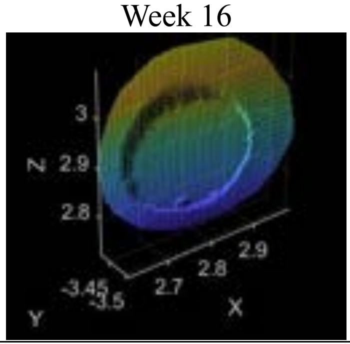	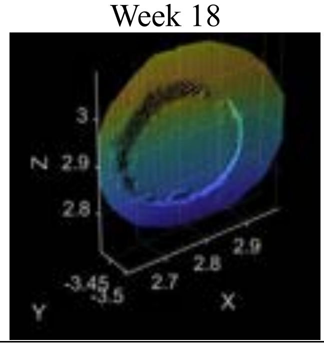

Figure C127. Change in meshed point cloud of exposed 2% area holiday data from Week 0 for FN1.

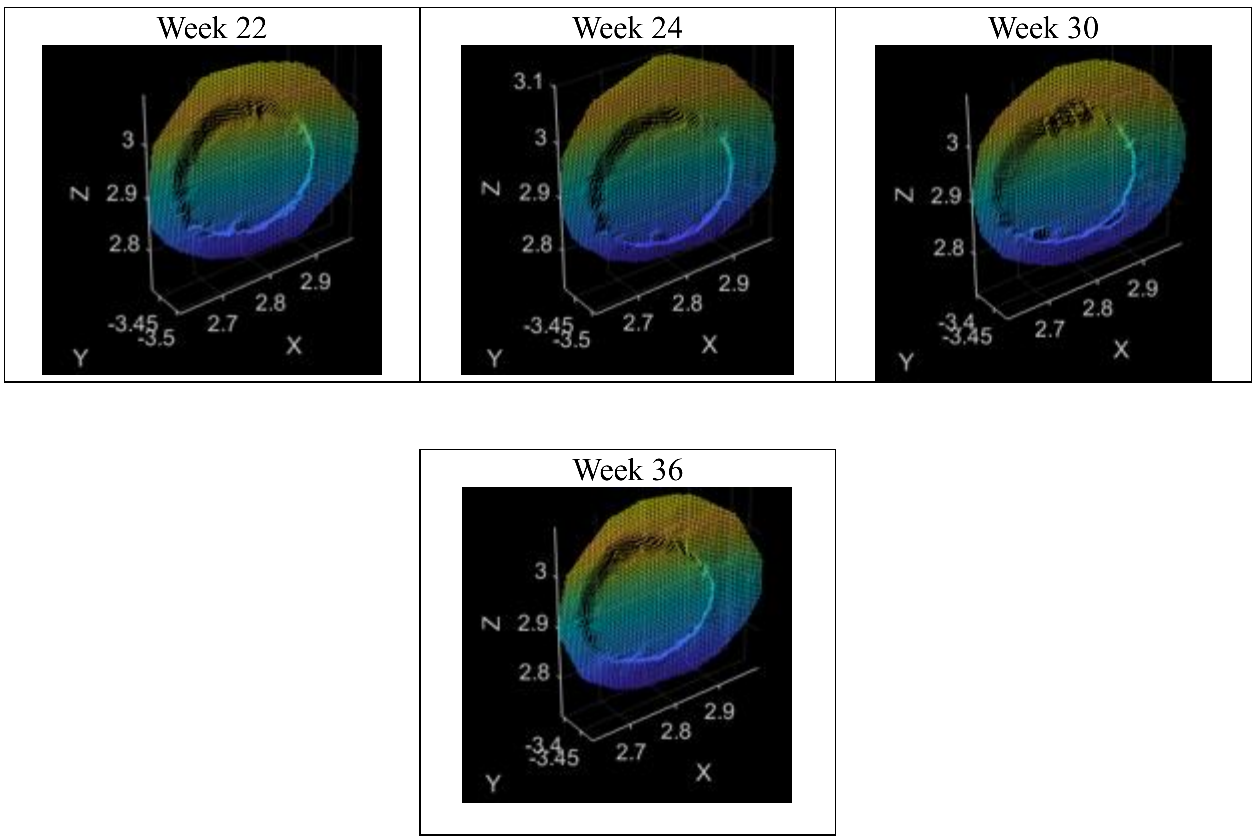

Figure C128. Change in meshed point cloud of exposed 2% area holiday data from Week 0 for FN1 continued.

Week 8	Week 12	Week 14
		

Week 16	Week 18	Week 22
		

Figure C129. Side with 2% area holidays for FN2.

Week 24	Week 30	Week 36
		

Figure C130. Side with 2% area holidays for FN2 continued.

Week 8 	Week 12 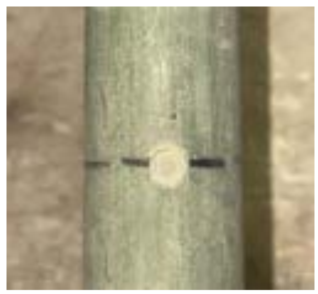	Week 14 

Week 16 	Week 18 	Week 22 

Week 24	Week 30	Week 36
		

Figure C131. Exposed 2% area holiday for FN2.

Week 8	Week 12	Week 14
		

Week 16	Week 18	Week 22
		

Figure C132. Side with 1% area holidays for FN2.

Week 24	Week 30	Week 36
		

Figure C133. Side with 1% area holidays for FN2 continued.

Week 8	Week 12	Week 14
		

Week 16	Week 18	Week 22
		

Week 24	Week 30	Week 36
		

Figure C134. Exposed 1% area holiday for FN2.

Week 0	Week 2	Week 4
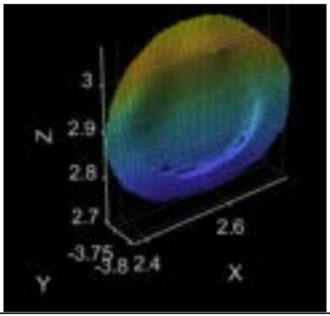	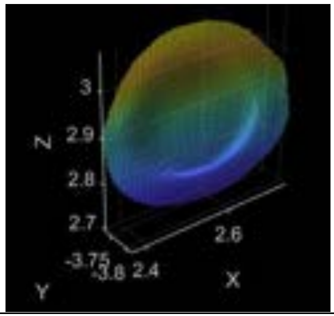	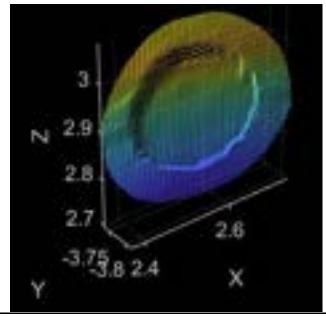
Week 6	Week 8	Week 12
Unavailable	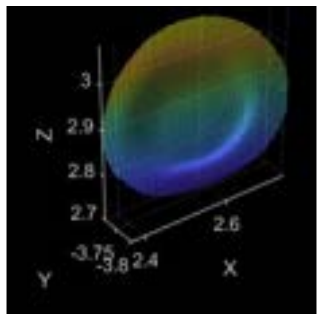	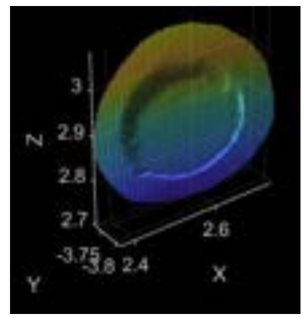
Week 14	Week 16	Week 18
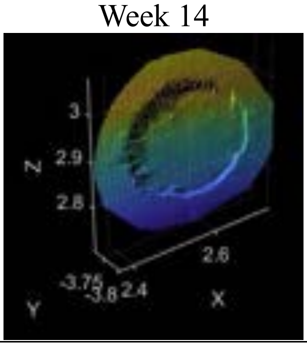	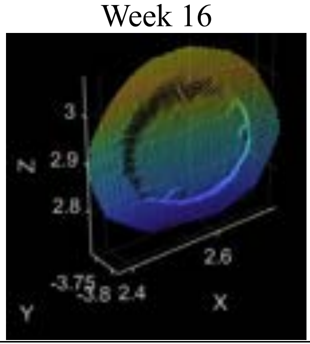	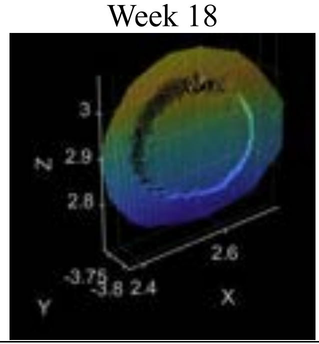

Figure C135. Change in meshed point cloud of exposed 2% area holiday data from Week 0 for FN2.

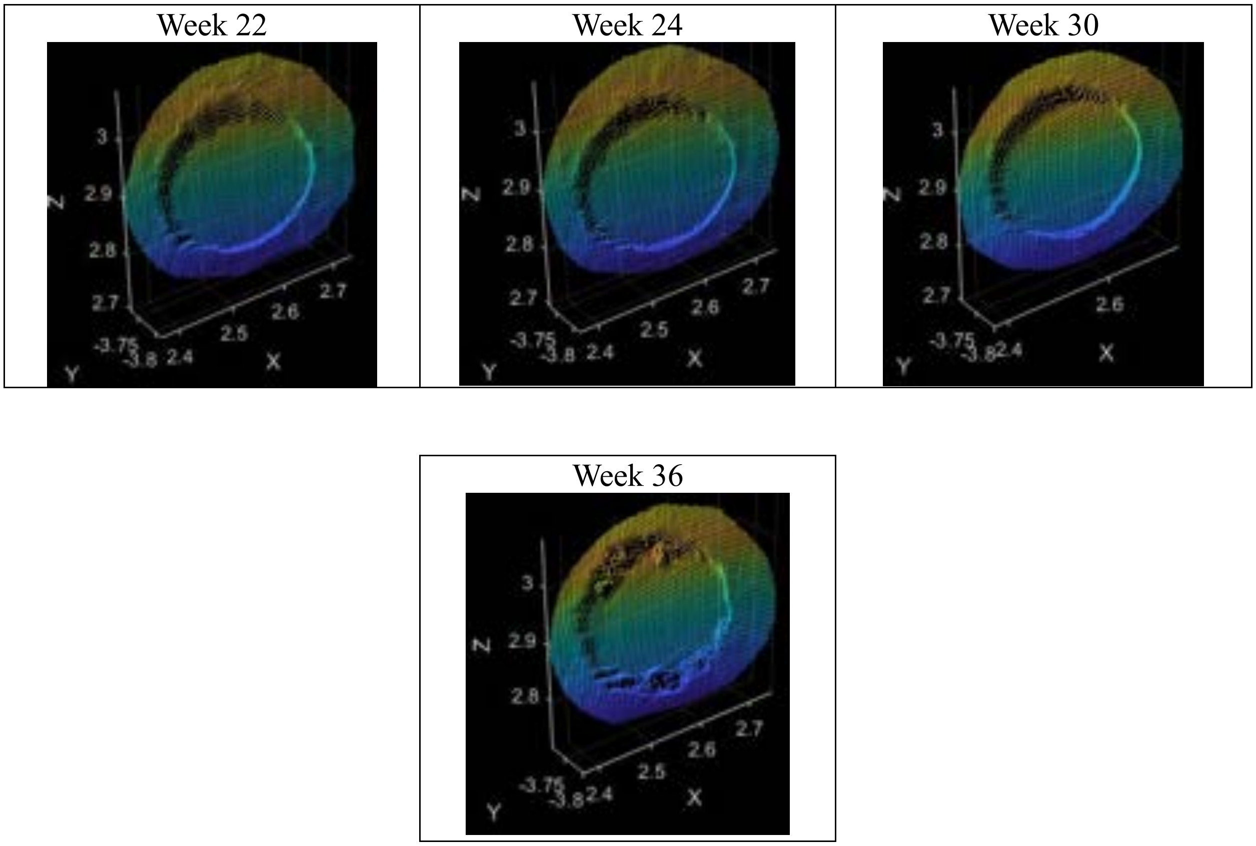

Figure C136. Change in meshed point cloud of exposed 2% area holiday data from Week 0 for FN2 continued.

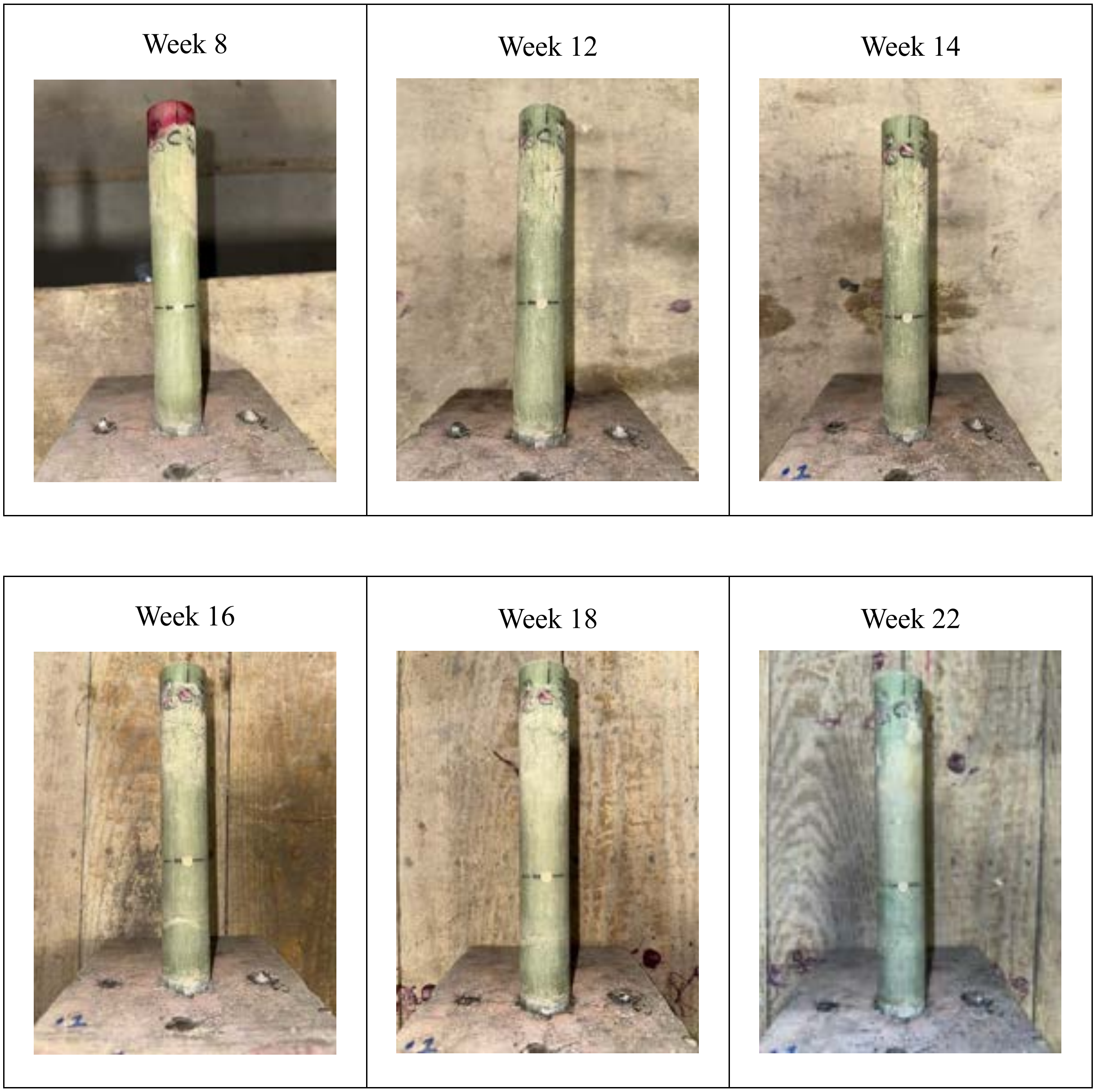

Figure C137. Side with 2% area holidays for FN3.

Week 24	Week 30	Week 36
		

Figure C138. Side with 2% area holidays for FN3 continued.

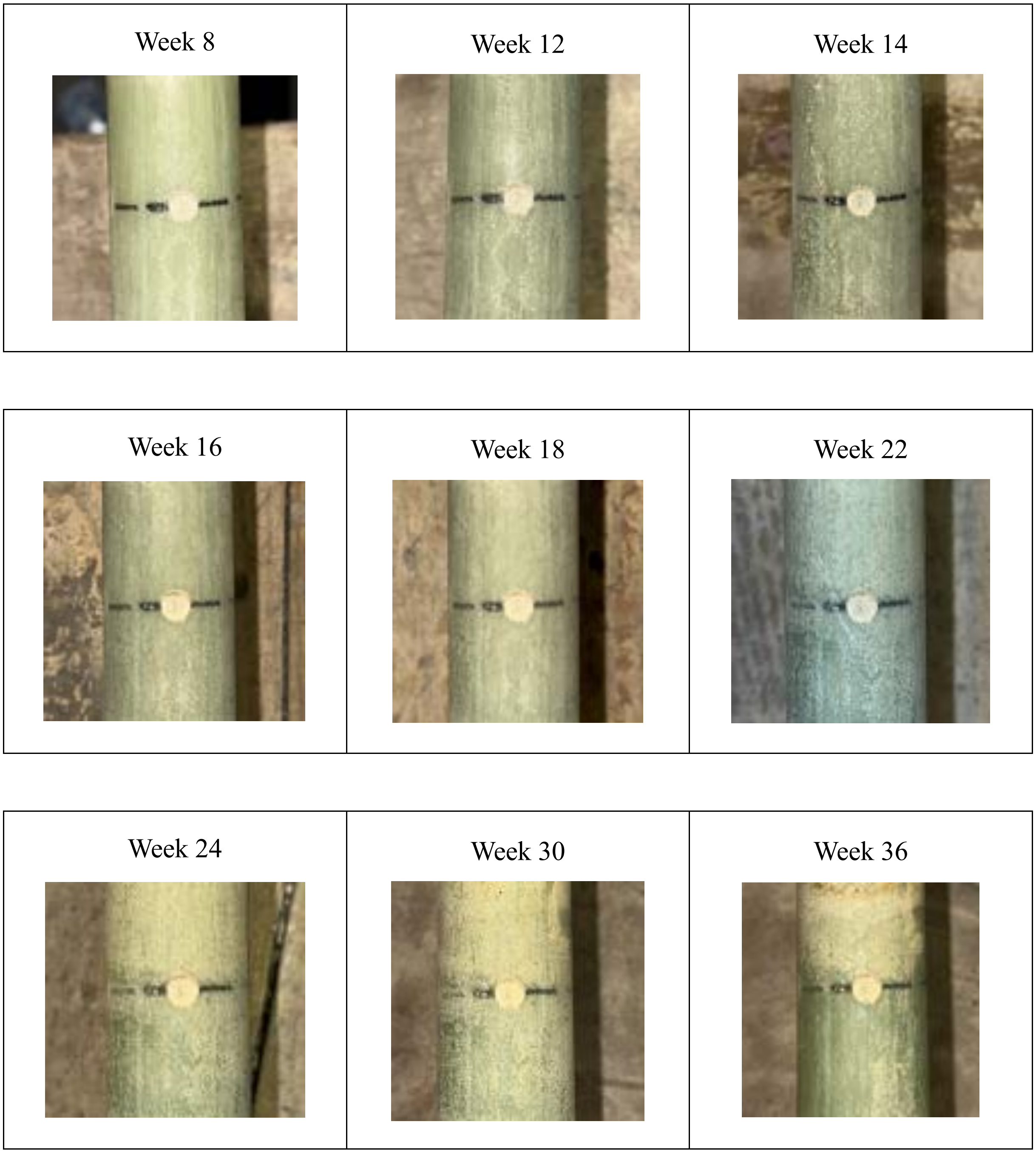

Figure C139. Exposed 2% area holiday for FN3.

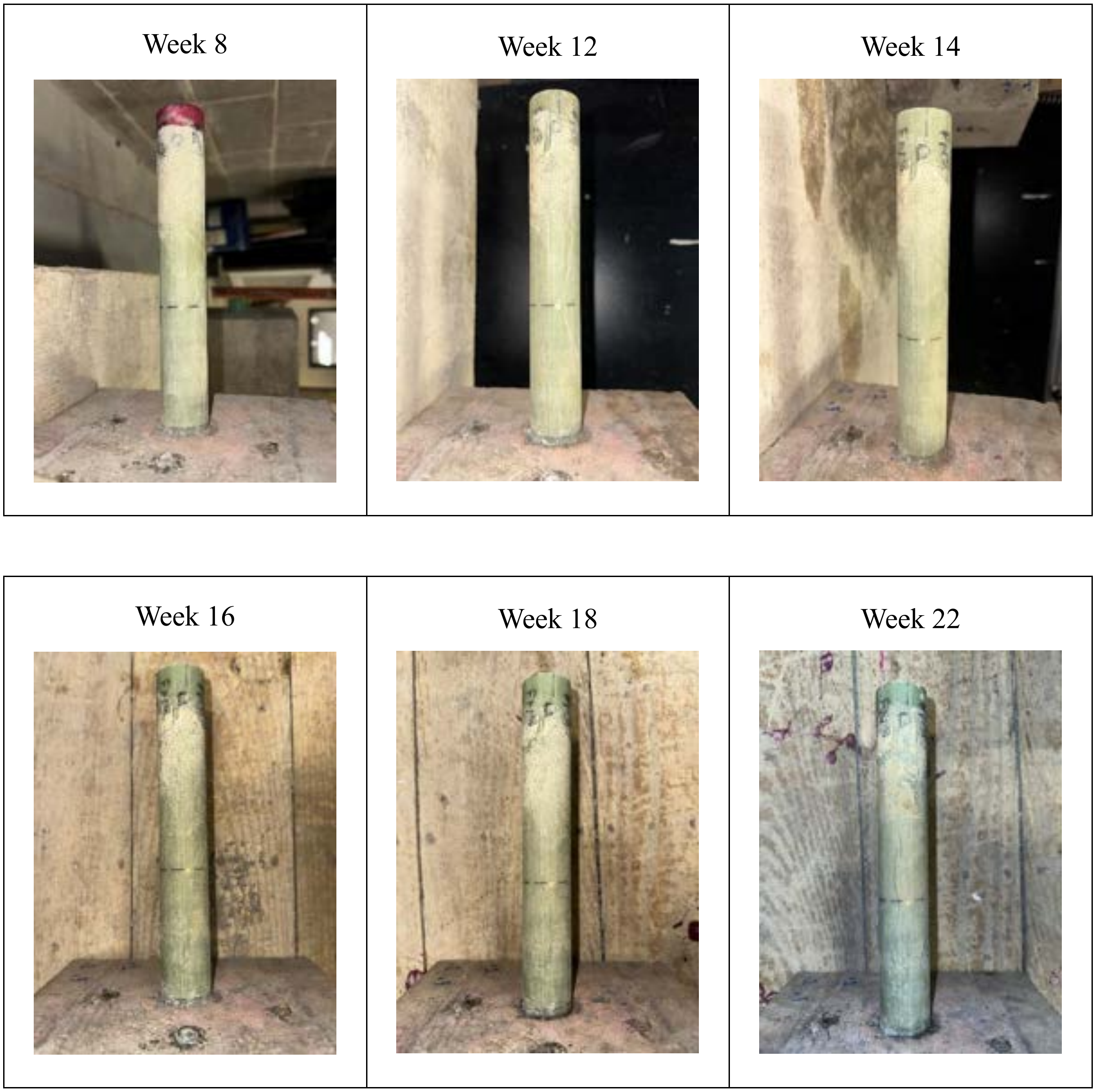

Figure C140. Side with 1% area holidays for FN3.

Week 24	Week 30	Week 36

Figure C141. Side with 1% area holidays for FN3 continued.

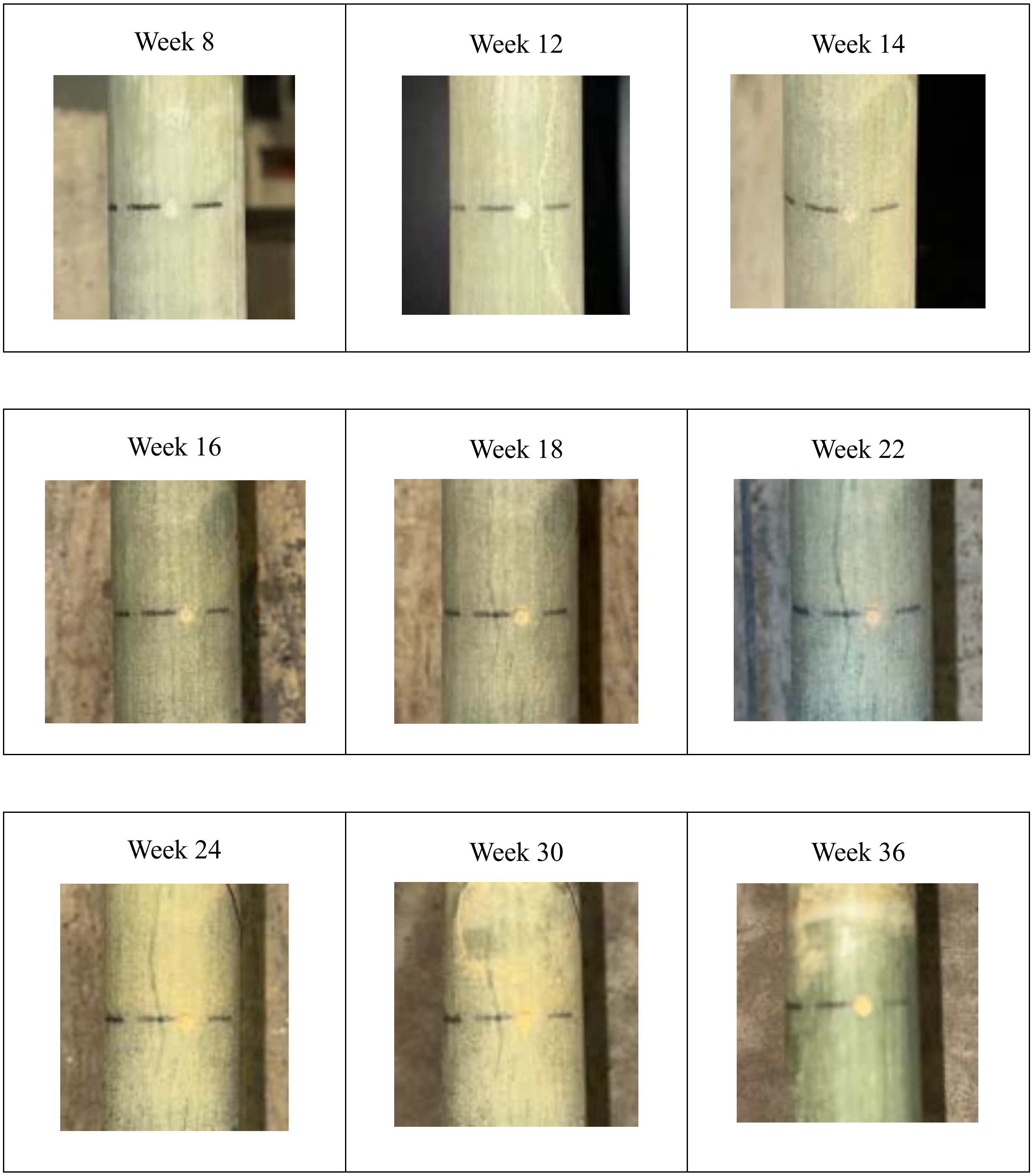

Figure C142. Exposed 1% area holiday for FN3.

Week 0

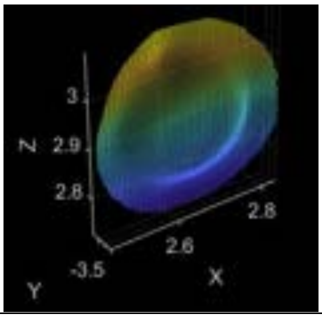

Week 2

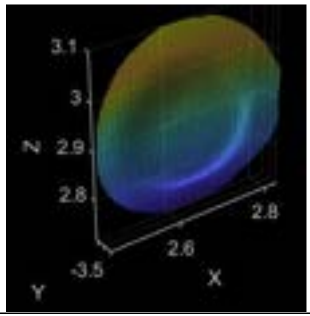

Week 4

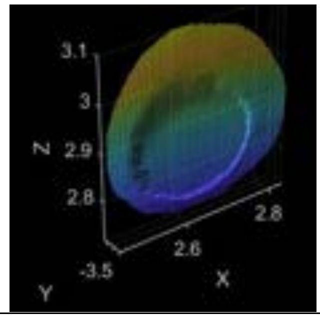

Week 6

Unavailable

Week 8

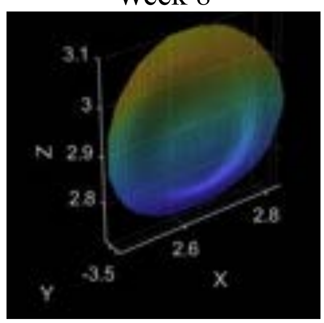

Week 12

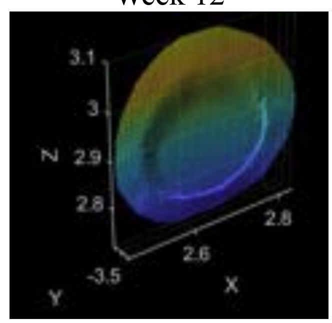

Week 14

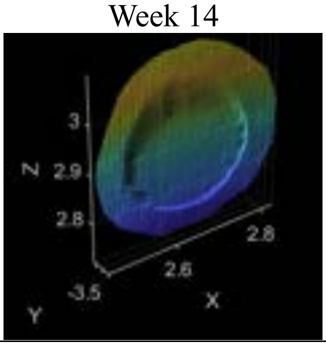

Week 16

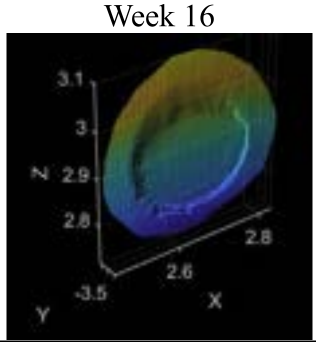

Week 18

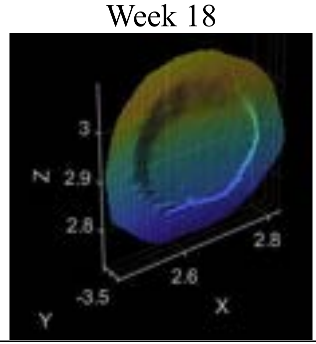

Figure C143. Change in meshed point cloud of exposed 2% area holiday data from Week 0 for FN3.

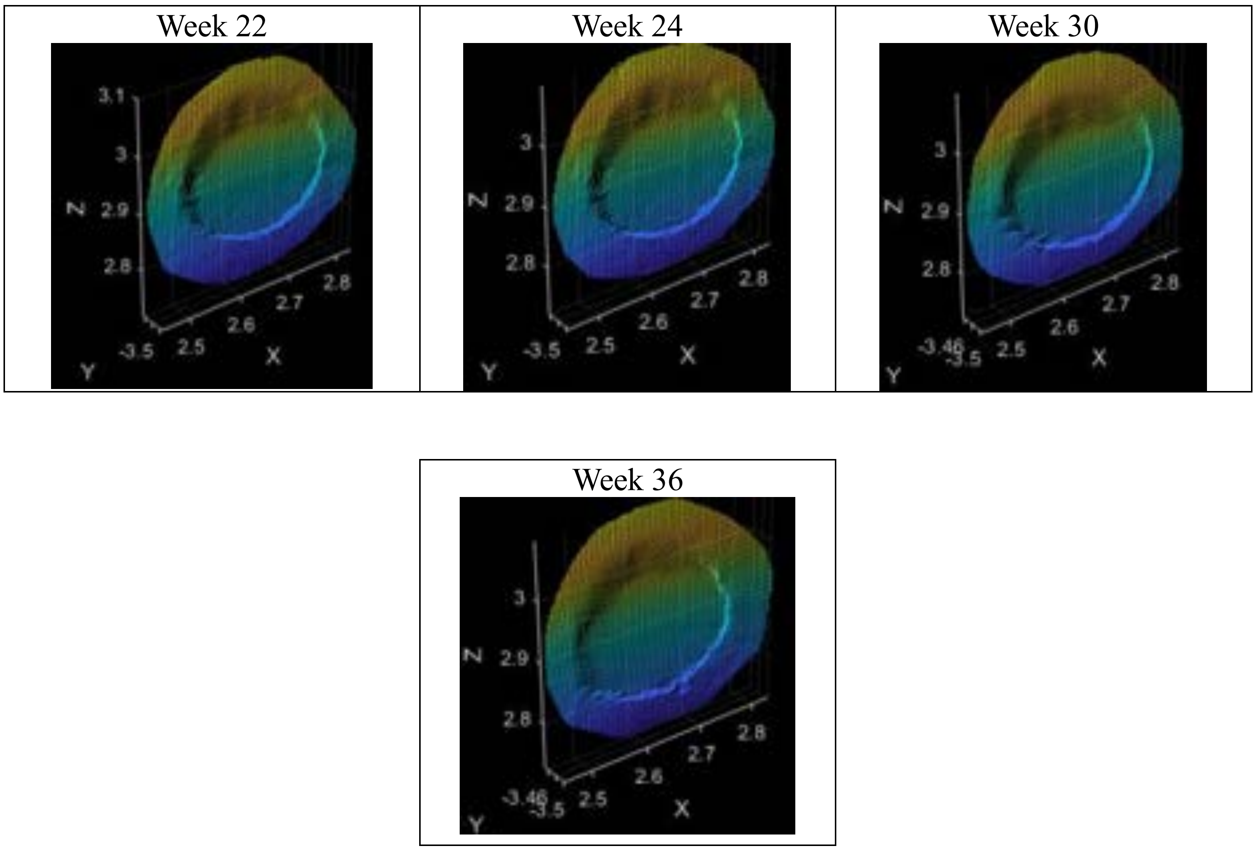

Figure C144. Change in meshed point cloud of exposed 2% area holiday data from Week 0 for FN3 continued.

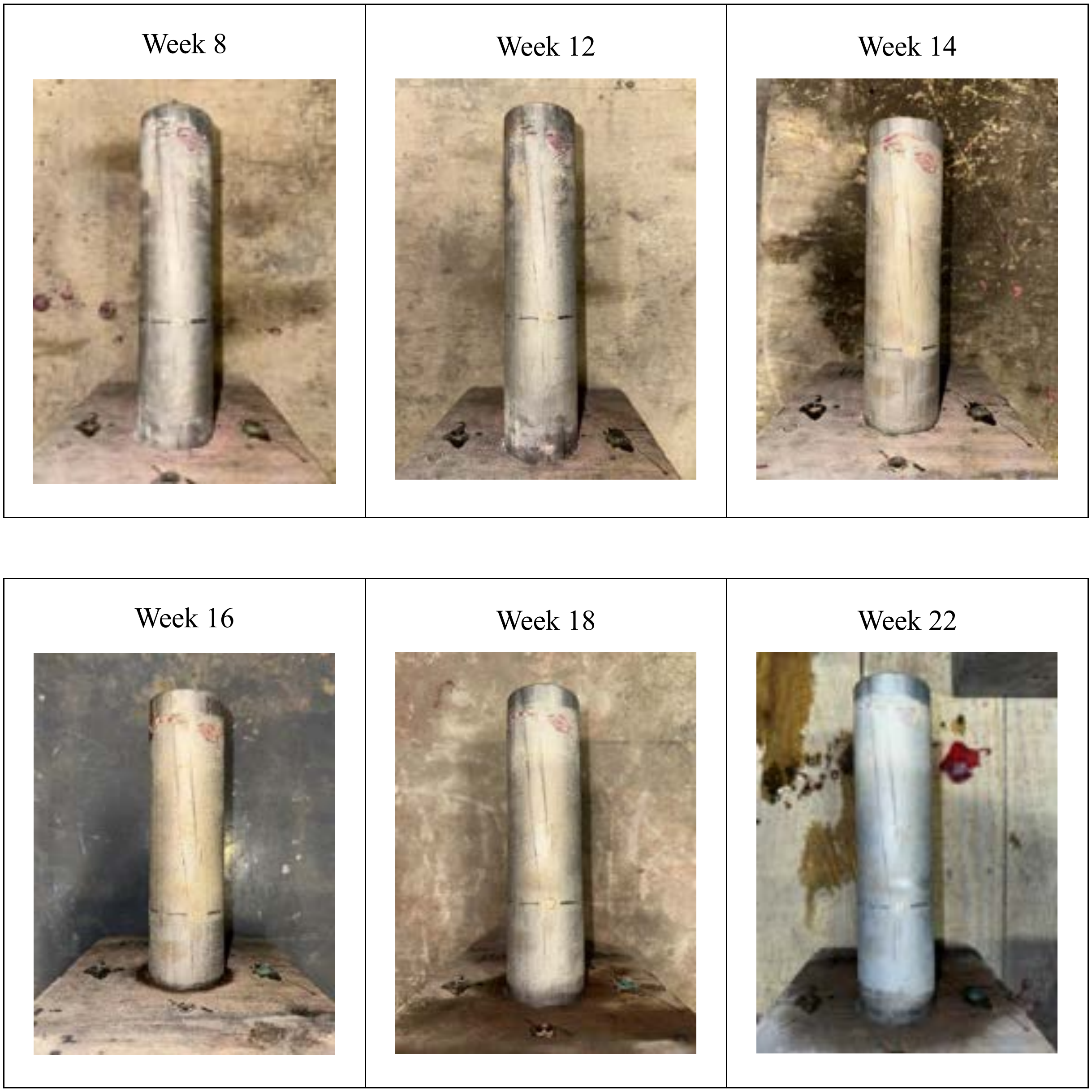

Figure C145. Side with 2% area holidays for SN1.

Week 24	Week 30	Week 36
		

Figure C146. Side with 2% area holidays for SN1 continued.

Week 8	Week 12	Week 14
		

Week 16	Week 18	Week 22
		

Week 24	Week 30	Week 36
		

Figure C147. Exposed 2% area holiday for SN1.

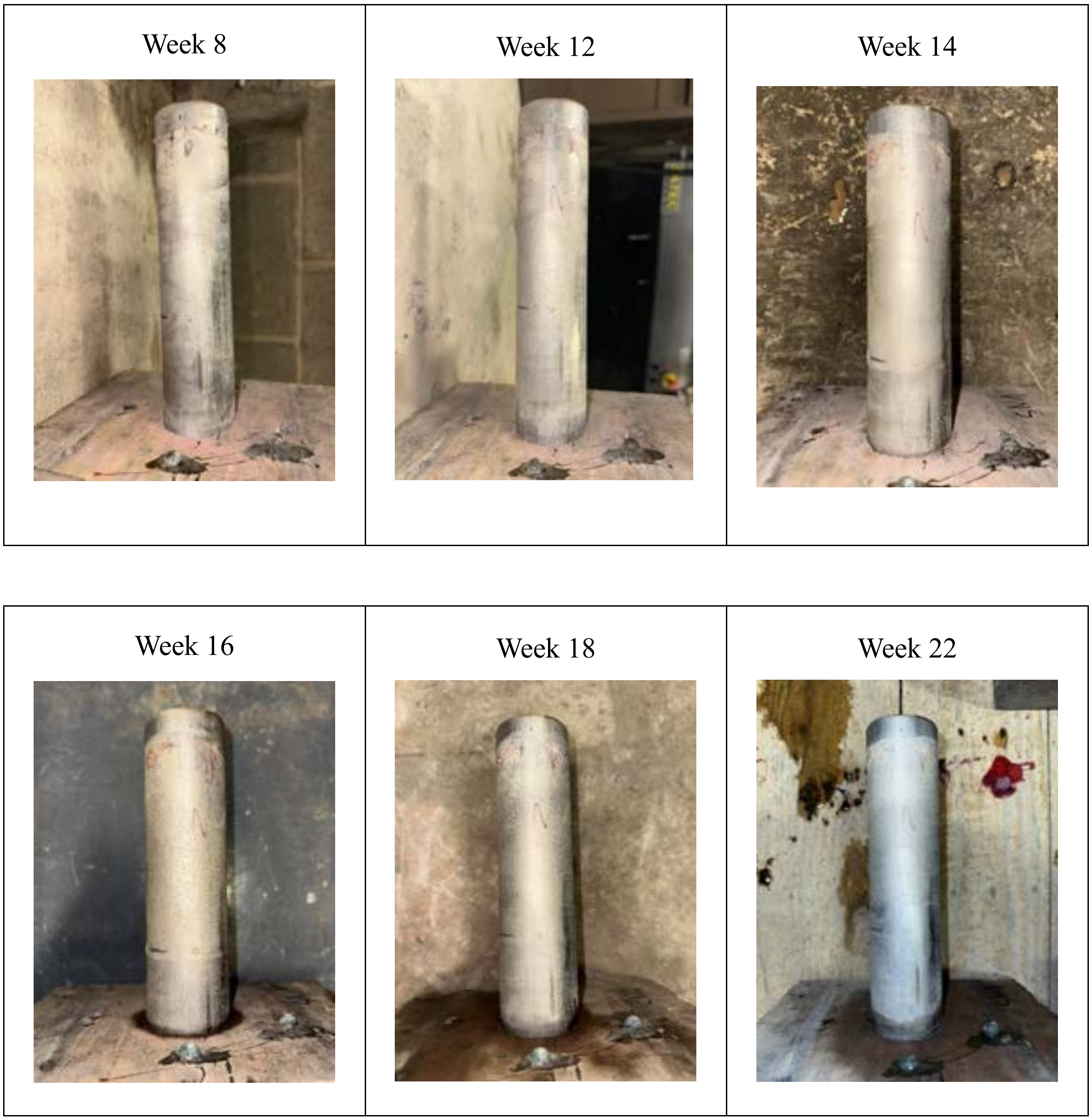

Figure C148. Side with 1% area holidays for SN1.

Week 24	Week 30	Week 36
		

Figure C149. Side with 1% area holidays for SN1 continued.

Week 8	Week 12	Week 14
		

Week 16	Week 18	Week 22
		

Week 24	Week 30	Week 36
		

Figure C150. Exposed 1% area holiday for SN1.

Week 0	Week 2	Week 4
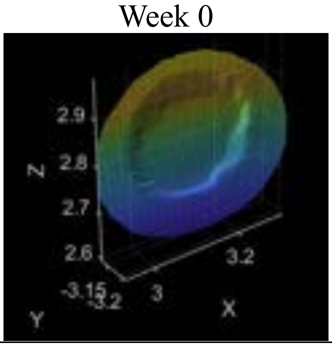	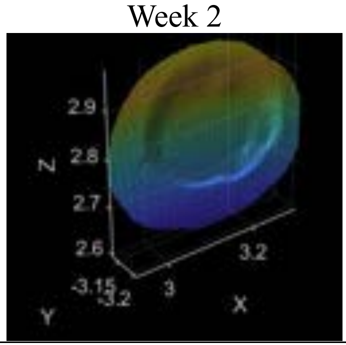	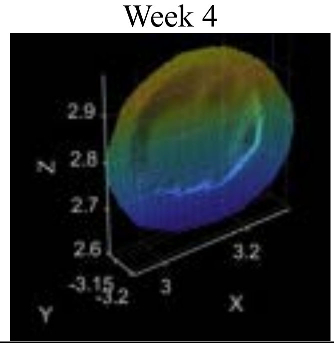
Week 6	Week 8	Week 12
Unavailable	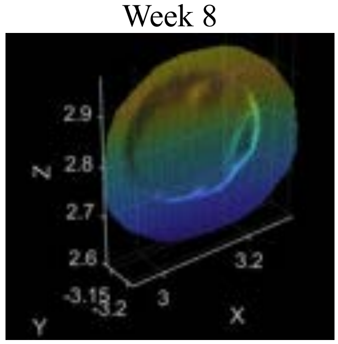	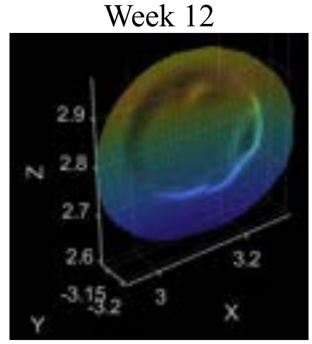
Week 14	Week 16	Week 18

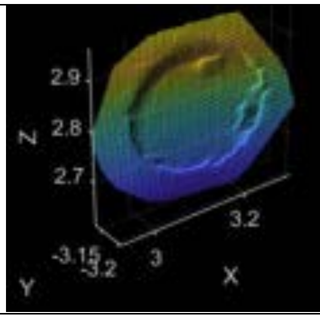	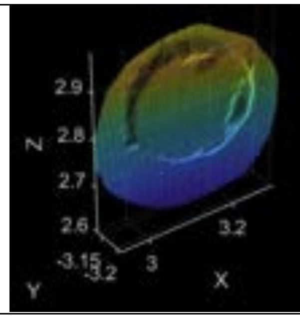	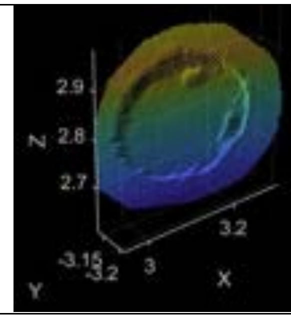

Figure C151. Change in meshed point cloud of exposed 2% area holiday data from Week 0 for SN1.

Week 22	Week 24	Week 30
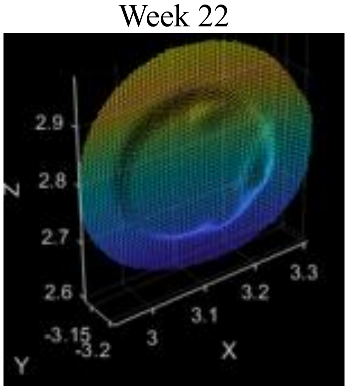	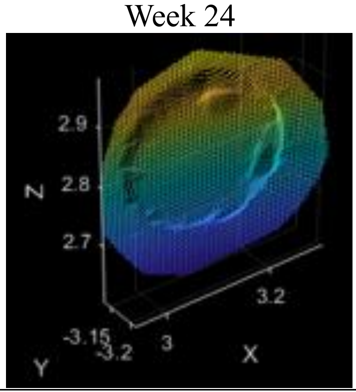	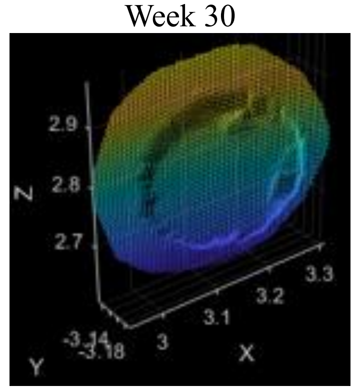

Week 36

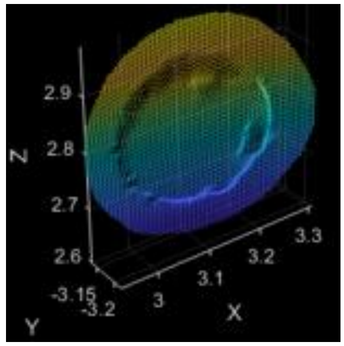

Figure C152. Change in meshed point cloud of exposed 2% area holiday data from Week 0 for SN1 continued.

Week 8	Week 12	Week 14
		

Week 16	Week 18	Week 22
		

Figure B.153. Side with 2% area holidays for SN2.

Week 24	Week 30	Week 36
		

Figure C154. Side with 2% area holidays for SN2 continued.

Week 8 	Week 12 	Week 14 
Week 16 	Week 18 	Week 22 

Week 24	Week 30	Week 36
		

Figure C155. Exposed 2% area holiday for SN2.

Week 8	Week 12	Week 14
		

Week 16	Week 18	Week 22
		

Figure C.156. Side with 1% area holidays for SN2.

Week 24	Week 30	Week 36
		

Figure C157. Side with 1% area holidays for SN2 continued.

Week 8	Week 12	Week 14
	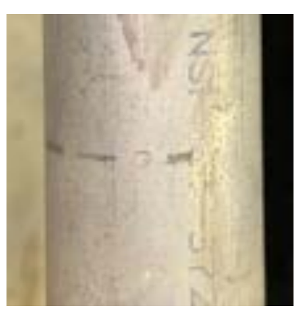	

Week 16	Week 18	Week 22
		

Week 24	Week 30	Week 36
		

Figure D.158. Exposed 1% area holiday for SN2.

Week 0

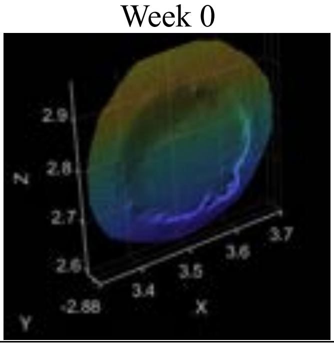

Week 2

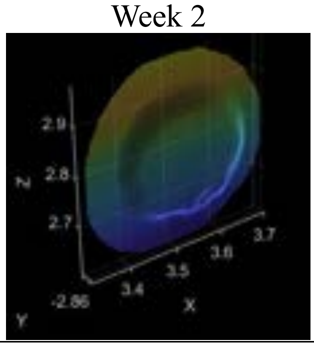

Week 4

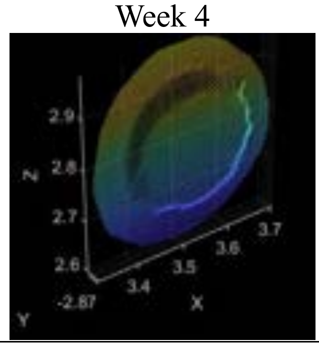

Week 6	Week 8	Week 12

Unavailable	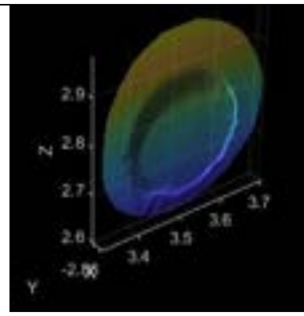	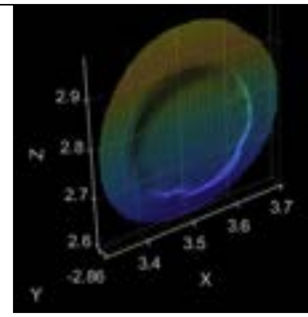
Week 14 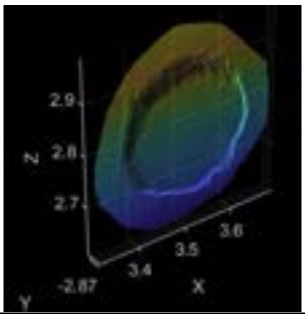	Week 16 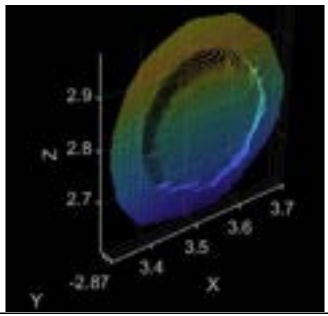	Week 18 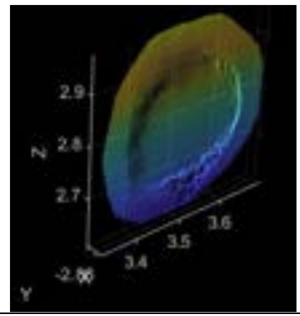

Figure C159. Change in meshed point cloud of exposed 2% area holiday data from Week 0 for SN2.

Week 22	Week 24	Week 30

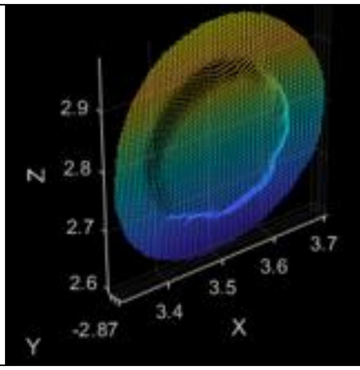

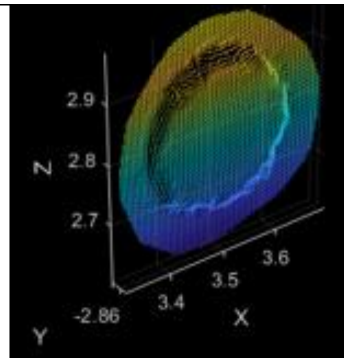

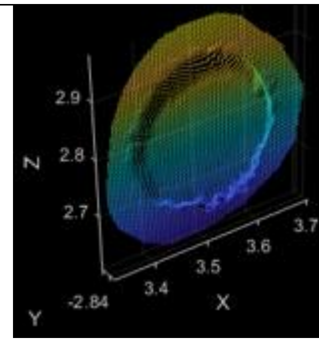

Week 36

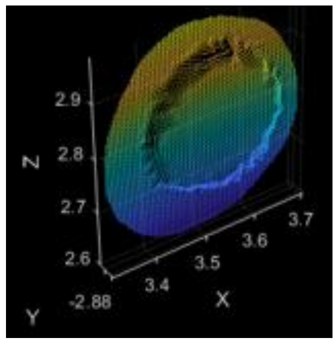

Figure C160. Change in meshed point cloud of exposed 2% area holiday data from Week 0 for SN2 continued.

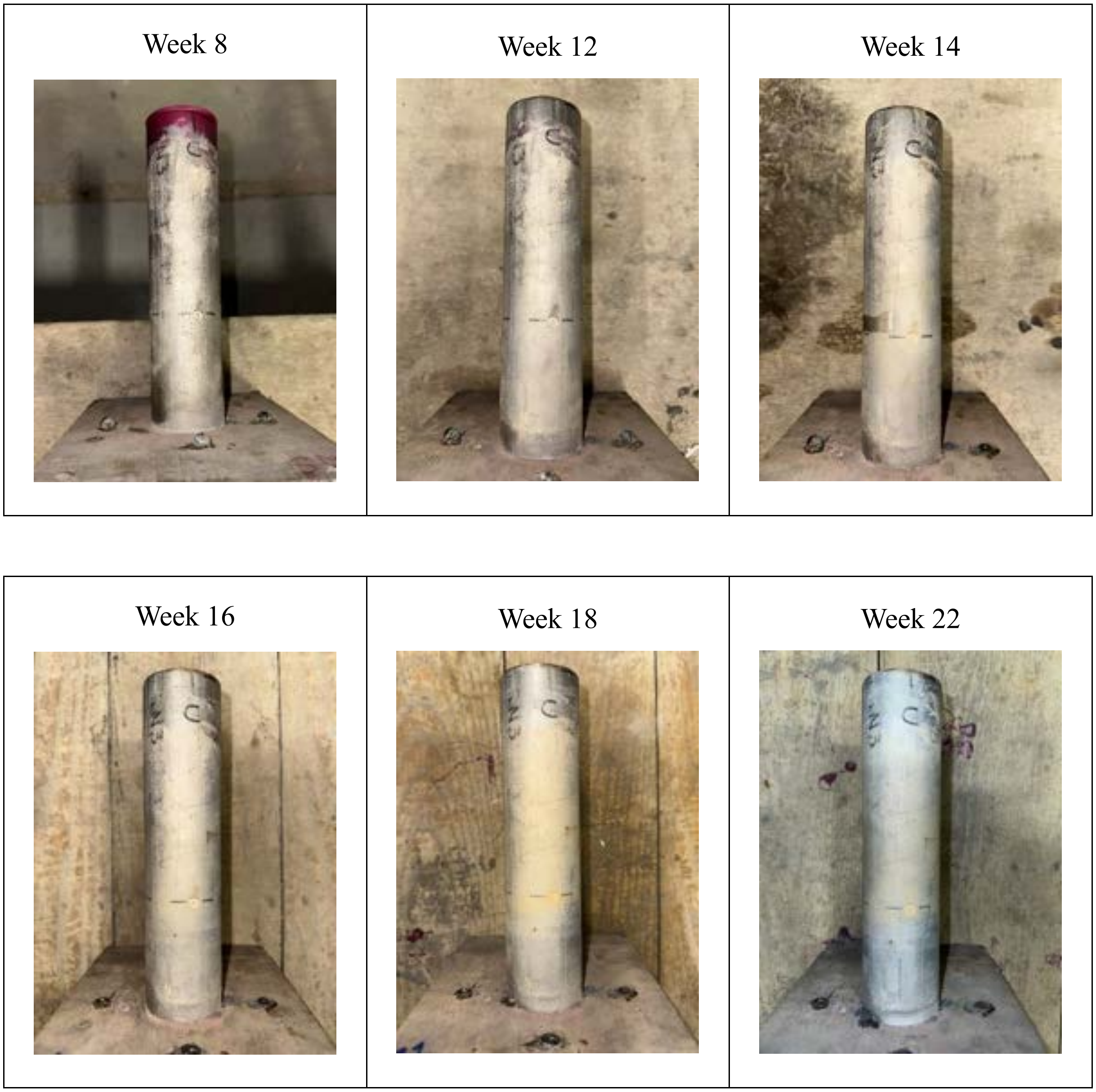

Figure E.161. Side with 2% area holidays for SN3.

Week 24	Week 30	Week 36
		

Figure C162. Side with 2% area holidays for SN3 continued.

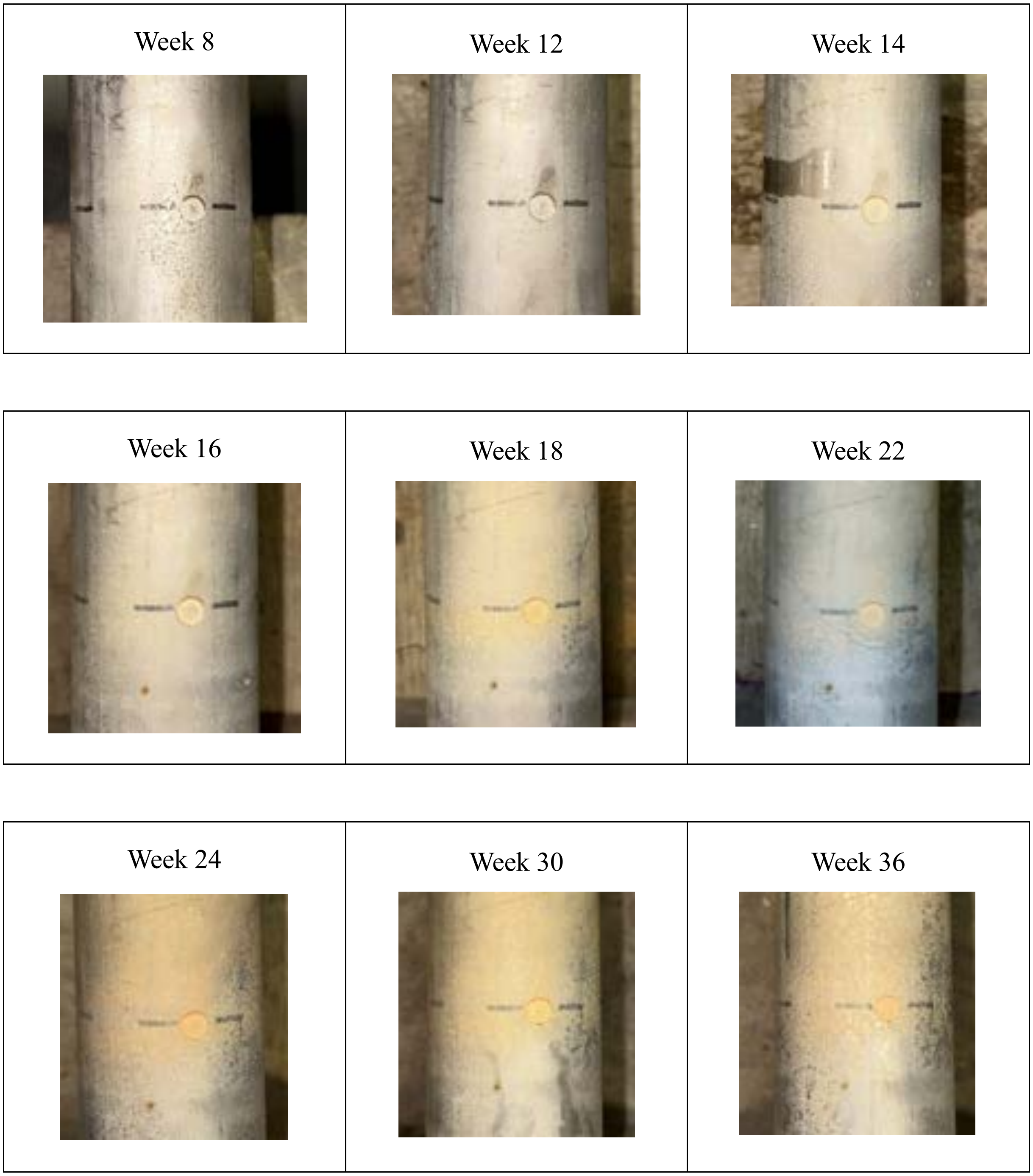

Figure F.163. Exposed 2% area holiday for SN3.

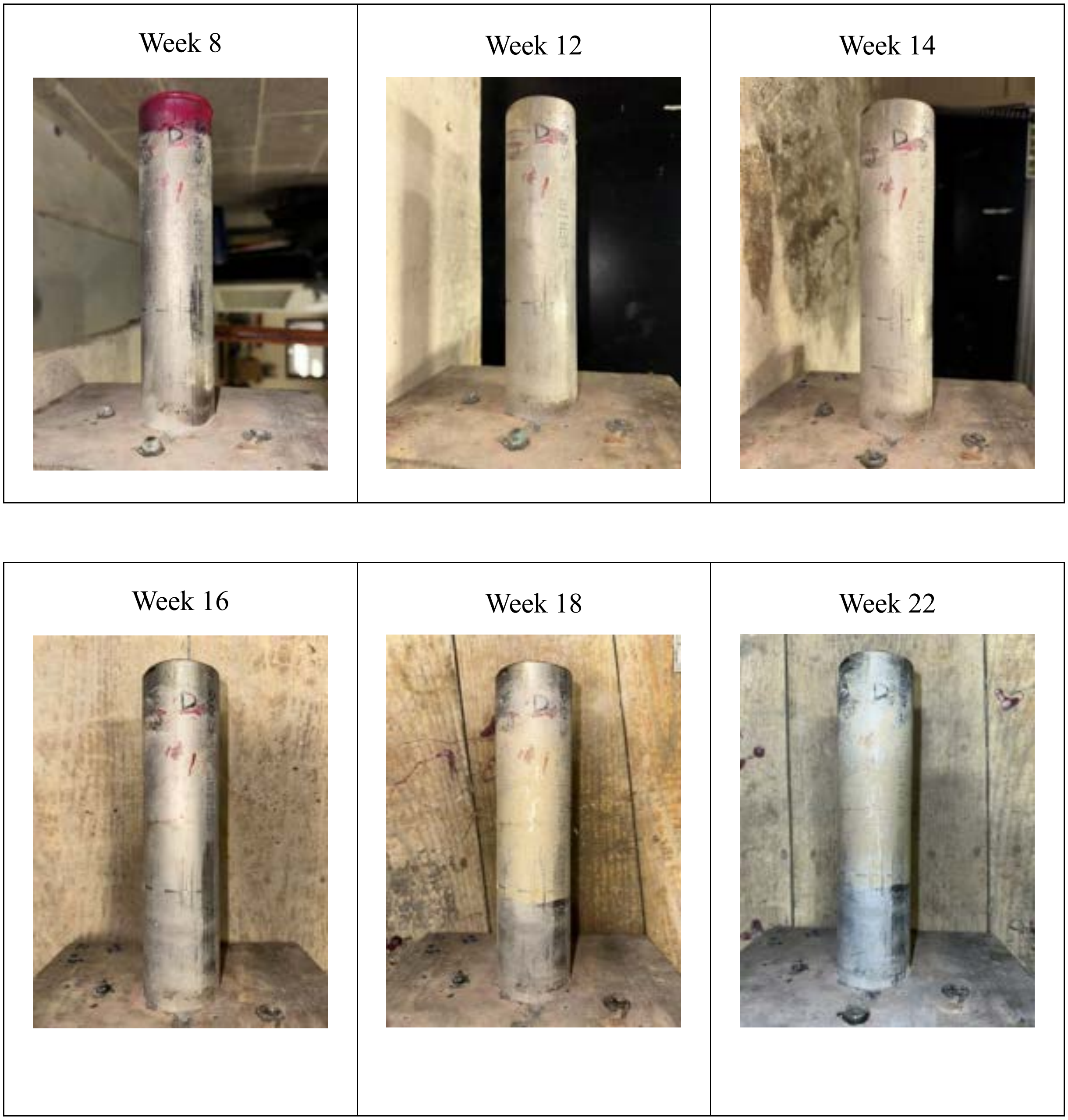

Figure G.164. Side with 1% area holidays for SN3.

Week 24	Week 30	Week 36
		

Figure C165. Side with 1% area holidays for SN3 continued.

Week 8 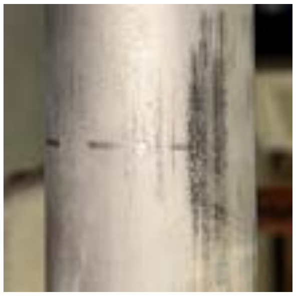	Week 12 	Week 14 
Week 16 	Week 18 	Week 22 
Week 24 	Week 30 	Week 36 

Figure H.166. Exposed 1% area holiday for SN3.

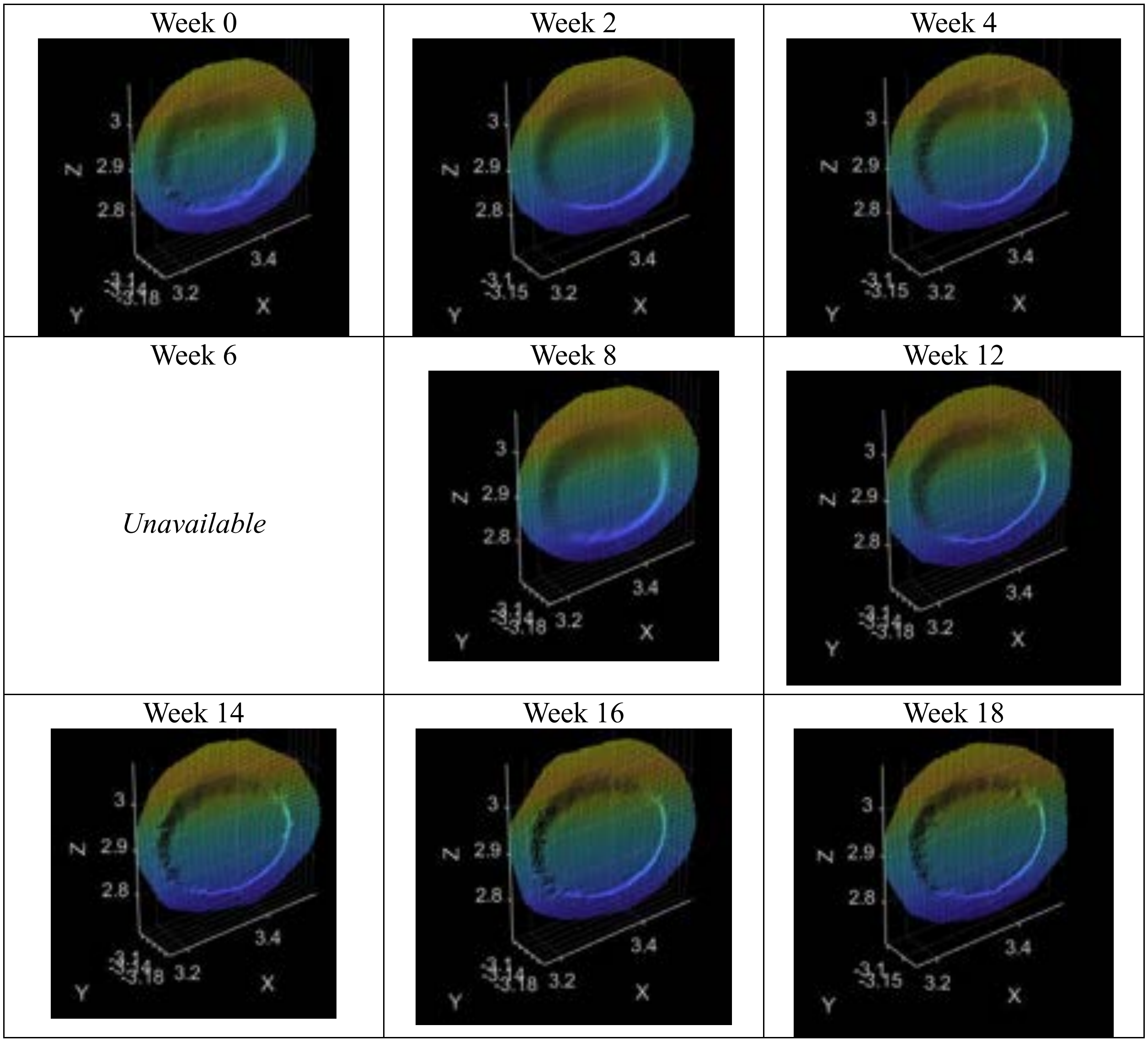

Figure C167. Change in meshed point cloud of exposed 2% area holiday data from Week 0 for SN3.

Week 22

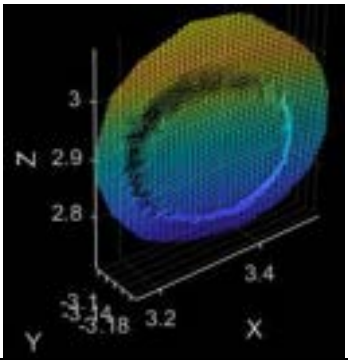

Week 24

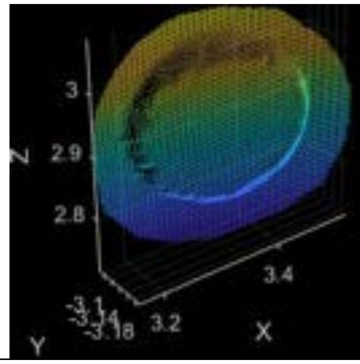

Week 30

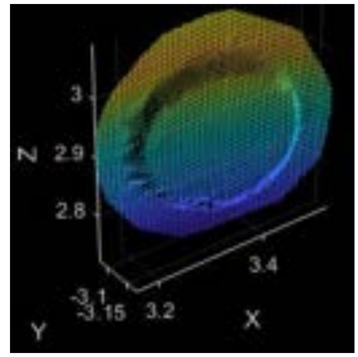

Week 36

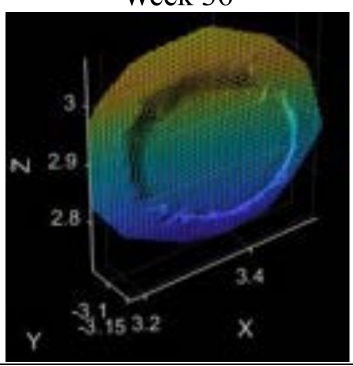

Figure C168. Change in meshed point cloud of exposed 2% area holiday data from Week 0 for SN3 continued.

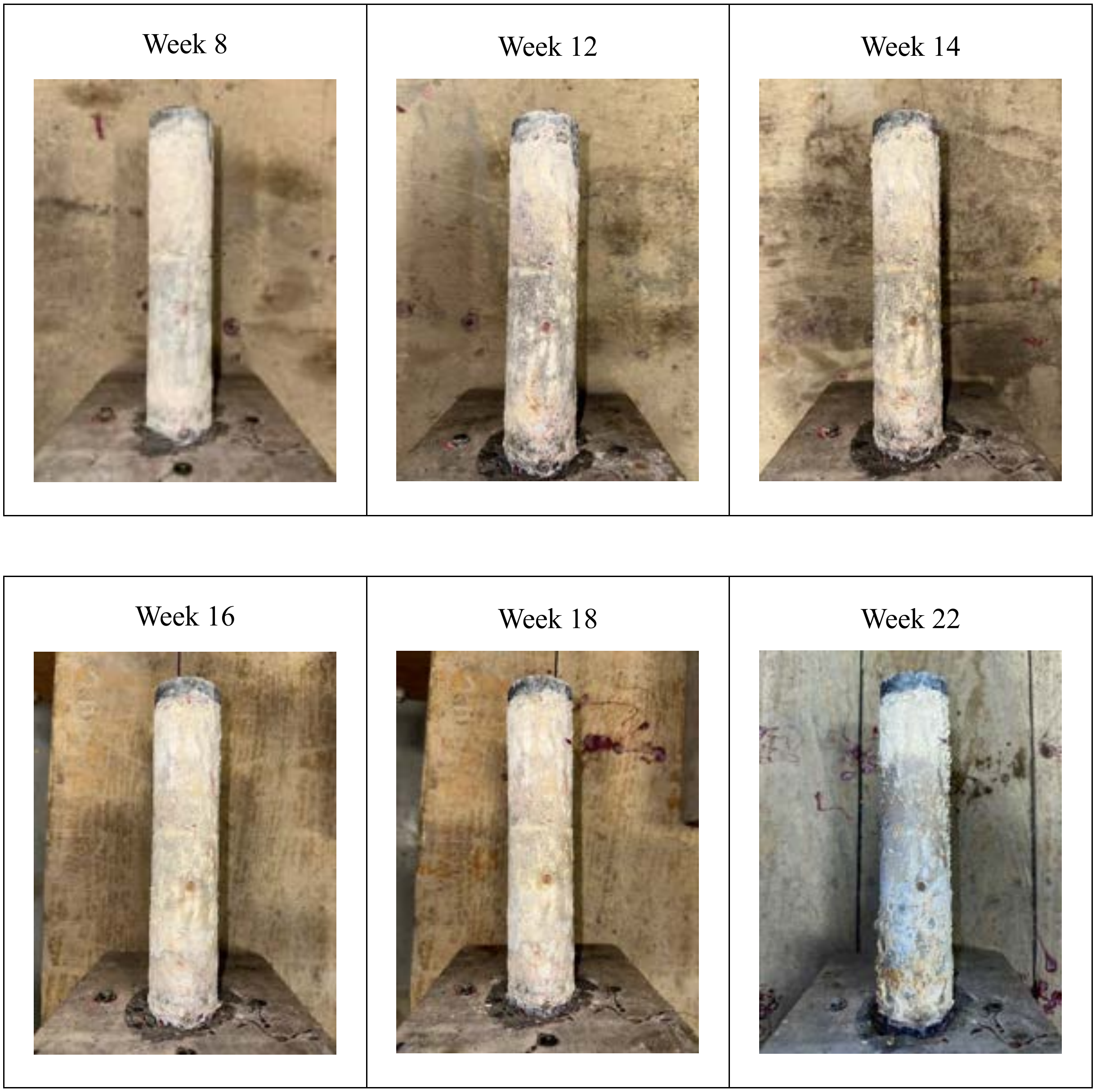

Figure C169. Side with 2% area holidays for C4Z1.

Week 24	Week 30	Week 36
		

Figure C170. Side with 2% area holidays for C4Z1 continued.

Figure C171. Exposed 2% area holiday for C4Z1.

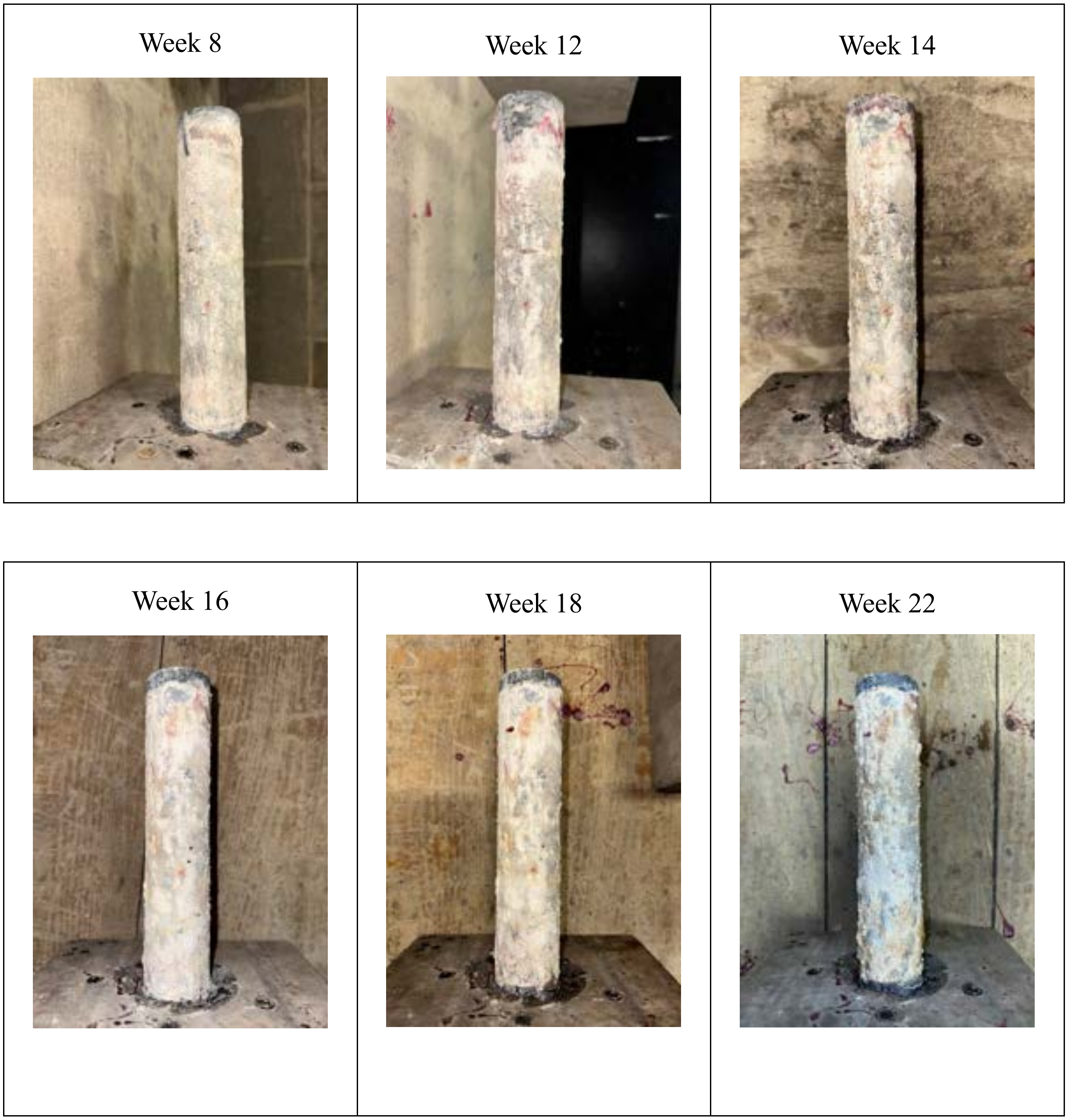

Figure C172. Side with 1% area holidays for C4Z1.

Week 24	Week 30	Week 36
		

Figure C173. Side with 1% area holidays for C4Z1 continued.

Figure C174. Exposed 1% area holiday for C4Z1.

Week 0	Week 2	Week 4
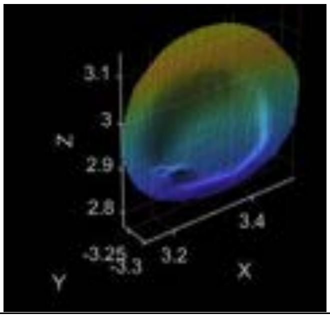	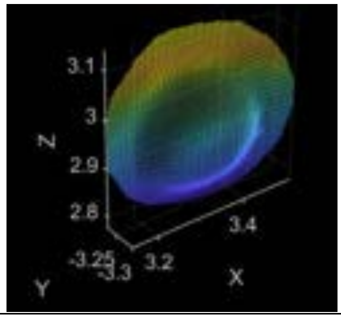	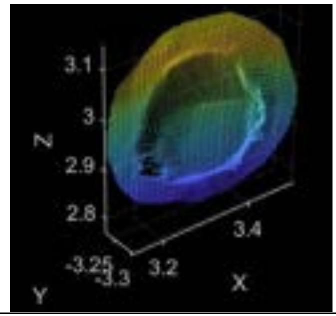
Week 6	Week 8	Week 12
Unavailable	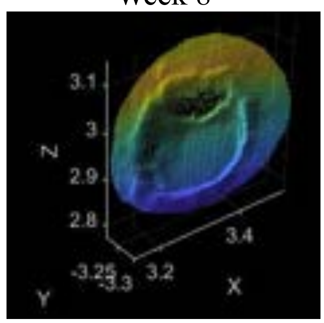	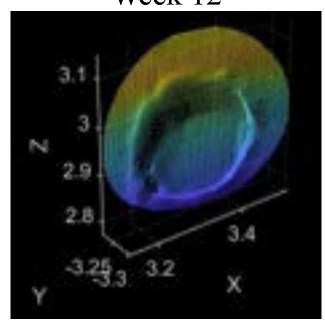
Week 14	Week 16	Week 18
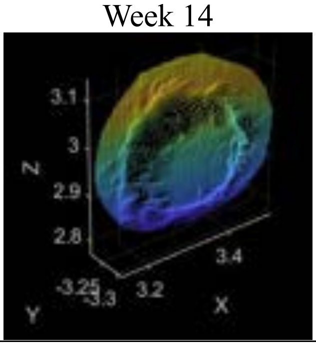	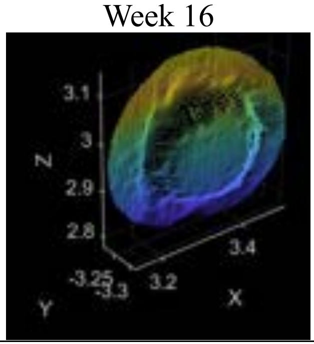	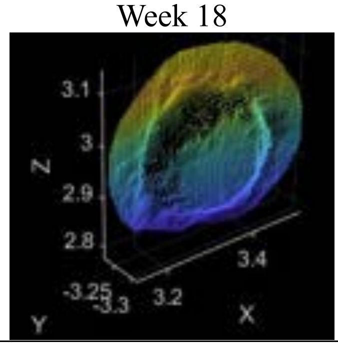

Figure C175. Change in meshed point cloud of exposed 2% area holiday data from Week 0 for C4Z1.

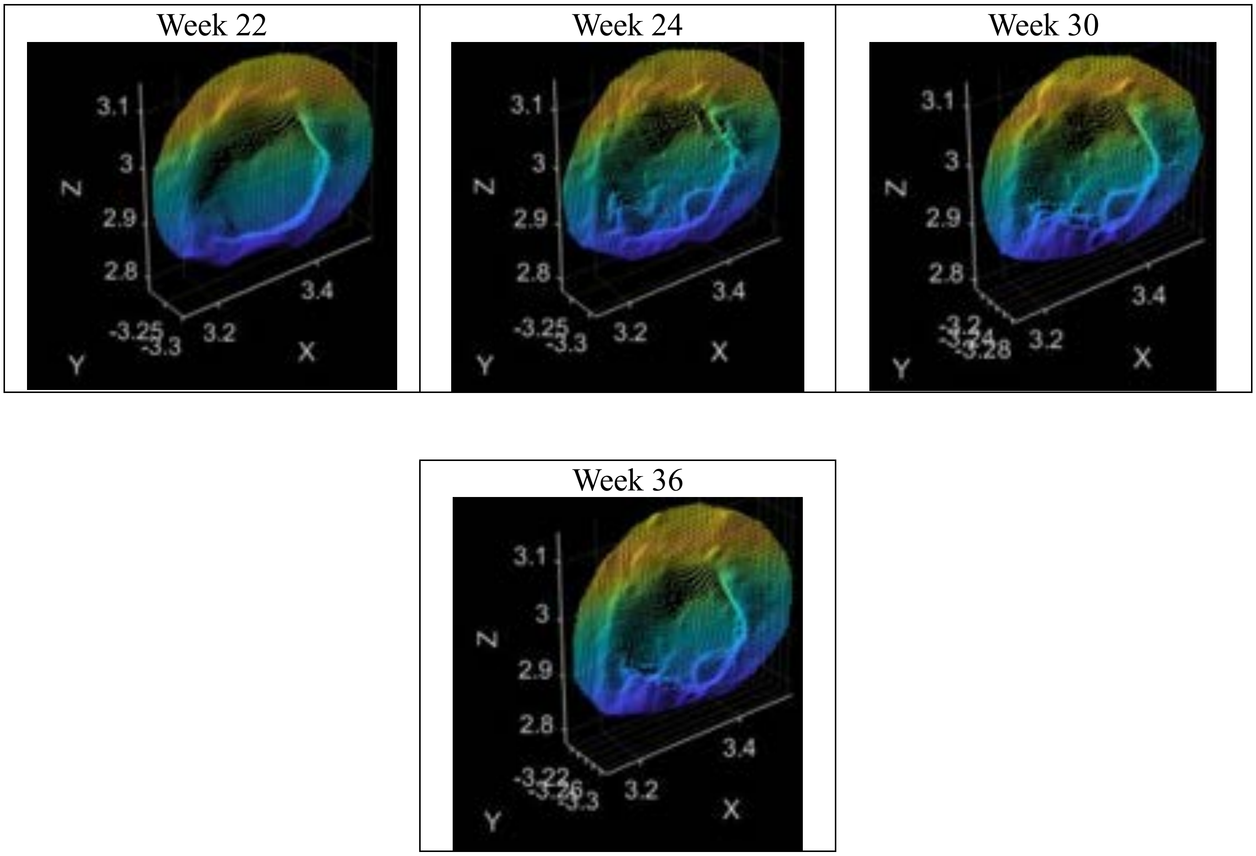

Figure C176. Change in meshed point cloud of exposed 2% area holiday data from Week 0 for C4Z1 continued.

Week 8	Week 12	Week 14
		

Week 16	Week 18	Week 22
		

Figure C177. Side with 2% area holidays for C4Z2.

Week 24	Week 30	Week 36
		

Figure C178. Side with 2% area holidays for C4Z2 continued.

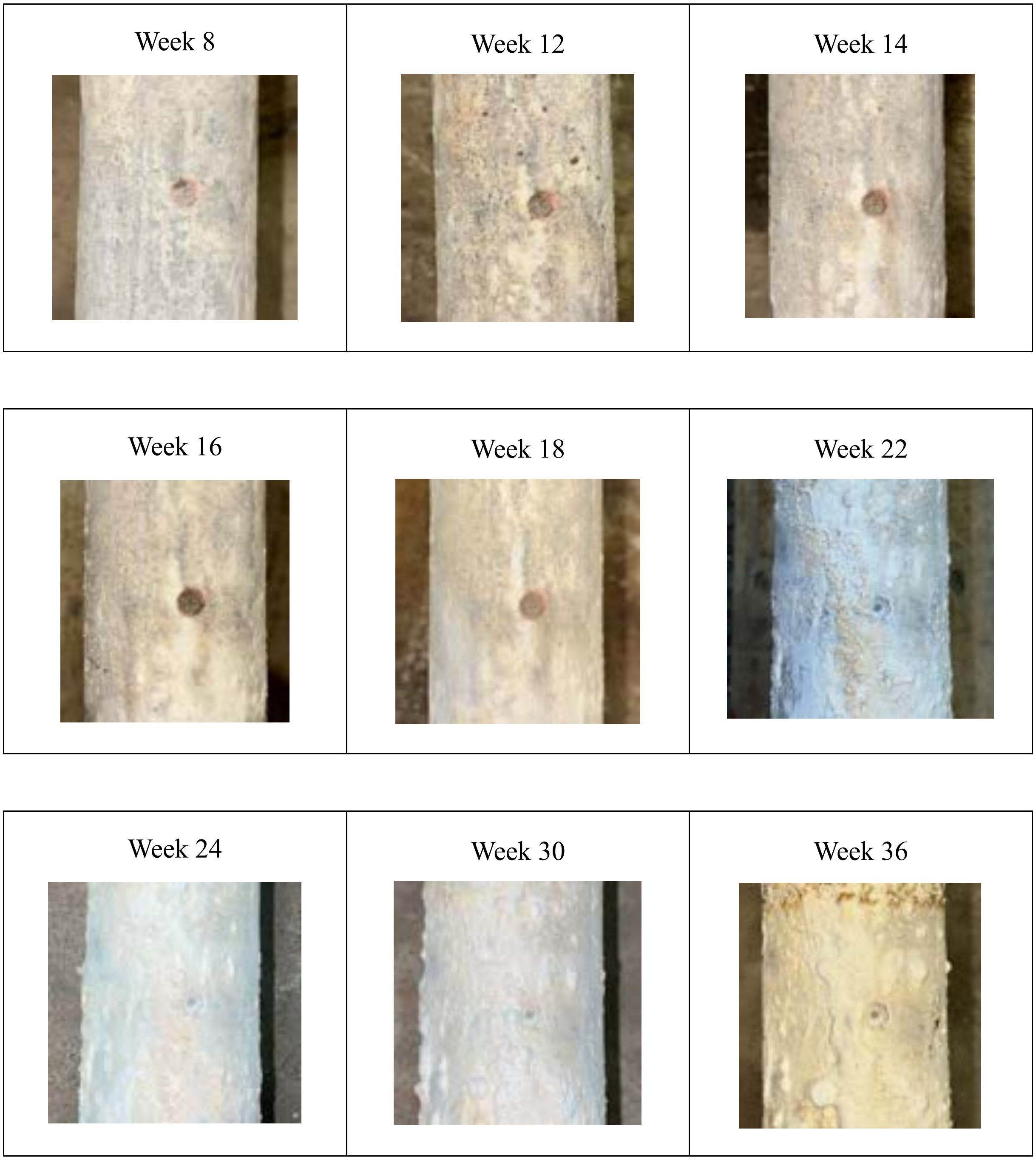

Figure C179. Exposed 2% area holiday for C4Z2.

Figure C180. Side with 1% area holidays for C4Z2.

Week 24	Week 30	Week 36
		

Figure C181. Side with 1% area holidays for C4Z2 continued.

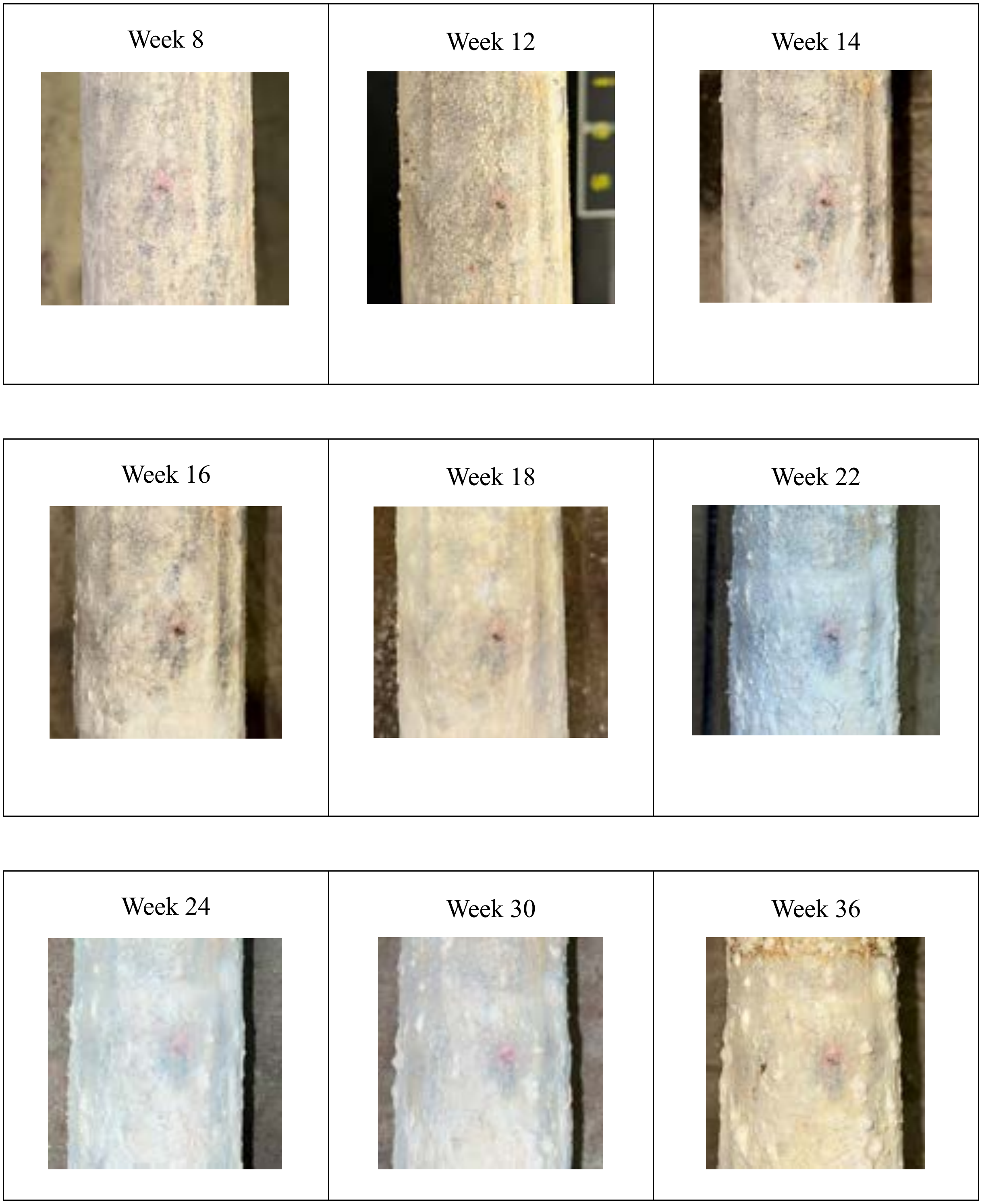

Figure C182. Exposed 1% area holiday for C4Z2.

Week 0

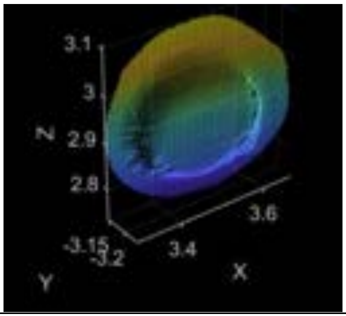

Week 2

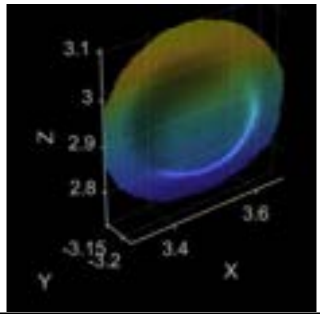

Week 4

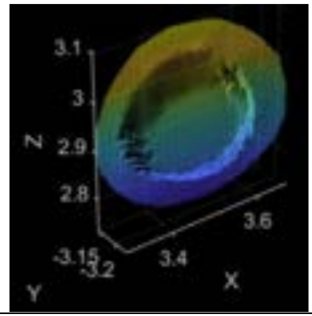

Week 6

Unavailable

Week 8

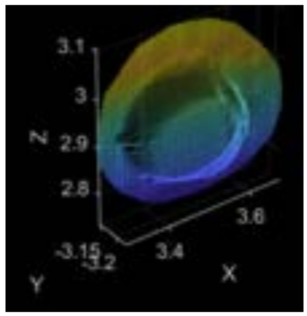

Week 12

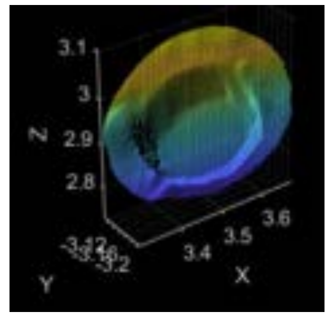

Week 14

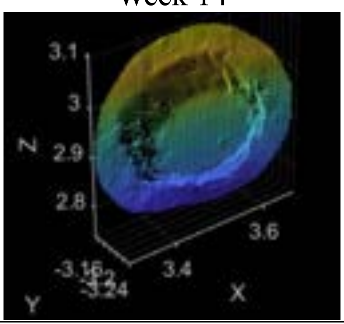

Week 16

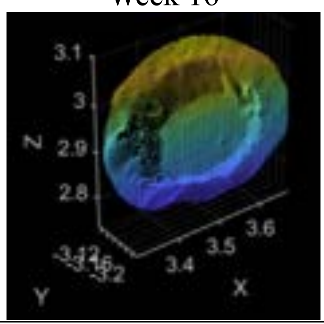

Week 18

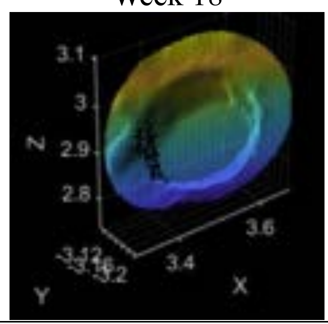

Figure C183. Change in meshed point cloud of exposed 2% area holiday data from Week 0 for C4Z2.

Week 22

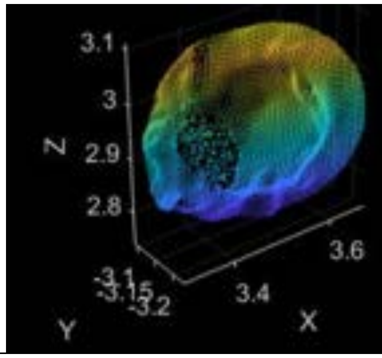

Week 24

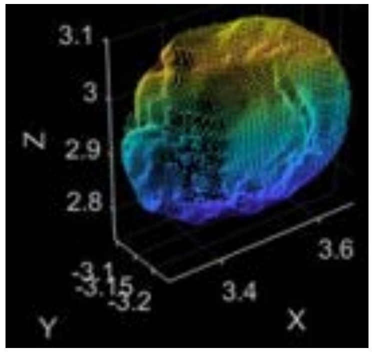

Week 30

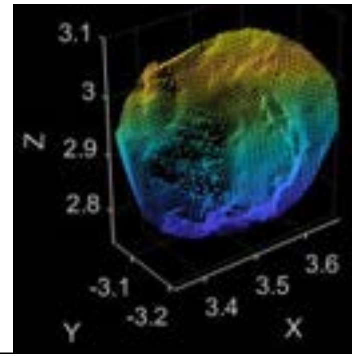

Week 36

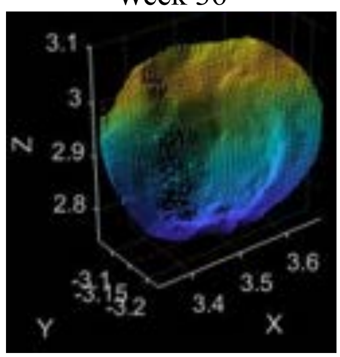

Figure C184. Change in meshed point cloud of exposed 2% area holiday data from Week 0 for C4Z2 continued.

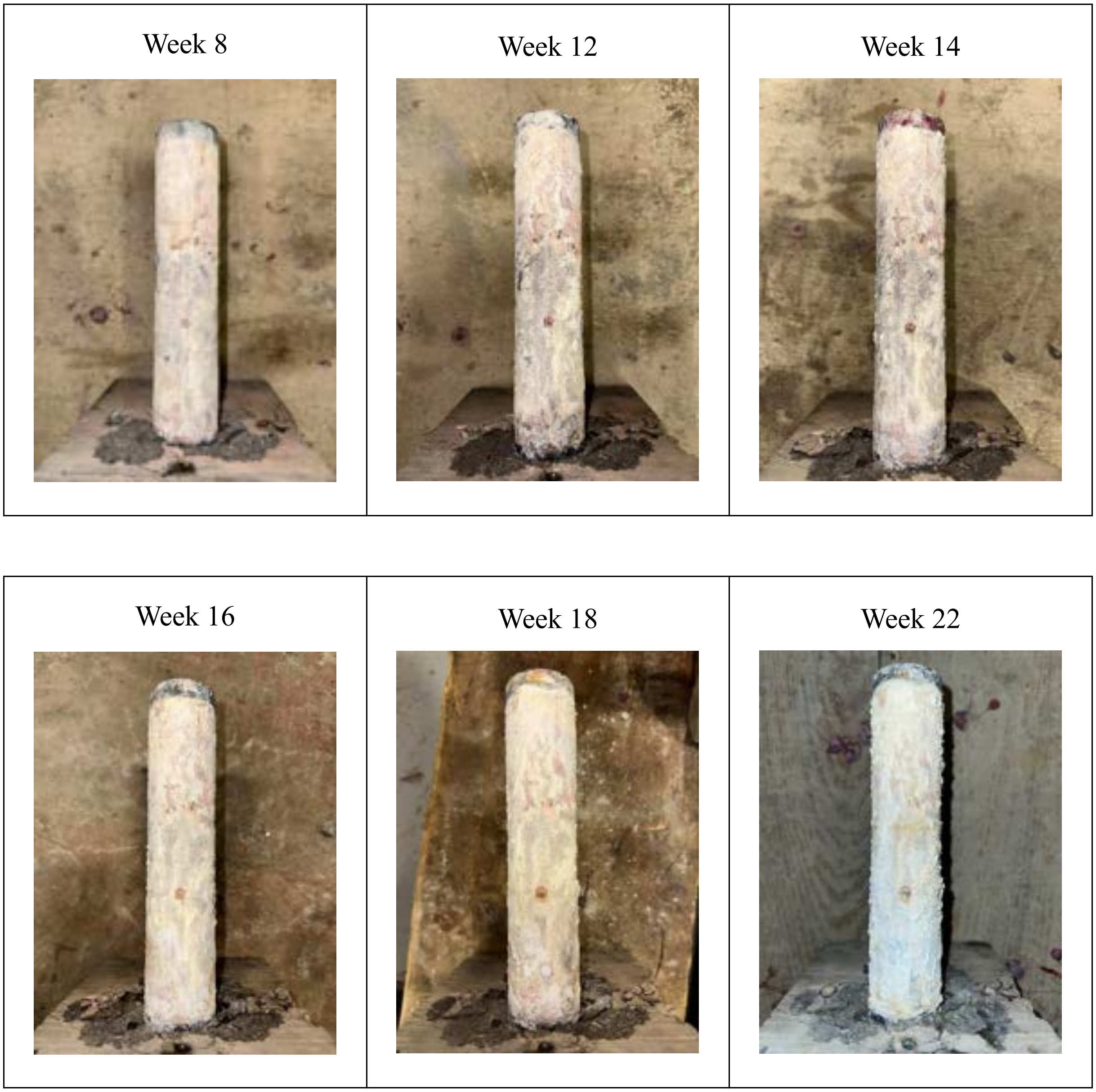

Figure C185. Side with 2% area holidays for C4Z3.

Week 24	Week 30	Week 36
		

Figure C186. Side with 2% area holidays for C4Z3 continued.

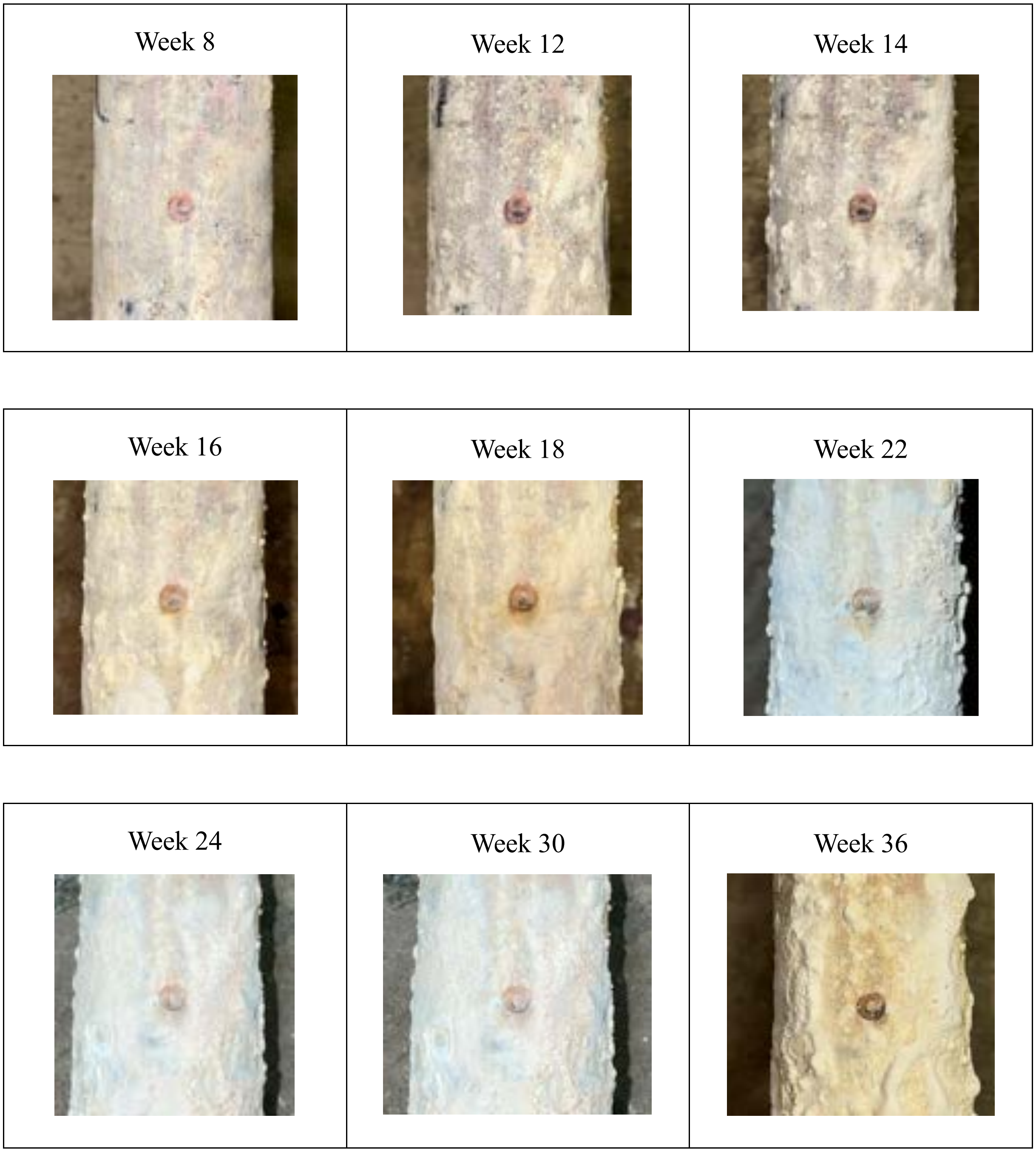

Figure C187. Exposed 2% area holiday for C4Z3.

Week 8	Week 12	Week 14
		

Week 16	Week 18	Week 22
		

Figure C188. Side with 1% area holidays for C4Z3.

Week 24	Week 30	Week 36
		

Figure C189. Side with 1% area holidays for C4Z3 continued.

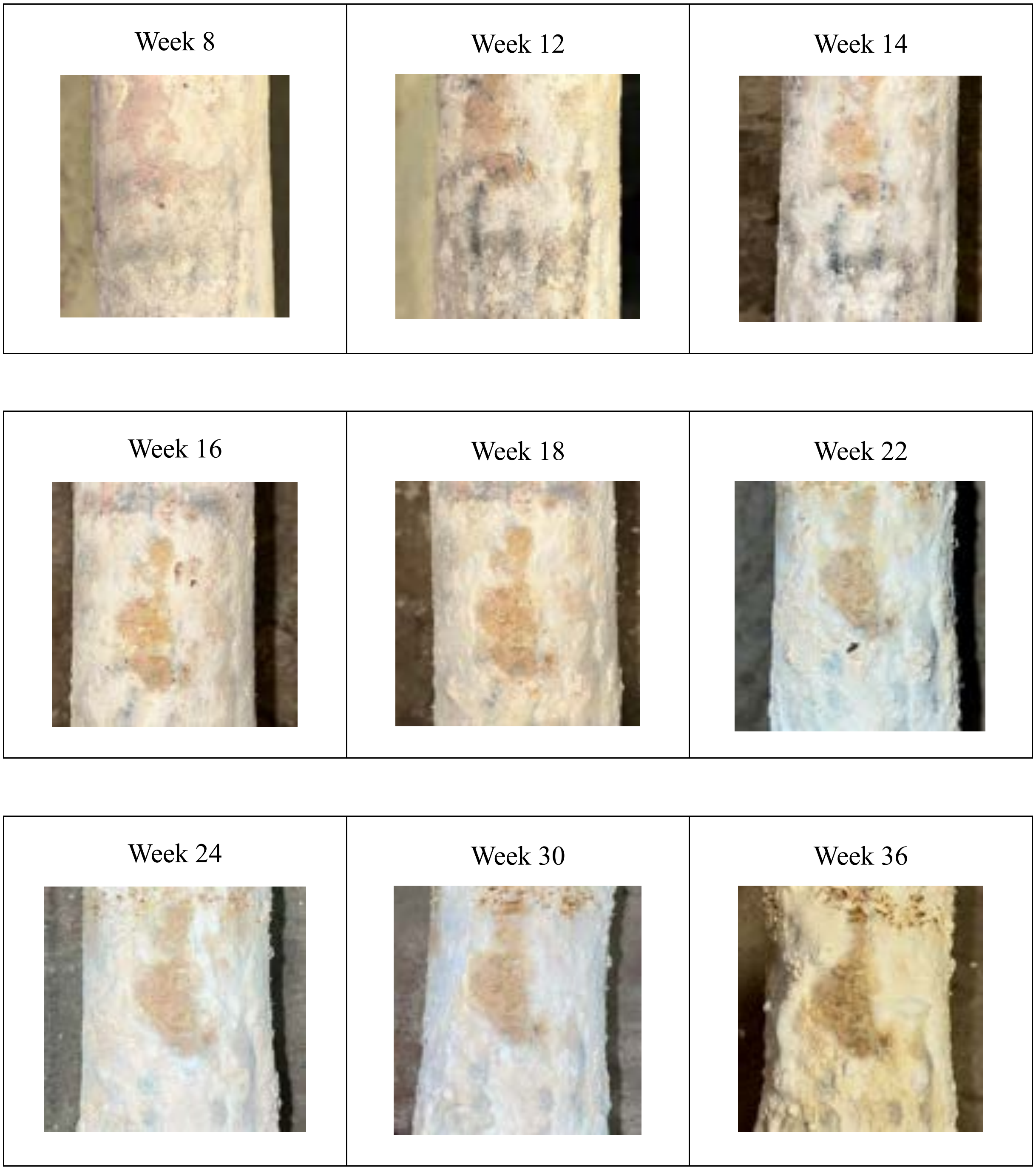

Figure C190. Exposed 1% area holiday for C4Z3.

Week 0	Week 2	Week 4
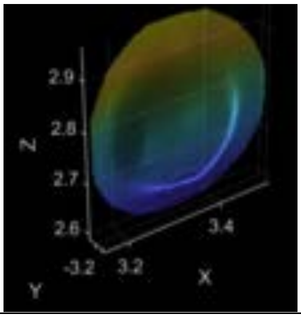	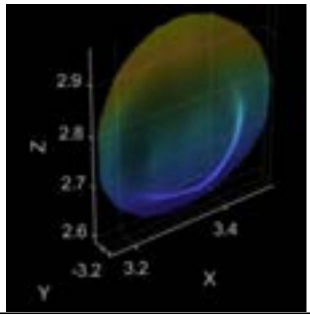	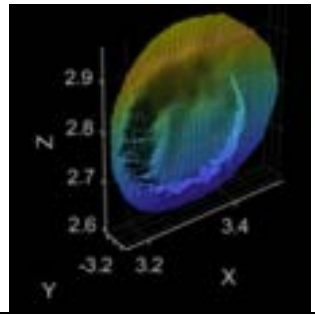
Week 6	Week 8	Week 12
Unavailable	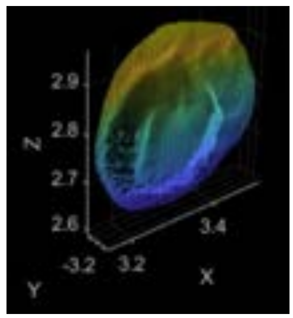	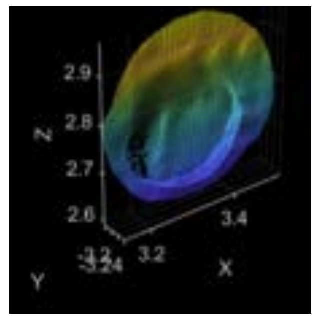
Week 14	Week 16	Week 18
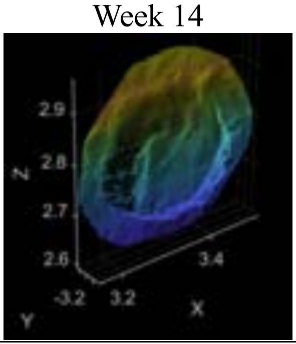	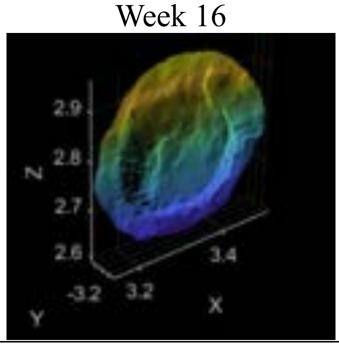	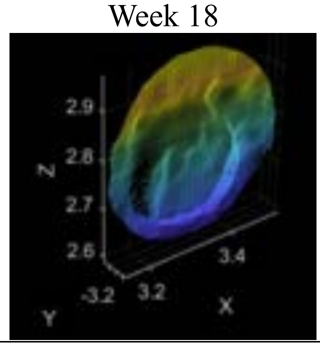

Figure C191. Change in meshed point cloud of exposed 2% area holiday data from Week 0 for C4Z3.

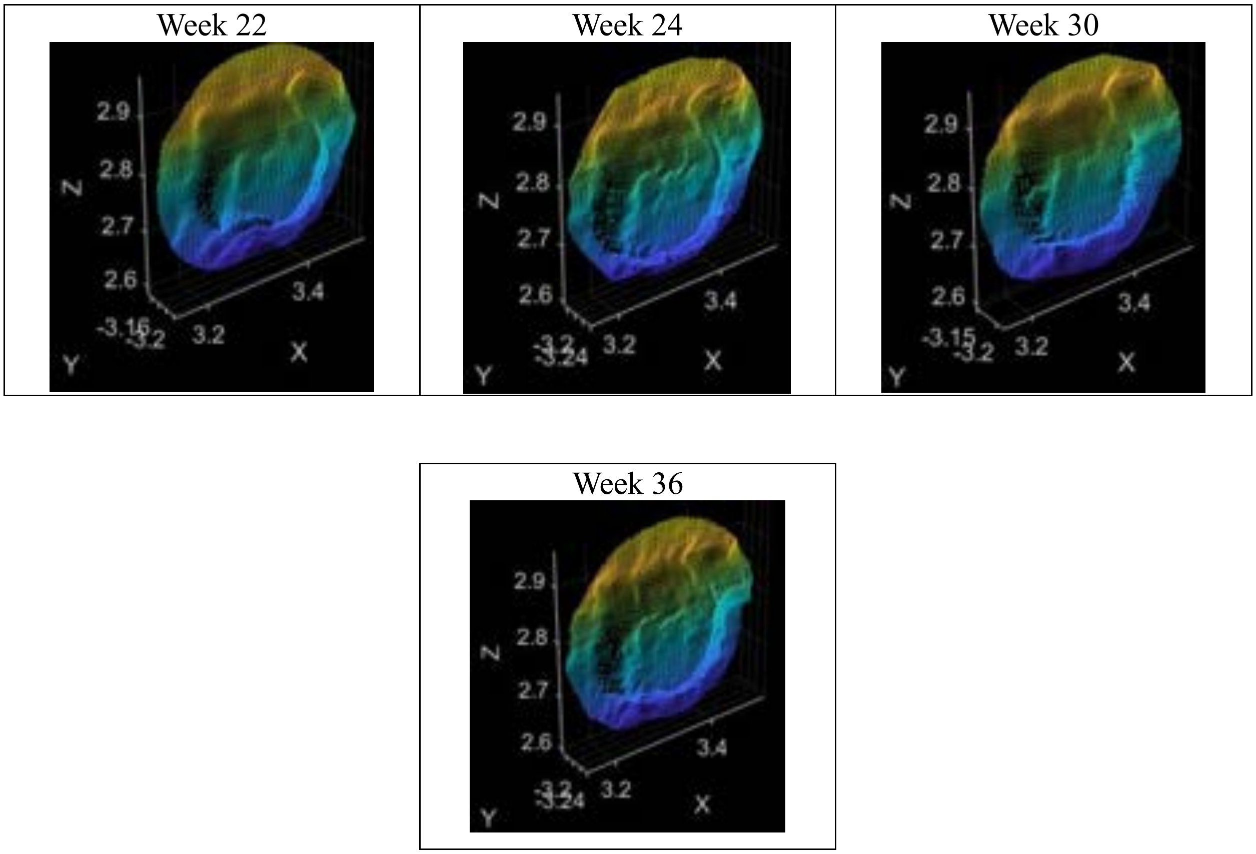

Figure C192. Change in meshed point cloud of exposed 2% area holiday data from Week 0 for C4Z3 continued.